Geology, structural evolution and controls of hydrothermal gold mineralization in the Eastern Karagwe-Ankole fold belt, North Western Tanzania

by

Corné Koegelenberg

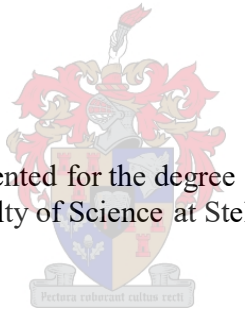

Dissertation presented for the degree of Doctor of Earth Sciences in the Faculty of Science at Stellenbosch University

Supervisor: Prof. Alexander F. M. Kisters

March 2016

Declaration

By submitting this thesis/dissertation electronically, I declare that the entirety of the work contained therein is my own, original work, that I am the sole author thereof (save to the extent explicitly otherwise stated), that reproduction and publication thereof by Stellenbosch University will not infringe any third party rights and that I have not previously in its entirety or in part submitted it for obtaining any qualification.

Signed:
Corné Koegelenberg
Date: March 2016

Abstract

In central-east Africa, the north-western margin of the Archaean Tanzania Craton (TC) is overlain by imbricated, low grade, volcano-sedimentary rocks of the Karagwe-Ankole belt's (KAB) Eastern Domain (ED). Centred in the ED, vast stretches of a sheared and Au mineralized basement-cover contact are exposed along margins of the Mugera-Nyakahura (MN) inlier. To date, no detail research has been done in the area and the regional geology has been described from only broad reconnaissance studies. As part of an exploration project the first high resolution geological maps of key prospects and larger, more encompassing, scale maps of the basement-cover region was compiled. Mapping was supplemented by a regional scale structural traverse of the ED and selected sampling for analysis of micro-structures, geochronology and oxygen isotopes.

The collective structural data has indicated that basement gneisses of the MN inlier may be considered as part of a forethrusted tectonic wedge caused by regional top-to-the-SE thick skinned thrusting. Above and in front of the wedge diagnostic back-thrusts and the reversal of kinematic fabrics in weak, often graphitic, metapelitic rocks of the Muyaga Group depict top-to-the-NW, hinterland-directed, tectonic transport along the main "roof" detachment. To the east under-thrusting of the coarse clastic Bukoba Group by the Muyaga Group has also created a distinct triangle zone at the frontal termination of the KAB.

^{39}Ar-^{40}Ar muscovite ages of detachment mylonites in the easternmost, and latest developing, parts of the KAB has constrained timing of D2 to at least 1326 ± 10 Ma. This age corresponds with the youngest end of the main phase of granite plutonism and mafic dyke emplacement in the KAB (1380 – 1328 Ma) and may point towards a Mesoproterozoic collisional event between the Congo- and Tanzania Cratons. U-Pb detrital zircon ages of the Muyaga- and Bukoba Groups have indicated uplift, erosion and subsequent reworking of Muyaga Group sediments and layered volcanics into the Bukoba basin after 1780 Ma, but before 1568 Ma. The Bukoba Group thus correlates with the Bwezigoro Group in SW Uganda, indicating the presence of an extensive Paleo- and/or Mesoproterozoic foreland basin overlying the western margin of the TC and Uganda Block.

Lastly, controls of D2 fluid flow and mineralization along the low angle phyllonitic detachment are linked to NE trending ramp structures that were most favourable for the initiation of slip and development auriferous quartz vein networks. Upwards into the Muyaga Group progressive

fold amplification and eventual fold-lock of second order anticlines, cored by competent and chemically re-active ferruginous mafic sills, are responsible for the late-kinematic development of auriferous quartz veins. Oxygen isotope values of D2 quartz veins and host rocks have indicated that fluids are derived from dehydrated clastic sediments of the Kagera Supergroup and, as such, may suggest that gold associated with greenstones of the TC have not been remobilized during D2 fold-and-thrust development in the ED.

Collectively these findings greatly enhance the understanding of the geological evolution of the KAB's easternmost parts and provides future research and exploration with a much improved geological background.

Opsomming

In Sentraal- en Oos-Afrika is die noord-westelike rand van die Argeïese Tanzanië Kraton (TK) oorlê deur geimbrikeerde, lae-graadse, vulkaan-sedimentêre gesteentes van die Karagwe-Ankole plooistelsel (KAP) se Oostelike Segment (OS). Sentraal in die OS is daar groot lengtes van ‘n gouddraende skuifskeur kontak tussen vloer- en bedekking gesteentes wat blootgestel is aan die rante van die Mugera-Nyakahura (MN) venster. Daar was nog geen navorsing in die omgewing gedoen nie en die regionale geologie is slegs vanuit breedvoerige verkenning beskryf. As deel van ‘n eksplorasie projek is die eerste hoë resolusie kartering van sleutel prospekte en groter, meer omvattende, skaal kaarte van die skuifskeur kontak vervaardig. Kartering is aangevul deur ‘n regionale skaal struktuur dwars-snit van die OS en selektiewe monsters vir die analiese van mikro-strukture, geokronologie and suurstof isotope.

Algehele struktuur data het aangedui dat basale gneisse van die MN venster wel deel mag wees van ‘n voor-stootverskuifde tektoniese wig gedurende regionale bo-na-die-SO dik vel stooting. Bo-op en voor die wig is kenmerkende terug-stote en die omkeer van kinematiese foliasies in swak, somtyds grafietise, meta-pelitiese gesteentes van die Muyaga Groep ‘n aanduiding van bo-na-die-NW, agterland gestuurde, tektoniese vervoer op die hoof “dak” vloeroorskuiwing. Na die ooste is onder-stoot van die Bukoba Groep deur die Muyaga Groep verantwoordelik vir die vorming van ‘n “driehoek” sone and die voorkant van die KAP.

^{39}Ar-^{40}Ar muskoviet ouderdomme van vloeroorskuiwing miloniete in die mees oostelike, en laasgevormde, dele van die KAP het D2 vervorming beraam tot en met 1326 ± 10 Ma. Die ouderdom vergelyk met die jongste fase van granite plutonisme and mafiese gang indringing in die KAP (1380 – 1328 Ma) en mag aanduidend wees van ‘n Mesoprotersoïese botsing tussen die Congo- en Tanzanië Kratons. U-Pb ditrale zirkoon ouderdomme van die Muyaga- en Bukoba Groepe het aangedui dat tektoniese oplig, erosie en gevolglike herwerk van Muyaga sedimente en vulkaniese lae binne in die Bukoba kom in na 1780 Ma, maar voor 1568 Ma. Die Bukoba Groep vergelyk dus met die Bwezigoro Groep van SW Uganda, wat aanduiding gee tot ‘n uitgebreide voorland kom oor die westerlike rand van die TK en Uganda blok.

Laastens, is die beheer van D2 vloeistof migrasie en mineralisasie langs die milonietiese vloeroorskuiwing gekoppel aan NO strekkende skuinstes wat mees gepas is vir begin van skuifskeer

glip en ontwikkeling van goud-yster draende kwarts aar netwerke. Opwaarts in die Muyaga Groep is aanhoudende vou-versterking en uiteindelike vou-sluiting van sekondêre antiklinale, gekern met harde en chemiese-reaktiewe plate, verantwoordelik vir die laat-kinematiese onwikkeling van goud-yster draende kwarts-are. Suurstof-isotoop waardes van D2 kwarts-are en gasheergesteentes dui aan dat vloeistowwe afkomstig is van gedehidreerde klastiese sedimente van die Kagera Supergroep en, gevolglik, aandui dat goud geassosieer met groenstene van die TK nie gemobiliseer was gedurende D2 verforming nie.

In die geheel het al die bevindinge grootliks bygedra tot die verstaan van die geologiese ontwikkeling van die KAP se OS en verskaf dit toekomstige navorsing en eksplorasie met ‘n verbeterde geologiese agtergrond.

Acknowledgements

I remember reading a note stuck on my father's desktop screen the night just before I was set to start studying at Stellenbosch. The note read, "Nou waarmee is jy nou regtig besig". At the time these words seemed simple: concentrate and do not get carried away doing things that are insignificant or meaningless. Now that I put pen to paper on the last paragraph of a journey that started nine years ago, those words put a lump in my throat, because they remind me of my parents' unwavering determination and sheer sacrifice to give their three sons the opportunities they never had. I dedicate this PhD whole heartedly to them and for their love and support I will be forever grateful.

My growth in a personal capacity and as a geologist has been influenced by many professors, lecturers and fellow students, but none more so than Alex Kisters. Your demeanour and conduct as a professional geologist and as a humble person has always been inspiring. Even more so, the trust you invested in my ability, even in the face of adversity, always gave me courage to pursue my dreams of becoming a passionate geologist. It seems fitting that you offered me this PhD opportunity and for that, I am immensely grateful. This project would certainly not have been possible, or such an enriching experience, without your seemingly endless knowledge and wit.

I would also like to thank geologists: Joas Kabete and the late Pieter Winkler, who initiated the project on behalf of Anglo Gold Ashanti Exploration (AGA). Without AGA's funding and support such a venture would have been impossible, given the remote location in NW Tanzania. Additional funding from the National Research Fund through a scarce skills bursary (Grant 81573) has also helped immensely. An integral part of my overall success in the field must however be attributed to the exceptional logistical organization by Gillian Williams. I have yet to meet a more charming person in the field. To my trustworthy field assistant, Esperius Kavako, I owe a great deal. His local knowledge and calm demeanour not only kept me safe and sane, but taught me invaluable lessons in life.

I cannot end without thanking Ian and Joey Basson, whom have given me the opportunity to express myself in the geological consultant industry, while also allowing me to complete my PhD. Thank you for your wholehearted encouragement and support.

Lastly to my wife, I can only be grateful for your unwavering support and patience. Since we met for the first time, you have been central in my reasoning. Thank you for sharing my tears, frustrations and excitement. I love you with all of my heart.

Table of Contents

List of Figures

List of tables

1. Introduction

1.1. Background and rationale

In Central- and East Africa the exploration of precious metals and minerals has a significant impact on the sustainability of major mining regions which serves as a powerful tool to enhance local and regional economic development. In the Lake Victoria region of Tanzania significant gold mining is largely confined to Neoarchaean greenstones of the Tanzania Craton (TC) which hosts some of the world's richest gold endowed terranes, including the East Lake Victoria- and Lake Nyanza Superterranes (Kabete et al., 2012). At present, an estimated 40 tonnes per year of gold is produced (Tanzania Chamber of Mines and Energy, 2015), but the industry as a whole has been earmarked for significant growth in the near future in order to contribute more towards the national GDP. However, in recent times the failure to identify new gold deposits or to increase present gold resources have raised concerns that traditional greenstone terranes of the TC are approaching maturity with regards to gold endowment and exploration (e.g. Goldfarb et al., 2009; Kabete et al., 2012).

As a result mining companies have shifted exploration efforts off craton and into the lesser known Paleo- to Mesoproterozoic belts bordering the TC. The north-western margin of the TC, which hosts the gold-endowed Lake Victoria Superterrane, is overlain by volcano-sedimentary rocks of the Karagwe-Ankole belt (KAB) (Tack et al., 2010). A unique feature of the KAB is that its frontal- or easternmost domain contains the regional scale, up to 150 km long and 20 km wide, Mugera-Nyakahura (MN) inlier (also referred to as the Nyakahura-Burigi Terrane) which exposes basement-cover contacts between younger overlying sequences and Archaean TTG's and greenstones of the TC (Cahen et al., 1987; Tack et al., 1994; Kabete et al., 2012). Several artisanal gold mines in the Kagera Province, close to rural towns of Muzani and Mihongoro, follow basement-cover contacts along the eastern margin of the MN inlier, but there is, to date, no research on the mineralization. Similarly, the geological setting of the easternmost parts of the KAB is only described in a broad regional context (e.g. Cahen et al., 1987; Klerkx et al., 1987; Fernandez-Alonso and Theunissen, 1998; Tack et al., 1994, 2010; Fernadez-Alonso et al., 2012) and mainly through reconnaissance and remote sensing studies. Also, the ages of major litho-tectonic units have become clear only in recent years (Deblond et al., 2001; Fernadez-Alonso et al., 2012). Regional, quarter degree, geological maps (1:125000)

were only compiled in 1967, while most structural traverses of a reconnaissance nature were done between 1922 and 1951 (Quarter degree sheets 29 and 30; Mineral Resources Division, Tanzania). In other words, the geological framework and, as such, the mineralization potential and the broader context of this region in Tanzania and bordering Burundi, Rwanda and SW Uganda have, to date, been relative unknowns.

The consequence of a changed exploration philosophy in Tanzania has led AngloGold Ashanti (AGA) Greenfields exploration, in May of 2012, to initiate a regional exploration programme focussing on the eastern basement-cover contacts of the MN inlier and associated artisanal mines. As a first step high resolution geological mapping of the mines and surrounding country rock was prioritized, followed by target generation for subsequent diamond drilling within designated licenced areas. The responsibility of mapping, geological evaluation and scientific reporting was undertaken by the author (Corné Koegelenberg) over a combined period of four months. Logistical support through AGA was also provided to access more remote areas of the eastern KAB and far outside exploration licence boundaries, in effect, to increase the scope of the PhD with more regional mapping, traversing and sampling.

1.2. The Kibara- and Karagwe-Ankole belt system

1.2.1. Regional geology

The Mesoproterozoic Kibara Belt (senso lato) of central east Africa has traditionally been known as a continuous 1300 km, NNE-SSW trending, belt spanning over southwest Uganda, northwards across Rwanda, Tanzania, Burundi and into the Democratic Republic of the Congo (DRC) (e.g. Cahen et al., 1984 and references therein). However, recent studies have distinguished a northern KAB from a southern Kibara Belt (sensu stricto) (KIB), separated by subsequent uplift and reactivation of the Paleoproterozoic Rusizi-Ubende Belt during Rodinian- and/or Pan-African orogenic events (Tack et al., 2010 and references therein; Fernandez-Alonso et al., 2012). Seemingly separate basin evolutions for the KAB and Kibara belt have also been suggested (Fernandez-Alonso et al., 2012).

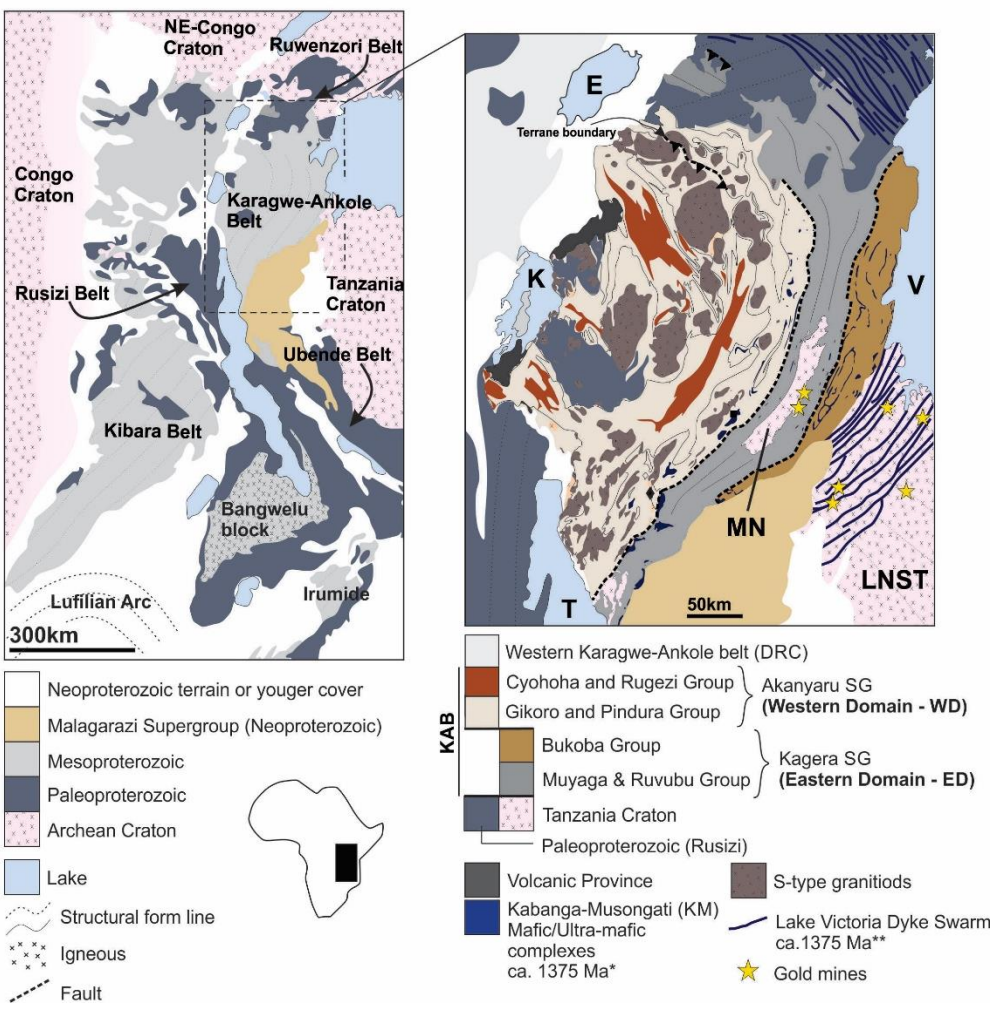

Figure 1: Regional geological framework of central-east Africa and the Karagwe-Ankole Belt (KAB). Geological maps modified after *Tack et al. (2010), Fernandez-Alonso et al. (2012) and **Mäkitie et al. (2014). Lakes: Kivu (K); Tanganyika (T); Edward (E); Victoria (V). Terranes: Mugera-Nyakahura inlier (MN); Lake Nyanza Superterrane (LNST)

The northern KAB was further divided into a structurally and lithologically distinct Western- and Eastern Domain (WD and ED) and is separated by a linear corridor of mafic- to ultramafic intrusions assigned to the Kabanga-Musongati (KM) alignment (Tack et al., 1994, 2010). The WD and ED are interpreted to be underlain by contrasting basements of the Paleoproterozoic Rusizian- and/or Ruwenzori belt in the west and the TC in the east (Tack et al., 2010). Consequently the WD and ED domains are viewed as separate tectonostratigraphic units, assigned to the Mesoproterozoic Akanyaru Supergroup and Paleoproterozoic Kagera Supergroup respectively (Fernandez-Alonso et al., 2012 and references therein), which record a significant decrease in deformation intensity and metamorphic grade (amphibolite to greenschist) from west to east and over the TC (Klerkx et al., 1987; Tack et al., 1994).

Much of the previous research in the KAB has focused on the higher-grade volcano-sedimentary sequences of the Akanyaru Supergroup (WD), associated granite plutonism, and metallogeny and mineralization (e.g 1994; Evans et al., 2000; Dewaele et al., 2008, 2010, 2011, 2013; Tack et al., 2010; Fernandez-Alonso et al., 2012). Intrusive into the Akanyaru Supergroup are several suites of mainly S-type granitiods ranging in age from ca. 1566 – 1445 Ma to 1380 – 1330 Ma, with an apparent peak of granite plutonism at ca. 1380 – 1375 Ma (Buchwaldt et al., 2008; Tack et al., 2010). Emplacement of later and less voluminous ca. 1205 Ma A-type granitoids and ca. 986 Ma tin granites are also recorded (Tack et al., 2010). Regional mafic plutonism is defined by ultra-mafic layered intrusives and plugs of the ca. 1400 – 1360 Ma KM alignment and the, ca. 600 km long and arcuate, ca. 1375 Ma Lake Victoria Dyke Swarm (LVDS) (Deblond et al., 2001; Maier et al., 2007; Tack et al., 2010; Mäkitie et al., 2014). Collectively these contemporaneous mafic to ultra-mafic rocks are referred as the Northern Kibaran Igneous Provence (Westerhof et al., 2014)

Notably, the base of the Akanyaru Supergroup has not been observed. However, quartzites from the lowermost described Gikoro Group have recorded maximum U-Pb detrital zircon ages of ca. 1412 – 1420 Ma and, as such, indicate significant sedimentation after ca. 1412 Ma, but before emplacement of the sills and dykes of ca. 1375 KM alignment. This period of sedimentation and volcanic activity has been suggested to relate to wide spread intracratonic rifting linked to the emplacement of the ca. 1375 Ma KM alignment, LVDS and peak granite plutonism at 1375 – 1380 Ma (see below). The uppermost Akanyaru Supergroup is defined by the younger Rugezi- and Cyohoha Groups which have an apparent maximum U-Pb detrital zircon age of ca. 1220 Ma (Fernandez-Alonso et al., 2012).

To the east, the unrelated Kagera Supergroup (ED) consists of lithologically distinct sub-basins of the Muyaga- and Bukoba Groups, of which the stratigraphical relationship is poorly constrained. Notably, felsic granitoids are conspicuously absent, compared to the WD. Felsic tuffs at the base of the shale dominated Muyaga Group have indicated a clear onset of sedimentation since ca. 1780 Ma, but no age constraints are available for the seemingly contemporaneous quartzite dominated Bukoba Group. Sedimentation of the Kagera Supergroup has likewise been constrained to before the emplacement of ca. 1375 Ma LVDS (Deblond et al., 2001).

1.2.2. Structural evolution of the KAB

The structural evolution and geodynamic setting of the KAB have been somewhat enigmatic and, to date, regional models were mainly based on reconnaissance mapping and geochemical and geochronological work on selected granites and sediments of the WD. Regional and detailed structural studies are lacking. Klerkx et al. (1987) initially suggested a series of D1, D2 and D2' deformation events in the KAB based on fabric relationships and associated magmatism. This was adopted and revised later by Fernadez-Alonso and Theunissen (1998) who also suggested three main deformation events, D1, D2 and D3. The early D1 deformation and associated bedding-parallel foliation was interpreted to have formed during a period of crustal extension and low-angle and/or bedding parallel shearing - the décollement phase, after Klerkx et al (1987). The structural contacts at the base of the Kagera Supergroup were argued to be a prominent S1 feature in the ED. Recently, Tack et al. (2010) further associated D1 with the main phase of mafic volcanism and related granite plutonism at ca. 1375 Ma. This rationale was adopted by Fernandez-Alonso et al. (2012) who envisaged a protracted episode of intracontinental rifting, subsequent basin formation and sedimentation between ca. 1412 – 1000 Ma. The subsequent and main D2 (S2) fabric forming event associated with the top-to-the-east fold-and-thrust kinematics causing the distinct arcuate trend of the KAB was attributed to late far-field stresses of the 1.0 Ga Irumide belt collision to the southeast (Fernandez-Alonso et al., 2012). A late Pan-African D3 (S3) shear event is also constrained to the WD and was likewise attributed to far-field stresses, but from plate margin processes relating to the ca. 550 Ma East African Orogen. These late deformation events where linked with the emplacement of ca. 986 Ma tin granites in the WD and associated Nb-Ta-Sb and Sn-W mineralized pegmatites and quartz veins which record tectono-thermal activity at ca. 975 Ma and ca. 592 Ma (Dewaele et al., 2011).

Recent models describing the D2 event (after Fernandez-Alonso et al., 2012) are, however, controversial and differs drastically from more traditional D2 subduction-driven, convergence and collisional stages postulated for the southern KIB (Kampunzu 1986; Kokonyagi et al., 2004, 2005, 2006, 2007) and previously for the KAB (Tack et al., 1994). Considering regional corresponding structural trends, both contrasting schools of thought, in effect, envisage a single tectonic setting for the KIB and KAB of either: [1)] oceanic-arc subduction, convergence and eventual collision between ca. 1380 – 1000 Ma; or [2)] intracontinental rifting, protracted extension and late (ca. 1.0 Ga) basin closure over the same period. Worth mentioning is that the most recent geochemical characterization

of granite plutonism the KIB and KAB supports regional subduction, convergence and collision between the Congo- and Tanzania Cratons (Debruyne et al., 2015).

1.3. Mesothermal lode gold mineralization

Globally mesothermal- or orogenic gold deposits are broadly defined as epigenetic, high grade, quartz ± carbonate vein hosted mineralized bodies spatially associated with large shear zones in tectonic settings with protracted deformation histories (e.g. Hodgson, 1987; Goldfarb et al., 2001). This distinct form of mineralization lends itself to collisional tectonics and subsequent accretion of terranes along continental plate margins (e.g. Kerrich and Cassidy, 1994), in other words, tectonic settings that are defined by significant periods of horizontal crustal compression and/or transpression (e.g. Sibson et al., 1988). The inherent association of mineralization with quartz veining along shear zones, over a broad range of upper- to mid-crustal conditions (200 – 650^{o}C, 1 – 5 Kbar), highlights supralithostatic fluid pressures and structural control of fluid flow (Groves et al., 1998, 2000; Ridley and Diamond, 2000; Goldfarb et al., 2001). The high volumes of fluid flow required for economic grade mineralization greatly focusses along active regional faults and/or shear zones which enhances rock permeability through either brittle failure and/or inducing lower hydrostatic gradients along high strain zones (Ridley, 1992; Sibson and Scott, 1998).

However, economic gold loads are always localized rather than following the entire extent of these fault systems. Studies (Hodgson, 1987; Sibson et al., 1988, Sibson, 1992; Ettner et al., 1994; Goldfarb et a., 2005) have emphasized the association of gold mineralization with kinematically late and/or “mis-orientated” shear zones, i.e. shear zones at relatively high angles to the principal direction of shortening, that record a distinct “brittle-ductile” behaviour, a condition mostly favoured under greenschist facies conditions. The subsequent development of discrete shears and fractures are key to the accumulation and/or containment of fluids that are overpressured to near lithostatic values and the intermitted release thereof, causing fault-valve behaviour (Sibson et al., 1988; Sibson, 1992). Cyclic fluid pressure fluctuations greatly affect gold solubility by destabilizing Au-S or Au-Cl complexes (Zhu et al., 2011, and references therein), which is essential to the mineralization process at a mid- to upper crustal level.

In general the relationship between brittle-ductile deformed terranes and fluid flow explains the close spatial distribution of auriferous quartz vein systems with regional “mis-orientated” shear

zones. The kinematics of shear zones together with the geometry and rheological strength host lithologies largely determine the orientation of quartz veins, but also the overall geometry of the ore bodies (Hodgson, 1987; Ridley and Diamond, 2000). Therefore, the controls and shape of a particular load gold system greatly depends on a comprehensive understanding of the underlying structural and lithological data and its implications for fluid flow during mineralization.

1.4. Research themes and thesis structure

The initial project design was aimed at two main aspects, namely to (1) provide a geological (lithological, structural, tectonic, geochronological) framework for the hitherto almost unknown eastern parts of the KAB, in order to (2) place existing gold prospects and artisanal mining of the area into a regional geological context, developing structural and lithological criteria and model concepts for gold exploration that would allow for the targeting of new prospects.

This approach and line of thought resulted in three main papers, that address, in chronological order, the structural evolution and architecture of the eastern KAB (paper 1), the broader regional setting and timing of tectonism (paper 2), integrated with the mine-scale controls of fluid flow and mineralization (paper 3).

1) Firstly, regional studies have described structural and/or sheared contacts at the base of the Kagera Supergroup (Tack et al., 1994), but little actual structural data is presented that describes the dynamic behaviour of the overriding sediments with respect the MN inlier. Regardless, Kabete et al. (2012) speculated that the MN inlier represented a basement wedge thrusted eastwards and over younger KAB sediments, while Feranadez-Alonso and Theunissen (1998) proposed a gentle basement “pop-up” structure. Furthermore, studies have mainly indicated overall gentle deformation for the eastern parts of the KAB, while the western parts of the KAB is contrastingly intensely deformed (e.g. Tack et al., 1994; Fernadez-Alonso and Theunissen, 1998). As such the structural setting of the MN inlier has remained largely enigmatic and somewhat insignificant with respect to the broader D2 evolution of the eastern KAB. The first research paper presented in this thesis addresses these issues and presents the first detailed kinematic structural data in the form of a regional traverse across the eastern KAB and onto the TC. From this, not only the structural evolution of the

MN inlier and rocks of the Kagera Supergroup, are described, but also the regional tectonic evolution of the KAB is discussed.

2) The new structural data and model highlight discrepancies between recently proposed far-field D2 compressional models (Fernandez-Alonso et al., 2012) and the overall kinematic fabric of the ED. The new model suggested that D2 structures where more aligned with collisional tectonics from the west, rather than the proposed far-field stresses from the east and north-east (Fernandez-Alonso et al., 2012). However, any tectonic model and particularly correlations of deformation events across the belts remain tentative as long as the actual timing of the main D2 event remained unconstrained by any age data. The second paper amends this by presenting kinematics and ^{39}Ar-^{40}Ar mineral age data from D2 phyllonites and mylonites along the base of the Kagera Supergroup, which constrain the timing of deformation in the eastern parts of the belt. Further U-Pb detrital zircons ages from the Kagera Supergroup are also presented to investigate the timing of sedimentation and subsequent basin reworking. Collectively the new age data has been used to constrain the timing of D2, but also provide new insights into formation of sub-basins of the Kagera Supergroup.
3) Given the geological background and context improved upon by the first two papers, the last research paper discusses structural controls on fluid flow and gold mineralization along the MN inlier. Several distinct deposits, located at different structural positions with respect to the sheared base of the Kagera Supergroup are presented in detail. Stable oxygen isotopes are presented for quartz vein stockworks to constrain possible fluid sources. Overall the data is used to describe a potential regional scale sheared basement-cover contact, exposed over a strike extent of ca. 150 km, along which there are structurally and/or lithologically controlled zones of significant silicification and Au mineralization.

Aspects of the research, mainly referring to data presented in the first and second paper, was also presented at the 25th Colloquium of African Geology (August, 2014). The published abstract can be viewed in Appendix A. A further presentation, regarding fluid flow and gold mineralization, is also planned for the International Geological Conference starting on the 27th of August 2016.

1.5. References

Buchwaldt, R., Toulkeridis, T., Todt, W., Ucakuwun, E.K., 2008. Crustal age domains in the Kibaran belt of SW-Uganda: combined zircon geochronology and Sm–Nd isotopic investigation. Journal of African Earth Sciences 51, 4–20.

Cahen, L., Snelling, N.J., Delhal, J., Vail, J.R., Bonhomme, M., Ledent, D., 1984. The Geochronology and Evolution of Africa. Oxford University Press, Oxford, 512 pp.

De Waele, B., Johnson, S.P., Pisarevski, S.A., 2008. Palaeoproterozoic to Neoproterozoic growth and evolution of the eastern Congo Craton: its role in the Rodinia puzzle. Precambrian Research 160, 127–141.

De Waele, S., Henjes-Kunst, F., Melcher, F., Sitnikova, M., Burgess, R., Gerdes, A., Alonso Fernandez, M., De Clercq, F., Muchez, P., Lenmann, B., 2011, Late Neoproterozoic overprinting of cassiterite and columbite-tantalite bearing pegmatites of the Gatumba area, Rwanda (Central Africa). Journal of African Earth Sciences 61, 10 – 26.

Deblond, A., Punzalan, L.E., Boven, A., Tack, L., 2001. The Malagarazi Supergroup of SE Burundi and its correlative Bukoban Supergroup of NW Tanzania: Neo- and Mesoproterozoic chronostratigraphic constraints from Ar–Ar ages on mafic intrusive rocks. Journal of African Earth Sciences 32, 435–449.

Debruyne, D., Hulsbosch, N., Van Wilderode, J., Balcaen, L., Vanhaecke, F., Muchez, P., 2015. Regional geodynamic context for the Mesoproterozoic Kibara Belt (KIB) and the Karagwe-Ankole Belt: evidence from geochemistry and isotopes in the KIB. Precambrian Res. 264, 82–97.

Dewaele, S., De Clercq, F., Muchez, P., Schneider, J., Burgess, R., Boyce, A. & Fernandez-Alonso, M., 2010. Geology of the cassiterite mineralization in the Rutongo Area, Rwanda (Central Africa): current state of knowledge'. Geologica Belgica, 13, 91-112.

Dewaele, S., Goethals, H., Thys, T., 2013. Mineralogical characterization of cassiterite concentrates from quartz vein and pegmatite mineralization of the Karagwe-Ankole and Kibara Belts, Central Africa. Geologica Belgica 16/1-2, 66-75

Ettner, C.D., Bjørlykke, A. and Anderson, T., 2003. Fluid evolution and Au-Cu genesis along a shear zone: a regional fluid inclusion study of shear zone-hosted alteration and gold and copper mineralization in the Kautokeino greenstone belt, Finnmark, Norway. Journal of Geochemical Exploration, 49, 233-267.

Evans, D.M., Boadi, I., Byemelwa, L., Gilligan, J., Kabete, J., Marcet, P., 2000. Kabanga magmatic sulphide deposits, Tanzania: morphology and geochemistry of associated intrusions. Journal of African Earth Sciences 30, 651–674.

Fernandez-Alonso, M., Cutten, H., De Waele, B., Tack, L., Tahon, A., Baudet, D., Barritt, S.D., 2012. The Mesoproterozoic Karagwe-Ankole Belt (formerly the NE Kibara Belt): The result of prolonged extensional intracratonic basin development punctuated by two short-lived far field compressional events. Precambrian Research 216-219, 63-86.

Fernandez-Alonso, M., Theunissen, K., 1998. Airborne geophysics and geochemistry provide new insights in the intracontinental evolution of the Mesoproterozoic Kibaran belt (Central Africa). Geological Magazine 135, 203–216.

Goldfarb, R.J., Baker, T., Dube, B., Groves, D.I., Hart, C.J.R., Craig, J.R., Gosselin, P., 2005. Distribution, character and genesis of gold deposits in metamorphic terranes, Economic Geology 100th Anniversary Volume, pp. 407-250

Goldfarb, R.J., Groves, D.I., Kerrich, R., Leach, D., 2009. Metallogenic evolution on an evolving Earth. In: Williams, P.J., et al. (Ed.), Smart Science for Exploration and Mining. Proceedings of the Tenth Biennial SGA Meeting, Townsville, pp. 11–13.

Groves, D.I., Goldfarb, R.J., Gebre-Mariam, M., Hagemann S.G. and Robert, F., 1998. Orogenic gold deposits: A proposed classification in the context of their crustal distribution and relationship to other gold deposit types, Ore Geology Reviews 13, 7–27.

Groves, D.I., Goldfarb, R.J., Knox-Robinson, C.M., Ojala, J., Gardoll, S., Yun, G., Holyland, P., 2000. Late-kinematic timing of orogenic gold deposits and significance for computer-based exploration techniques with emphasis on the Yilgarn block, Western Australia, Ore Geology Reviews 17, 1-38.

Hodgson, C.J., 1987. The structure of shear-related, vein-type gold deposits: A review, Ore Geology Reviews, Vol. 4, pp. 231-273 Goldfarb et al., 2001

Kabete, J.M., Groves, D.I., McNaughton, N.J., Mruma, A.H., 2012. A new tectonic and temporal framework for the Tanzanian Shield: implications for gold metallogeny and undiscovered endowment. Ore Geology Reviews. doi:10.1016/j.oregeorev.2012.02.009

Kampunzu, A.B., Rumvegeri, B.T., Kapenda, D., Lubala, R.T., Caron, J.P.H., 1986. Les Kibarides d'Afrique centrale et orientale: une chaîne de collision. UNESCO, Geology for Development Newsletter 5, 125–137.

Kerrich, R., and Cassidy, K.F., 1994. Temporal relationships of lode gold mineralization to accretion, magmatism, metamorphism and deformation – Archean to present: A review, Ore Geology Reviews, Vol. 8, pp. 263-310

Klerkx, J., Liégeois, J.-P., Lavreau, J., Claessens, W., 1987. Crustal evolution of the northern Kibaran Belt, eastern and central Africa. In: Kröner, A. (Ed.), Proterozoic Lithospheric Evolution, volume 17, American Geophysical Union and the Geological Society of America, pp. 217–233.

Kokonyangi, J., Armstrong, R.A., Kampunzu, A.B., Yoshida, M., Okudaira, T., 2004. U–Pb zircon geochronology and petrology of granitoids from Mitwaba (Katanga, Congo): implications for the evolution of the Mesoproterozoic Kibaran belt. Precambrian Research 132, 79–106.

Kokonyangi, J., Kampunzu, A.B., Armstrong, R., Arima, M., Yoshida, M., Okudaira, T., 2007. U–Pb SHRIMP Dating of Detrital Zircons from the Nzilo Group (Kibaran Belt): implications for the source of sediments and Mesoproterozoic Evolution of Central Africa. Journal of Geology 115, 99–113.

Kokonyangi, J., Kampunzu, A.B., Armstrong, R., Yoshida, M., Okudaira, T., Arima, M., Ngulube, D.A., 2006. The Mesoproterozoic Kibaride belt (Katanga, SE D.R. Congo). Journal of African Earth Sciences 46, 1–35.

Kokonyangi, J., Kampunzu, A.B., Poujol, M., Okudaira, T., Yoshida, M., Shabeer, K.P., 2005. Petrology and geochronology of Mesoproterozoic mafic–intermediate plutonic rocks from Mitwaba (D. R. Congo): implications for the evolution of the Kibaran belt in central Africa. Geological Magazine 142, 109–130.

Maier, W.D., Peltonen, P., Livesey, T., 2007. The ages of the Kabanga North and Kapalagulu intrusions, Western Tanzania: a reconnaissance study. Economic Geology 102, 147–154.

Mäkitie, H., Data, G., Isabirye, E., Manttari, I., Huhma, H., Klausen, M. B., Pakkanen, L. & Virransalo, P., 2014. Petrology, geochronology and emplacement model of the giant 1.37 Ga arcuate Lake Victoria Dyke Swarm on the margin of a large igneous province in eastern Africa. Journal of African Earth Science 97, 273–297.

Ridley, J., 1992. The relations between mean rock stress and fluid flow in the crust: With reference to vein- and lode-style gold deposits, Ore Geology Reviews 8, 23-37.

Ridley, J.R. and Diamond, L.W., 2000. Fluid chemistry of orogenic lode gold deposits and implications for genetic models, Society of Economic Geologist Reviews 13, 141-162.

Sibson, R.H. and Scott, J., 1998. Stress/fault controls on the containment and release of overpressured fluids: Examples from gold-quartz vein systems in Juneau, Alaska; Victoria, Australia and Otago, New Zealand, Ore Geology Reviews 13, 293–306.

Sibson, R.H., Robert, F., Poulsen, K.H., 1988. High-angle reverse faults, fluid-pressure cycling, and mesothermal gold-quartz deposits, Geology 16, 551-555.

Tack, L., Liégeois, J.P., Deblond, A., Duchesne, J.C., 1994. Kibaran A-type granitoids and mafic rocks generated by two mantle sources in a late orogenic setting (Burundi). Precambrian Research 68, 323–356.

Tack, L., Wingate, M.T.D., De Waele, B., Meert, J., Belousova, E., Griffin, A., Tahon, A., Fernandez-Alonso, M., 2010. The 1375 Ma “Kibaran event” in Central Africa: prominent emplacement of bimodal magmatism under extensional regime. Precambrian Research 180, 63–84.

Westerhof, A. B. P., Härmä, P., Isabirye, E., Katto, E., Koistinen, T., Kuosmanen, E., Letho, T., Lehtonen, M. I., Mäkitie, H., Manninen, T., Mänttäri, I., Pekkala, Y., Pokki, J., Saalmann, K., Virransalo, P., 2014. Geology and Geodynamic Development of Uganda with Explanation of the 1:1,000,000 Scale Geological Map. Geological Survey of Finland, Special Paper 55.

Zhu, Y., An, F. and Tan, J., 2011. Geochemistry of hydrothermal gold deposits: A review. Geoscience Frontiers, 2(3), 367-374.

2. Tectonic wedging, back-thrusting and basin development in the frontal parts of the Mesoproterozoic Karagwe-Ankole belt in NW Tanzania

This research manuscript was submitted to the Journal of African Earth Science on the 28th of January 2014, and was accepted for publication on the 23rd of April 2014. I am the senior author and the work is co-authored by Alex Kisters.

The paper aims to condense a combined total of four months of fieldwork, detailed structural and lithological mapping, sampling and more regional reconnaissance work into a structural analysis of the eastern termination of the KAB in the Biharamulo region. Except for a one week introduction to the area, I undertook all of the field work and data gathering on my own. I am also responsible for the literature review, compilation of internal company reports and the majority of the written work presented in the paper. Professor Kisters reviewed the structural data and contributed to the conceptualization of a regional structural model. He also contributed towards the structuring and editing of the final manuscript.

Journal of African Earth Sciences 97 (2014) 87–98

Contents lists available at ScienceDirect

Journal of African Earth Sciences

journal homepage: www.elsevier.com/locate/jafrearsci

Tectonic wedging, back-thrusting and basin development in the frontal parts of the Mesoproterozoic Karagwe-Ankole belt in NW Tanzania

C. Koegelenberg, A.F.M. Kisters *

Department of Earth Science, Stellenbosch University, Private Bag X1, Matieland 7620, South Africa

ARTICLE INFO

Article history:
Received 28 January 2014
Received in revised form 22 April 2014
Accepted 23 April 2014
Available online 9 May 2014

Keywords:
Karagwe-Ankole belt
Muyaga Group
Bukoban Group
Structural analysis
Thick skinned thrusting
Mesoproterozoic foreland basin development

ABSTRACT

Structural complexities in the Mesoproterozoic Karagwe-Ankole fold belt in northwest Tanzania have led to conflicting interpretations of regional kinematics and the geodynamic significance of the belt. Structural mapping of an eastern portion of the belt indicates that the regional-scale (>100 km) Mugera-Nyakahura basement inlier may be considered a forethrusted tectonic wedge. Tectonic wedging in the frontal parts of the belt occurred during top-to-the southeast thick-skinned thrusting of the gneissic Archaean basement. The diagnostic feature of tectonic wedging is the reversal of vergence directions of kinematic fabrics on either side of the basement wedge, resulting in hinterland-directed, top-to-the northwest kinematics in front and on top of the wedge. Strain is localised into the often graphitic metapelitic rocks of the Upper Muyaga Group. The mainly coarse-grained clastic Mesoproterozoic sediments of the Bukoba Group represent the foreland, molasse-type deposits of the Karagwe-Ankole fold belt. The only gently folded Bukoba Group is separated from the underthrusted, highly deformed Muyaga Group by a passive roof thrust. This corresponds to the regional-scale asymmetry of the synclinal structure of the Bukoba basin in the frontal parts of the belt. The gentle folding is the result of the underthrusting and lifting of the Bukoba sediments above the basement wedge creating a triangle zone. The kinematics and geometry of the frontal parts of the Karagwe-Ankole belt described here confirm the belt to represent a top-to-the-east and -southeast verging foreland fold-and-thrust belt. The actual timing of deformation is, at present, unknown, but regional-scale kinematics and the metamorphic zonation are compatible with an origin of the belt during convergence between the Congo and Tanzania Cratons in the west.

1. Introduction

South-Central Africa is transected by a system of Meso- to Neoproterozoic (1.4–1.0 Ga) orogenic belts, collectively referred to as the Kibara orogenic system (Cahen et al., 1984) (Fig. 1a). These belts record the amalgamation of the Archaean Congo, Kalahari and Tanzania Cratons and smaller continental fragments to form part of the supercontinent Rodinia by ca. 1.0 Ga (Fernandez-Alonso et al., 2012, and references therein). The "Kibaran knot" (De Waele et al., 2003) of orogenic belts in Central Africa is far from being untied and the overall geodynamic settings and correlation between belts are still controversial (e.g. Tack et al., 2010 and references therein). There are currently two main schools of thought to explain the geological evolution of Kibara (sensu lato) belts. More conventional models interpret Kibara-age belts to document basin formation in the Mesoproterozoic, followed by the prolonged subduction and convergence and associated arc formation, episodic accretion and eventual collision of cratonic blocks in the late Mesoproterozoic (Kokonyangi et al., 2006, 2007; Johnson and Oliver, 2000). However, numerous recent studies emphasise similarities of sedimentary basins on adjacent cratons and the evidently limited displacement between them (De Waele et al., 2008; Tack et al., 2010; Fernandez-Alonso et al., 2012). These models suggest rather intracratonic processes and basin formation is envisaged to have occurred during episodic crustal extension of pre-existing Paleoproterozoic crust, driven by and associated with voluminous mafic under- and intraplating and spatially and temporally related granite plutonism between ca. 1.8 and 1.3 Ga (Tack et al., 2010; Fernandez-Alonso et al., 2012). The deformation of these basins is attributed to later orogenic episodes and far-field stresses unrelated to earlier basin formation. Most of these tectonic models rely mainly on geochronological and geochemical data. In contrast, detailed structural data that could constrain actual kinematics for individual belts are limited and our understanding of spatial and kinematic relationships relies, in many parts, on regional reconnaissance mapping or remote sensing data (e.g. Fernandez-Alonso and Theunissen, 1998).

* Corresponding author. Tel.: +27 (021) 808 3113; fax: +27 (021) 808 3129.
E-mail addresses: ckoegelenberg@sun.ac.za (C. Koegelenberg), akisters@sun.ac.za (A.F.M. Kisters).

http://dx.doi.org/10.1016/j.jafrearsci.2014.04.018
1464-343X/

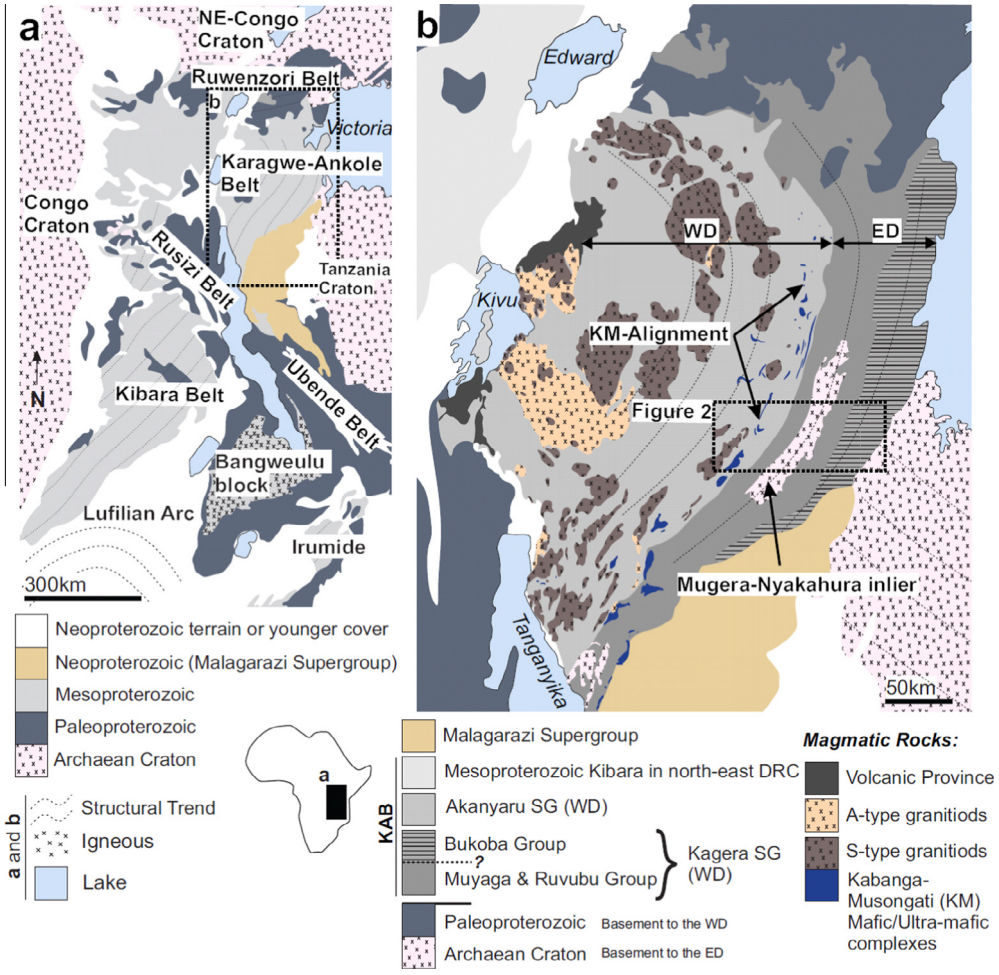

Fig. 1. (a) Simplified map of Central-East African geological belts. (b) Regional framework of the Karagwe-Ankole belt (KAB) with major magmatic outcrops. (a and b modified after Tack et al., 2010; Fernandez-Alonso, 2007), WD – Western Domain; ED – Eastern Domain.

The Karagwe-Ankole belt (KAB) represents the northernmost extension of Mesoproterozoic belts in Central Africa and has featured prominently in the controversy about subduction-related versus intracratonic processes (Kampunzu, 2001; Klerkx et al., 1987). The KAB represents an arcuate, northerly trending orogenic belt that extends for approximately 600 km from SW Uganda in the north to Lake Tanganyika in Burundi in the south, straddling the western margin of the Tanzania Craton (TC) (Fig. 1b). A number of studies have attempted a broad tectonic and lithostratigraphic subdivision of the belt and provided geochemical and geochronological data on syn- to post-tectonic granitic intrusives and mafic volcanic rocks (Klerkx et al., 1987; Tack et al., 1994; Deblond et al., 2001; Fernandez-Alonso et al., 2012). Regional reconnaissance mapping and remote sensing studies have focused on the western parts of the KAB (e.g. Klerkx et al., 1987; Fernandez-Alonso and Theunissen, 1998), but there is little detailed structural information about the kinematic framework, regional setting and timing of deformation in the eastern parts of the belt.

The present paper reports results of a structural analysis of the eastern parts of the KAB based on the detailed structural and lithological mapping of a 60 × 15 km square area traverse (Fig. 1b). The frontal parts of orogenic belts are geometrically and kinematically often complex with significant changes in structural style along strike (e.g., Price, 1986). The eastern parts of the KAB bordering against and overlying Archaean gneisses and granitoids of the Tanzania Craton are no exception comprising a regional-scale (>100 km) basement window, structural domains with often opposing vergence directions and overlying, relatively undeformed sedimentary basins (e.g., Fernandez-Alonso et al., 2012). These complexities, together with the lack of outcrop and regionally correlatable stratigraphy, have undoubtedly contributed to the poorly described frontal parts of the KAB. The aim of this paper is to provide the first detailed structural data on the eastern parts of the KAB that allows for better regional constraints on the formation and structural significance of the belt and associated basins.

1.1. Regional geology of the Karagwe-Ankole belt

The Kibara belt has traditionally been depicted as a continuous 1500 km long, arcuate northeast to northwest trending belt extending from the Democratic Republic of Congo in the south through Burundi, Rwanda, northwest Tanzania and into southwest Uganda (Cahen et al., 1984). More recent studies suggest a subdivision of the belt into a northern Karagwe-Ankole Belt and a southern Kibara Belt (sensu stricto) separated by the NW–SE trending Paleoproterozoic Rusizi belt exposed as a basement high in the Democratic Republic of Congo (Tack et al., 2010) (Fig. 1a). This subdivision emphasises the supposedly very different geological evolution of the two adjacent belts. Kokonyangi et al. (2006) suggest the southern KIB to have evolved during successive stages of subduction-driven accretionary and eventual collisional tectonics between ca. 1.4 to 1.0 Ga. In contrast, basin formation and subsequent deformation of the northern KAB are interpreted to have occurred in an intracratonic setting (e.g., Tack et al., 2010).

This study focuses on the eastern parts of the KAB. Tack et al., (1994), further subdivided the KAB into a Western and an Eastern Domain. The boundary between the two domains is delineated by a belt of intrusive mafic and ultra-mafic complexes referred to as the Kibanga-Musongati alignment (Evans et al., 2000). This lineament is suggested to represent a major crustal suture in the underlying basement of the KAB between the Paleoproterozoic rocks of the Ruwenzori belt and Archaean rocks of the Tanzania Craton, unconformably overlain by the Western Domain and Eastern Domain respectively (Tack et al., 1994). Rocks of the Western Domain form the interior parts of the KAB. The predominantly greenschist- to amphibolite-facies, often graphitic metapelites and minor metapsammites are assigned to the Akanyaru Supergroup (Fernandez-Alonso et al., 2012). Youngest detrital zircon ages from close to the base of the Akanyaru Supergroup indicate a maximum deposition age of ca. 1380–1420 Ma (Fernandez-Alonso et al., 2012). The metasediments are intruded by several distinct magmatic suites including: (1) voluminous S-type granites and a coevally emplaced suite of voluminous mafic sills and dykes at ca. 1375 Ma; (2) lesser A-type granites at 1250 Ma; and (3) late stanniferous S-type granites at 1000 Ma (Tack et al., 2010). The earlier episode of bi-modal plutonism at ca. 1375 Ma is interpreted to have occurred in a rift-type intracontinental setting that controlled basin formation and sedimentation (Tack et al., 2010).

Rocks of the Eastern Domain from the eastern, exterior parts of the KAB are assigned to the Kagera Supergroup, made up of greenschist- to sub-greenschist-facies metapelites and metapsammites (Fernandez-Alonso et al., 2012). Granites are conspicuous by their absence from the Eastern Domain (e.g. Tack et al., 1994). The Kagera Supergroup is further subdivided into the western Muyaga and Ruvubu Groups, and an eastern Bukoba Group interpreted to have been deposited in two different sub-basins (Fernandez-Alonso et al., 2012). Isolated felsic volcanic units at the base of the Muyaga Group yield U–Pb zircon ages of ca. 1780 Ma and constrain the onset of sedimentation of the Kagera Supergroup (Fernandez-Alonso et al., 2012). The Bukoba Group in the eastern parts of the KAB comprises a sequence of weakly metamorphosed and only gently folded, mainly thickly bedded quartzites, minor shales and intruded by voluminous mafic sills (Fernandez-Alonso et al., 2012). The Bukoba Group has traditionally been interpreted to represent a younger, Neoproterozoic basin (Cahen et al., 1984), but the presence of intrusive 1375 Ma mafic sills point to the Mesoproterozoic age of the sediments (Deblond et al., 2001). The mafic sills correlate with the emplacement of the larger Lake Victoria Arcuate Dyke Swarm (Reeves, 2000; Mänttäri et al., 2011; Ruotoistenmäki, 2014). The evidently Mesoproterozic age of the Bukoba Group also suggests a much closer temporal association of the Bukoba sedimentation to the rest of the tightly folded KAB to the immediate west (Fernandez-Alonso et al., 2012). Rocks of the Bukoba describe a broadly arcuate, N trending, narrow depository between the intensely deformed western parts of the KAB and Archaean basement of the Tanzania Craton in the east. The western contact of the Bukoba against the Muyaga Group has been speculated to represent a steep easterly dipping normal fault or a westerly dipping thrust (Macdonald, 1966; Kabete et al., 2012). In contrast, Bukoba rocks unconformably overlie Archaean basement of the Tanzania Craton in the east.

1.2. Deformation of the Karagwe-Ankole belt

Reconnaissance mapping by Klerkx et al. (1987) distinguished a sequence of deformational events (D1–D2, D2′) in the KAB based on fabric relationships and associated magmatism. Fernandez-Alonso and Theunissen (1998) formulated a more detailed structural evolution of the belt based mainly on the structural characteristics developed by Klerkx et al. (1987). These models emphasise the intracontinental setting of basin formation and sedimentation, but also deformation, culminating in the voluminous bimodal plutonism at ca. 1375 Ma (Tack et al., 2010). The presence of low-angle, bedding-parallel fabrics is interpreted to have accompanied D1 crustal extension and basin formation (e.g. Fernandez-Alonso and Theunissen, 1998). Klerkx et al. (1987) noted the often inconsistent westerly and easterly vergence directions of structures in the KAB and the intensification of fabrics around the ca. 1.38 Ga granite plutons in the Western Domain. The opposing vergence directions were, at the time, difficult to reconcile with a regional fold-and-thrust belt model and Klerkx et al. (1987) suggested that the fabrics rather recorded emplacement strains related to the older suite of granites that intruded during the D1 extensional event. The regional, slightly arcuate D2 structural trend of the KAB consists of NW–SE to NNE–SSW trending, upright and both SE- and/or NW-verging folds that refold earlier D1 fabrics. This fold phase (D2) is suggested to have occurred in response to later far-field stresses originating from the south-eastern and eastern margins of the Tanzania Craton, related to collisional tectonics in the Irumide Belt (1.0 Ga) and Mozambique Belt (570–530 Ma), respectively (Klerkx et al., 1987; Fernandez-Alonso et al., 2012). These later orogenic phases are suggested to have caused the reactivation of structures and transfer of stresses along the Ubende-Rusizi shear belt (Fig. 1a) and into the basement underlying the Western Domain of the KAB. D2 fabrics and structures are most prominent in the Western Domain and western parts of the Eastern Domain, but almost absent in the Bukoba Group (Fernandez-Alonso and Theunissen, 1998). Subvertical, conjugate, NE- and NW-trending shear zones are the last structures recorded in the KAB (D2′, after Klerkx et al. (1987)).

2. Tectonostratigraphy of the Eastern Domain

Regional mapping was done on a 1:20,000 to 1:2000 scale, depending on outcrop conditions and accessibility, and covered a 60 km long and up to 15 km wide traverse across strike of the Eastern Domain from the Kibanga-Musongati alignment in the west to the Bukoba basin and underlying basement rocks of the Tanzania Craton in the east (Fig. 2).

2.1. Archaean basement

Quartzo-feldspathic gneisses and granitoids form the basement to the overlying Eastern Domain exposed as the 140 km long and up to 20 km wide Mugera-Nyakahura inlier (Fig. 1b). The gneisses are interpreted to form the westernmost extension of Archaean TTG-greenstone terrains of the Tanzania Craton in the east (Cahen et al., 1984; Kabete et al., 2012). The basement rocks are typically leucocratic, medium-grained, often augen-textured trondhjemites and granodiorites, made up of quartz, plagioclase, biotite and/or hornblende and occasional K-feldspar. Secondary minerals include muscovite and chlorite. Finer-grained biotite gneisses also occur. Closer to the basement-cover contact, the gneisses are strongly foliated and retrogressed to muscovite– and muscovite–chlorite schists (see below). Retrogression is associated with abundant quartz veining developed as quartz-vein stock works or single veins that can reach widths of up to 40 m.

2.2. Muyaga Group

The basement (Mugera-Nyakahura inlier) is overlain by the mainly metapelitic succession of the Muyaga Group (Fig. 2). The Muyaga Group can be subdivided into a coarse-clastic basal succession of the Lower Muyaga Group, previously named the Karagwe-Ankolean Lower Division (Macdonald, 1966), and a stratigraphically higher, much thicker metapelite dominated Upper Muyaga Group. The Lower Muyaga Group consists mainly of

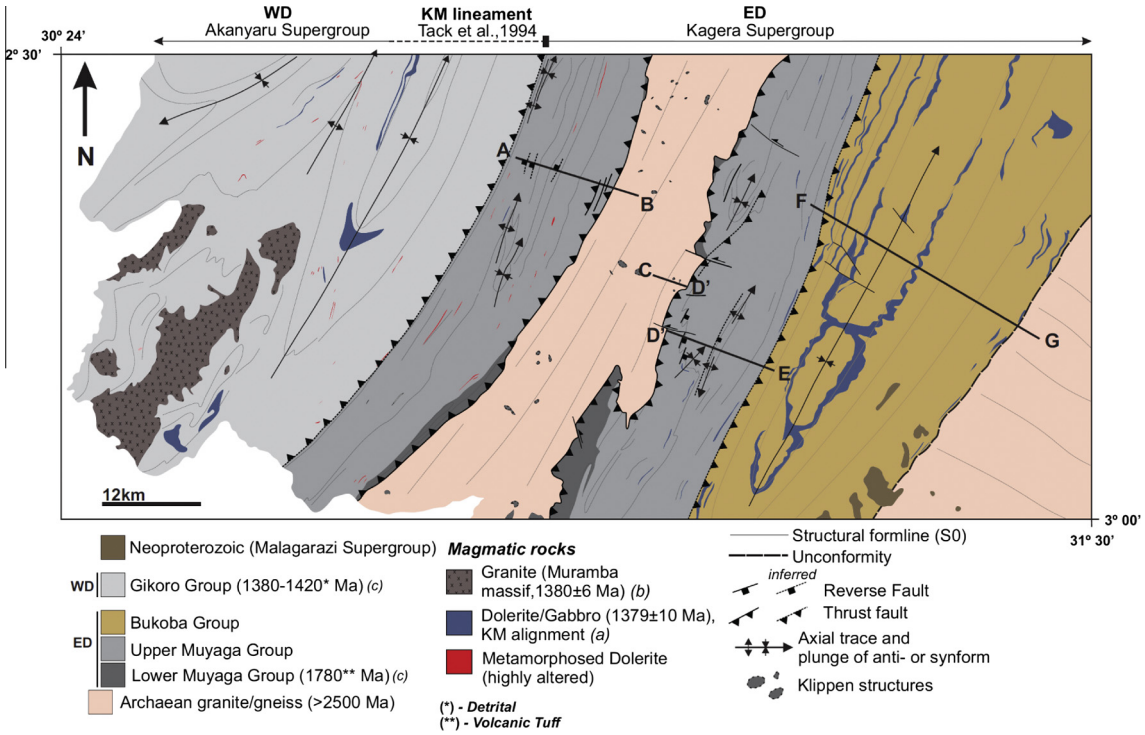

Fig. 2. Regional map of the Western Domain (WD) and Eastern Domain (ED) with general lithostratigraphy and modified structure. Schematic section A–G portrays the general structure of the ED as observed by this study (Fig. 4). Inferred thrust between WD and ED is interpreted from Tack et al. (2010), and Fernandez-Alonso and Theunissen (1998). The base geological maps are from Gray (1967), and Macdonald (1966). Ages: (a and b) Tack et al. (2010); (c) Fernandez-Alonso et al. (2012).

poorly-sorted, coarse-grained grits (0.5–3 mm grain size), impure quartzites and pink- to light-grey shales with quartzite intercalations. Outcrops of the Lower Muyaga Group are highly tectonized and discontinuous, and the omission of large parts along strike suggests that the rocks have been excised along the tectonized basement-cover contact along the margins of the Mugera-Nyakahura inlier. Deformation of the Lower Muyaga Group limits the lateral correlation of units or a detailed lithostratigraphy to be established.

The base of the Upper Muyaga Group, previously referred to as the Karagwe-Ankolean Middle Division (Macdonald, 1966), overlies most of the eastern and western margin of the Mugera-Nyakahura inlier (Fig. 2). In the east, the Upper Muyaga Group is overlain by rocks of the Bukoba Group. The base of the Upper Muyaga Group is dominated by thick, 200–300 m, dark-grey and, in parts, highly graphitic shales, white and reddish shales and intercalated, volumetrically subordinate, often pyritic quartzite horizons. Upwards the sequence of predominantly dark shales grades into a 30–120 m thick package of lighter coloured pinkish to light brown, locally siliceous shale with intercalated arkoses and is capped by up to 15 m thick, quartzites. The rest of the sequence is dominated by an up to 1.5 km thick, finely laminated and well bedded red, pink and white shale unit with cm-thick siliceous and ferruginous bands. The homogenous to finely laminated shale units contain, in places, up to several metre thick intra-formational breccias and slumps. Close to the top of the sequence and the transition to the overlying Bukoba Group, an up to 10 m thick light-grey to bluish ortho-quartzite is developed. The Ruvubu Group only outcrops in SE Burundi (Fernandez-Alonso, 2007) and has not been encountered in this study.

The Upper Muyaga Group is intruded by abundant mafic sills and dykes. Quartzite horizons and mafic sills tend to weather positively and form marker horizons that can be followed for several kilometres along strike. However, the entire succession has been affected by tight folding, intense foliation development and faulting, rendering lithostratigraphic correlations and thickness estimates tentative at best. A minimum thickness of ca. 2 km for the Upper Muyaga Group is assumed.

2.3. Bukoba Group

The mainly coarse-clastic sedimentary rocks of the Bukoba Group are preserved in a regional-scale, open, slightly arcuate, northerly trending and shallow doubly-plunging syncline (Fernandez-Alonso, 2007). The only gentle folding and lack of penetrative fabrics have preserved primary sedimentary structures in Bukoba rocks. From the base upwards, the Bukoba Group consists of light grey to buff siliceous shale, siltstone, mudstone and arkose coarsening upwards into a sequence of coarse ripple and/or cross laminated to massive cross-bedded ortho-sandstone. The shale, mudstone and siltstone horizons are sandwiched between at least three thick successive cycles of up to 350 m thick massive, well sorted, ortho-sandstone horizons. The overall preserved thickness for the Bukoba Group is estimated at ca. 2 km.

The suggested faulted contact between the Upper Muyaga and Bukoba Groups is only poorly exposed. The base of the Bukoba Group consists of alternating siltstones, mudstones and shale grading into sandstone, while the top of the Upper Muyaga is made up of finely-bedded shale with isolated sandstone units so that a clear contact between the two is difficult to identify. Eastward dipping bedding on either side of the inferred contact is sub-parallel and encloses only small angles on a regional scale, but regional fabrics are deflected along this contact suggesting the presence of a fault zone (see below). In the east, the mainly shales and minor intercalated sandstones at the base of the Bukoba Group unconformably overlie the Archaean basement gneisses of the Tanzania Craton. This also indicates the stratigraphic pinch out of the thick Upper Muyaga Group below the Bukoba Group.

2.4. Mafic dykes and sills

Two distinct groups of mafic sills and dykes are intrusive into the Muyaga and Bukoba Groups. A seemingly older generation of low-grade metamorphic mafic sills and dykes occurs particularly in the Muyaga Group, but also in the Bukoba Group. The mafic intrusives are deformed together with the tightly folded Muyaga Group, indicating their emplacement prior to the main phase of deformation (Fig. 3a). Original igneous parageneses have been replaced and, in places, pseudomorphed by actinolite–tremolite–chlorite–carbonate-bearing assemblages, corresponding to the greenschist-facie metamorphic grade of the wall rocks (Fig. 3b). Tight folding of the mafic sheets is associated with intense quartz veining and in zones of pervasive alteration the mafic rocks have been altered to massive magnesite, sericite and Fe-oxides. This generation of dolerites is commonly highly weathered (Fig. 3c).

A younger and more voluminous generation of largely undeformed and un-altered dolerites consists of primary clino-pyroxene, plagioclase and quartz together with Fe-oxides and sulphides, mainly pyrrhotite and pyrite (Fig. 3d and e). Secondary minerals include minor actinolite and chlorite replacing clino-pyroxene and plagioclase is, in places, saussuritized. Despite this, the dolerites are remarkably fresh (Fig. 3f) forming prominent topographic highs in the otherwise deep weathering profiles of the region. These dolerites are particularly prominent in the gently-dipping Bukoba Group, where they occur as up to 30 m thick sills preferentially emplaced in shale units between massive sandstone units (Fig. 3d), also truncating older generation dykes and sills. This younger generation of dolerites is only rarely recorded in the Muyaga Group where it truncates the folded metasediments and older mafic sheets. These dolerites form part of the 1375 Ma Lake Victoria Arcuate Dyke Swarm (LVADS) (Deblond et al., 2001).

3. Structural geology

The structural traverse through the Eastern Domain of the KAB transects four distinct structural domains and includes the structurally lowermost Mugera-Nyakahura basement inlier in the central parts of the profile, the Muyaga Group bordering the basement gneisses in the west and east, and the Bukoba Group to the far east (Fig. 4). Each domain is characterised by different kinematics and structural vergence.

3.1. Mugera-Nyakahura basement inlier

Archaean gneisses of the northeast-trending Mugera-Nyakahura basement inlier contain a north-easterly trending, steep westerly dipping gneissosity, parallel to the overall north-easterly trend of the inlier (Fig. 4). In places, networks of anastomosing or streaky cataclasite zones have transposed the original gneissosity (Fig. 5a). Closer to the basement-cover contact, gneisses contain abundant quartz veins and veining is associated with the retrogression of the feldspathic gneisses to quartz–muscovite and muscovite–chlorite schists. The schists contain a pervasive, shallow east dipping to sub-horizontal S-C foliation (Fig. 5b) and the basement gneissosity and earlier quartz veins are transposed into this shallow fabric (Fig. 5c and d). Shallowly SE-plunging mineral stretching lineations contained in the schistosity are defined by stretched quartz–muscovite aggregates or rodded quartz veins. In cases of pervasive retrogression, up to 30 m wide phyllonites are developed, made up of muscovite, chlorite, quartz and minor sulphides. This phyllonite zone marks the sheared contact between the basement and the Muyaga Group cover rocks. The high-strain zone (detachment) can intermittently be traced for tens of kilometres along the basement-cover contact, particularly along the eastern

Fig. 3. (a) Tightly folded older generation metamorphosed dolerite sill, Upper Muyaga Group. (b) Cross-polar thin section of metamorphosed sill shows greenschist grade actinolite–tremolite–chlorite–carbonate-bearing assemblages. Note pseudomorphed pyroxene crystal faces. (c) Deformed and metamorphosed sills at the surface always show a typical reddish-brown colour as a result of limonite, hematite, sericite and magnesite alteration. (d) Younger generation dolerite sill, Bukoba Group (view to the SSW). (e) Cross-polar thin section of fresh dolerite sill reveals typical phaneritic texture of primary clino-pyroxene, feldspar and quartz. (f) Dolerites sills in the field are relatively fresh with little to no alteration. (For interpretation of the references to colour in this figure legend, the reader is referred to the web version of this article.)

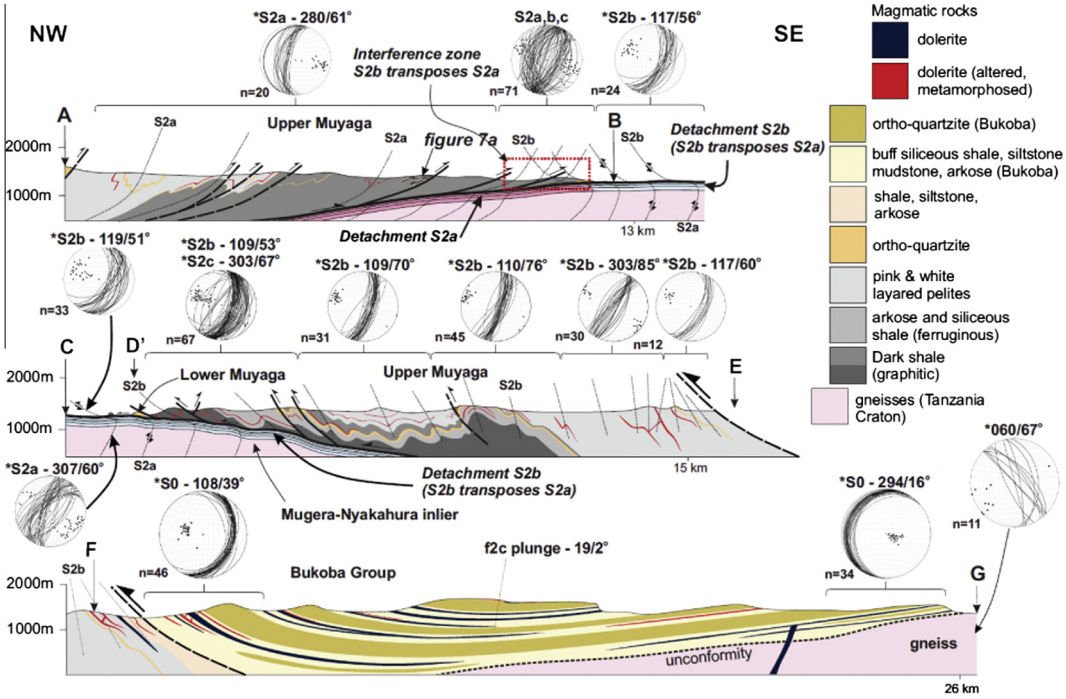

Fig. 4. Detail regional traverse of the Eastern Domain (ED). Section AB, CD′E and FG outlined in Fig. 2. Lower hemisphere, equal-area plans and poles show overall orientation of the ED. Note sub-perpendicular gneissosity of the Tanzania Craton to the KAB.

boundary of the Mugera-Nyakahura inlier (Fig. 5e). Erosional relics of Muyaga Group sediments form klippen structures bounded by phyllonites against the underlying basement indicating the continuous extent of the high-strain phyllonite zone above the basement inlier. The actual contact is irregular and defines a basement topography that may undulate by as much as 30 m on the eastern boundary. The basement highs and lows show north-easterly trends, parallel to the inlier, and form ramp and flat structures in which the foliation in phyllonites may vary from horizontal to as steep as 70°. The average dip of the high-strain basement-cover contact is, however, less than 10° to the southeast and northwest on either side of the basement inlier, respectively. Shear-sense indicators in the phyllonites include S-C bands and mica fish and uniformly point to top-to-the-NW kinematics parallel to the stretching lineation (Figs. 5b and 6a).

3.1.1. Muyaga Group west of the basement inlier

From the Kabanga-Musongati (KM) lineament to close to the western margin of the Mugera-Nyakahura basement inlier the Muyaga Group has been deformed into a SE- or ESE-verging fold-and-thrust belt (Fig. 4). A rarely observed early, bedding-parallel S1 foliation is present in tightly folded graphitic shale units. Quartzite horizons form isoclinal, often rootless folds and testify to the at least partial transposition of fabrics (S1/S0). All rocks have been deformed by tight, kilometre- to cm-scale folds, here assigned to a F2a fold phase (D2a deformation, following the regional sequence of deformation events formulated by Klerkx et al. (1987)). F2a folds show shallow north-westerly dipping to near-horizontal axial planes and an associated axial-planar foliation, S2a, underlining the south-easterly vergence of D2a structures in this part of the KAB (Fig. 7a). Folds are doubly plunging to both the northeast and southwest (Fig. 6a). In better exposed road cuts, many of the first- and second-order F2a folds are enveloped by shallow west dipping, strongly foliated high-strain zones (Fig. 7b). Stretching lineations, L2a(s), on the S2a faults predominantly plunge shallowly NW (Figs. 6a and 7c). These high strain zones are commonly located in graphitic schist packages and are interpreted as D2a thrusts that accommodate top-to-the-SE transport and associated southeast-verging folding of the Muyaga Group.

Eastwards and within ca. 3 km of the basement inlier, F2a folds are refolded and the S2a foliation is crenulated by west-verging folds (F2b) and an associated shallow east-dipping axial planar foliation (S2b) (Fig. 7d). These west-verging fabrics and structures become more penetrative further east, where they dominate the structural inventory of Muyaga Group rocks east of the basement inlier.

3.1.2. Muyaga Group east of the basement inlier

Folds and penetrative fabrics rather than faults dominate the Muyaga Group east of the basement inlier. Structures in this domain verge consistently to the west and west-northwest, opposite to D2a structures and fabrics that dominate to the west of the Mugera-Nyakahura inlier. The actual overprinting relationships between earlier east- and later west-verging fabrics are well preserved in an up to 1 km wide corridor parallel to the western margin of the Mugera-Nyakahura inlier (see above) and west-northwest verging structures are assigned to a D2b phase of deformation. The Muyaga Group east of the basement inlier is underlain by a regional-scale, first-order, northwest-verging synform-antiform pair with a wavelength of >15 km (Fig. 4). Lower-order F2b folds are ubiquitous. Folds range from isoclinal to open and show, for the most part, shallow north-easterly or south-westerly plunges, similar to F2a folds west of the basement inlier (Fig. 6b). An axial planar foliation (S2b) is very prominent and results in a mostly shallowly plunging intersection lineation (L2b(i), S0/S3), parallel to F2b folds (Fig. 8a). Earlier bedding-parallel D1 or D2a fabrics and structures found west of the basement inlier are not recorded. Close to the basement-cover contact, D2b fabrics dip at shallow to moderate angles to the east-southeast. The fabrics

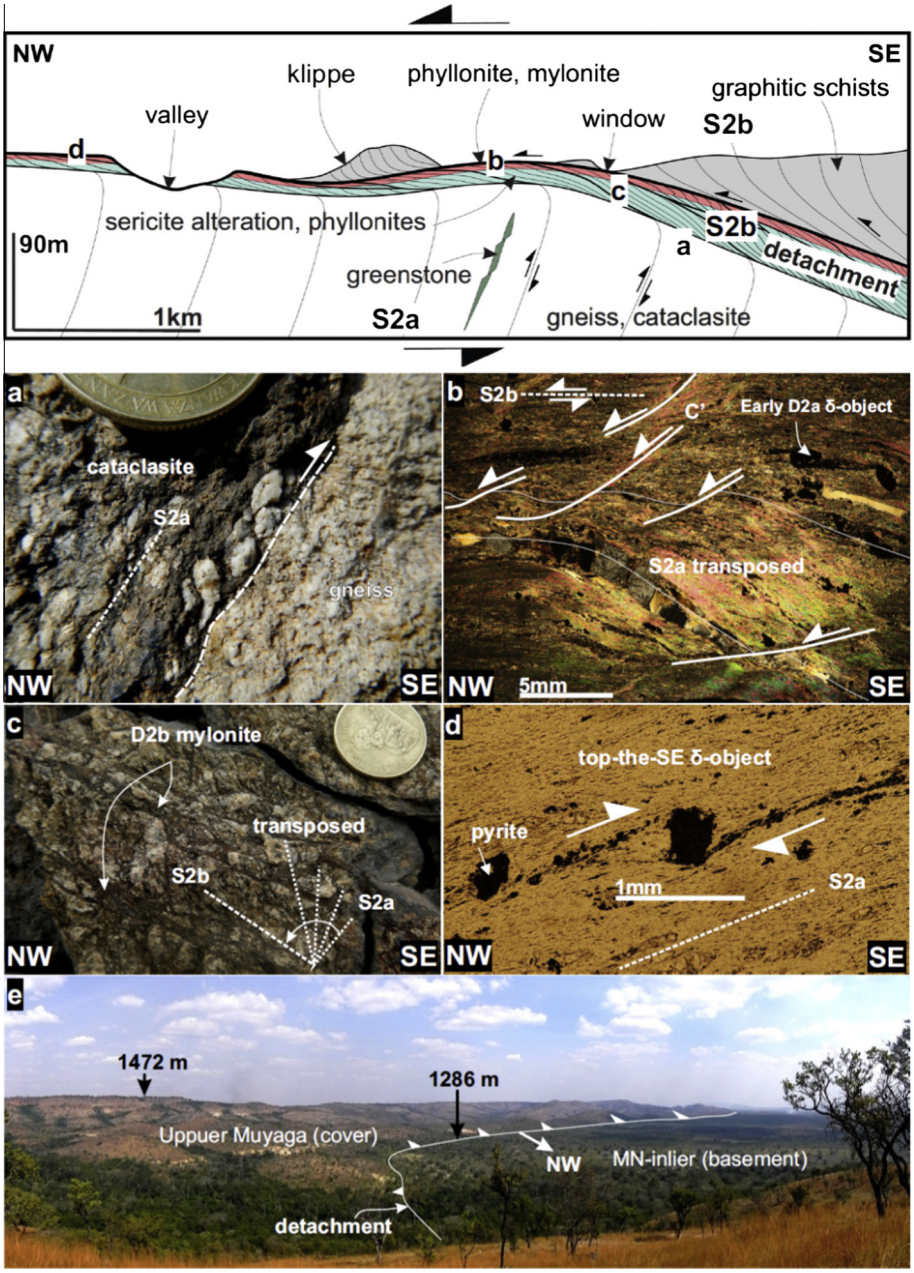

Fig. 5. Schematic sketch of the Upper Muyaga overlying the eastern margin of the Mugera-Nyakahura Inlier. (a) S2a gneisses with cataclastic bands showing top-to-the-SE sense of shear. (b) Cross-polar section of S2b phyllonite shows top-to-the-NW S-C and mica fish fabrics. (c) Shallow SE dipping mylonite bands in S2b transposed basement cataclastic gneiss. (d) Enlargement of a early top-to-the-SE rotated δ-clast in S2a gneiss. Similar orientated δ-clasts are observed in section of 5b. Greenstone slivers are inferred from Kabete et al. (2012). (e) Regional overview of the eastern margin of the NM-inlier and underthrusted cover (Upper Muyaga Group). Approximate view direction to the south.

gradually steepen to the east and assume sub-vertical to steep overturned westerly dips within ca. 2 km of the contact with the Bukoba Group (Fig. 4). Within 50–100 m of the contact with the overlying Bukoba Group, S2b appears deflected against this contact and rotated back to steep- to moderate east-southeast dips (Fig. 4).

The steepening of fabrics is associated with systematic variations in fabric intensities. High-strain fabrics dominate the structurally lower parts and S2b rotates into parallelism with the flat lying mylonitic fabrics and phyllonites along the basement-cover contact. The phyllonites carry an east-southeasterly plunging down-dip mineral stretching lineation, L2b(s), defined by rodded quartz veins or stretched quartz–muscovite aggregates (Fig. 6b). High-strain zones are particularly localised in graphitic shale units. Shear-sense indicators are mainly S-C and S-C′ fabrics and consistently point to a top-to-the-WNW sense of a shear, corresponding to the kinematics recorded in the underlying phyllonites along the basement-cover contact. The top-to-the-WNW kinematics along the easterly-dipping thrust faults (Fig. 8b) correspond to the WNW vergence of F2b and indicate folding and faulting to form part of an overall D2b WNW-verging fold-and-thrust belt to the east and on top of the basement inlier. In the eastern parts of the Muyaga Group, D2b fault zones are developed as steep east-dipping reverse faults, but are difficult to identify in the field (Fig. 8c). Locally recorded steeper and south-easterly plunges of

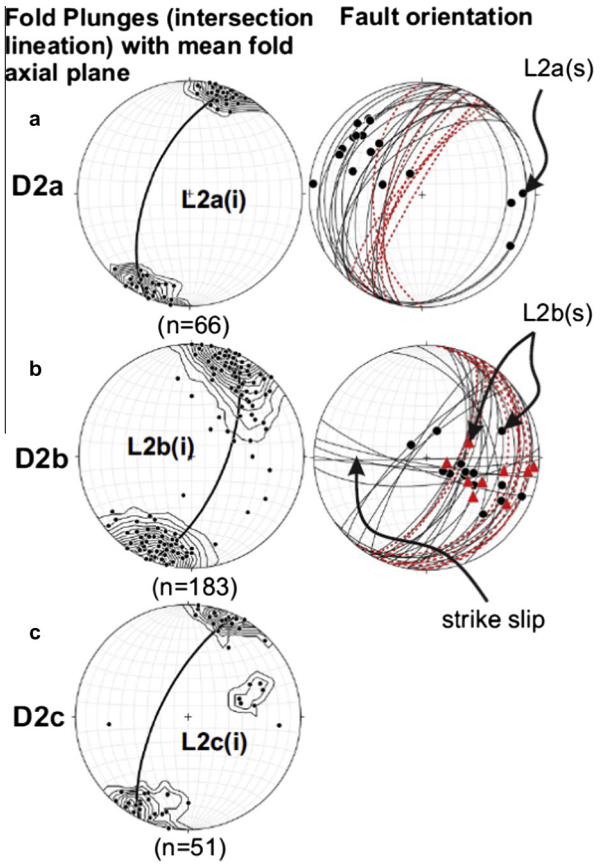

Fig. 6. Regional (a) D2a, (b) D2b and (c) D2c fold axial trends and fault orientations on lower-hemisphere, equal-area stereonet plots. Intersection lineations, indicating regional fold plunges, are parallel to the fold axial planes and define an overall NNE–SSW for D2a, D2b and D2c deformation. Notably faulting during D2c arguably reactivated D2a faults, thus D2c faults are difficult to distinguish. L(i) – intersection lineation; L(s) – stretch lineation. Fault orientation – black circles (cover); red triangles (basement); black solid planes (cover); stippled red planes (basement). (For interpretation of the references to colour in this figure legend, the reader is referred to the web version of this article.)

F2b folds and L2b(i) lineations are interpreted to indicate the presence of D2b faults in which fold hinges have been rotated towards parallelism with the down-dip stretch in the faults (Fig. 8c).

The latest stage of deformation, D2c, is defined by a ESE verging axial-planar foliation S2c crenulating earlier S2b structures (Fig. 7e). S4 is sub- to co-planar with the foliation recorded further west of the Mugera-Nyakahura inlier (Fig. 7c). F2c crenulation folds are tight and shallow doubly plunging to the NNE and SSW. S2c structures are only observed where earlier S2b fabrics are distinguishable and occur mostly west of the inlier and decreases eastwards.

3.1.3. Bukoba Group

Rocks of the Bukoba Group are gently folded into a north-east trending, shallow north-east plunging syncline. The Bukoba syncline has a wavelength of between 15–25 km and consists of a slightly steeper (25–40°) north-western and a very shallow (10–15°) south-eastern limb, giving it a south-easterly vergence (Fig. 4). Folding is not associated with any penetrative fabrics, in stark contrast with the fabric intensities in the underlying Muyaga Group. On a regional scale, the Bukoba fold hinge is arcuate over a strike distance of >150 km and sub-parallel to the main trend of F2a/F2b folds in the Muyaga Group.

4. Discussion

4.1. Structure of the Eastern Domain

The eastern parts of the KAB mapped in this study are underlain by two regional-scale domains with opposing vergences centred around the Mugera-Nyakahura basement gneisses. Overprinting relationships allow to distinguish an earlier phase of ESE-verging low-angle thrusting and folding (D2a) from a later phase of WNW-verging folding and thrusting (D2b), mostly east of the gneisses. The easternmost parts of the belt, in contrast, are made up of the gently folded, coarse-clastic sediments of the Bukoba Group that, in turn, rest unconformably on the Tanzania Craton.

Structural overprinting and regional reversals in vergence direction are a common feature of particularly the frontal parts of foreland fold-and-thrust belts consisting of hinterland-dipping forethrusts at deeper levels that are overridden by foreland-dipping, hinterland-verging backthrusts (Price, 1981, 1986; Banks and Warburton, 1986; Vann et al., 1986; Dean et al., 2013). This pattern of conjugate thrust faults with opposing vergence directions defines a wedge-shaped tectonic duplex that underthrusts rocks of the foreland, also referred to as a triangle zone (Price, 1981; Jones, 1996). The underthrusted rocks above the triangle zone are wedged up and commonly only gently deformed as they passively ride on top of the underlying backthrust or passive roof thrust (Banks and Warburton, 1986; Price, 1986; Couzens and Wiltschko, 1996).

The geometry and kinematics of structures described here are consistent with the frontal parts of the KAB representing a triangle zone above the underthrusted tectonic wedge of the Mugera-Nyakahura basement gneisses. The regional-scale basement inlier rocks have variably been described as an erosional window (Kabete et al., 2012) or an antiformal uplift (Fernandez-Alonso and Theunissen, 1998). We suggest that the inlier forms the hinge of a regional-scale hanging-wall antiform of a basement wedge upthrusted over a basement ramp during thick-skinned top-to-the-southeast forethrusting (Fig. 9). D2a strains in the gneisses are indicated by the widespread northeast-trending, steep north-westerly dipping cataclasite zones and the crenulation of the older, presumably Archaean gneissosity. The actual floor detachment is not exposed and its position must remain speculative. In contrast, the top of the wedge is clearly delineated by high-strain phyllonites and basement-cover contacts are clearly tectonic. The top-to-the-northwest kinematics along the roof detachment are consistent with the backthrusting of the roof sequence of the Upper Muyaga Group towards the hinterland and above the basement wedge (Fig. 9). Similarly, northwest-verging folds, thrusts and fabrics (D2b) in the Upper Muyaga Group to the east of the inlier correspond to the hinterland-verging transport of the entire sequence in front and above the basement wedge. The fan-like steepening of fabrics and structures (D2b) in this Eastern Domain indicates its location in the frontal parts of the foreland dipping basement wedge. Strain in the cover sequence seems rather distributed and not localised along distinct thrust zones and folds and associated pervasive S2b fabrics dominate instead. The roof detachment seems to be localised within the thick and often graphitic shale units predominantly in the Upper Muyaga Group. Voluminous quartz veining in gneisses along the basement-cover contact points to high-fluid pressures in the basal parts of the detachment. The combination of high fluid pressures and reaction weakening associated with the hydration of feldspathic gneisses to muscovite–quartz schist have most likely assisted low-angle thrusting along the roof detachment.

Towards the west, the main backthrust cuts up and away from the roof detachment into the Upper Muyaga Group. The location of

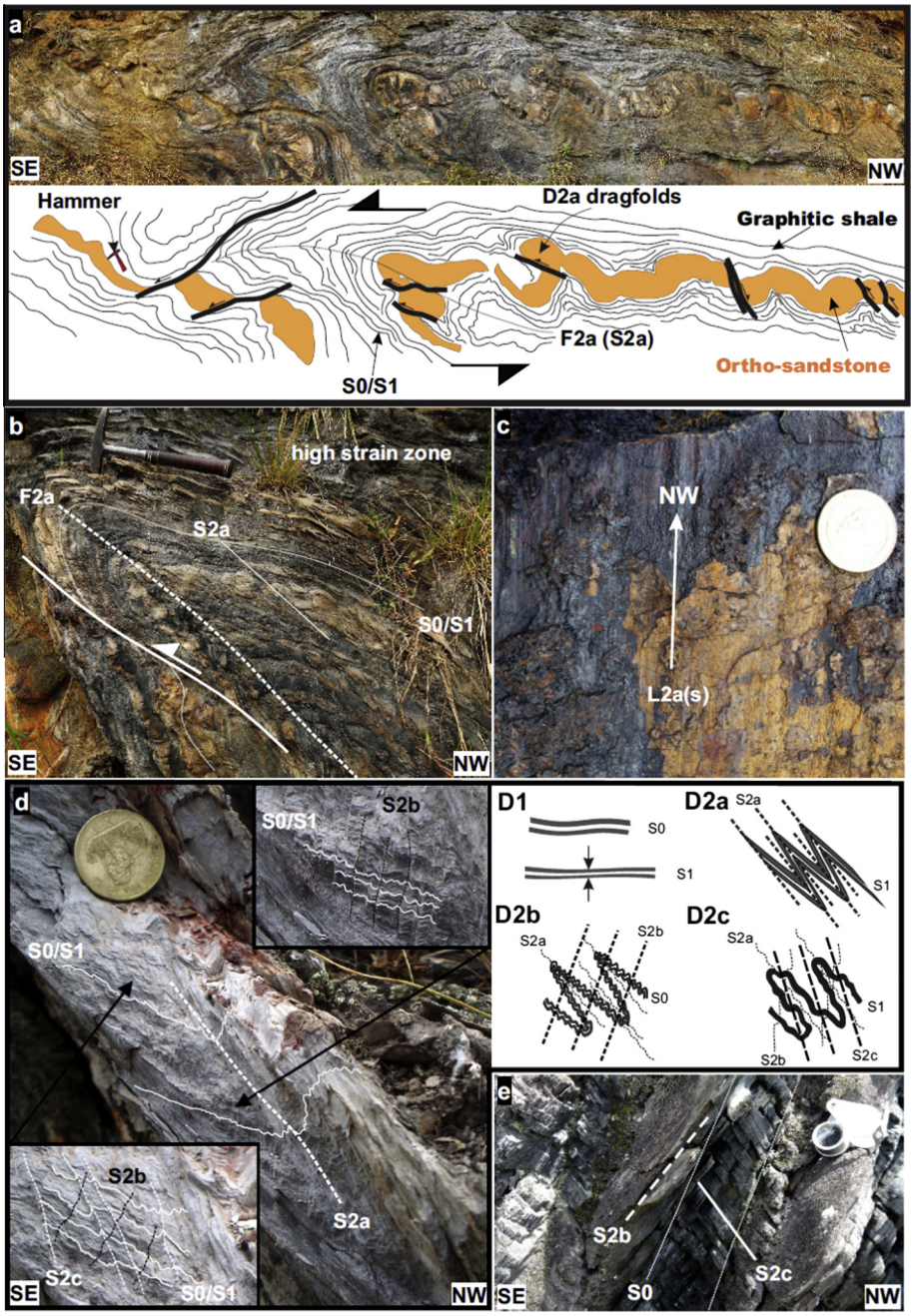

Fig. 7. (a) Roadside outcrop in the Upper Muyaga Group with tight F2a folds and partially refolded F2a dragfolds along D2a thrusts with pervasive S2a foliation. This section represents the hanging wall to a regional scale D2a thrust (Fig. 4). (b) Roadside outcrop of D2a high strain zone (thrust) with top-to-the-SE sense of shear, Upper Muyaga Group (Western Domain). Note multiple dragfolds and pinch-and-swell boudins parallel to S2a stretched foliations and shearbands. (c) L2a(s) stretch lineation on ferruginous mylonite. (d) S1, S2a, S2b and S2c fabric overprinting relationships in tightly folded shale, interference zone (Fig. 4), Upper Muyaga Group. (e) Graphitic shale showing only bedding (S1 absent) with S2b crenulated by late S2c fabrics, interference zone (Fig. 4).

the ramp is indicated by the interference of D2a west-verging with D2b east-verging structures some ca. 2 km to the west of the Mugera-Nyakahura inlier (Fig. 4). This location may also mark the presence of the footwall ramp above which the basement rocks have ramped up into the Muyaga Group (Fig. 9).

Towards the east, fabric and strain intensities decrease abruptly from the tightly folded and steeply dipping Upper Muyaga Group in the west into the overlying, only gently folded Bukoba Group. The abrupt change in strain between the Muyaga and Bukoba Groups points to the presence of a detachment along this contact. This detachment accommodates the underthrusting and passive wedging of the Bukoba cover rocks above the backthrusted, hinterland-verging Upper Muyaga Group. The extent of deformation experienced by the cover sequence depends on a number of factors, including the degree of coupling between the underthrusted wedge and the cover, but also the strength and thickness of the cover rocks (Erickson, 1995). Unconformable contacts between the Bukoba Group and the Tanzania Craton in the east demonstrate that the Bukoba sediments have not been displaced and remained attached to the foreland. Similarly, the lack of penetrative fabrics or faulting suggests that tectonic wedging only caused the gentle lifting of strata. This results in the distinct asymmetry and

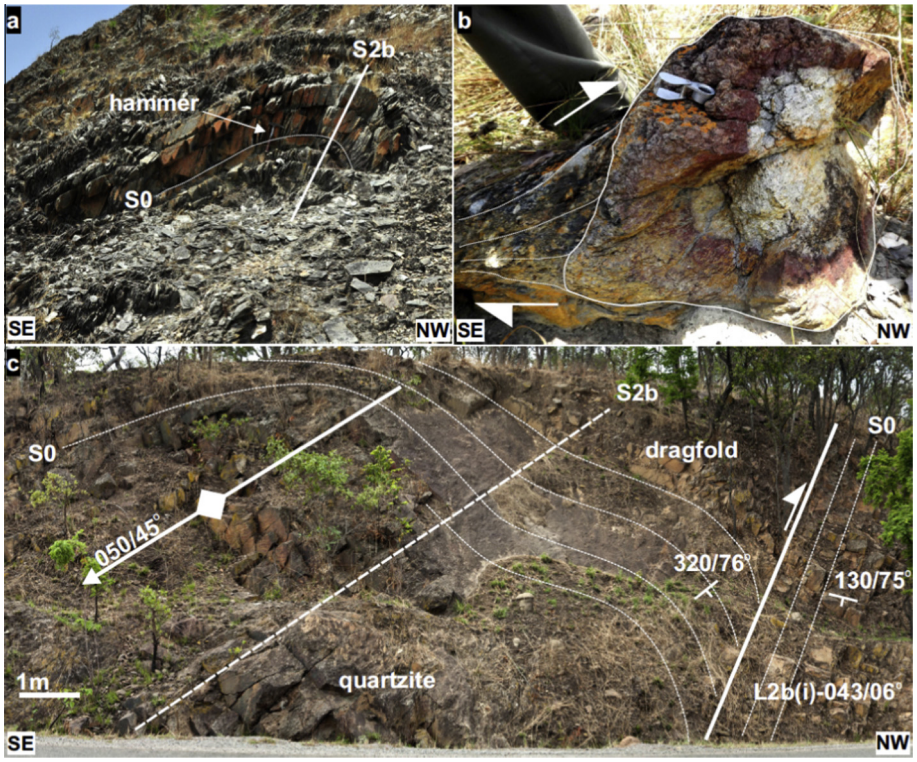

Fig. 8. (a) Tight, NW verging, F2b parasitic fold with pervasive S2b axial planar foliation, Upper Muyaga Group. (b) Shallow dipping, top-to-the-NW sense of shear, D2b fault breccia (graphitic shale) near the basement detachment with rotated clasts of gritstone, Lower Muyaga Group. (c) Roadside outcrop showing steep D2b reverse fault accentuated by rotated dragfold with steep plunge (050/45°) in the hanging wall. Note relatively shallow plunge (L2b(i) – 043/06°) in footwall to the fault.

southeast- and foreland vergence of the Bukoba syncline, consistent with the regional-scale top-to-the-southeast kinematics of the KAB. We have not been able to identify the passive roof thrust along he Bukoba Muyaga Group contacts with certainty due to poor exposure. However, the rotation of steep S2b fabrics in the Muyaga Group to shallower south-easterly dips close to the Bukoba contact indicates the presence of this hinterland-verging detachment (Figs. 4 and 9).

The present work suggests that backthrusting is initiated by southeast, foreland-verging ramping in front of and above the Mugera-Nyakahura basement wedge. Field (Doglioni et al., 1999; Bonini, 2001, 2007), but also analogue and numerical modelling studies (Couzens-Schultz et al., 2003; Dean et al., 2013) of foreland-fold -and-thrust belts emphasise that backthrust development may also initiate along stratigraphic pinchouts of weak lithologies that localise the detachment. Regional maps show that rocks of the Muyaga Group do not extend beyond the Bukoba Group to the east and onto the Tanzania Craton. This indicates the pinchout of the metapelites below Bukoba Group rocks and may point to a more regional along-strike extent of the backthrusted frontal parts of the KAB.

4.2. Implications for the tectonic setting of the KAB

The recognition of large parts of the eastern KAB as a triangle zone and backthrusted domain has implications for regional interpretations of the KAB. Recent models have emphasised the intracratonic setting of sedimentation in the KAB. Basin formation is envisaged to have occurred during a prolonged or episodic phases of crustal extension accentuated by the widespread bimodal plutonism recorded at ca. 1.38 Ga (Tack et al., 2010; Fernandez-Alonso et al., 2012). This raises the question as to the origin and timing of deformation recorded in the KAB. There are several regional-scale features that point to an origin of the KAB belt as an overall southeast-vergent (D2, after Klerkx et al., 1987) fold and thrust belt related to crustal convergence and or collisional tectonics in the far west. Backthrusting and associated triangle zones documented here for the Eastern Domain of the KAB are a common feature of the frontal parts of many foreland fold-and-thrust belts. The kinematics and overprinting relationships (D2a/b/c) are entirely consistent with the overall southeast-vergent kinematics of the belt. On a regional scale, the KAB describes a distinctly arcuate geometry and the convex geometry of D2 folds and thrusts suggests a southeast vergent transport direction (Fig. 1b). This agrees with the west to east decrease in metamorphic grade and the occurrence of syn- to late tectonic granitoids confined to the Western Domain. Lastly, fabric and strain intensities decrease from west to east and the far eastern parts of the KAB are made up of the only gently deformed rocks of the Mesoproterozoic Bukoba Group. These regional-scale features are difficult to reconcile with far-field effects of collisional tectonics and the transfer of stresses from the east during younger orogenic events along the margins of the Tanzania Craton as suggested by Tack et al. (2010) or Fernandez-Alonso et al., (2012). At this stage, the geodynamic setting of the KAB must remain speculative although deformation and regional patterns of metamorphism and plutonims rather point to an origin of the belt in response to crustal convergence and/or collision. As such, the structural evolution of the KAB portrayed here resembles, in many aspects, the D1 accretionary stage described by Kokonyangi et al. (2006) for the southern Kibara belt (sensu stricto). This would imply a closer relationship between the northern and southern segment of the larger Kibaran orogenic system. However, better constraints on the setting and regional-scale correlation of events can only be attempted once absolute ages of the timing of deformation become available.

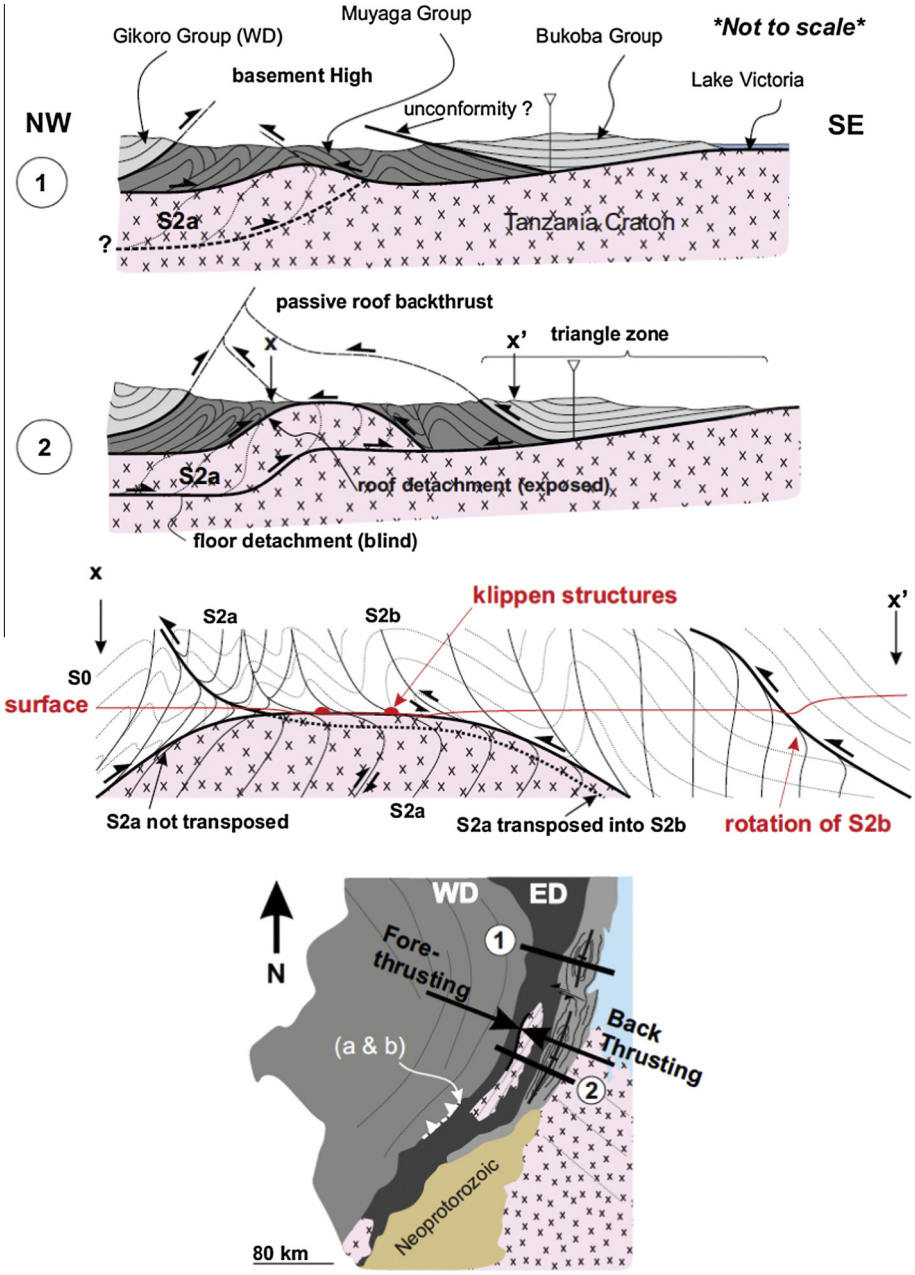

Fig. 9. Schematic illustration of the deformation in the Eastern Domain. Section 2 illustrates forethrusted basement wedge model. Additional X-section shows fabric observed geometries relative to the basement wedge and passive roof backthrust. Section 1 illustrates the possible structure nortwards of the main back-thrusted domain. Major ESE thrust after (a) Fernandez-Alonso and Theunissen (1998), and (b) Tack et al. (2010). Regional map modified after Fernandez-Alonso (2007).

5. Conclusions

(1) The eastern parts of the Karagwe-Ankole belt in NW Tanzania are underlain by a regional-scale backthrusted domain recording top-to-the-northwest and hinterland directed transport. Backthrust development occurs in front and above the Mugera-Nyakahura basement uplift that represents a regional-scale tectonic wedge. Thrusting records top-to-the southeast displacement and towards the foreland of the Tanzania Craton.

(2) Rocks of the Bukoba Group represent relics of a Mesoproterozoic foreland basin (>1375 Ma) to the Karagwe-Ankole belt in the west. The broad, arcuate, southeast-verging synclinal structure of the preserved Bukoba basin is a result of the tectonic wedging and passive lifting of the Bukoba cover above a passive roof thrust on top the underthrusted Muyaga Group.

(3) Graphitic and thick metapelites of the Upper Muyaga Group are considered to be important for the localisation and development of the backthrusted domains. Backthrust development north and south of the Mugera-Nyakahura basement wedge is conceivable, given the stratigraphic pinchout of the metapelites below the molasse-type Bukoba Group.

(4) The geometry, location and kinematics of backthrusting in the frontal parts of the Karagwe-Ankole belt are entirely consistent with an origin of the Kargawe-Ankole belt as a southeast verging fold and thrust belt (Tack et al., 1994).

Recently suggested later far-field stresses acting from the east or southeast across the Tanzania Craton (Fernandez-Alonso et al., 2012) can neither account for the structural development and kinematics, nor for the regional-scale metamorphic zonation and overall geometry of the belt.

Acknowledgements

This project was made possible through financial and logistic support by Anglo Gold Ashanti Exploration (AGA) and is published with permission of AGA. Special thanks go to Gillian Williams for exceptional logistics, and Joas Kabete and the late Peter Winkler for initiating this project. Esperius Kavoko provided invaluable help during the field work. Additional bursary funding through the NRF Scarce Skills Development Fund (Grant 81573) C. Koegelenberg was greatly appreciated. We gratefully acknowledge the very constructive and helpful comments of two anonymous reviewers and Pat Eriksson's editorial handling of the manuscript.

References

Banks, C.J., Warburton, J., 1986. 'Passive-Roof' duplex geometry in the frontal structures of Kirthar and Sulaiman belts, Pakistan. J. Struct. Geol. 8, 229–237.

Bonini, M., 2001. Passive roof thrusting and forelandward fold propagation in scaled brittle–ductile physical models of thrust wedges. J. Geophys. Res. 106 (B2), 2291–2311.

Bonini, M., 2007. Deformation patterns and structural vergence in brittle–ductile thrust wedges: an additional analogue modelling perspective. J. Struct. Geol. 29, 141–158.

Cahen, L., Snelling, N.J., Delhal, J., Vail, J.R., Bonhomme, M., Ledent, D., 1984. The Geochronology and Evolution of Africa. Oxford University Press, Oxford, 512 pp.

Couzens, B.A., Wiltschko, D.V., 1996. The control of mechanical stratigraphy on the formation of triangle zones. Bull. Can. Pet. Geol. 44 (2), 165–179.

Couzens-Schultz, B.A., Vendeville, B.C., Wiltschko, D.V., 2003. Duplex style and triangle zone formation: insights from physical modeling. J. Struct. Geol. 25, 1623–1644.

De Waele, B., Wingate, M.T.D., Fitzsimons, I.C.W., Mapani, B.S.E., 2003. Untying the Kibaran knot: a reassessment of Mesoproterozoic correlations in southern Africa based on SHRIMPU-Pb data from the Irumide belt. Geology 31 (6), 509–512.

De Waele, B., Johnson, S.P., Pisarevsky, S.A., 2008. Paleoproterozoic to Neoproterozoic growth and evolution of the eastern Congo Craton: Its role in the Rodinia puzzle. Precambr. Res. 160, 127–141.

Dean, S.L., Morgan, J.K., Fournier, T., 2013. Geometries of fold and thrust belts: insights from discrete element simulations. J. Struct. Geol. 53, 43–53.

Deblond, A., Punzalan, L.E., Boven, A., Tack, L., 2001. The Malagarazi Supergroup of SE Burundi and its correlative Bukoban Supergroup of NW Tanzania: Neo-and Mesoproterozoic chronostratigraphic constraints from Ar–Ar ages on mafic intrusive rocks. J. Afr. Earth Sci. 32, 435–449.

Doglioni, C., Merlini, S., Cantarella, G., 1999. Foredeep geometries at the front of the Apennines in the Ionian Sea (central Mediterranean). Earth Planet. Sci. Lett. 168, 243–254.

Erickson, S.G., 1995. Mechanics of triangle zones and passive-roof duplexes: implications of finite element models. Tectonophysics 245, 1–11.

Evans, D.M., Boadi, I., Byemelwa, L., Gilligan, J., Kabete, J., Marcet, P., 2000. Kabanga magmatic sulphide deposits, Tanzania: morphology and geochemistry of associated intrusions. J. Afr. Earth Sci. 30, 651–674.

Fernandez-Alonso, M., 2007. Geological Map of the Mesoproterozoic Northeastern Kibara Belt. Royal Museum for Central Africa, Tervuren (Belgium): Catalogue of Maps and Digital Data, and "http://www.africamuseum.be".

Fernandez-Alonso, M., Theunissen, K., 1998. Airborne geophysics and geochemistry provide new insights in the intracontinental evolution of the Mesoproterozoic Kibaran belt (Central Africa). Geol. Mag. 135, 203–216.

Fernandez-Alonso, M., Cutten, H., De Waele, B., Tack, L., Tahon, A., Baudet, D., Barritt, S.D., 2012. The Mesoproterozoic Karagwe-Ankole Belt (formerly the NE Kibara Belt): the result of prolonged extensional intracratonic basin development punctuated by two short-lived far field compressional events. Precambr. Res. 216, 63–86.

Gray, I.M., 1967. Quarter Degree Sheet 29 (Ngara). Mineral Resources Division of Tanzania, Dodoma.

Johnson, S.P., Oliver, G.J.H., 2000. Mesoproterozoic oceanic subduction, island-arc formation and the initiation of back-arc spreading in the Kibaran Belt of, southern Africa: evidence from the Ophiolite Terrane, Chewore Inliers, northern Zimbabwe. Precambr. Res. 103 (2000), 125–146.

Jones, P.B., 1996. Triangle zone geometry, terminology, and kinematics. Bull. Can. Pet. Geol. 44 (2), 139–152.

Kabete, J.M., Groves, D.I., McNaughton, N.J., Mruma, A.H., 2012. A new tectonic and temporal framework for the Tanzanian Shield: implications for gold metallogeny and undiscovered endowment. Ore Geol. Rev.. http://dx.doi.org/10.1016/j.oregeorev.2012.02.009.

Kampunzu, A.B., 2001. Assembly and break-up of Rodinia – no link with Gondwana assembly. Gondwana Res. 4, 647–650.

Klerkx, J., Liégeois, J.-P., Lavreau, J., Claessens, W., 1987. Crustal evolution of the northern Kibaran Belt, eastern and central Africa. In: Kröner, A. (Ed.), Proterozoic Lithospheric Evolution, vol. 17. American Geophysical Union and the Geological Society of America, pp. 217–233.

Kokonyangi, J., Kampunzu, A.B., Armstrong, R., Yoshida, M., Okudaira, T., Arima, M., Ngulube, D.A., 2006. The Mesoproterozoic Kibaride belt (Katanga, SE D.R. Congo). J. Afr. Earth Sci. 46, 1–35.

Kokonyangi, J., Kampunzu, A.B., Armstrong, R., Arima, M., Yoshida, M., Okudaira, T., 2007. U–Pb SHRIMP Dating of Detrital Zircons from the Nzilo Group (Kibaran Belt): implications for the source of sediments and Mesoproterozoic Evolution of Central Africa. J. Geol. 115, 99–113.

Macdonald, A.S., 1966. Quarter Degree Sheet 30 (Biharamulo). Mineral Resources Division of Tanzania, Dodoma.

Mänttäri, I., Kigereigu, F., Huhma, H., de Kock, G.S., Koistinen, T., Kuosmanen, E., Lahaye, Y., Lehtonen, M.I., Mäkitie, H., Manninen, T., O'Brien, H., Saalmann, K., Virransalo, P., Westerhof, A.B., 2011. New Precambrian Rock Ages from Uganda. 23rd Colloquium of African Geology, Abstract volume, Johannesburg, South Africa.

Price, R.A., 1981. The Cordilleran foreland thrust and fold belt in the southern Canadian Rocky Mountains. In: McClay, K.R., Price, N.J. (Eds.), Thrust and Nappe Tectonics. Spec. Pubis Geol. Soc. Lond. 9,427–448.

Price, R.A., 1986. The southeastern Canadian Cordillera: thrust faulting, tectonic wedging, and delamination of the lithosphere. J. Struct. Geol. 8, 239–254.

Reeves, C.V., 2000. The geophysical mapping of Mesozoic dyke swarms in southern Africa and their origin in the disruption of Gondwana. J. Afr. Earth Sci. 30, 499–513.

Ruotoistenmäki, T., 2014. Geophysical characteristics of Aswa shear, Nagasongola discontinuity and ring dyke complex in Uganda. J. Afr. Earth Sci. 93 (2014), 23–41.

Tack, L., Liégeois, J.P., Deblond, A., Duchesne, J.C., 1994. Kibaran A-type granitoids and mafic rocks generated by two mantle sources in a late orogenic setting (Burundi). Precambr. Res. 68, 323–356.

Tack, L., Wingate, M.T.D., De Waele, B., Meert, J., Belousova, E., Griffin, A., Tahon, A., Fernandez-Alonso, M., 2010. The 1375 Ma "Kibaran event" in Central Africa: prominent emplacement of bimodal magmatism under extensional regime. Precambr. Res. 180 (2010), 63–84.

Vann, I.R., Graham, R.H., Hayward, A.B., 1986. The structure of mountain fronts. J. Struct. Geol. 8, 215–227.

3. U-Pb detrital zircon and 39Ar-40Ar muscovite ages from the eastern parts of the Karagwe-Ankole Belt: Tracking Paleoproterozoic basin formation and Mesoproterozoic crustal amalgamation along the western margin of the Tanzania Craton

This research manuscript was submitted to the Precambrian Research on the 2nd of December 2014, and was accepted for publication on the 6th August 2015. I am the senior author and co-authors are Alex Kisters, Jan Kramers (University of Johannesburg) and Dirk Frei (Central Analytical Facilities, University of Stellenbosch).

I did the sampling in the field, mineral separation for zircon geochronology, zircon imaging with scanning electron microscope (SEM) and petrography. I was also responsible for the literature review and the majority of the written work. Alex Kisters contributed to the editing of the paper and regional concepts and tectonics. Jan Kramers was responsible for radiometric ^{39}Ar-^{40}Ar analysis and, due to the complexity of the raw data, was also instrumental in the interpretation and processing of the data. Dirk Frei was responsible for U-Pb zircon dating (LA ICP-MS) and subsequent review of U-Pb data (Chapter 6: Appendices B and C).

Precambrian Research 269 (2015) 147–161

Contents lists available at ScienceDirect

Precambrian Research

journal homepage: www.elsevier.com/locate/precamres

U–Pb detrital zircon and ^{39}Ar–^{40}Ar muscovite ages from the eastern parts of the Karagwe-Ankole Belt: Tracking Paleoproterozoic basin formation and Mesoproterozoic crustal amalgamation along the western margin of the Tanzania Craton

C. Koegelenberg[a,*], A.F.M. Kisters[a,**], J.D. Kramers[b,1], D. Frei[c,2]

[a] Department of Earth Science, Stellenbosch University, Private Bag X1, Matieland 7620, South Africa
[b] Department of Geology, University of Johannesburg, Auckland Park 2006, APK Campus, Johannesburg, South Africa
[c] University of Stellenbosch, Department of Earth Science, Room 1017, Stellenbosch, South Africa

ARTICLE INFO

Article history:
Received 2 December 2014
Received in revised form 3 July 2015
Accepted 6 August 2015
Available online 18 August 2015

Keywords:
Karagwe-Ankole belt
Eastern Domain
Kagera Supergroup
Basin formation
Deformation

ABSTRACT

The Karagwe-Ankole belt forms part of a complex system of orogenic belts in Central-East Africa that record the amalgamation of Archaean and/or Paleoproterozoic continental kernels in the Proterozoic. The actual timing of tectonic processes, including initial basin formation and subsequent deformation, is only poorly constrained so that the geodynamic significance of the Karagwe-Ankole belt within the broader system of Proterozoic orogens in Central-East Africa is not well understood. This paper presents U–Pb ages of detrital zircons constraining the age of sediments of the eastern parts of the Karagwe-Ankole fold belt overlying the western Tanzania Craton and ^{39}Ar–^{40}Ar muscovite ages from mylonites and phyllonites associated with the main phase of subsequent shortening and fold-and-thrust tectonics (D2).

^{39}Ar–^{40}Ar muscovite ages from the main detachment between Archaean basement gneisses and imbricated cover rocks of the Kagera Supergroup in the eastern, frontal parts of the Karagwe-Ankole Belt constrain the timing of the main fabric forming event and thrusting (D2) to 1326 ± 10 Ma. This age is at the young end of the age range for the main phase of granite plutonism and mafic dyke emplacement that have previously been related to crustal extension and associated intracontinental rifting. If correct and representative for the main phase of deformation in the rest of the Karagwe-Ankole belt, the ages may rather point to a collisional event between the Congo and Tanzania Cratons west of the Karagwe-Ankole belt in Mesoproterozoic times, indicating a closer correlation with rocks of the Kibara Belt (sensu stricto) to the immediate south.

U–Pb detrital zircon ages for the older Muyaga and overlying Bukoba Group of the Kagera Supergroup confirm the Paleoproterozoic timing of sedimentation from ca. 1780 Ma, but before ca. 1568 Ma. The presence of a distinct group of ca. 1750–1790 Ma zircons in the Bukoba Group indicate uplift, erosion and subsequent reworking of sediments and volcanic units contained in the Lower Muyaga Group to the west. The ages also suggest a correlation between the Bwezigoro Group of SW Uganda and the Bukoba Group indicating the presence of a far more extensive Paleoproterozoic and/or Early Mesoproterozoic foreland basin overlying the western margin of the Archaean Tanzania Craton and Paleoproterozoic Uganda Block.

1. Introduction

Archaean cratons of Central and East Africa (Fig. 1) are overlain by a series of Paleo-, Meso-, and Neoproterozoic sedimentary basins (De Waele et al., 2008). Basin evolution is commonly regarded to be in response to rift-related processes associated with subduction or collisional tectonics along the margins of the major cratonic blocks (De Waele et al., 2008) and/or intracratonic extensional and associated magmatic processes (Tack et al., 2010).

* Corresponding author. Tel.: +27 783977679.
** Corresponding author. Tel.: +27 21 808 3113; fax: +27 21 808 3129.
E-mail addresses: ckoegelenberg@sun.ac.za (C. Koegelenberg), akisters@sun.ac.za (A.F.M. Kisters), jkramers@uj.ac.za (J.D. Kramers), dirkfrei@sun.ac.za (D. Frei).
[1] Tel.: +27 11 559 4755; fax: +27 11 559 4702.
[2] Tel.: +27 21 808 9342; fax: +27 21 808 2837.

http://dx.doi.org/10.1016/j.precamres.2015.08.014
0301-9268/

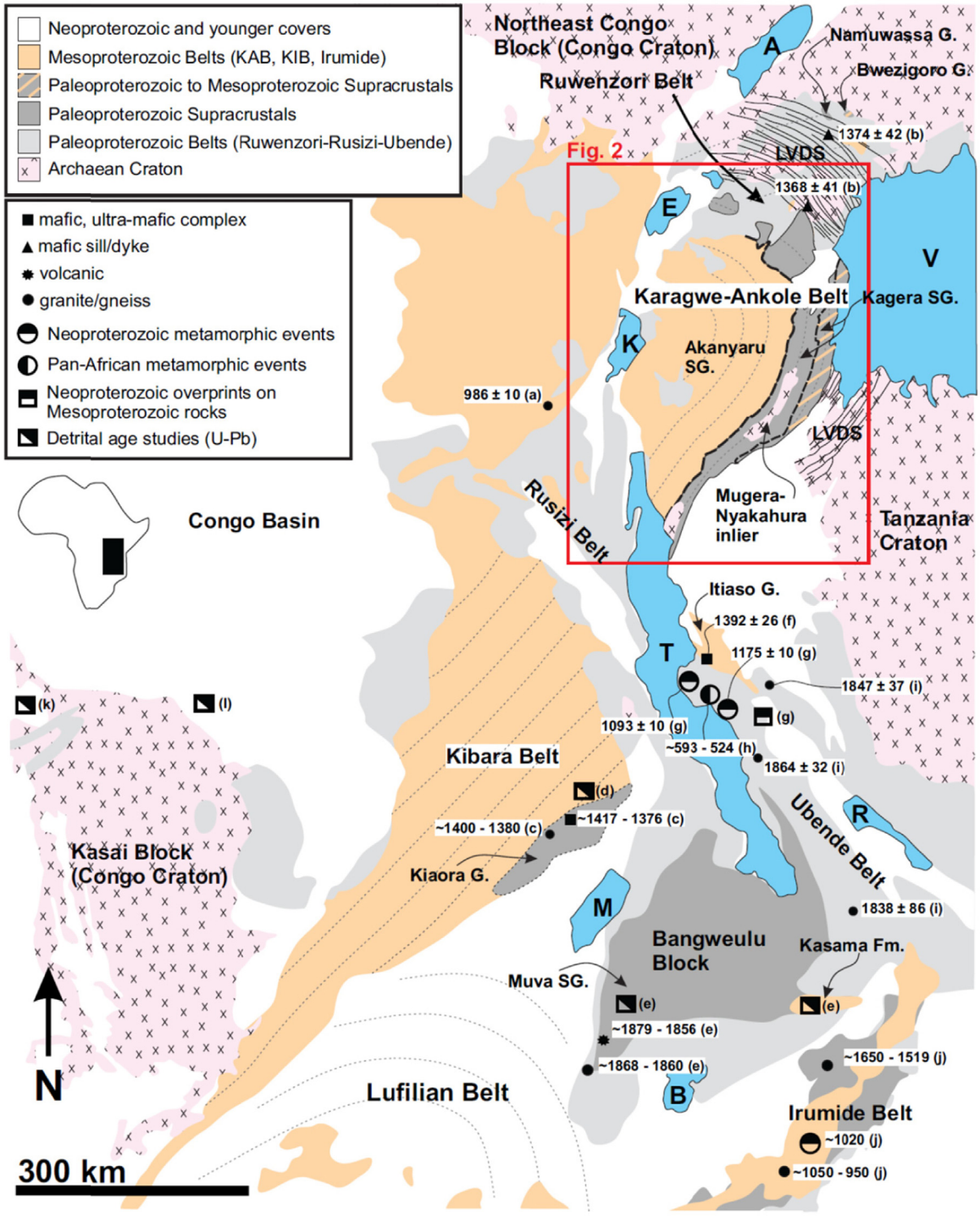

Fig. 1. Regional geological framework of central-east Africa (modified after Fernandez-Alonso et al., 2012). Geochronological; data after – (a) Tack et al. (2010); (b) Mäkitie et al. (2014); (c) Kokonyangi et al. (2004, 2005, 2006); (d) Kokonyangi et al. (2007); (e) De Waele and Fitzsimons (2007); (f) Maier et al. (2007); (g) Boniface et al. (2014); (h) Boniface and Schenk (2012); (i) Lenoir et al. (1994); (j) De Waele et al. (2008); (k) Batumike et al. (2009); (l) Delpomdor et al. (2013). Lakes – A, Albert; E, Edward; V, Victoria; K, Kivu; T, Tanganyika; M, Mweru; B, Bangweulu and R, Rukwa. LVDS – Lake Victoria Dyke Swarm, KAB – Karagwe-Ankole Belt, KIB – Kibara Belt.

However, the timing of basin evolution, the ages of sedimentary successions and subsequent deformation are only poorly constrained and stratigraphic correlations between basins on adjacent cratons are preliminary (e.g. Kokonyangi et al., 2007; Fernandez-Alonso et al., 2012). Moreover, recent geochronological studies emphasize the multiphase reactivation of orogenic belts from the Paleoproterozoic, preserved in the Usagaran, Ubendian, Rusizian and Ruwenzori Belts (ca. 2.2–1.8 Ga) via the Mesoproterozoic Kibara and Irumide Belts (ca. 1.4–1.0 Ga) to the late Neoproterozoic Zambezi, Lufilian and Mozambique Belts (ca. 880–530 Ma) that record the amalgamation of East Gondwana (De Waele et al., 2008; Batumike et al., 2009; Boniface et al., 2012). The result is that, in the absence of detailed geochronological, structural and stratigraphic studies, correlations between basin formation and orogenic episodes remain speculative (e.g. Fernandez-Alonso et al., 2012).

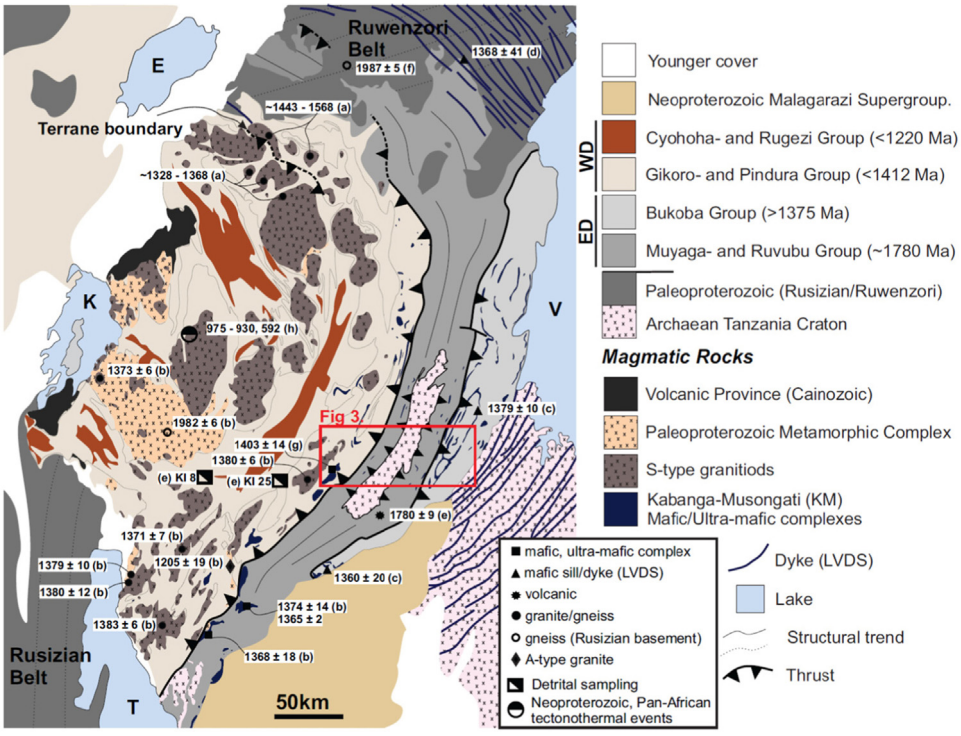

Fig. 2. Regional geology of the Kragwe-Ankole Belt (modified after Fernandez-Alonso et al., 2012). Geochronological data from – (a) Buchwaldt et al. (2008); (b) Tack et al. (2010); (c) Deblond et al. (2001); (d) Mäkitie et al. (2014); (e) Fernandez-Alonso et al. (2012); (f) Westerhof et al. (2014); (g) Maier et al. (2007); (h) De Waele et al. (2011). Lakes – refer to Fig. 1.

The western margin of the Tanzania Craton (TC) is overlain by variably deformed sedimentary cover sequences that form part of the Karagwe-Ankole Belt (KAB) (Fig. 2), the northernmost segment of the Kibara Belt (sensu lato) located between the Congo and Tanzania Cratons of Central-East Africa (Fig. 1). The actual timing of sedimentation and deformation, and consequently the geodynamic setting and significance of the KAB for the broader tectonic evolution of the region are controversially discussed (Tack et al., 2010; Fernandez-Alonso et al., 2012) and two main schools of thought can be distinguished. More recent studies propose an intracontinental rifting (aulacogen) model for the volcano-sedimentary sequences of the KAB (Fernandez-Alonso et al., 2012). This model suggests the juxtaposition of the Congo Craton and TC already in the Paleoproterozoic at ca. 1.8 Ga followed by protracted intracontinental rifting of the cratonic crust during the Mesoproterozoic. Deformation of the KAB is believed to be related to later episodes of shortening associated with younger orogenic events that have affected the south and south-eastern margins of the TC in the Neoproterozoic. In contrast, models invoked for the southernmost Kibara Belt (sensu stricto) (Fig. 1) suggest a depositional setting and deformation in response to crustal convergence and subduction processes during the Mesoproterozoic along the western margin of the amalgamated TC and Bangweulu Block (Kampunzu et al., 1986; Kokonyangi et al., 2006,and references therein).

In this paper we present U–Pb ages from detrital zircons of the Kagera Supergroup from the eastern parts of the KAB overlying the TC (Fig. 3). This data is combined with ^{40}Ar–^{39}Ar muscovite ages taken from phyllonites that form the basal detachment of the sedimentary cover (Kagera Supergroup) above Archaean basement gneisses of the TC in the eastern and frontal parts of the belt. The data sets are used to constrain the timing of basin formation and sedimentation, but also deformation in the eastern parts of the KAB. We further discuss the potential regional implications for the structural evolution of the KAB within a broader Kibaran orogenic system.

2. Geological setting

2.1. The Kibaran orogenic system

The Mesoproterozoic Kibara Belt (senso lato) has traditionally been viewed as a continuous NE trending belt stretching for ca. 1300 km from southwest Uganda northwards across Rwanda, Tanzania, Burundi and into the Democratic Republic of the Congo (DRC) (e.g. Cahen et al., 1984 and references therein) (Fig. 1). More recent studies distinguish a northern KAB from a southern Kibara Belt (sensu stricto), considered to have distinct geological evolutions, and separated from each other by the Paleoproterozoic Rusizi-Ubende Belt (Tack et al., 2010 and references therein) (Fig. 1). Tack et al. (1994) further divided the eastern part of the KAB into structurally and lithologically distinct Western and Eastern Domains (WD and ED) separated by a linear corridor of mafic to ultramafic intrusions known as the Kabanga-Musongati alignment (Fig. 2). The WD and ED are underlain by two lithostratigraphically distinct units assigned to the Akanyaru Supergroup and the Kagera Supergroup, respectively (Fernandez-Alonso et al., 2012 and references therein). The two basins share no apparent correlation and are juxtaposed along the sheared Kabanga-Musongati alignment (Fig. 3).

2.1.1. Geology of the Western- and Eastern Domains of the KAB

Western Domain – The Akanyaru Supergroup of the WD forms the interior parts of the KAB and consists of mainly amphibolite- to greenschist facies metapelites and metapsammites and subordinate interlayered metavolcanic sequences (Tack et al., 2010). In the lower parts of the Akanyaru Supergroup, the Gikoro- and Pindura Groups have been intruded by several suites of mainly S-type granitoids ranging in age from ca. 1566–1445 Ma to 1380–1330 Ma with an apparent peak of granite plutonism at ca. 1380–1375 Ma (Buchwaldt et al., 2008; Tack et al., 2010) (Fig. 2). The peak of granite plutonism is coeval with the emplacement of voluminous mafic dyke and sill complexes. The mafic plutonism is referred

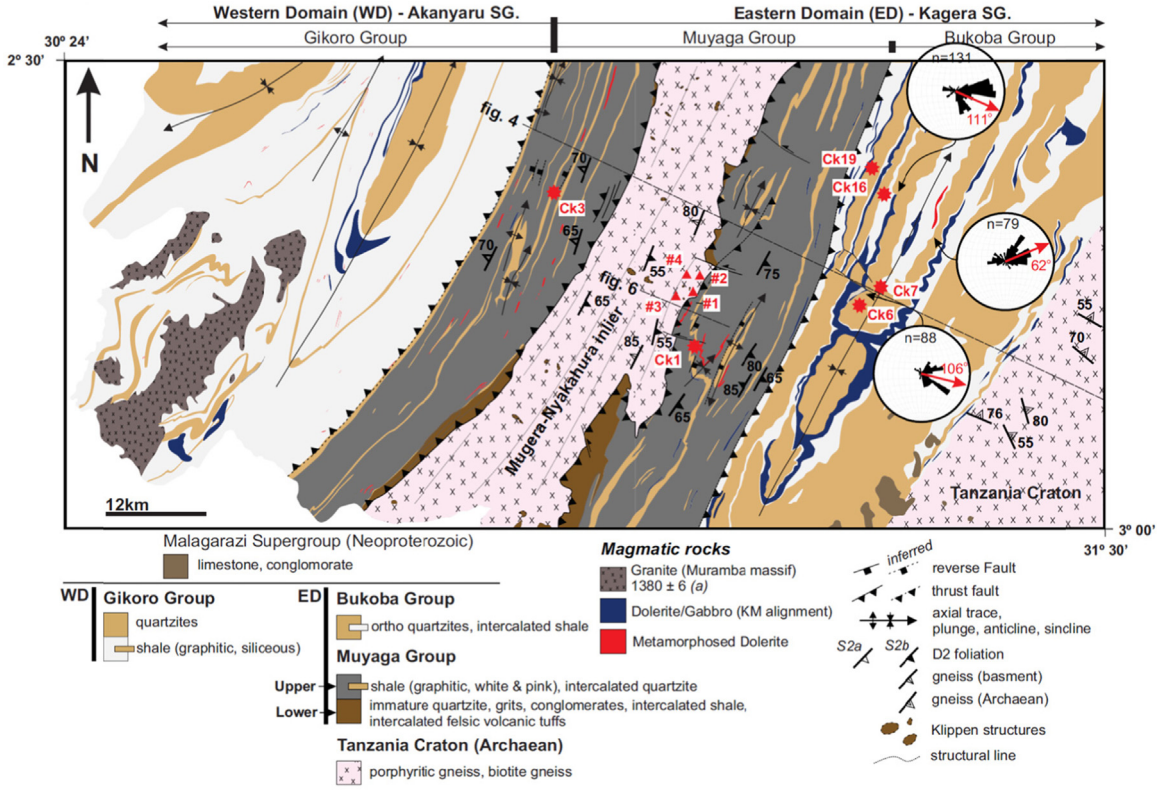

Fig. 3. Geology of the Karagwe-Ankole Belt's Eastern and Western Domain in NW Tanzania (modified after Koegelenberg and Kisters, 2014). Note locations of sections in Figs. 4 and 6.

to as the Northern Kibaran Igneous Province in Uganda (after Westerhof et al., 2014), but also includes the ca. 1375 Ma arcuate Lake Victoria Dyke Swarm (LVDS) on the Tanzania Craton and the ca. 1400–1360 Ma mafic to ultra-mafic plugs and layered intrusions of the Kabanga-Musongati alignment that form the boundary between the Western and Eastern Domains (Deblond et al., 2001; Maier et al., 2007; Tack et al., 2010; Mäkitie et al., 2014) (Fig. 3). Notably, the base of the Akanyaru Supergroup has not been identified, but the youngest detrital zircon ages from the uppermost formations of the Gikoro Group have yielded U–Pb ages of ca. 1412–1420 Ma (Fernandez-Alonso et al., 2012) (Figs. 2 and 4). Further zircon populations showed prominent Paleoproterozoic input with peaks at ca. 1.83 Ga (45%) and lesser peaks at ca. 2.14–1.93 Ga (20%). Significant late-Archaean to early-Paleoproterozoic peaks are also recorded between 2.79 and 2.4 Ga (30%). The Gikoro- and Pindura Groups have been intruded by mafic dykes and sills. Syn-sedimentary volcanic activity in the Pindura Group has been suggested to represent the surface expression of the underlying, ca. 1375 Ma dykes and sills (Fernandez-Alonso et al., 2012). A later sedimentation period is indicated by the unconformably overlying Cyohoha and Rugezi Groups with detrital zircons constraining onset of sedimentation to at least ca. 1222 Ma (Fernandez-Alonso et al., 2012; Villeneuve and Chorowicz, 2004). Much less voluminous phases of granite magmatism in the WD are recorded by ca. 1205 Ma A-type granitoids and ca. 1.0 Ga tin granites (Tack et al., 2010).

Eastern Domain – The Kagera Supergroup east of the Kabanga-Musongati alignment also consists of metapelites and metapsammites, but at markedly lower, greenschist to sub-greenschist facies grades of metamorphism. Moreover, strain intensities in the Kagera Supergoup are markedly lower compared to the Akanyura Supergroup (e.g. Tack et al., 1994). The Kagera Supergroup has been subdivided into a western sub-basin underlain by the Muyaga Group, and an eastern sub-basin consisting of the Bukoba Group (Fernandez-Alonso et al., 2012). The Muyaga Group comprises mostly of a thick (>2 km) sequence of metapsammites at its base, grading upwards into partly graphitic metapelites (Fernandez-Alonso et al., 2012; Koegelenberg and Kisters, 2014). Towards the east, the Muyaga Group pinches out below the Bukoba Group. The Bukoba Group comprises of a ca. 2 km thick sequence of almost unmetamorphosed shales and siltstones interlayered with thick (>300 m) packages of orthoquarzites (Koegelenberg and Kisters, 2014). Granite plutonism is conspicuous by its absence from the ED, but all rocks have been intruded by variably deformed mafic dykes and sills of the LVDS (Deblond et al., 2001). In addition, deformation and metamorphism of mafic dykes and sills also indicate the presence of an older suite of mafic intrusives that pre-date dykes and sills of the LVDS (Koegelenberg and Kisters, 2014).

The onset of sedimentation of the Kagera Supergroup is indicated by an U–Pb zircon age of ca. 1780 ± 9 Ma from felsic tuffs of the Murore Formation at the base of the Muyaga Group (Figs. 2 and 4) (Fernandez-Alonso et al., 2012). U–Pb detrital zircon ages from the clastic base of the Lower Muyaga Subgroup (Figs. 2 and 4) yielded relatively prominent Archaean peaks between 2.67 and 2.4 Ga (51%) and two slightly less prominent Paleoproterozoic peaks at 1.85 Ga and 2.02 Ga (40%), similar to rocks of the WD (Fernandez-Alonso et al., 2012). The youngest zircon from the Muyaga Group recorded an age of 1846 ± 5 Ma. The dominant Paleoproterozoic populations for the Lower Muyaga Subgroup correlate with U–Pb zircon ages from ca. 1780 Ma volcanic tuffs of the Murore Formation. The upper age for deposition of both the Muyaga and Bukoba Groups is only loosely constrained by the emplacement ages of mafic sills of the LVDS at ca. 1375 Ma (Deblond et al., 2001; Fernandez-Alonso et al., 2012).

2.1.2. The Kabanga-Musongati alignment

The Kabanga-Musongati alignment describes a narrow and slightly arcuate zone of mafic to ultra-mafic bodies that have

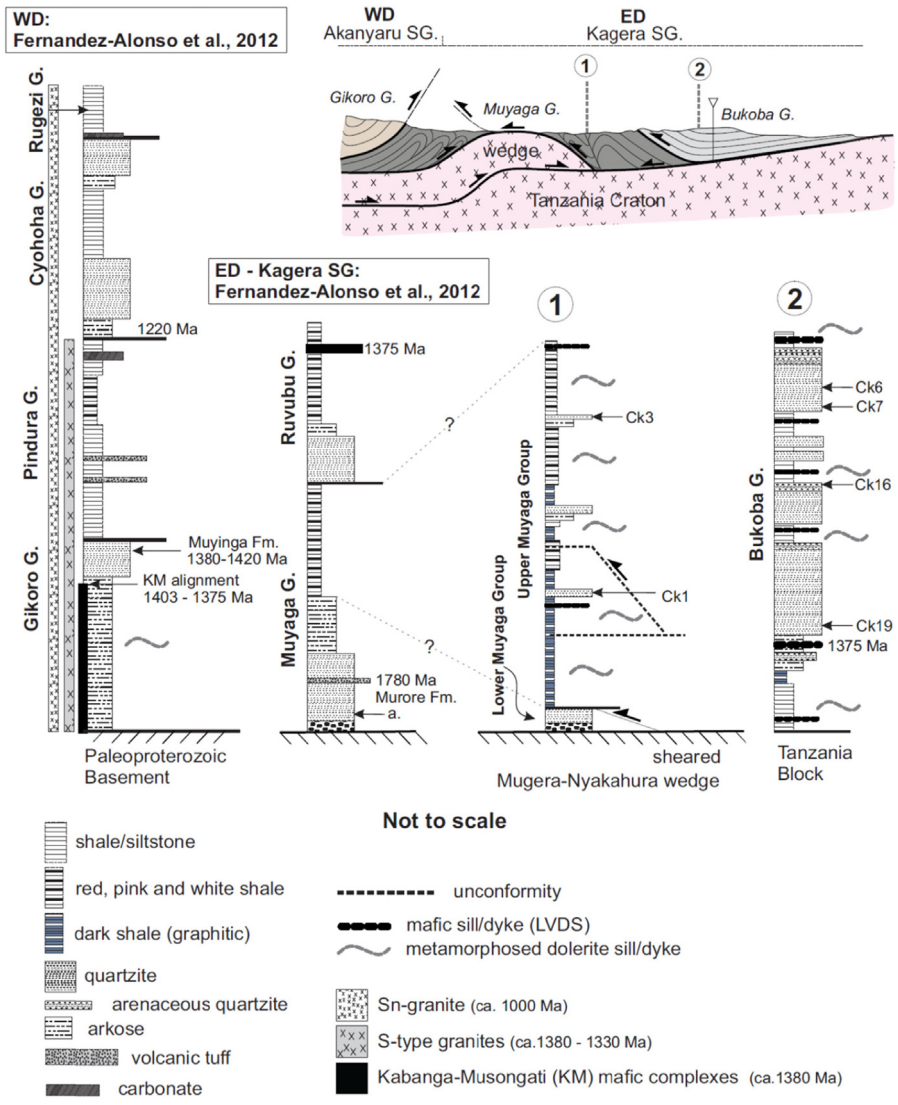

Fig. 4. Correlation of the regional lithostratigraphy of the Western and Eastern Domain after Fernandez-Alonso et al. (2012), Koegelenberg and Kisters (2014) and this study. Geochronology – Kabanga-Musongati (KM) alignment (Maier et al., 2007; Tack et al., 2010); Muyinga Formation (Fernandez-Alonso et al., 2012); Bukoba mafic sill (Deblond et al., 2001); S-type granites (Buchwaldt et al., 2008; Tack et al., 2010). Location of the schematic E-W structural section is shown in Fig. 3.

intruded between the WD and ED (Tack et al., 1994, 2010; Evans et al., 2000) (Fig. 2). Emplacement ages of ca. 1403–1392 Ma for the mafic to ultramafic complexes (Maier et al., 2007) are tentatively correlated with those of the larger ca. 1375 Ma LVDS and stratigraphically higher emplaced sills (Deblond et al., 2001; Tack et al., 2010). The sheared contact separating metasediments of the WD and ED is portrayed as a shallow to steep west dipping listric detachment and Tack et al. (2010) suggest the Kabanga-Musongati alignment to represent a regional contact in the basement below the KAB between the Paleoproterozoic Rusizian Belt, including the underlying Archaean Congo Craton to the west, with Archaean rocks of the TC. This suture is suggested to have been central to the basin and structural evolution of the eastern KAB during later Mesoproterozoic to Neoproterozoic extensional and compressional episodes (Fernandez-Alonso and Theunissen, 1998; Fernandez-Alonso et al., 2012).

2.1.3. Deformation

Much of our knowledge about the structural evolution of the KAB relies on regional reconnaissance and remote sensing studies. Klerkx et al. (1987) and subsequent studies by Fernandez-Alonso and Theunissen (1998), Tack et al. (2010), and Fernandez-Alonso et al. (2012) distinguish two main deformational events, D1 and D2, and a subsequent, more localized D3 deformation. Early bedding-concordant fabrics and structures are attributed to a D1 deformation and related to intracratonic extensional tectonics and subsequent basin formation. Later, pervasive D2 fabrics and structures are responsible for the northwest- to northeast-trending arcuate trend of the belt and the main phase of fold and thrusting (Fig. 2). D1 fabrics are mainly recorded from the Akanyaru Supergroup of the WD, whereas D2 structures have pervasively affected both the WD and ED. D3 structures are late-stage conjugate shear zones in the WD (Fernandez-Alonso and Theunissen, 1998). Tack et al. (2010) correlate the timing of D1 with a phase of regional extensional tectonics associated with the emplacement of the bimodal ca. 1403–1360 Ma plutonism referred to as the Kibara event. The main shortening recorded throughout the KAB is thought to have formed later and in response to far-field stresses during reactivation of the underlying Rusizian-Ubendian basement, related to collisional tectonics recorded in the Southern Irumide Belt at ca. 1.0 Ga (D2), and to Pan-African collisional tectonics recorded in the Mozambique Belt along the eastern margin of the TC (D3). Koegelenberg and Kisters (2014) suggested that far-field stresses from the east were unlikely to account for the metamorphic

zonation, kinematics and overall pronounced convex-eastward geometry of the KAB, also since the timing of the D2/3 tectonism remained unconstrained by any geochronological data.

3. Geology of the Eastern Domain

3.1. Lithostratigraphy of the Eastern Domain

The lithostratigraphic subdivision developed here for the Kagera Supergroup is based on the detailed (1:2000–1:5000) mapping of the rocks in the central parts of the ED, Kagera district (Fig. 3). The regional lithostratigraphy of the Kagera Supergroup (ED) compared to that of the Akanyaru Supergroup (WD) (after Fernandez-Alonso et al., 2012) is shown in Fig. 4 lithologically and structurally, there is clear distinction between the dominantly metapelitic and intensely deformed Muyaga Group in the west and the very-low grade metamorphic, only gently deformed, Bukoba Group dominated by coarse-clastic sedimentary rocks (e.g. Koegelenberg and Kisters, 2014) (Fig. 3).

The Muyaga Group is presently exposed over an area measuring 100 by 500 km in an E-W and N-S direction, respectively, but subsequent shortening and associated folding, thrusting and fabric development must be assumed to have greatly reduced the original E-W extent of the basin. Following previous regional subdivisions (Macdonald, 1966; Gray, 1967), the Muyaga Group can be subdivided into a Lower- (previously the Karagwe-Ankolean Lower Division; Gray 1963) and an Upper Muyaga Subgroup (previously the Karagwe-Ankolean Middle Division; Gray 1963). The lower Muyaga Subgroup varies considerably in thickness, mainly as a result of the tight folding and thrusting (D2) localized close to the basement-cover contacts (Koegelenberg and Kisters, 2014). On a regional scale, the Lower Muyaga Subgroup is characterized, from the base upwards, by coarse-clastic fluvial sediments including conglomerates, grits, immature quartzites and intercalated psammites distinctive of sub-areal to shallow-water environments and intercalated pyroclastic rocks and tuffs (Fernandez-Alonso et al., 2012; Koegelenberg and Kisters, 2014) (Fig. 5a). Van Straaten (1984) documented paleo-current directions indicating sediment flow mainly from E to W, i.e., from the TC towards the KAB. The overall thickness of the Lower Muyaga Subgroup is ca. 100–150 m, although structural duplication and/or excision complicate thickness estimates. The Upper Muyaga is dominated by thick graphitic, but also light coloured shale sequences with several intercalated, up to 15 m thick quartzite horizons that form good marker units. Pyrite is common in graphitic shales, but textural relationships rather suggest a syn to late tectonic growth of pyrite during the main phase of deformation (D2) and associated fluid flow (Fig. 5b). Thick (up to 1 km) shale packages are commonly finely laminated and individual beds may vary from <10 cm to >2–3 m in thickness. Intraformational breccias are locally intercalated with the finely bedded shale units. Quartzite horizons range from immature pebble beds, grits and arkoses to well-sorted quartzites with cross laminations and weakly developed asymmetric ripple marks. Quartzite intercalations occur more frequent and are thickest close to the base of the Upper Muyaga Group, while the Lower Muyaga is dominated by even coarser clastic quartzites (see above), thus depicting an overall upward fining sequence. West of the Mugera-Nyakahura basement inlier, the Muyaga Group is tectonically overlain by rocks of the Akanyaru Supergroup (WD), whereas east of the inlier, the metapelitic rocks pinch out below the Bukoba Group within probably less than 10 km (Koegelenberg and Kisters, 2014) (Fig. 3).

The Bukoba Group is exposed as a 50 by 300 km, northerly trending, slightly arcuate basin forming the easternmost expression of the Kagera Supergroup and the KAB. Rocks of the Bukoba Group unconformably overlie Archaean basement of the TC in the east, but are in structural contact with underthrusted low-grade metasediments of the Upper Muyaga Group in the west (Koegelenberg and Kisters, 2014). The Bukoba Group has only experienced gentle folding and primary sedimentary features are well preserved. In its central parts, the Bukoba Group contains three main, up to 350 m thick packages of mature ortho-quartzites. From the base upwards, ortho-quartzite beds grade from medium-grained (>1 mm) and finely ripple laminated (2–3 mm) to coarse-grained (>2 mm) and thick cross laminated (1–2 cm) (Fig. 5c). An increased arenaceous content and well developed symmetrical ripple marks are more prominent towards the top of quartzites cycles. Paleo-current directions indicate sediment transport mainly from W to E (Fig. 3) and from the KAB towards the TC. The quartzite beds are laterally continuous, but thicknesses can vary from 10 to 50 m, or quartzite units pinch out over several kilometres along strike, hence, forming wide, lensoid sandstone bodies. In numerous places, abrupt facies and thickness variations suggest the presence of growth faults with mainly W to NW trends. Quartzites are sandwiched by buff-coloured mudstone and shale units and, towards the top, are intercalated with thin (>10 cm) beds of cross-ripple laminated quartzites. Contacts between mudstone/shale and quartzite are sharp and typically show syneresis cracks, ball-and-pillow structures and mudstone diapirs. Overall, the Bukoba Group defines an upward coarsening sequence characteristic of shallow marine to shoreline environments, recording the main sediment input from the W.

3.2. Structure of the Eastern Domain

Recent structural work by Koegelenberg and Kisters (2014) suggests that the easternmost parts of the KAB represent the back-thrusted, hinterland-verging frontal parts of the belt, related to regional-scale, east-verging (D2) fold and thrust belt tectonics of the KAB (Fig. 3). Top-to-the west backthrusting has developed in response to thick-skinned tectonic wedging in which Archaean gneisses (Fig. 5e), preserved as the regional-scale Mugera-Nyakahura inlier, were up-thrusted into the Muyaga Group. Backthrusting is localized along a major, mylonitic detachment (D2b) in the roof and in front of the basement inlier. Pinning of the Muyaga Group between the front of the eastwards transported basement wedge and Bukoba Group in the far east has created a tectonic wedge underthrusting the Bukoba Group, gently tilting the coarse-clastic Bukoba Group in a foreland direction (Koegelenberg and Kisters, 2014). As a result, the detachment between the Muyaga Group and the top of the basement wedge (Fig. 6), as well as between the Muyaga- and Bukoba Groups, record top-to-the-WNW passive back-thrusting (D2b) opposite to the regional top-to-the-ESE kinematics (D2a) of the KAB (Fig. 5f). Regionally, this back-thrusted domain represents the termination of eastwards propagating folds and thrusts in the KAB. West of the inlier, towards the interior of the KAB, top-to-the-ESE fore-thrusting dominates (e.g. Tack et al., 1994; Koegelenberg and Kisters, 2014).

4. Pb detrital zircon geochronology

4.1. Analytical Methodology – U–Pb zircon geochronology

Altogether six samples were collected from quartzite horizons from the Upper Muyaga Subgroup (Ck1 and Ck3) and the Bukoba Group (Ck19, Ck16, Ck7 and Ck6) (Figs. 3 and 4) in order to constrain the timing of sedimentation in the eastern parts of the KAB. Sample localities and detailed descriptions are provided in Figs 3 and 4.

All U–Pb age data obtained at the Central Analytical Facility, Stellenbosch University, were acquired by laser ablation–single collector–magnetic sectorfield–inductively coupled plasma–mass

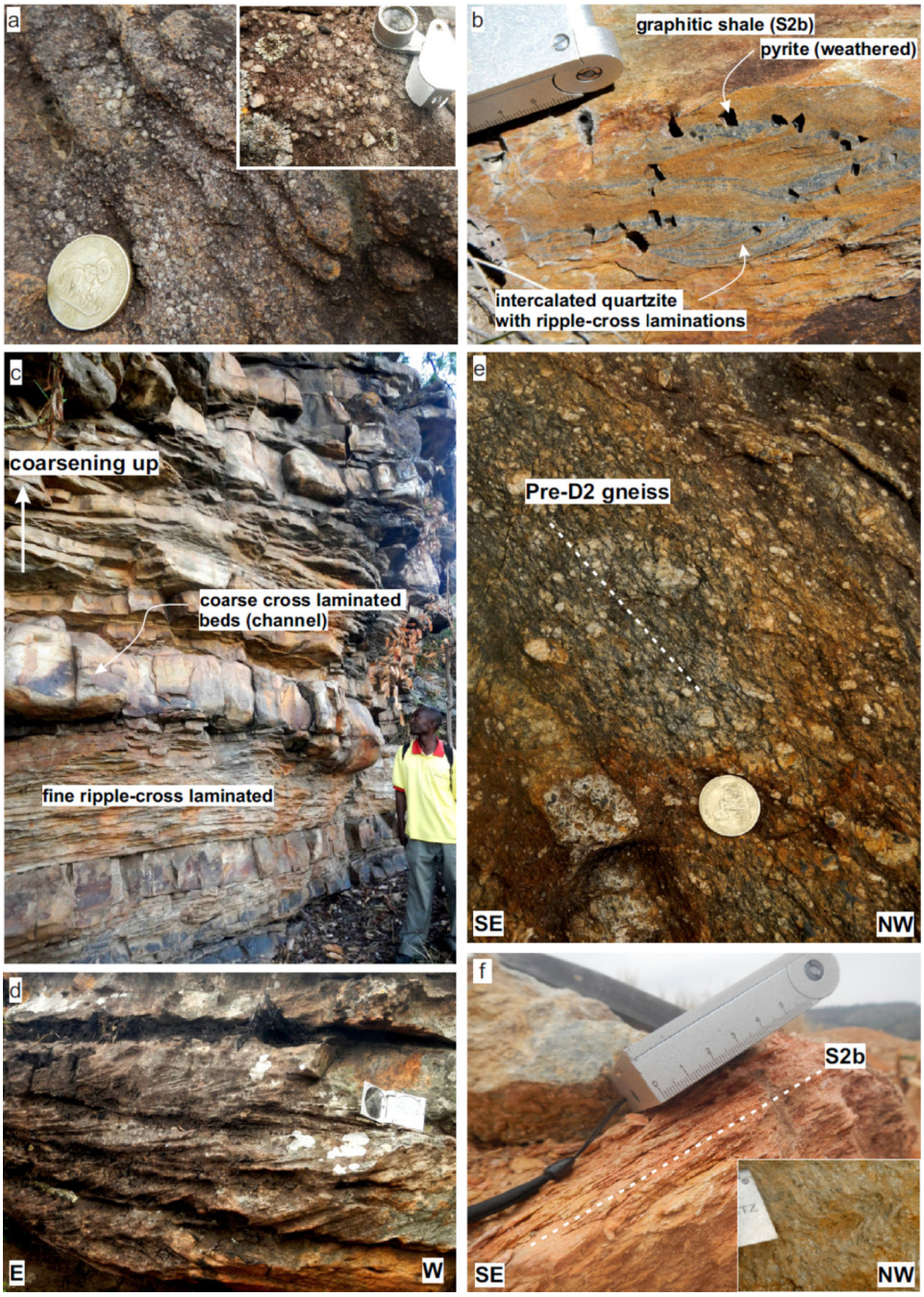

Fig. 5. (a) Coarse clastic grits (fluvial) in the Lower Muyaga Group. (b) Intercalated and cross-ripple laminated quartzite beds in graphitic shale horizon, Upper Muyaga. Note syn to late tectonic euhedral pyrite (weathered) growth at contacts between quartzite and graphitic shale. (c) Thick upward coarsening quartzite beds in the Bukoba Group. (d) Well-developed cross-lamination in coarse quartzite beds indicating paleo-current flow predominantly from west to east, Bukoba Group. (e) Cataclastically deformed porphyritic gneiss with a pervasive pre-D2 (basement) foliation. These gneisses constitute deep basement rocks which likely have not been affected by the detachment (i.e. D2 deformation). (f) Transposed and retrogressed basement gneiss to muscovite schist with S2b foliation. Lower right insert shows fresher muscovite schists, sampled for ^{39}Ar–^{40}Ar geochronology (see Fig. 8b and c1).

spectrometry (LA-SF-ICP-MS) employing a Thermo Finnigan Element2 mass spectrometer coupled to a Resonetics Resolution S155 excimer laser ablation system. All age data presented here were obtained by single spot analyses with a spot diameter of 30 μm and a crater depth of approximately 15–20 μm. The methods employed for analysis and data processing are described in detail by (Frei and Gerdes, 2009). For quality control, the 91500 (Wiedenbeck et al., 1995), Plesovice (Sláma et al., 2008) and M127 (Nasdala et al., 2008; Mattinson, 2010) zircon reference materials were analysed, and the results were consistently in excellent agreement with the published ID-TIMS ages. Full analytical details and the results for all quality control materials analysed are reported in Table 1.1 and 1.2 in the electronic supplementary material. The calculation of concordia ages and plotting of concordia diagrams were performed using Isoplot/Ex 3.0 (Ludwig, 2003).

4.2. U–Pb zircon ages from the Muyaga and Bukoba Group

Upper Muyaga Subgroup – Samples Ck1 and Ck3 are white to grey-bluish, massive and well sorted quartzites that occur as 0.5–5 m thick sandstone horizons within graphitic shale at the base

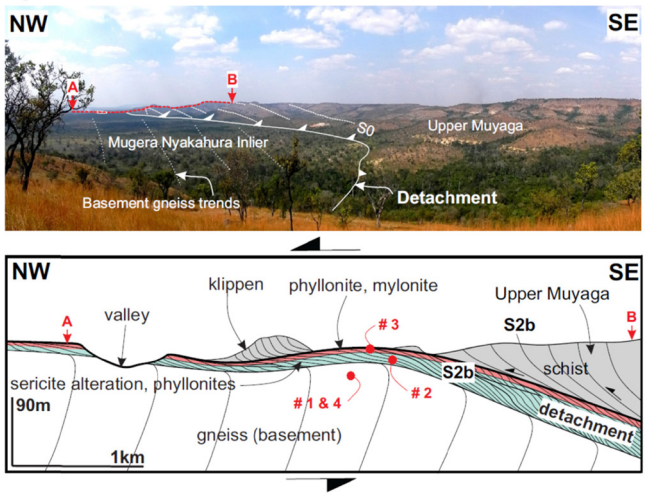

Fig. 6. Schematic cross-section (A and B) of the regional detachment between the Kagera Supergroup and the Mugera-Nyakahura basement inlier (after Koegelenberg and Kisters, 2014) (outlined in Fig. 3). Image below (looking NE): view of tightly folded and NW-verging cover sediments of the Upper Muyaga structurally overlying exposed basement gneisses of the Mugera-Nyakahura inlier. #1 to 4 – sample number with approximate depth location for ^{39}Ar–^{40}Ar geochronology.

of the Upper Muyaga (Ck1) and sharply layered white and pink shale in the uppermost parts of the Upper Muyaga (Ck3) respectively (Fig. 4). Ck1 and Ck3 yielded a combined total of 160 zircons of which 107 gave between 90 and 110% concordant analyses. Both samples show similar, mainly Paleoproterozoic zircon population distributions ranging between 1834 and 1990 Ma (21%), and 2079–2173 Ma (49%), while 30% of zircons are older than 2215 Ma. Zircon ages yield the most prominent peak at ca. 2090 Ma and to a lesser extent ca. 1898–1990 Ma (Fig. 7). The remaining zircon populations are Archaean in age and define smaller peaks, with the oldest zircon yielding an age of 2935 ± 19 Ma. The youngest zircon yields an age of 1834 ± 16 Ma. Zircon grain sizes range from 50 to 190 μm and have variable width-to-length ratios of 1:1–3:1. The bulk of the Paleoproterozoic zircon grains are subhedral with well rounded to subrounded edges (Fig. 7). Archaean grains, in particular, are very well rounded. In general, zircon grains consistently display well developed concentric zoning indicating a magmatic origin.

Bukoba Group – Samples Ck6, Ck7, C16 and Ck19 are light coloured, very mature, coarse grained quartzites from the Bukoba Group (Fig. 4). The samples yielded a combined total of 291 zircons of which 222 gave between 90 and 110% concordant analyses. All samples show broadly similar zircon population distributions and are as follows: 48% have ages ranging between 1878 and 1993 Ma, 18% between 2069 and 2172 Ma and 28% are older than 2495 Ma. The most prominent peaks show a clustering of zircon ages at 1878 Ma, 1993 Ma and 2083 Ma (Fig. 4). In addition, prominent peaks with late-Archaean to early Paleoproterozoic ages are observed between 2417 and 2712 Ma. Four zircons yield distinctly older, Meso- and Paleoarchaean ages between 3152 ± 16 and 3474 ± 10 Ma. Notably, a distinctly youngest group of zircons (n = 10) ranges in age from 1753 ± 23 to 1792 ± 19 Ma. The bulk of zircon grains are mainly subhedral with sub-rounded to completely rounded edges and display well developed concentric- and sector zoning indicating mostly a magmatic origin. Grain sizes are variable and range between 40 μm and 180 μm with width-to-length ratios of 1:1–1:2. Zircons of the younger group (ca. <1800 Ma) are typically elongated with width-to-length ratios of up to 1:5 (Fig. 7). Older Archaean grains are extremely well rounded and typically smaller than 100 μm.

5. ^{39}Ar–^{40}Ar geochronology

To date, there is no direct geochronological data that could constrain the timing of the main D2 deformation in the ED and the KAB as a whole. Existing and geochronological constraints are only inferred from relative age relationships of D2 fabrics with intrusive granites in the WD (Tack et al., 2010 and references therein), although fabric and intrusive relationships are not clear (e.g. Klerkx et al., 1987). In this study, we sampled phyllonites and micaceous mylonites from the main basement-cover detachment (Fig. 6) (Koegelenberg and Kisters, 2014) for ^{39}Ar–^{40}Ar geochronology in order to constrain the timing of the fabric-forming event and, thus, D2 shearing along the basement-cover contact in the ED.

The samples are from the eastern margin of the Mugera-Nyakahura inlier where the detachment between low-grade metamorphic metapelites of the Muyaga Group and the Archaean quartzo-feldpathic gneisses of the basement wedge is well exposed. The basement-cover detachment is developed as up to 20 m thick, pervasively retrogressed and, in places, mylonitic quartz–muscovite–chlorite phyllonites. Shear-sense indicators in the mylonites consistently point to top-to-the northwest kinematics and indicate the backthrusting of the cover above the tectonic basement wedge related to the main D2 phase of deformation (Koegelenberg and Kisters, 2014).

Sample 1 is from steeply (>80°) westwards dipping and highly deformed quartz veins exposed in artisanal mining pits situated in the footwall gneisses and some >20 m below the main phyllonitic detachment. The milky white and homogeneous quartz veins contain micro fractures filled by well preserved, up to 2 cm large muscovite grains (Fig. 8a). Due to the deformed nature and depth from the detachment of the veins, veins are suggested to record deformation of the basement before the D2 event. Samples 2 and 3 are medium- to coarse-grained muscovite schists with quartz porphyroclasts and lesser biotite from within the main D2 detachment (Fig. 8b, c1 and c2) and record a pervasive foliation developed during top-to-the-northwest backthrusting. Sample 4 is a highly foliated, cataclastically deformed, muscovite-bearing porphyritic gneiss located well below the main detachment. The gneissosity has steep (~80°) westerly dips with top-to-the-ESE sense of shear and NNE trends (Figs. 8d and 5e). These gneisses constitute the wall rocks to quartz veins represented by sample 1 (see above) from several metres (>20 m) below the detachment.

5.1. *Analytical methods – ^{39}Ar–^{40}Ar geochronology*

Several handpicked ca. 0.2 mg grains per sample were wrapped in single aluminium foils, and up to 40 wrapped samples were vacuum sealed in a silica glass tube along with standards at the bottom and top of the package. Irradiation was done at NTP radioisotopes' SAFARI1 nuclear reactor at Pelindaba, South Africa, for 20 h in position B2W with the reactor running at 20 MW. Two to three grains of each sample were analysed by stepwise heating at the University of Johannesburg's SPECTRUM analytical facility. This was done using a defocused beam from a continuous Nd-YAG 1064 nm wavelength laser, with the sample port, holding up to 50 grains, connected to a MAP 215-50 noble gas mass spectrometer. This is equipped with a Johnston focused-flow electron multiplier operated in analogue mode. Blank measurements for correction were interspersed routinely before sessions and at 4 step intervals. The Fish Canyon Sanidine standard as well as amphiboles McClure Mountains and Hb3GR were used as monitors, yielding identical *J*-values within uncertainty limits. Measurement control and data reduction was done using an in-house software suite that includes full error propagation via Monte Carlo procedures. The ^{40}Ar decay parameters of Renne et al. (2010) were used.

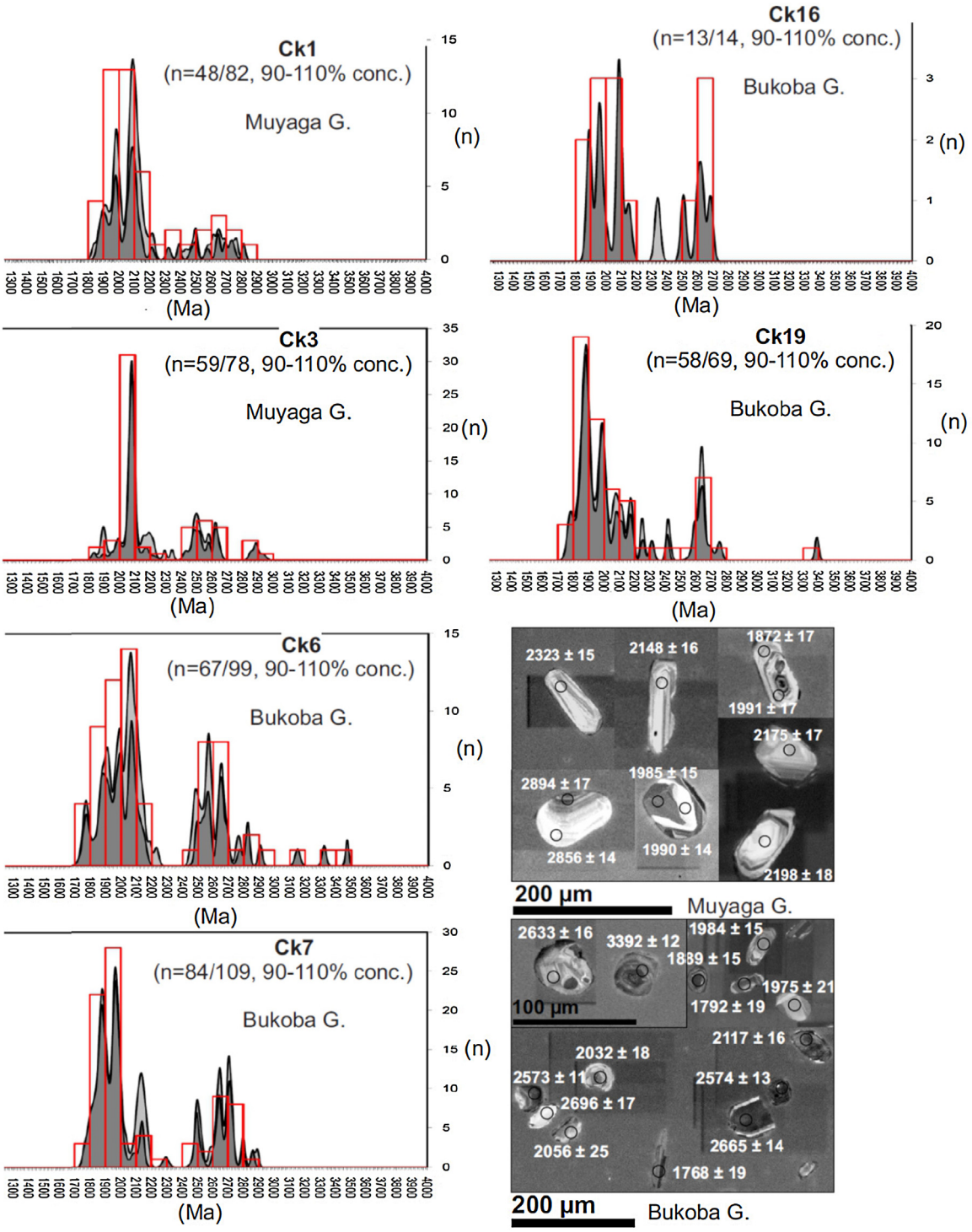

Fig. 7. U–Pb detrital zircon age histograms with probability density distributions for the Muyaga and Bukoba Group. Below: CL images of zircons from respective Groups.

5.2. ^{39}Ar–^{40}Ar results

^{39}Ar–^{40}Ar step graphs are shown in Fig. 9, while analytical data is listed in detail in Table 2 of the electronic supplementary material. The term "integrated age" is used there, as in common usage, for an apparent age obtained from the summed argon release of the included steps and its associated uncertainties. In non-plateau results the uncertainty quoted for integrated ages is therefore usually smaller than the standard deviation of the individual step ages. Cl/K ratios (obtained from $^{38}Ar/^{39}Ar$ ratios, Table 2) are seen to be slightly elevated in the lowest temperature steps, showing the presence of an alteration phase only in those steps. Ca/K ratios (from $^{37}Ar/^{39}Ar$ ratios) are in all cases insignificantly above zero and are not listed.

In all samples (Fig. 9), the lowest temperature steps yield young ages. In view of the slightly elevated Cl/K ratios of these steps, an interpretation of these as resulting from alteration is reasonable. The results do not present age plateaus in the strict sense (i.e. overlap of uncertainty limits) and duplicate analyses also in most cases do not reproduce results within uncertainty limits. This

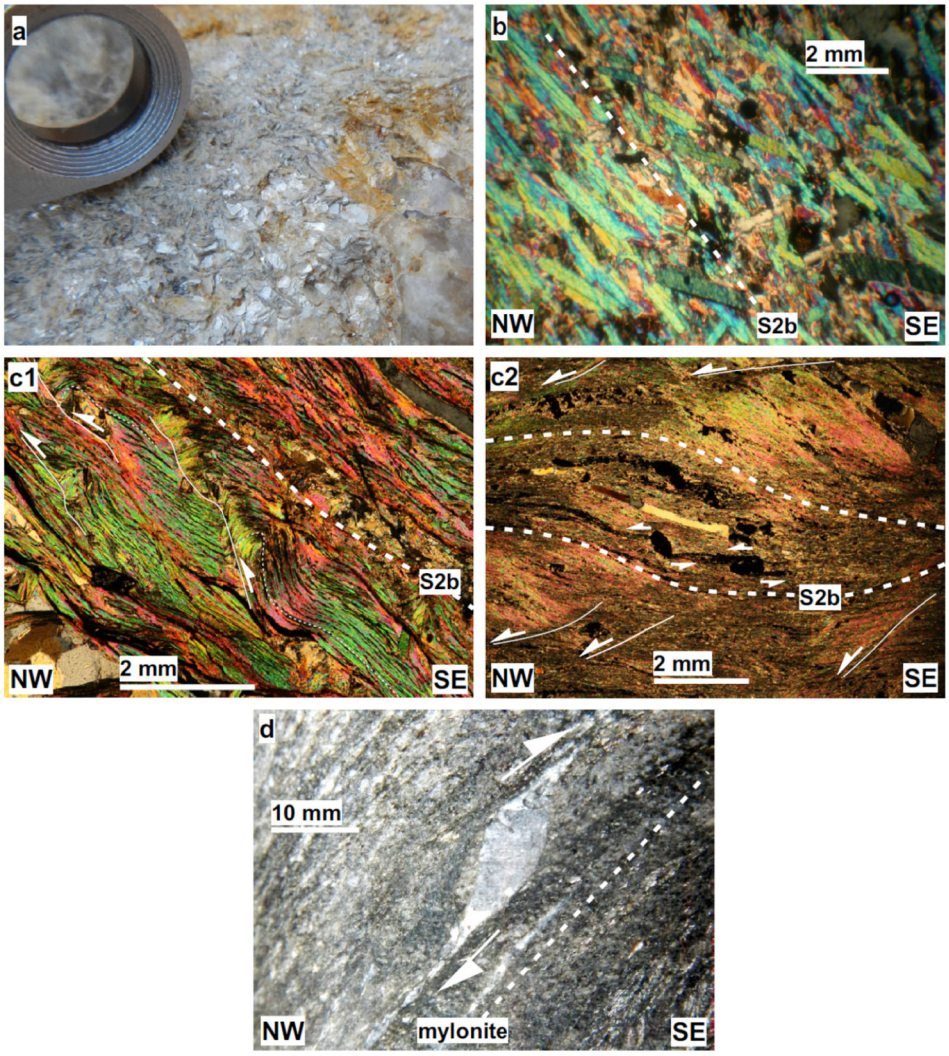

Fig. 8. (a) Well preserved muscovite grains in a brittle deformed massive white quartz vein, hosted by basement gneiss. (b) Cross-polar section of highly foliated (S2b) muscovite-schist from the basement proximal to the main D2 detachment. (c1 and c2) Cross-polar section of a phyllonite (S2b) from the main D2 detachment (outcrop scale, Fig. 5f). Note low angle top-to-the-NW thrusts (c1) and S-C' and σ-objects (c2). (d) Mylonite (chlorite–biotite) bands in basement gneisses with top-to-the-SE sense of shear (outcrop scale, Fig. 5e).

indicates some disturbance of Ar systematics in all samples. However, the results from duplicate analyses are mostly close to each other, which gives confidence.

The muscovites from samples 1 and 4 taken below the D2 detachment zone yield near-plateau ages in the range 1900–1960 Ma, essentially indistinguishable from each other. There is no indication of excess ^{40}Ar (which usually results in a concave-up age spectrum) or of an older relict phase. The dips in the pseudoplataeus probably point to a younger event, or events, in which percolating fluid and/or stress-related minor recrystallization disturbed the K–Ar systematics (Villa, 2010). The age spectra for the muscovites from sample 2 and those from sample 3, both taken in the main D2 detachment zone (Fig. 8b and c) are very different from each other. Both spectra from sample 2 are strongly disturbed, showing an irregular and a staircase pattern yielding no defined age or age range, while those from sample 3 yield pseudoplateaus giving (within error) identical integrated ages, which can be combined to 1326 ± 10 Ma, with no indication of a relict older age.

As muscovite is thermally retentive for Ar up to mid-amphibolite facies conditions (Villa, 1998) a thermochronological approach to the difference between the age spectra of samples 2 and 3 is inapplicable. This difference may however be understood in the context of the textures shown in Fig. 8b (sample 2) and Fig. 8c1 (sample 3). The former shows discrete muscovite grains which, although aligned with the foliation, may be in part inherited, while in the latter, full recrystallization is observed. Following this accord between the textures and the age spectra, it is our interpretation that the date of 1326 ± 10 Ma given by sample 3 correspond to the age of deformation, in which the sample 3 muscovite was fully recrystallized and its age completely reset, whereas sample 2 muscovite was only partially recrystallized and retained some pre-existing radiogenic ^{40}Ar, thus showing relics of its indeterminate original age. The observation that the youngest significant steps in the sample 2 muscovites are not much older than the sample 3 age is in accord with this interpretation.

6. Discussion

6.1. Sedimentation of the Kagera Supergroup

Muyaga Group – U–Pb zircon ages of ca. 1780 Ma (Fernandez-Alonso et al., 2012) from felsic volcanic tuffs of the Murore Formation near the base of the Lower Muyaga Subgroup (Fig. 4) indicate the onset of sedimentation in the Kagera Supergroup (ED)

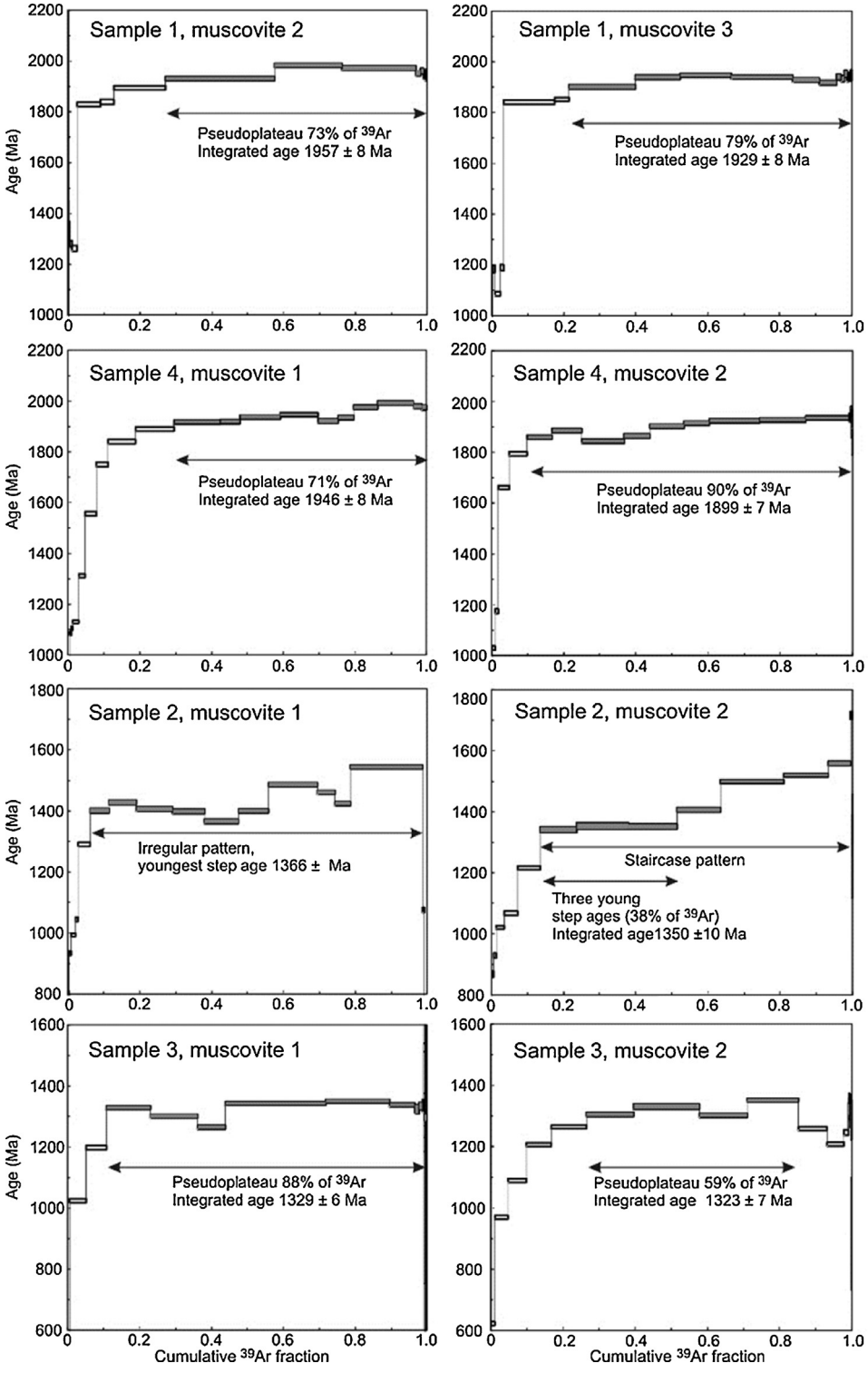

Fig. 9. ^{39}Ar–^{40}Ar step heating release spectrum diagrams with calculated ages for micas, samples 1–4. Sample 1: muscovite contained in quartz vein below the main detachment; samples 2 and 3: mica schist and phyllonite from the main D2 detachment; sample 4: porphyritic gneiss from the basement below main detachment.

occurred in the late Paleoproterozoic. In the northernmost parts of the KAB in SW Uganda, the Kagera Supergroup (also Kagera-Buhjewa Supergroup) is unconformably overlain by the Akanyaru Supergroup (also Karagwe-Ankole Supergroup) (Westerhof et al., 2014). Buchwaldt et al. (2008) documented U–Pb zircon ages of ca. 1568 Ma for the oldest Chitwe granite phase to have intruded the Akanyaru Supergroup in SW Uganda. This constrains sedimentation of the underlying Kagera Supergroup and, by inference, the Muyaga Group to between ca. 1780 and 1568 Ma. This also agrees with the age of 1834 ± 16 Ma of the youngest detrital zircons in the Lower Muyaga Subgroup.

Quartzites from the Upper Muyaga Subgroup studied here (Fig. 4) show a significant proportion of Paleoproterozoic (~74%) compared to Archaean zircons (~27%). The sources of Archaean zircons are likely from the Nyanzian-age TTG-greenstone terranes (2.5–3.0 Ga) of the underlying TC to the east (e.g. Kabete et al.,

2012). Paleoproterozoic zircons are sourced from broadly coeval and continuous Eburnean-aged orogenic belts (2.2–1.98 Ga) wrapping around the southern and western margin of the TC, including the Ubendian-Rusizian- and Ruwenzori Belt (also referred to as Buganda-Toro Belt) (De Waele et al., 2008; Link et al., 2010) (Fig. 1). The Ubende-, Rusizi- and Ruwenzori Belts also record relatively late metamorphic and magmatic events at ca. 1.93 Ga (Boven et al., 1999) and ca. 1.85 Ga (e.g. Singo granite, Nagudi et al., 2003). ^{39}Ar–^{40}Ar ages of ca. 1900–1960 Ma (samples 1 and 4) recorded by relict gneissosities of the Archaean Mugera-Nyakahura inlier likely reflect the effects of these late Eburnean tectonomagmatic events on basement rocks constituting the western margin of the TC. K–Ar geochronology from micas in the Ruwenzori Belt, underlying the northern parts of the KAB, has yielded even younger ages of 1864 ± 37 Ma and 1811 ± 60 Ma (Cahen and Snelling, 1966; Harper et al., 1972). This indicates tectonism of the Rusizi-Ruwenzori Belts was likely complete before ca. 1800 Ma and shortly before or during the onset of sedimentation of the Muyaga Group at 1780 Ma (Fernandez-Alonso et al., 2012).

Zircon populations in the Muyaga Group record an almost even distribution of Paleoproterozoic (41%) and Archaean (51%) ages at the base (Fernandez-Alonso et al., 2012; sample KI 7), but are predominated by Paleoproterozoic (74%) zircons towards the top of the succession. Similarly, the ratio of Paleoproterozoic zircons representing early Eburnean (2.2–1.98 Ga) and late Ubende-Rusizi-Ruwenzori events (1.93–1.85 Ga) increases from the Lower into the Upper Muyaga Subgroup from 1:1 (e.g. Fernandez-Alonso et al., 2012) to 2:1, respectively, and indicates a significant sediment derivation from an older 2.2–1.98 Ga basement during the later stages of sedimentation. In summary, detrital zircon ages indicate sedimentation of the Muyaga Group in the late Paleoproterozoic from ca. 1780 Ma to before ca. 1570 Ma with sediments mainly derived from Eburnean hinterlands that probably underwent post-tectonic uplift and erosion since ca. 1800 Ma.

Bukoba Group – The Bukoba Group overlies the Muyaga Group (Koegelenberg and Kisters, 2014) and is similarly dominated by Paleoproterozoic zircons, but with a slightly higher abundance of Archaean zircons and a more prominent late Ubende-Rusizi age (1.93–1.8 Ga) population compared to the Muyaga Group. The greater abundance of Archaean zircons most likely reflects the proximity of the TC and the unconformable contact of the Bukoba Group overlying Nyanzian (>2.5 Ga) basement (e.g. Kabete et al., 2012). The presence of Meso- and Paleoarchaean zircons points to sediment input from the 3.5–3.2 Ga TTG-greenstone terranes situated to the east of Lake Victoria (Kabete et al., 2012 and references therein). The slight shift to a more prominent late Ubende-Rusizi-Ruwenzori (ca. 1.93–1.85 Ga) zircon population, compared to the underlying Muyaga Group, corresponds to a later deposition and further exhumation of nearby late Ubende-Rusizi-Ruwenzori basement. Notably, a distinctly younger population of 1753–1792 Ma age zircons (n = 10, >90% con.) occurs in most samples of the Bukoba Group. These younger zircons are conspicuously absent from the pelitic Upper- and coarse-clastic Lower Muyaga Subgroup (see also Fernandez-Alonso et al., 2012), but correspond to the age of the ca. 1780 Ma volcanic units of the Murore Formation close to the base of the Muyaga Group. This may indicate the uplift and erosion of the Muyaga Group and reworking of the Murore Formation felsic volcanic units into the Bukoba Group. Sediment transport from the west is, indeed, suggested by paleo-current directions recorded in the mature ortho-sandstones of the Bukoba Group (Fig. 3). Reworking of the Muyaga Group may, thus, indicate sedimentation of the Bukoba Group in a foreland position with respect to the Muyaga Group that undergoes uplift and erosion in the west. Uplift and erosion of the Muyaga Group and the timing of Bukoba sedimentation cannot be accurately constrained, but the absence of Mesoproterozoic zircons from any of the Bukoba Group samples suggests that sedimentation occurred at least before ca. 1568 Ma and after sedimentation of the Muyaga Group. In summary and in agreement with Fernandez-Alonso et al. (2012), detrital zircon ages in the Bukoba Group indicate a late Paleoproterozoic timing of deposition, but after Muyaga Group sedimentation and with sediments derived from reworking of the Muyaga Group and underlying Eburnean basement rocks.

6.2. Timing of deformation in the ED

^{40}Ar–^{39}Ar geochronology of white mica (muscovite) defining the mylonitic fabrics in the main D2 detachment between basement gneisses and the overlying Upper Muyaga Group in the eastern, frontal parts of the KAB yielded effectively identical near-plateau ages combined to 1326 ± 10 Ma (sample 3). A similar timing is further indicated by the overprint of older muscovite grains by a ca. 1350 Ma or younger event (sample 2). The ^{40}Ar–^{39}Ar age of 1326 ± 10 Ma yielded by the fabric forming micas of sample 3 are interpreted to indicate the timing of the main D2 phase of folding and thrusting recorded in the ED of the KAB.

The co-axial orientation of D2 folds and thrusts in the ED with those in the WD (Cahen et al., 1984; Tack et al., 1994; Fernandez-Alonso and Theunissen, 1998; Fernandez-Alonso et al., 2012) suggests that deformation along the eastern frontal parts of the KAB is related to tectonism in the WD of the belt. This would also imply that the timing of deformation documented here for the ED must be considered to be the minimum age of the regional D2 tectonism due to the structural position of the ED in the easternmost parts and along the toe of the KAB (e.g. Koegelenberg and Kisters, 2014). Assuming an average propagation rate of between 10 and 20 mm p/a of continental fold-and-thrust belts (De Celles and De Celles, 2001), backthrusting in the ED may only record the arrival of the deformation front some ca. 15–30 Ma after structures had formed some ca. 300 km to the west and across the KAB. This calculation must be taken as a minimum estimate, given that the present width of the KAB records a significant amount of shortening.

If correct, the Mesoproterozoic timing of deformation points to a close temporal relationship between D2 crustal shortening and peraluminous granites intruding the higher-grade western parts of the KAB between ca. 1328–1380 Ma (Buchwaldt et al., 2008; Tack et al., 2010; Debruyne et al., 2015). Similarly, the age of mafic dykes and sills of the LVDS and Kabanga-Musongati alignment ranges between ca. 1340–1375 Ma (Deblond et al., 2001; Tack et al., 2010; Mäkitie et al., 2014) and likewise almost overlaps with the Mesoproterozoic timing of D2 deformation recorded here for the ED. This timing of the main D2 deformation agrees with field relationships showing that mafic sills emplaced in the ED at ca. 1375 or earlier (Deblond et al., 2001; Koegelenberg and Kisters, 2014) are variably folded (Evans et al., 2000; Koegelenberg and Kisters, 2014). Importantly, the arcuate geometry of the giant LVDS is parallel to that of the arcuate D2 fold and thrust belt structures (Fig. 1), suggesting a close relationship between the emplacement of the mafic suite and compressional tectonics and loading of the leading edge of the Tanzania Craton.

The mid-Mesoproterozoic timing of crustal shortening in the ED is at variance with existing tectonic models for the belt that suggest the main regional deformation to be the result of far-field stresses related to Neoproterozoic (ca. 1.0 Ga) re-activation of the Ubende-Rusizi Belt in the SE of the KAB, or Pan-African (550–530 Ma) strains, related to the collisional tectonics recorded in the Mozambique Belt along the eastern margin of the TC (Tack et al., 2010; Fernandez-Alonso et al., 2012). Studies postulating a late Neoproterozoic and/or Pan-African tectonism have mainly focussed on the internal WD of the KAB (Tack et al., 2010; Fernandez-Alonso et al., 2012), however ^{40}Ar–^{39}Ar mica ages presented here from the ED

do not indicate any major and younger deformation event or later reactivation of structures.

6.3. Mesoproterozoic sedimentation in the KAB and Kibara Belt (KIB)

Recent models have suggested the deconstruction of the Kibara orogenic system (sensu lato) into a southern Kibara Belt (KIB) and a northern KAB (Fig. 1), both with supposedly separately evolved lithostratigraphic sequences (Kokonyangi et al., 2007; Fernandez-Alonso et al., 2012). The expanded geochronological data base of sedimentary sequences and intrusive relationships in the KIB and KAB hint, however, at possible correlations between sedimentary successions. The lowermost Kiaora Group in the KIB is intruded by ca. 1380 Ma granites, similar to the Gikoro and Pindura Groups of the Akanyura Supergroup in the KAB, and not only suggests a broadly contemporaneous sedimentation before ca. 1380 Ma, but also coeval plutonism in the KIB and KAB (Kokonyangi et al., 2006; Tack et al., 2010). Following sedimentation of the Kiaora, Gikoro- and Pindura Groups a distinct depositional hiatus of ca. 50 Ma is recorded before the sedimentation of the overlying Nzilo Group in the KIB (<1329 Ma), and likewise a ca. 150 Ma hiatus before sedimentation of the Cyohoha Group in the KAB (<1220 Ma) (Kokonyangi et al., 2007; Fernandez-Alonso et al., 2012). The depositional hiatus after the Kiaora Group sedimentation coincides with the pre-D2 convergence stage postulated for the KIB after ca. 1380 Ma (Kokonyangi et al., 2006, 2007) and the D2 phase of crustal shortening and thickening proposed here for the KAB, rather than intracratonic basin formation (Fernandez-Alonso et al., 2012). Indeed, detrital zircon populations in the Nzilo Group of the KIB (KIB) with an age range of ca. 1499–1329 Ma, suggest the uplift and reworking of regions with distinctly Mesoproterozoic age signatures such as rocks in the KAB of SW Uganda, containing ca. 1568–1443 Ma and ca. 1368–1328 Ma old granites, as a possible source (Buchwaldt et al., 2008).

6.4. Regional correlations of sedimentary successions in the ED

The Kagera Supergroup of the ED in Tanzania correlates with rocks assigned to the Kagera-Buhjewa Supergroup in the northernmost parts of the KAB in SW Uganda (Fernandez-Alonso et al., 2012; Westerhof et al., 2014). Further north-east, seemingly older rocks of the Namuwasa Group (Fig. 1) are variably deformed by thin- and thick skin thrusting processes and are, in turn, unconformably overlain by the only gently deformed Bwezigoro Group (Westerhof et al., 2014). The youngest detrital volcanic zircon from the Bwezigoro Group has yielded an age of ca. 1.79 Ga (Mänttäri, 2014), similar to the youngest zircon population in the lithologically similar Bukoba Group in NW-Tanzania (Fig. 1; see chapter 4.2) (Koegelenberg and Kisters, 2014; Kock and Natukunda, 2011).

This implies that the Muyaga- and Namuwassa Groups and the stratigraphically overlying Bukoba- and Bwezigoro Groups record distinct periods of sedimentation and basin formation. Sedimentation of the Namuwassa Group is constrained to after the youngest recorded detrital zircons of 2.05 Ga and before the intrusion of ca. 1.98 Ga Ma Kyato dolerites (Mänttäri, 2014; Kock and Natukunda, 2011). In contrast, the Muyaga Group containing ca. 1.78 Ga felsic tuff layers of the Murore Formation (Fernandez-Alonso et al., 2012) indicate sedimentation up to 200 Ma later than Namuwasa Group. Later sedimentation in the Muyaga Group is consistent with a relatively small Late Eburnean population of detrital zircons between ca. 1990 and 1824 Ma. However, both the Namuwasa- and younger Muyaga Group share a predominantly Eburnean (2.2–2.0 Ga) zircon population, indicating that these groups formed part of a once laterally extensive sequence of successor basins deposited between ca. 2050 Ma and 1750 Ma to the east of an Eburnean orogenic hinterland.

The absence of the Muyaga Group or sediments of a similar age underlying the Bwezigoro Group in SW-Uganda suggests, by inference, a regional unconformity between the Bukoba- and underlying Muyaga Group in NW Tanzania. This is supported by distinct lithological contrasts between Muyaga- and Bukoba Group. Regional correlations may, thus, imply the Bukoba- and Bwezigoro Group once formed part of an originally much larger and laterally continuous sedimentary sequence extending from SW-Uganda and NW-Tanzania into Burundi, unconformably overlying a range of Eburnean basins (e.g. Muyaga-, Namuwassa Group). The geodynamic setting and timing of sedimentation however remains speculative, but we tentatively suggest Eburnean sedimentary basins (e.g. Muyaga Group, Numawassa Group) were subjected to uplift and reworking into foreland basins of the Bukoba and Bwezigoro Groups to the east.

7. Conclusions

U–Pb detrital constraints indicate that sub-basins of the Kagera Supergroup (WD) in NW-Tanzania, namely the Muyaga and Bukoba Group, were not contemporaneous and are lithologically distinct basins. The onset of sedimentation of the Muyaga Group is constrained to ca. 1780 Ma (see also Fernandez-Alonso et al., 2012) forming part of regionally extensive successor basins deriving detritus from Eburnean-age hinterlands consisting of the Ubende-Rusizi-Ruwenzori Belts to the west. Rocks of the Muyaga Group are overlain by the Bukoba Group that records, at least in part, the reworking of the underlying Muyaga Group. Based on their stratigraphic position and detrital zircon inventory, regional correlations between the Bukoba and Bwezigoro Group in SW-Uganda seem likely, both deriving detritus from the erosion and reworking of the Muyaga Group and older, regionally extensive Eburnean basins (Namuwasa Group) and forming foreland basins with respect to the uplifted Eburnean-age rocks to the west. The timing of basin formation remains elusive, but can be constrained to before the intrusion of the oldest phases of granites into the overlying Akanyaru Supergroup at ca. 1568 Ma, and sometime after deposition of the Muyaga Group (ca. 1780 Ma).

^{39}Ar–^{40}Ar geochronology of the regional detachment between the Kagera Supergroup and Tanzania Craton indicates a timing of ca. 1326 ± 10 Ma for the main phase of D2 shortening in the ED of the KAB. The timing of the main phase of crustal shortening in the ED coincides with the end of the main phase of peraluminous granite plutonism in the WD at ca. 1380–1330 Ma. Notably, the orientation of D2 structures in the ED also corresponds with that of the giant arcuate LVDS mafic volcanism and plutonism at ca. 1375–1340 Ma. The ^{39}Ar–^{40}Ar geochronology does not indicate an overprint of structures of the ED during later Neoproterozoic or Pan-African events and the main structural grain was evidently acquired during E-W shortening and in the Mesoproterozoic. These results suggest a closer correlation between the Karagwe-Ankole and Kibara (sensu stricto) fold and thrust belts.

Acknowledgements

The project was only possible through the financial and logistical support of Anglo Gold Ashanti (AGA) and with permission from AGA to publish. A special thanks to the late Peter Winkler and Joas Kabete for initiating the project, Gillian Williams for logistics and Esperius Kavako for invaluable help with sample preparation and fieldwork. Additional funding through the NRF Scarce Skills Development Fund (Grant 81573) was also greatly appreciated. Critical comments by two journal reviewers are greatly appreciated.

Appendix A. Supplementary data

Supplementary data associated with this article can be found, in the online version, at http://dx.doi.org/10.1016/j.precamres.2015.08.014.

References

Batumike, J.M., Griffin, W.L., O'Reilly, S.Y., Belousova, E.A., Pawlitschek, M., 2009. Crustal evolution in the central Congo-Kasai Craton, Luebo, D.R. Congo: insights from zircon U–Pb ages, Hf-isotope and trace-element data. Precambrian Res. 170, 107–115.

Boniface, N., Schenk, V., 2012. Neoproterozoic eclogites in the Paleoproterozoic Ubendian belt of Tanzania: evidence for a Pan-African suture between the Bangweulu Block and the Tanzania Craton. Precambrian Res. 208–211, 72–89.

Boniface, N., Schenk, V., Appel, P., 2012. Paleoproterozoic eclogites of MORB-type chemistry and three Proterozoic orogenic cycles in the Ubendian belt (Tanzania): evidence from monazite and zircon geochronology, and geochemistry. Precambrian Res. 192–195, 16–33.

Boniface, N., Schenk, V., Appel, P., 2014. Mesoproterozoic high-grade metamorphism in pelitic rocks of the north western Ubendian Belt: implication for the extension of the Kibaran intra-continental basins to Tanzania. Precambrian Res. 249, 215–228.

Boven, A., Theunissen, K., Sklyarov, E., Klerkx, J., Melnikov, A., Mruma, A., Punzalan, L., 1999. Timing of exhumation of a high-pressure granulite terrane of the Palaeoproterozoic Ubende belt (west Tanzania). Precambrian Research 93, 119–137.

Buchwaldt, R., Toulkeridis, T., Todt, W., Ucakuwun, E.K., 2008. Crustal age domains in the Kibaran belt of SW-Uganda: combined zircon geochronology and Sm–Nd isotopic investigation. J. Afr. Earth Sci. 51, 4–20.

Cahen, L., Snelling, N.J., 1966. The Geochronology of Equatorial Africa. North-Holland Publishing Company, Amsterdam, pp. 195.

Cahen, L., Snelling, N.J., Delhal, J., Vail, J.R., Bonhomme, M., Ledent, D., 1984. The Geochronology and Evolution of Africa. Oxford University Press, Oxford, pp. 512.

Debruyne, D., Hulsbosch, N., Van Wilderode, J., Balcaen, L., Vanhaecke, F., Muchez, P., 2015. Regional geodynamic context for the Mesoproterozoic Kibara Belt (KIB) and the Karagwe-Ankole Belt: evidence from geochemistry and isotopes in the KIB. Precambrian Res. 264, 82–97.

De Celles, P.G., De Celles, P.C., 2001. Rates of shortening, propagation, underthrusting, and flexural wave migration in continental orogenic systems. Geology 29, 135–138.

De Waele, B., Fitzsimons, I.C.W., 2007. The nature and timing of Palaeoproterozoic sedimentation at the south eastern margin of the Congo Craton; zircon U–Pb geochronology of plutonic, volcanic and clastic units in northern Zambia. Precambrian Res. 159, 95–116.

De Waele, B., Johnson, S.P., Pisarevski, S.A., 2008. Palaeoproterozoic to Neoproterozoic growth and evolution of the eastern Congo Craton: its role in the Rodinia puzzle. Precambrian Research 160, 127–141.

De Waele, S., Henjes-Kunst, F., Melcher, F., Sitnikova, M., Burgess, R., Gerdes, A., Alonso Fernandez, M., De Clercq, F., Muchez, P., Lenmann, B., 2011. Late Neoproterozoic overprinting of cassiterite and columbite–tantalite bearing pegmatites of the Gatumba area, Rwanda (Central Africa). J. Afr. Earth Sci. 61, 10–26.

Deblond, A., Punzalan, L.E., Boven, A., Tack, L., 2001. The Malagarazi Supergroup of SE Burundi and its correlative Bukoban Supergroup of NW Tanzania: Neo- and Mesoproterozoic chronostratigraphic constraints from Ar–Ar ages on mafic intrusive rocks. J. Afr. Earth Sci. 32, 435–449.

Delpomdor, F., Linnemann, U., Boven, A., Gärtner, A., Travin, A., Blanpied, C., Virgone, A., Jelsma, H., Préat, H., 2013. Depositional age, provenance, and tectonic and paleoclimatic settings of the late Mesoproterozoic–middle Neoproterozoic Mbuji-Mayi Supergroup Democratic Republic of Congo. Palaeogeogr. Palaeoclim. Palaeoecol. 389, 4–34.

Evans, D.M., Boadi, I., Byemelwa, L., Gilligan, J., Kabete, J., Marcet, P., 2000. Kabanga magmatic sulphide deposits, Tanzania: morphology and geochemistry of associated intrusions. J. Afr. Earth Sci. 30, 651–674.

Fernandez-Alonso, M., Cutten, H., De Waele, B., Tack, L., Tahon, A., Baudet, D., Barritt, S.D., 2012. The Mesoproterozoic Karagwe-Ankole Belt (formerly the NE Kibara Belt): the result of prolonged extensional intracratonic basin development punctuated by two short-lived far field compressional events. Precambrian Res. 216–219, 63–86.

Fernandez-Alonso, M., Theunissen, K., 1998. Airborne geophysics and geochemistry provide new insights in the intracontinental evolution of the Mesoproterozoic Kibaran belt (Central Africa). Geol. Mag. 135, 203–216.

Frei, D., Gerdes, A., 2009. Precise and accurate in situ U–Pb dating of zircon with high sample throughput by automated LA-SF-ICPMS. Chem. Geol. 261, 261–270.

Kock, G.S. de, Manninen, T., Mänttäri I. Natukunda, J.F. 2011. Zircon ages from the Namuwaza and Bwezigoro-Gunga Plateau sequences, Uganda. 23rd Coll. Afr. Geol. (CAG23), 8–14 Jan. 2011, Univ. of Johannesburg, Abstract volume, 101.

Gray, I.M., 1967. Quarter Degree Sheet 29 (Ngara). Mineral Resources Division of Tanzania, Dodoma.

Harper, C.T., Shacklet, R.M., Weintrau, G.S., Leggo, P.J., 1972. Potassium-Argon retention ages from basement complex and associated Precambrian metasedimentary rocks of Uganda. Geol. Soc. Am. Bull. 83 (11), 3449, IAGOD Quadrennial Symposium and Geocongress, Windhoek Namibia, p. 6.

Kabete, J.M., Groves, D.I., McNaughton, N.J., Mruma, A.H., 2012. A new tectonic and temporal framework for the Tanzanian Shield: implications for gold metallogeny and undiscovered endowment. Ore Geol. Rev., http://dx.doi.org/10.1016/j.oregeorev.2012.02.009.

Kampunzu, A.B., Rumvegeri, B.T., Kapenda, D., Lubala, R.T., Caron, J.P.H., 1986. Les Kibarides d'Afrique centrale et orientale: une chaîne de collision. UNESCO Geol. Devel. Newslett. 5, 125–137.

Klerkx, J., Liégeois, J.-P., Lavreau, J., Claessens, W., 1987. Crustal evolution of the northern Kibaran Belt, eastern and central Africa. In: Kröner, A. (Ed.), Proterozoic Lithospheric Evolution, 17. American Geophysical Union and the Geological Society of America, pp. 217–233.

Koegelenberg, C., Kisters, A.F.M., 2014. Tectonic wedging, back-thrusting and basin development in the frontal parts of the Mesoproterozoic Karagwe-Ankole belt in NW Tanzania. J. Afr. Earth Sci. 97, 87–98.

Kokonyangi, J., Armstrong, R.A., Kampunzu, A.B., Yoshida, M., Okudaira, T., 2004. U–Pb zircon geochronology and petrology of granitoids from Mitwaba (Katanga Congo): implications for the evolution of the Mesoproterozoic Kibaran belt. Precambrian Res. 132, 79–106.

Kokonyangi, J., Kampunzu, A.B., Poujol, M., Okudaira, T., Yoshida, M., Shabeer, K.P., 2005. Petrology and geochronology of Mesoproterozoic mafic–intermediate plutonic rocks from Mitwaba (D. R. Congo): implications for the evolution of the Kibaran belt in central Africa. Geol. Mag. 142, 109–130.

Kokonyangi, J., Kampunzu, A.B., Armstrong, R., Arima, M., Yoshida, M., Okudaira, T., 2007. U–Pb SHRIMP Dating of Detrital Zircons from the Nzilo Group (Kibaran Belt): implications for the source of sediments and Mesoproterozoic Evolution of Central Africa. J. Geol. 115, 99–113.

Kokonyangi, J., Kampunzu, A.B., Armstrong, R., Yoshida, M., Okudaira, T., Arima, M., Ngulube, D.A., 2006. The Mesoproterozoic Kibaride belt (Katanga, SE D.R. Congo). J. Afr. Earth Sci. 46, 1–35.

Lenoir, J.L., Liegeois, J.P., Theunissen, K., Klerkx, J., 1994. The Palaeoproterozoic Ubendian shear Belt in Tanzania: geochronology and structure. J. Afr. Earth Sci. 19 (3), 169–184.

Link, K., Koehn, D., Barth, M.G., Tiberindwa, J.V., Barifaijo, E., Aanyu, K., Foley, S.F., 2010. Continuous cratonic crust between the Congo and Tanzania blocks in western Uganda. Int. J. Earth Sci. (Geol. Rundsch.) 99, 1559–1573.

Ludwig, K., 2003. Isoplot/Ex version 3: A Geochronological Toolkit for Microsoft Excel. Geochronology Center, Berkeley.

Macdonald, A.S., 1966. Quarter Degree Sheet 30 (Biharamulo). Mineral Resources Division of Tanzania, Dodoma.

Maier, W.D., Peltonen, P., Livesey, T., 2007. The ages of the Kabanga North and Kapalagulu intrusions Western Tanzania: a reconnaissance study. Econ. Geol. 102, 147–154.

Makitie, H., Data, G., Isabirye, E., Manttari, I., Huhma, H., Klausen, M.B., Pakkanen, L., Virransalo, P., 2014. Petrology, geochronology and emplacement model of the giant 1.37 Ga arcuate Lake Victoria Dyke Swarm on the margin of a large igneous province in eastern Africa. J. Afr. Earth Sci. 97, 273–297.

Mänttäri, I., 2014. Mesoarchaean to Neoproterozoic crustal evolution of Uganda: evidence from new U–Pb and Sm–Nd rock ages. In: Lehto, T., Katto, E. (Eds.), GTK Consortium Geological Surveys in Uganda 2008–2012. Sustainable Management of Mineral Resources Project. , pp. 121–164, Geological Survey of Finland, Special Paper 56.

Mattinson, J.M., 2010. Analysis of the relative decay constants of 235U and 238U by multi-step CA-TIMS measurements of closed-system natural zircon samples. Chem. Geol. 275, 186–198.

Nagudi, B., Koeberl, C., Kurat, G., 2003. Petrography and geochemistry of the Singo granite, Uganda, and implications for its origin. J. Afr. Earth Sci. 36, 73–87.

Nasdala, L., Hofmeister, W., Norberg, N., Mattinson, J.M., Corfu, F., Dörr, W., Kamo, S.L., Kennedy, A.K., Kronz, A., Reiners, P.W., Frei, D., Košler, J., Wan, Y., Götze, J., Häger, T., Kröner, A., Valley, J.W., 2008. Zircon M257 – a homogeneous natural reference material for the ion microprobe U–Pb analysis of zircon. Geostand. Geoanal. Res. 32, 247–265.

Renne, P.R., Mundil, R., Balco, G., Min, K.R., Ludwig, K.R., 2010. Joint determination of ^{40}K decay constants and ^{40}Ar*/^{40}K for the Fish Canyon sanidine standard, and improved accuracy for ^{40}Ar/^{39}Ar geochronology. Geochim. Cosmochim. Acta 74, 5349–5367.

Sláma, J., Košler, J., Condon, D.J., Crowley, J.L., Gerdes, A., Hanchar, J.M., Horstwood, M.S.A., Morris, G.A., Nasdala, L., Norberg, N., Schaltegger, U., Schoene, B., Tubrett, M.N., Whitehouse, M.J., 2008. Plešovice zircon – a new natural reference material for U–Pb and Hf isotopic microanalysis. Chem. Geol. 249, 1–35.

Tack, L., Liégeois, J.P., Deblond, A., Duchesne, J.C., 1994. Kibaran A-type granitoids and mafic rocks generated by two mantle sources in a late orogenic setting (Burundi). Precambrian Res. 68, 323–356.

Tack, L., Wingate, M.T.D., De Waele, B., Meert, J., Belousova, E., Griffin, A., Tahon, A., Fernandez-Alonso, M., 2010. The 1375 Ma "Kibaran event" in Central Africa: prominent emplacement of bimodal magmatism under extensional regime. Precambrian Res. 180, 63–84.

Van Straaten, H.P., 1984. Contribution to the geology of the Kibaran Belt in northwest Tanzania. UNESCO geology for development. Newslett./Bull. 3, 59–68.

Villa, I.M., 2010. Disequilibrium textures versus equilibrium modelling: geochronology at the crossroads. In: Spalla, M., Marotta, A.M., Gosso, G. (Eds.), Advances in Interpretation of Geological Processes: Refinement of Multi-scale Data and Integration in Numerical Modelling. Geological Society, Special Publications, 332, London, pp. 1–15.

Villeneuve, M., Chorowicz, J., 2004. Les sillons plisses du Burundien superieur dans la chaine Kibarienne d'Afrique centrale. Comptes Rendus Geosciences 336, 807–814.

Westerhof, A.B.P., Härmä, P., Isabirye, E., Katto, E., Koistinen, T., Kuosmanen, E., Letho, T., Lehtonen, M.I., Mäkitie, H., Manninen, T., Mänttäri, I., Pekkala, Y., Pokki, J., Saalmann, K., Virransalo, P., 2014. Geology and Geodynamic Development of Uganda with Explanation of the 1:1 000,000 Scale Geological Map. Geological Survey of Finland, Special Paper 55.

Wiedenbeck, M., Alle, P., Corfu, F., Griffin, W.L., Meier, M., Oberli, F., Von Quadt, A., Roddick, W., Speigel, W., 1995. Three natural Zircon standards for U–Th–Pb, Lu–Hf trace-element and REE analyses. Geostand. Newslett. 19, 1–23.

4. Structural controls and fluid sources of auriferous quartz veins in Paleoproterozoic metasediments of the Karagwe-Ankole Belt on the western margin of the Tanzania Craton

This manuscript was submitted to Ore Geology Reviews on the 7th of December 2015 and is currently under review. I am the principal author and the paper is co-authored by Alex Kisters and Chris Harris (Department of Geological Sciences, University of Cape Town).

The original field work entailed the detailed structural analysis of gold prospects in the region, sampling of quartz veins and host lithologies. I was further responsible for the literature review, majority of the writing and compilation of all diagrams. Alex Kisters contributed editorial work towards the final draft and helped with the structural interpretation and concepts of the mineralization. Chris Harris undertook the stable oxygen isotope analysis and assisted with the interpretation of the data, as well as reviewing the integration thereof into a broader mineralization model.

Structural controls of fluid flow and gold mineralization in the easternmost parts of the Karagwe-Ankole Belt of north-western Tanzania

C. KOEGELENBERG[1], A.F.M. KISTERS[1], C. HARRIS[2]

[1]*Department of Earth Sciences, University of Stellenbosch, Matieland 7602, South Africa (ckoegelenberg@sun.ac.za; akisters@sun.ac.za)*

[2]*Department of Geological Sciences, University of Cape Town, Private Bag X3, Rondebosch 7701, South Africa (chris.harris@uct.ac.za)*

ABSTRACT

Gold mineralization in the Biharumulo region of western Tanzania is confined to the sheared, low-angle basement-cover contact between Archaean basement gneisses of the Tanzania Craton and the structurally overlying, low-grade metamorphic metasediments of the Mesoproterozoic Karagwe-Ankole Belt. Regional-scale fluid flow along this detachment is indicated by the pervasive silicification and retrogression of wall rocks to pervasively foliated phyllonites and pyritization of particularly metasediments, commonly graphite-rich, in the hangingwall of the shear zone. Gold mining centers on specific structural sites along the detachment, but also in stratigraphically higher sections in the structurally overlying metasediments. Zones of gold mineralization along the detachment correlate with NE trending ramp structures (dip angles 20º – 35º) that are most ideally orientated for slip and reactivation within the low-angle phyllonitic detachment. Repeatedly overprinted auriferous quartz-vein stockworks in quartzofeldspathic gneisses immediately below the detachment indicate brittle fracturing of the competent footwall lithotypes during slip along the weaker detachment. In cases of massive silicification, up to 50 m thick quartz blows are formed along the contacts between detachment phyllonites and footwall gneisses. The multiple overprinting relationships of successive quartz-vein generations in these zones of massive silicification suggests that the quartz blows acted as competent blocks in the weak detachment, causing the repeated overprint of earlier silicification by later fracturing and quartz-veining events. Gold mineralization above the detachment and in stratigraphically higher metasediments is closely associated with fold structures that form part of the low-grade metamorphic fold-and-thrust belt. Veining is particularly abundant in competent lithotypes, such as quartzite and chemically reactive ferruginous mafic sills. Overprinting relationships between quartz vein sets illustrate fluid flow during fold amplification and, importantly,

the final lock-up stage of folds, during which much of the mineralization was introduced. Oxygen isotope values for quartz veins indicate fluids were likely derived from clastic, mainly metapelitic sedimentary sequences of the Karagwe-Ankole Fold Belt. The data also implies that the partially reworked Archaean granitoid-greenstone basement of the Tanzania Craton has not contributed to the fluid evolution and possibly gold mineralization. The extent (>100 km) of the basement-cover detachment and associated alteration is indicative for a regional-scale fluid system. Gold mineralization is, however, controlled by local structures and lithological contrasts that require the detailed mapping and sampling of the regional structure.

1. Introduction

Tanzania is Africa's 4th largest gold producer with an annual production of ca. 40 tonnes Au (Tanzania Chamber of Minerals and Energy, 2015). Some 90% of the gold production comes from late-Archaean greenstone belts of the Tanzania Craton (TC), mainly from the Lake Victoria region and the Lake Nyanza- and East Lake Victoria Superterranes (Borg and Shackleton, 1997; Borg and Krogh, 1999; Kabete et al., 2012). There have been very few recent gold discoveries on the TC and the apparent maturation of gold exploration on the craton has shifted exploration efforts towards the less explored margins of the TC (Kabete et al., 2012) (Figure 1). For the most part, the TC is bordered by younger orogenic belts including the Pan-African Mozambique Belt in the east (Fritz et al., 2013) and the Paleoproterozoic Usagaran-, Ubendian-, Rusizian- and Ruwenzori Belts from the southern to north-western margins of the TC (e.g., De Waele et al., 2008, and references therein) (Figure 1). These are mostly deeply eroded amphibolite- and granulite-facies terrains with somewhat limited potential for hydrothermal gold mineralization compared to the greenschist-facies deposits of the TC. In contrast, low-grade metamorphic, late Paleo- to Mesoproterozoic fold-and-thrust Belts and foreland basins unconformably or structurally overlie much of the western parts of the TC. These belts belong to the broader Mesoproterozoic Kibara system (sensu lato) (Cahen et al., 1987; Tack et al., 2010; Fernandez-Alonso et al., 2012).

The Karagwe-Ankole Belt (KAB) (sensu stricto) represents the northernmost segment of the Kibara system (Tack et al., 1994) (Figure 1). The eastern margin of the KAB overlies basement gneisses of the TC along a broadly flatlying, mylonitic detachment. This detachment is well exposed in and around the regional-scale structural window of the Mugera-Nyakahura (MN) inlier where Archaean basement outcrops over a strike length of > 100 km below the low-grade rocks of the eastern KAB (Figure 2; Kabete et al., 2012; Koegelenberg and Kisters, 2014). Pervasive silicification and alteration of both basement gneisses and commonly graphitic metasedimentary rocks of the KAB around much

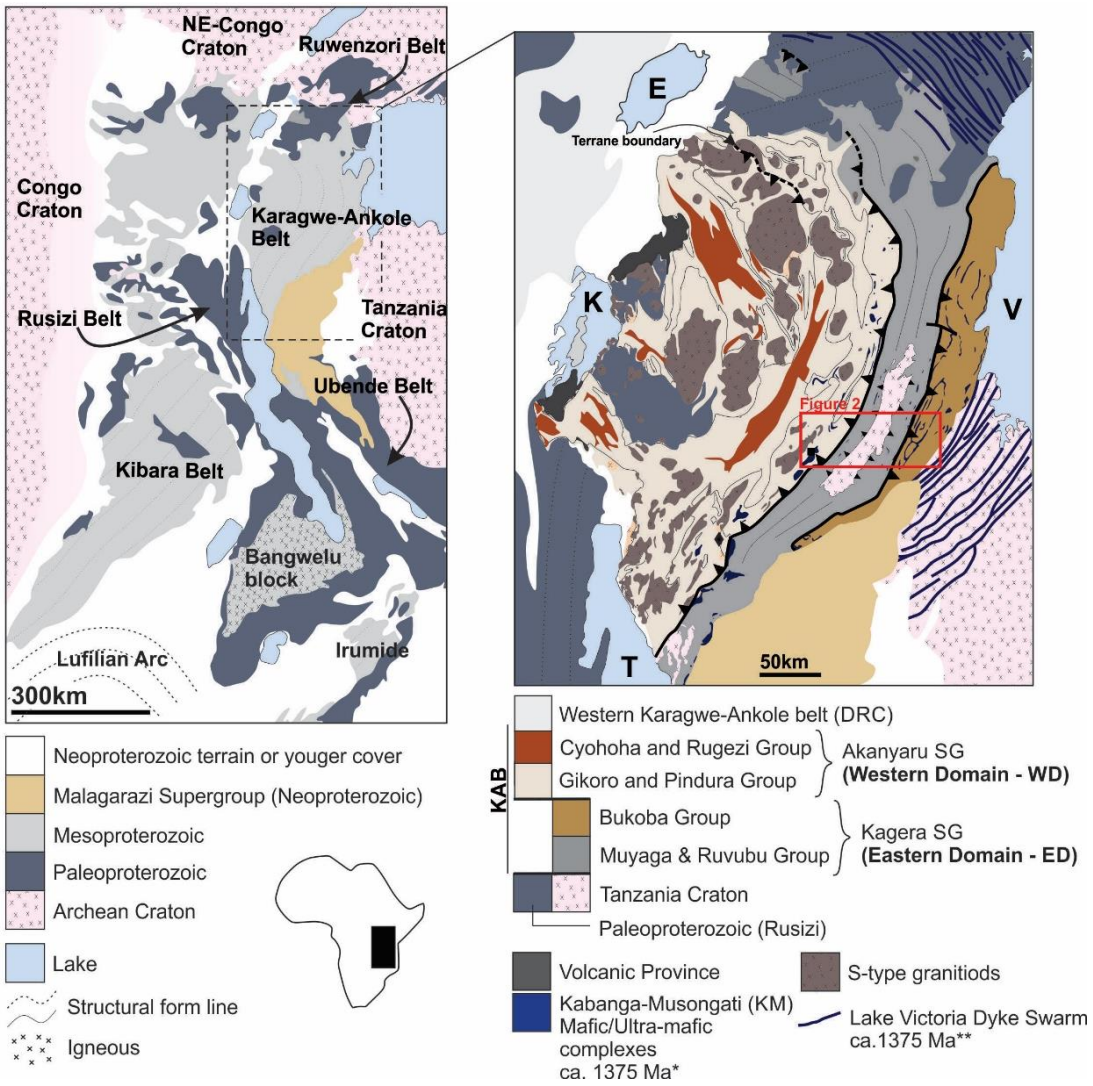

Figure 1: Regional geological framework of central-east Africa and the Karagwe-Ankole Belt (KAB). Geological maps modified after *Tack et al. (2010), Fernandez-Alonso et al. (2012) and **Mäkitie et al. (2014). Lakes: Kivu (K); Tanganyika (T); Edward (E); Victoria (V).

of the MN inlier testify to regional-scale fluid flow (e.g. Koegelenberg and Kisters, 2014). Artisanal gold mining operations target both the highly silicified detachment zone and the overlying rocks of the KAB and can be traced for several tens of kilometres along strike of the basement cover contact. However, mining is highly focused on smaller sections of the basement-cover contact suggesting distinct controls and focussing of the regional-scale fluid flow and associated gold mineralization around the MN inlier.

The aim of this paper is to characterize the structural controls of fluid flow along the basement cover contact around the MN inlier in the Biharamulo region in NW Tanzania as a potentially regionally significant gold mining district. Detailed case histories around existing mining camps are used to highlight the structural controls of fluid flow and mineralization in

specific sites of known gold mineralization. Whole-rock and mineral oxygen isotope data are used to constrain possible fluid sources for the mineralization.

2. Regional Geology of the Karagwe-Ankole Belt's eastern domain

The Archaean granitoid-greenstone basement of the western TC is structurally and/or unconformably overlain by the eastern extremities of the Mesoproterozoic Karagwe-Ankole fold-and-thrust belt. In the Biharamulo region, basement rocks are exposed in the regional- scale (ca. 100 x 20 km) Mugera-Nyakahura inlier (Figure 2). Rocks of the easternmost Karagwe-Ankole Fold Belt comprise a low-grade metamorphic, multiply deformed, up to 2.5 km thick Paleo- to Mesoproterozoic sequence of pelites, psammites and minor volcanic rocks assigned to the Kagera Supergroup (Tack et al., 2010; Fernandez-Alonso et al., 2012; Koegelenberg et al., 2015). The meta-sediments have been intruded by ca. 1375 - 1380 Ma mafic sills and dykes of the Lake Victoria Dyke Swarm (Deblond et al., 2001; Tack et al., 2010; Mäkitie et al., 2014). In the eastern KAB, the mafic rocks have been deformed and metamorphosed during the subsequent main phase of tectonism (D2) at ca. 1350 Ma (Evans, 2000; Koegelenberg et al., 2015). Coeval granite plutonism between 1350-1380 Ma is only recorded from the high-grade metamorphic (amphibolite-facies) Akanyaru Supergroup of the Western Domains of the KAB, but is absent for the low-grade Kagera Supergroup in the east.

The decrease in metamorphic grade coincides with the decrease in deformation and fabric intensity of D2 structures from west to east and from the Akanyaru- into the Kagera Supergroup corresponding to the frontal termination of the KAB to the east and over the TC (Tack et al., 1994; Koegelenberg and Kisters, 2014). D2 structures and fabrics in the KAB record top-to-the-east thrusting and associated folding and fabric development related to the east-vergent propagation of the KAB over the western margin of the TC. The eastern termination of the KAB is developed as a km-scale triangle zone in which the Archaean MN basement inlier forms a tectonic wedge bounded by foreland-(SE-) verging thrusts in the floor and hinterland-(NW-) verging backthrusts at the top and in the roof (Koegelenberg and Kisters, 2014). The timing of the D2 tectonic event is controversial (e.g. Fernandez-Alonso et al., 2012), but Ar-Ar age data from the main detachment zone suggest the main phase of fold-and-thrust belt formation at ca. 1326 Ma (Koegelenberg et al., 2015). Younger thermal events and associated granite plutonism at ca. 1000 Ma seem restricted to the Western Domain (Tack et al., 2010) but are not recorded in the ED of the KAB (Koegelenberg et al., 2015).

Figure 2

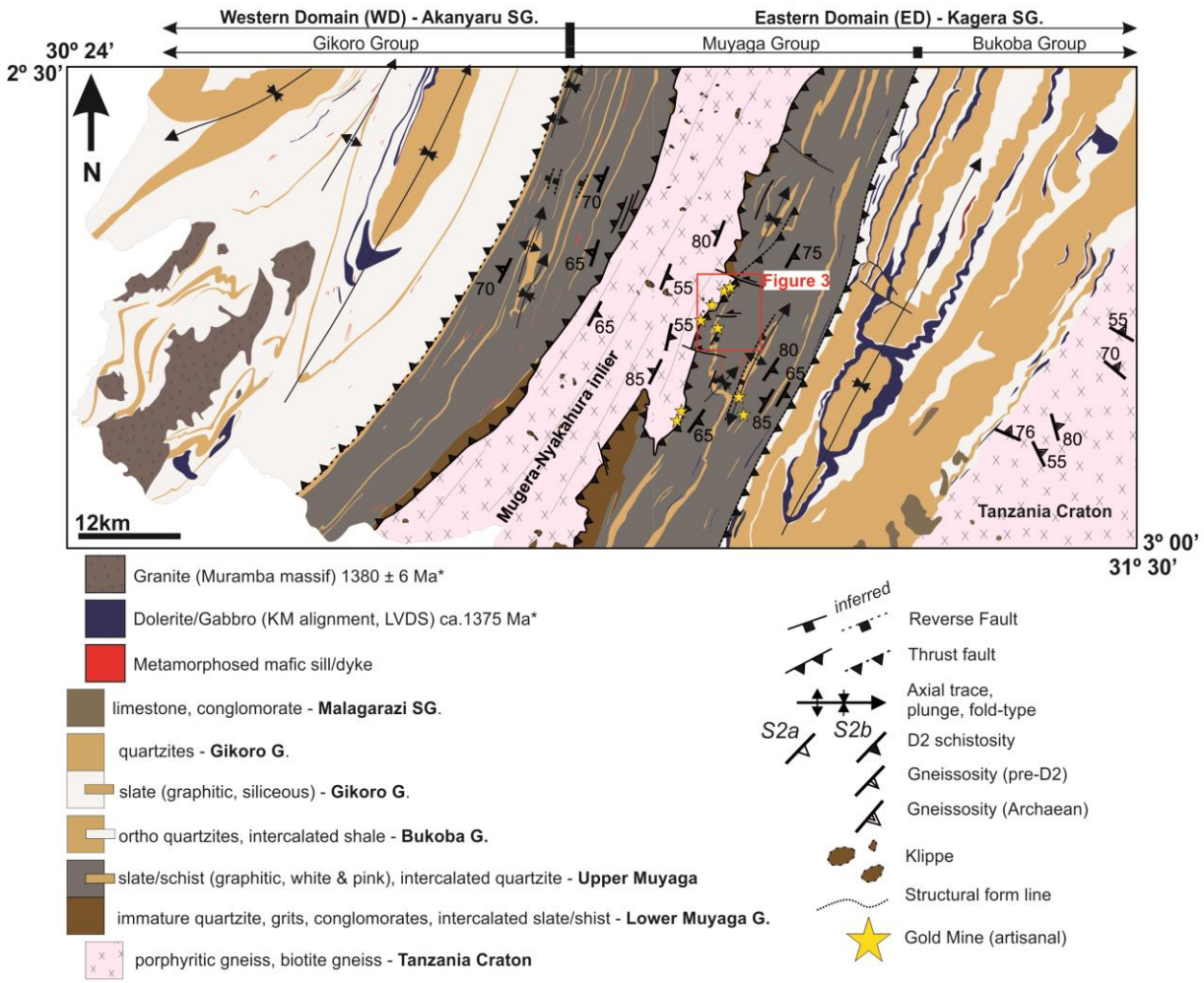

Figure 2: Geology of the Western- and Eastern Domain (WD and ED) of the Karagwe-Ankole belt, NW Tanzania, with locations of artisanal gold mines. Modified after Koegelenberg and Kisters (2014). Ages after *Tack et al. (2010) and geological groupings of the WD after Fernandez-Alonso et al. (2012).

3. Geology of the Biharamulo District, NW Tanzania

3.1. Tectonostratigraphy

3.1.1. Mugera-Nyakahura inlier

The geology of the western Biharamulo District can be sub-divided into three main, structurally overlying tectonostratigraphic units, namely (1) Archaean basement gneisses of the MN inlier, interpreted to form part of the western TC, overlain by (2) tightly folded and thrusted, low-grade metamorphic rocks of the Muyaga Group that are, in the east, underthrusted below (3) only very gently folded, mainly coarse-clastic succession of the Bukoba Group. The latter two constitute the Paleoproterozoic Kagera Supergroup of the eastern KAB (Figure 2) (Fernandez-Alonso et al., 2012; Koegelenberg and Kisters, 2014; Koegelenberg et al., 2015). Gold mineralization is confined to the basement-cover contact and the lower parts of the Muyaga Group.

Figure 3

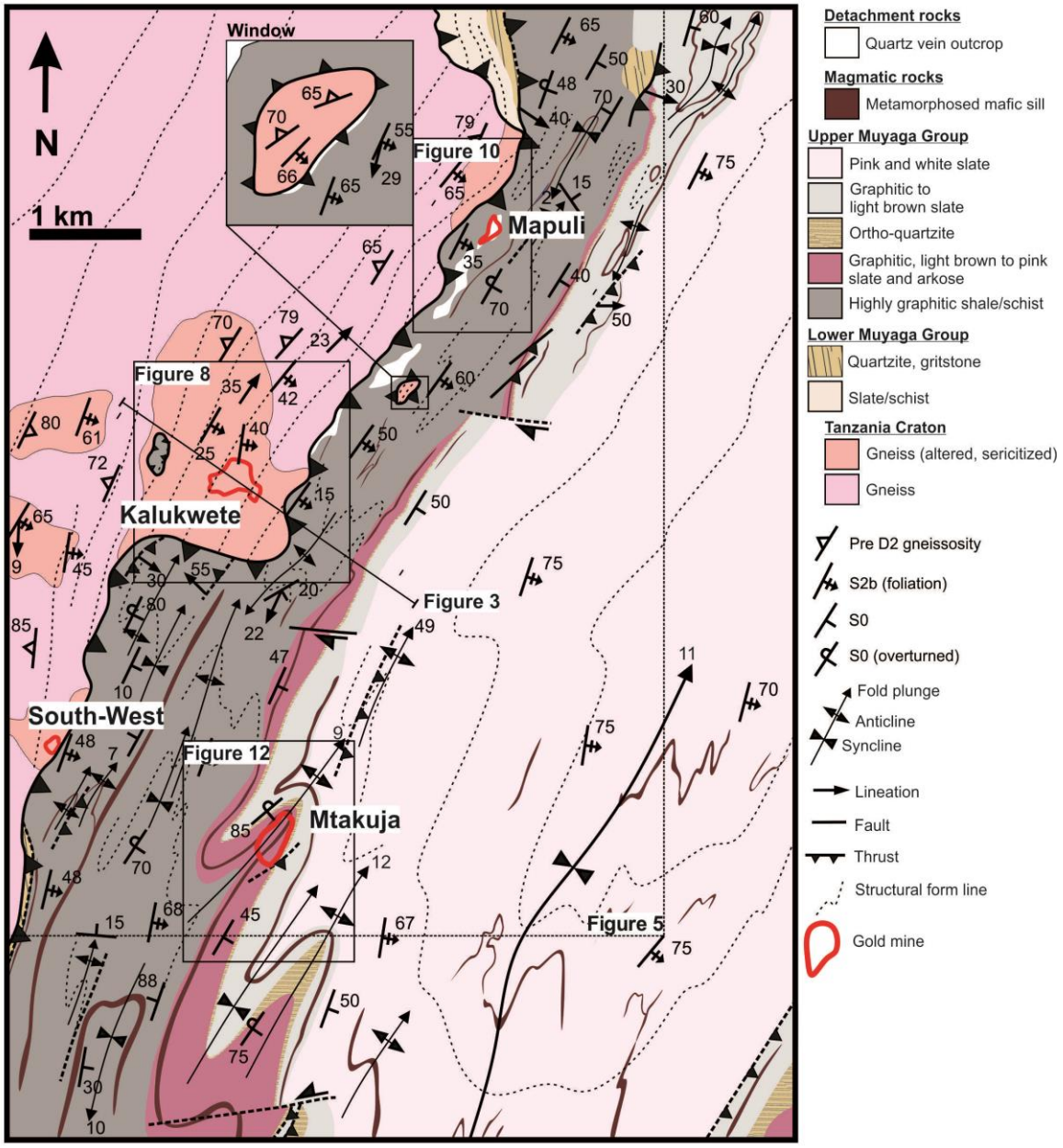

Figure 3: Geology of the eastern margin of the Mugera-Nyakahura inlier and basement-cover detachment with Mapuli-, Kalukwete- and Mtakuja artisanal mines. Note South-West artisanal mine is not discussed due to the limited extent of the workings.

Archaean gneisses of the MN inlier were previously interpreted as an erosional window through the structurally overlying KAB (e.g Figure 3 and 5). More recently, Koegelenberg and Kisters (2014) recognized the regional change of fold-and-thrust vergence centred around the MN inlier and interpreted the basement gneisses as the roof of an eastward transported and ramped-up basement wedge (Figure 2). Rocks of the MN inlier are commonly deeply weathered. River sections and isolated pavements expose fine crystalline, leucocratic biotite gneisses and coarser, commonly cataclastic augen gneisses of trondhjemitic to

granodioritic composition (Figure 3) (Kabete et al., 2012). Primary mineral assemblages are quartz, plagioclase, biotite, hornblende and, in case of more granodioritic compositions, K-feldspar. Highly weathered amphibole and/or chlorite schists and amphibolites in the northern parts of the MN inlier have tentatively been correlated with greenstone lithotypes, similar to those of the Lake Nyanza Super Terrane of the TC to the immediate east of the KAB (Kabete et al., 2012).

3.1.2. Muyaga Group

The ca. 1780 Ma old Muyaga Group forms the lowermost sequence of the Kagera Supergroup (Fernandez-Alonso et al., 2012) and can be subdivided into a lithologically distinct Lower- and Upper Muyaga Group (Figure 3 and 4) (Koegelenberg and Kisters, 2014). The Lower Muyaga Group (also the Kiganga Formation, after Westerhof et al.,2014, in Uganda) is a mainly coarse-clastic sequence made up of conglomerates, grits and impure quartzites interlayered with grey slate units. Cross-ripple lamina and asymmetrical ripples are common in quartzites and indicative of a fluvial to shallow marine setting. Intense folding and imbrication complicates thickness estimates for the Muyaga Group, but a minimum thickness of ca. 100 m seems likely. Unconformable contacts between the mainly coarse-clastic cover rocks and basement gneisses are reported from the southern parts of the MN inlier (Fernandez-Alonso et al., 2012), but much of the Lower Muyaga Group is absent further north, probably due to tectonic excision (Koegelenberg and Kisters, 2014).

The Lower Muyaga Group fines upwards into the ca. 2 km thick slate dominated Upper Muyaga Group (correlating with the Rakai Formation of Westerhof at al., 2014, in Uganda). The base of the Upper Muyaga Group is defined by a distinct, up to 300m thick sequence of dark and highly graphitic slate units. Higher up in the succession, the slates are intercalated with isolated, but up to 15m thick arkoses and/or mature quartzites that form distinct marker horizons (Koegelenberg and Kisters, 2014). The upper parts of the Upper Muyaga Group are dominated by a ca. 1.5 km thick, finely laminated and well bedded succession of pink to white-grey slate with subordinate arkose and ortho-quartzite units.

Towards the east, the Muyaga Group forms an underthrusted wedge structurally overlain by the ca. 2 km thick mainly coarse-clastic, thickly bedded and only gently folded Bukoba Group (Koegelenberg and Kisters, 2014).

3.2. Structure

Archaean basement gneisses and the overlying Muyaga Group are separated by a 20-50 m wide, gently undulating (see below) D2 detachment zone. Reworked Archaean basement gneisses below the detachment record at least 2 distinct periods of seemingly co-axial deformation (e.g. Pre-D2 vs. D2). The oldest episode is indicated by a steep west dipping to upright (pre-D2)

gneissosity trending broadly NNE to NE across the MN inlier. Associated shearing is accommodated by mylonite bands and cataclasites in the coarse augen gneisses, showing top-to-the-SE kinematics. Notably these NE gneissic trends are at high angles to structural grain of the TC and may be the result of the thick-skinned thrusting and subsequent reworking of the north-western margin of the TC during the 2.2 – 1.8 Ga Eburnean Orogeny (Koegelenberg et al., 2015).

The overlying Muyaga Group is part of the regional scale, D2a, SE –verging, fold-and-thrust belt of the KAB. However, folding along the eastern MN inlier margin forms part of a, D2b, regional and top-to-the-NW verging back-thrusted domain (Koegelenberg et al., 2014). Associated F2b folds are tight and near recumbent along the base, but stratigraphically higher and to the east, folding progressively becomes more open with a steepening of the axial planar S2b foliation. Notably, tight, overturned and strongly north-west verging F2b folds are still recorded laterally within ca. 3 km east of the roof detachment and into the Upper Muyaga Group. Pervasive NW verging axial planar foliations (S2b), sub-horizontal and N to NNE trending intersection lineations (L2bi) are well developed and correspond with top-to-the-NW tectonic transport and D2 backthrusting of the cover rocks on top of the basement gneisses (Koegelenberg and Kisters, 2014) (see below).

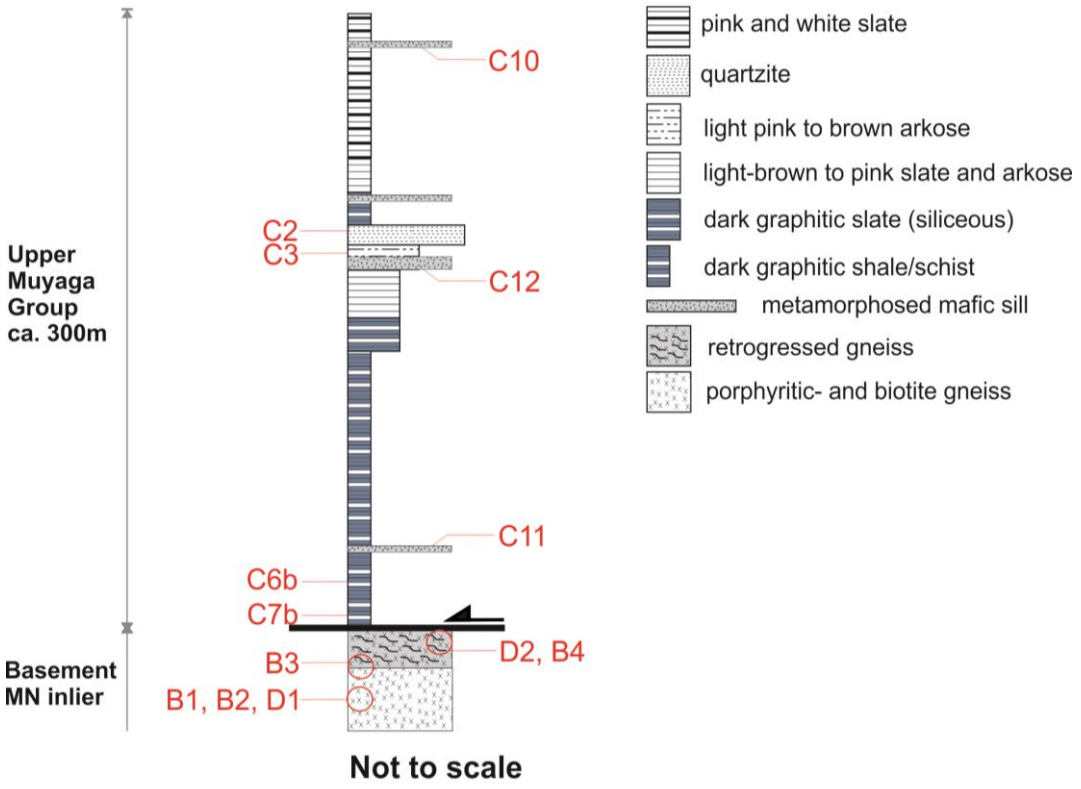

Figure 4: Litho-stratigraphical log of the foot- and hanging wall of the detachment with sample locations of quartz veins and wall rock for oxygen isotope analysis (section location on figure 3).

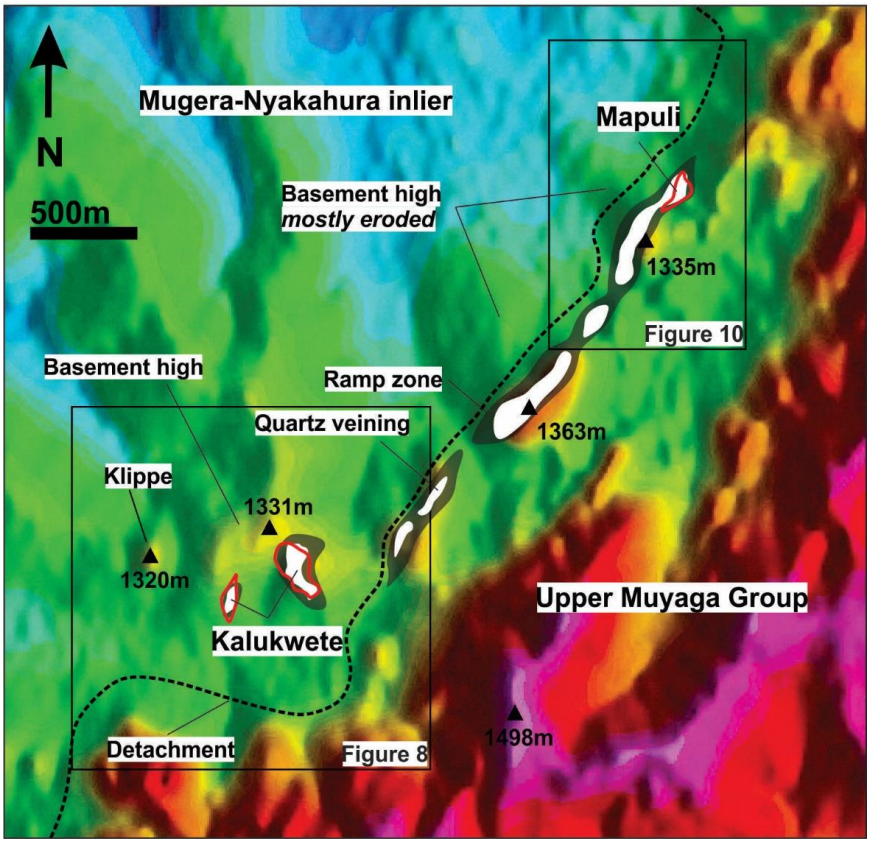

Figure 5: Regional digital terrain model (DTM) of the detachment and artisanal mines with inferred basement ramp zones and significant quartz veining.

The detachment that marks the basement-cover contact is defined by an up to 50 m thick unit of imbricated muscovite-chlorite schists, phyllonites and mylonites (Koegelenberg and Kisters, 2014) (Figure 3). Deformation and associated fluid flow has also caused near-pervasive retrogression of quartzo-feldspathic footwall gneisses to muscovite- (sericite) and/or muscovite-chlorite schists to a depth up to 30 m below the actual detachment. The detachment is characterized by a pervasive shallow SE dipping schistosity (S2b) and a shallow, mainly SE plunging stretching lineation (L2b) developed on the foliation plane. Shear sense indicators include mainly S-C' fabrics and rotated quartz clasts in mylonites and/or phyllonites and record top-to-the-NW kinematics corresponding to north-westwards back thrusting of the Muyaga Group on top of the basement wedge. Archaean basement gneisses and the overlying Muyaga Group are separated by a 20-50 m wide, gently undulating (see below) D2 detachment zone. Reworked Archaean basement gneisses below the detachment record at least 2 distinct periods of seemingly co-axial deformation (e.g. Pre-D2 vs. D2). The oldest episode is indicated by a steep west dipping to upright (pre-D2) gneissosity trending broadly NNE to NE across the MN inlier. Associated shearing is accommodated by mylonite bands and cataclasites in the coarse

augen gneisses, showing top-to-the-SE kinematics. Notably these NE gneissic trends are at high angles to structural grain of the TC and may be the result of the thick-skinned thrusting and subsequent reworking of the north-western margin of the TC during the 2.2 – 1.8 Ga Eburnean orogeny (Koegelenberg et al., 2015).

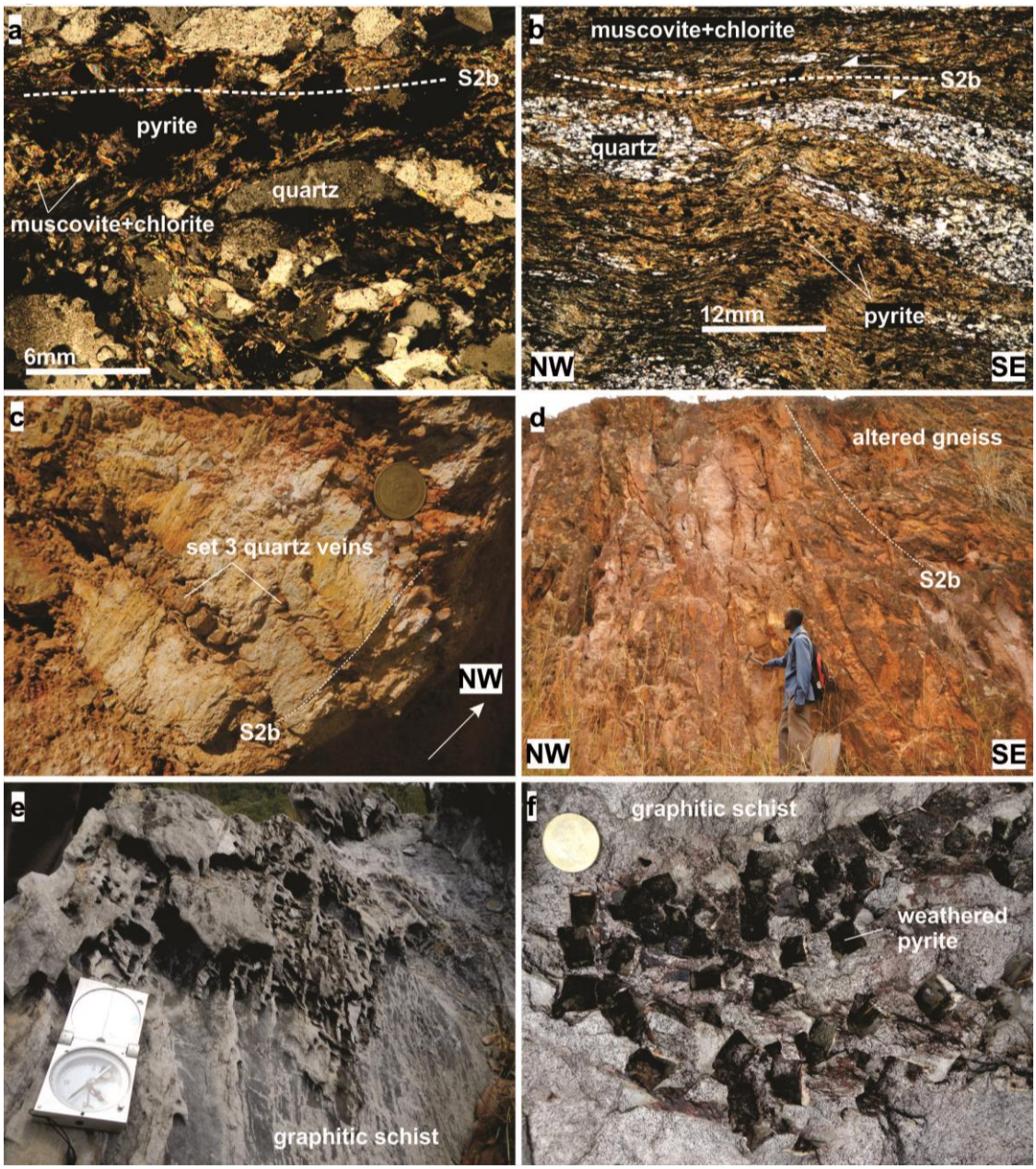

Figure 6: a) Mica bearing shear band in gneiss with abundant pyrite. **b)** Intensely foliated and fully developed phyllonite with re-crystallized quartz lenses and pyrite showing weak top-to-the-NW S-C fabrics. **c)** Sericitized feldspathic gneiss with pervasive set 3 shear quartz veins. **d)** Highly altered gneiss exposed in quarry showing pervasive limonite and hematite staining **e)** Graphitic schist with pervasive hydraulic fracture network and associated abitization and sericitization. **f)** Late-tectonic large, almost euhedral, pyrite pseudomorphs in graphitic schist.

3.3. Metamorphism

Phyllonites and mylonites in the detachment are characterized by quartz-sericite-chlorite-albite assemblages (Figure 6a, b), mainly derived from the retrogression of original plagioclase-K-feldspar-biotite and/or hornblende-bearing assemblages of the underlying gneisses (Koegelenberg et al., 2015). The absence of biotite in phyllonites derived from gneisses suggests T conditions of ca. < 400°C during deformation and retrogression (Powell and Evans, 1983; Coggon and Holland, 2002). This corresponds to deformation textures in the basal detachment. Quartz is dynamically recrystallized and forms, in places, quartz ribbons that define the high-strain foliation (S2b). Quartzofeldspathic gneisses in the immediate footwall of the detachment, in turn, show pervasive cataclastic textures. Metapelites of the Muyaga Group are phyllitic, in places, showing similar quartz-sericite-chlorite-albite assemblages. Original igneous assemblages in metamafic sills and dykes in the Muyaga Group are replaced by tremolite-actinolite-chlorite-epidote-carbonate assemblages and plagioclase is pervasively saussuritised. These assemblages are not very well suited to tightly constrain P-T conditions, but both mineral parageneses and deformation textures point to lower-greenschist-facies metamorphic conditions during the overall D2 fold-and-thrust event.

4. Artisanal mining

4.1. Description of mines

Artisinal mining operations target auriferous quartz veins at two structural levels in (1) the sheared basement-cover contact; and (2) stratigraphically higher sections in rocks of the overlying Muyaga Group (Figure 3).

The Kalukwete and Mapuli prospects illustrate different styles and controls of Au mineralization in the detachment along the basement-cover contact (Figure 3). Kalukwete is the largest mining camp in the region located in basement gneisses in the immediate footwall of the main detachment. The gneisses are exposed in an erosional window through dark graphitic schists at the base of the Upper Muyaga Group. The Mapuli mine is located some 3 km north of Kalukwete, but is hosted in graphitic schists that form the base of the Upper Muyaga Group in the immediate hangingwall of the detachment. Mining operations of the Mtakuja prospect are located stratigraphically higher and away from the detachment in rocks of the Upper Muyaga Group, some 2 km east of the basement-cover contact (Figure 5). Here, auriferous quartz-vein sets are spatially closely associated with tightly folded (F2b) horizons of siliceous slate, quartzite and mafic sills.

4.2. Gold mineralization along the basement-cover detachment

4.2.1. Fluid Alteration

Regional-scale, syn-tectonic (D2) fluid flow and alteration described by Koegelenberg and Kisters

(2014) and Koegelenberg et al. (2015) in rocks below and above the basement-cover contact (e.g. Figure 7a and b) are indicated by a number of features. Pervasive quartz veining attests to fluid flow both in footwall gneisses and the detachment zones (Figure 7c). Based on cross-cutting relationships and relative deformation, several generations of quartz veins can be distinguished (see section 4.2.2 and 4.2.3). In places, quartz veins form up to 50 m thick and 550 m long lens-like quartz blows along the basement-cover detachment. The brecciation of quartz-blows and multiple quartz-vein generations indicate the multiphase reactivation of fluid conduits and protracted duration of the fluid flow. Muscovite-chlorite phyllonites (Figure 6b) in the detachment are derived from the hydration of mainly quartzofelspathic basement gneisses associated (Figure 6a) with this fluid flow and quartz veining. The hydration is associated with the syn-D2 pyritization of the rocks, although primary sulphides are only very locally preserved and, for the most part,

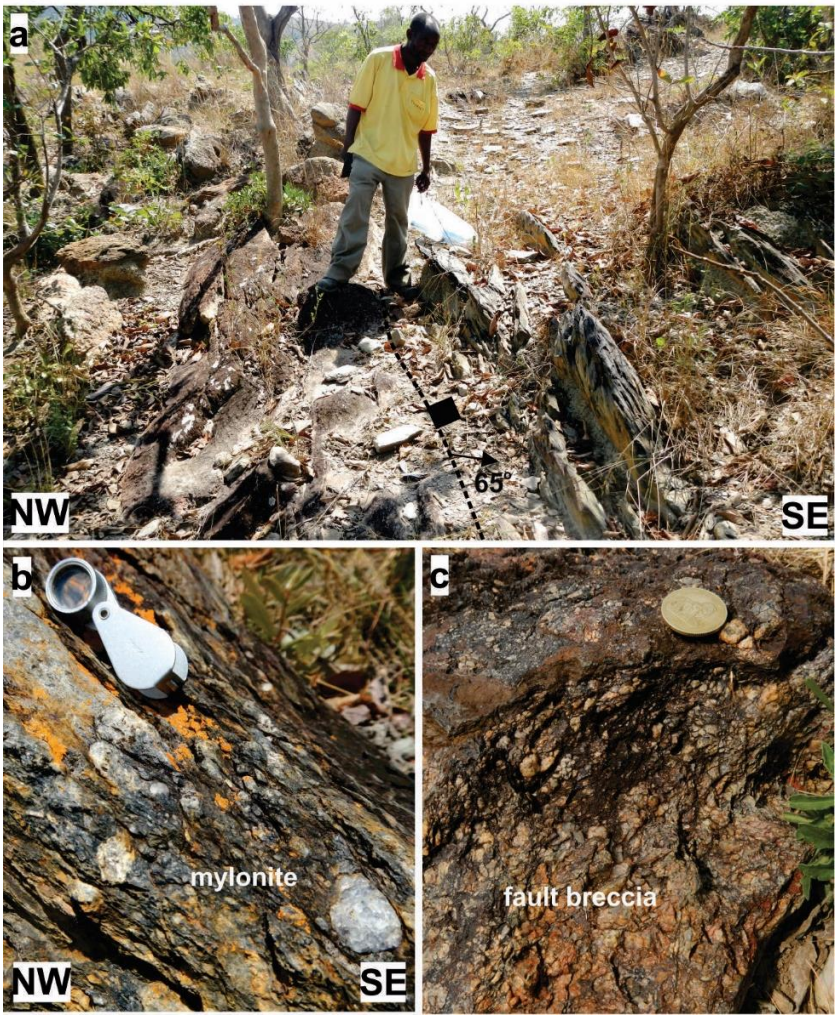

Figure 7: a) Steep SE dipping contact between altered gneiss and graphitic schist **b)** Thick mylonite along detachment in graphitic schist with competent clasts of quartz vein and quartzite **c)** Highly ferruginous and siliceous fault breccia at basement-cover contact consisting of mostly fractured quartz vein clasts.

pseudomorphed by iron hydroxides (Figure 6a, b, c, d, f).

In the hanging wall intensely deformed graphitic schists of the Upper Muyaga Group are likewise characterized by pervasive sericitization, abitization, secondary Fe oxides and pyrite (pseudomorphed by limonite and hematite) along foliation- and bedding planes and quartz veins (Figure 6e, 6f). Schists with a high graphite content in close proximity to the detachment are particularly laced with pyrite and contain single pyrite minerals of up to 6 cm in diameter (Figure 6f). Euhedral pyrite is syn-tectonic and has grown during the formation of the S2 foliation in the detachment, as the high strain S2 fabric in metapelites can be seen to be both deflected and overgrown by pyrite. Quartz strain shadows around pyrite grains are also common.

4.2.2. Kalukwete

4.2.2.1. Site description

Artisanal mining at Kalukwete has been active for several years. Mining is concentrated in a NNE-trending 4 km long and up to 800 m wide

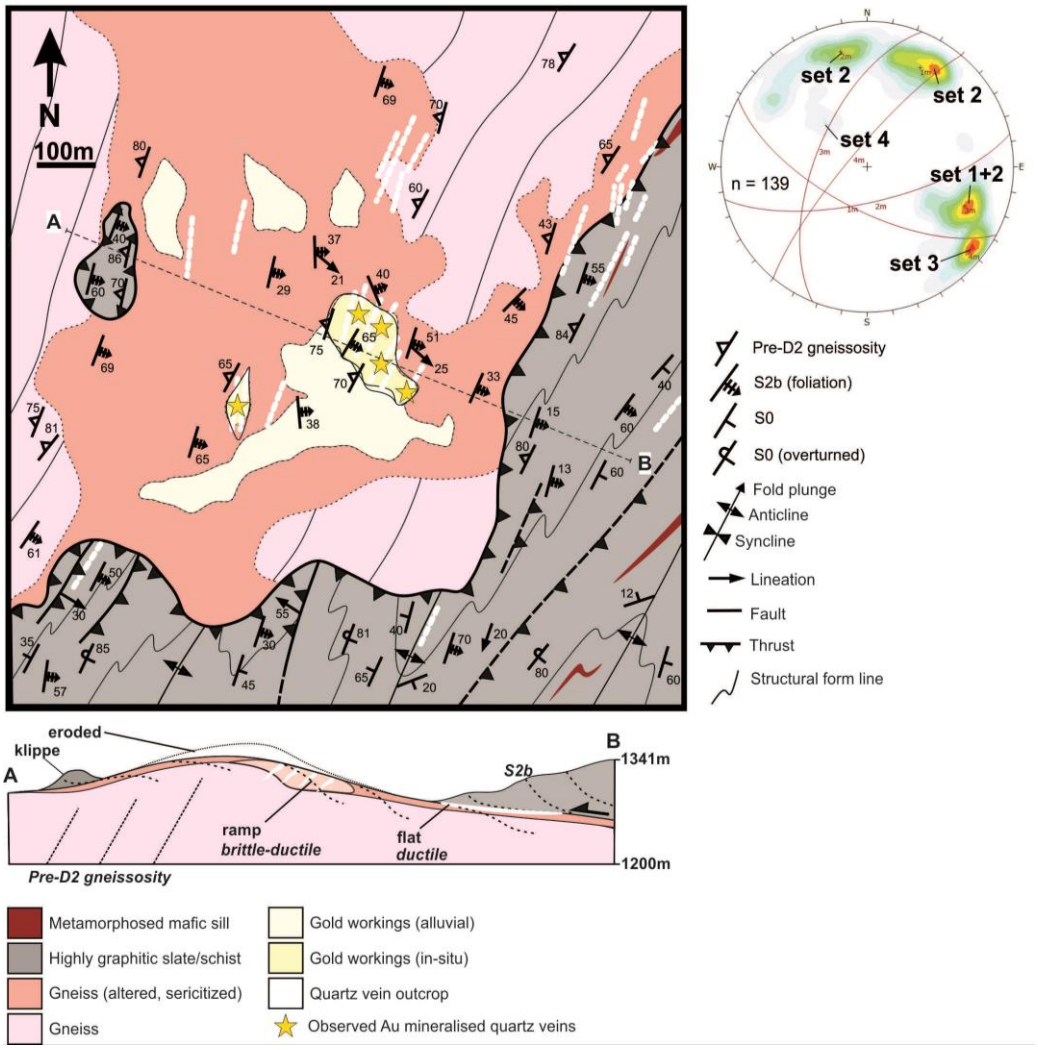

Figure 8: Geological map of Kalukwete and surrounding country rock including a cross section (A-B). Dominant quartz vein geometries are shown as contours of poles-to-plane points on a lower hemisphere, equal area, stereonet.

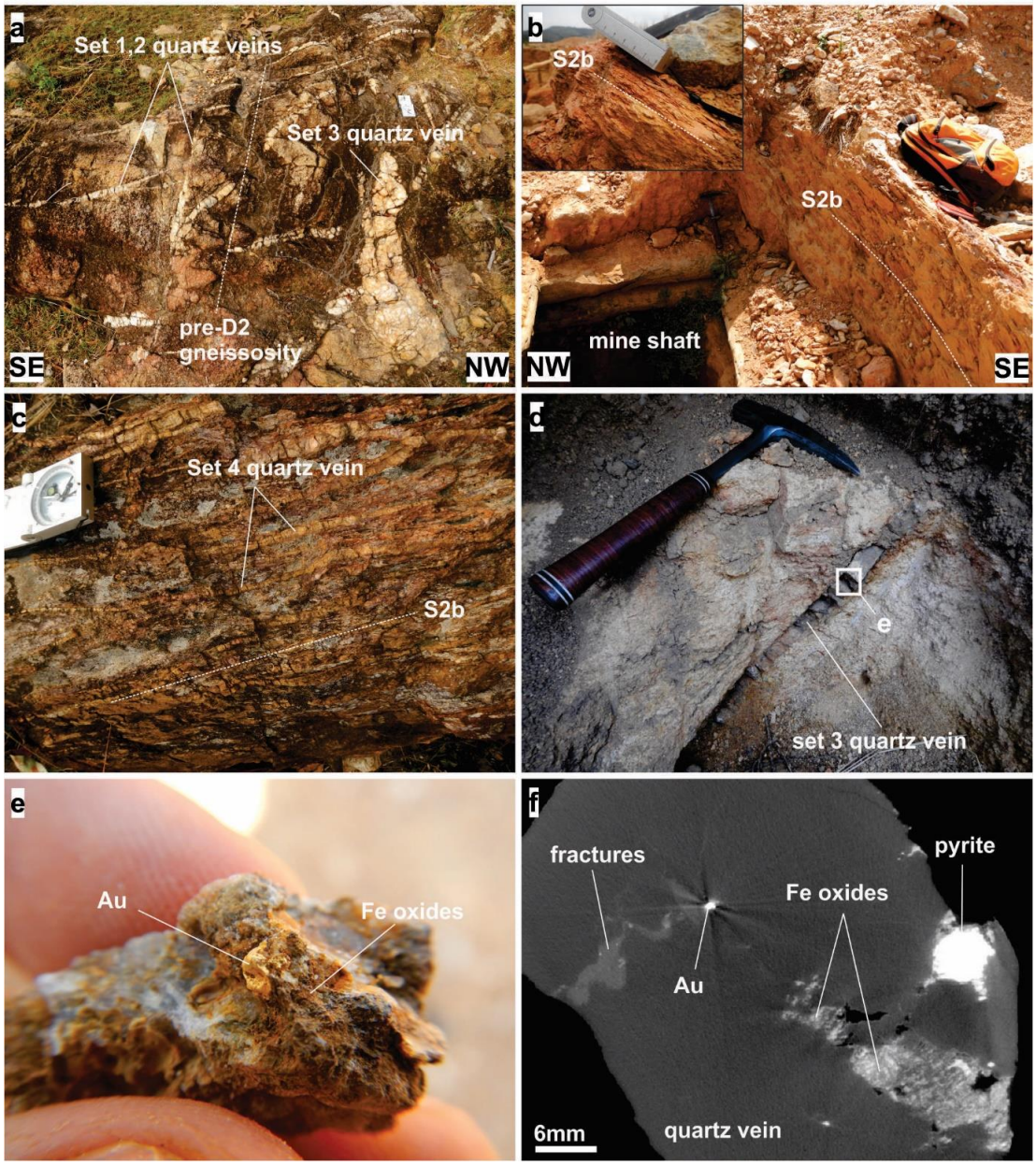

Figure 9: a) Gneiss pavement showing clear cross-cutting relationship between early pre-D2 (set 1, 2) and D2 (set 3) quartz veins. **b)** A shallow mine shaft within transposed and highly foliated (S2b) altered gneiss. **c)** Intensely strained phyllonites laced with mylonite bands and associated lenticular quartz veins along the detachment. **d)** Mining of fractured mineralized set 3 shear vein. **e)** A cluster of a set 3 shear vein with specs of disseminated gold, limonite and massive hematite in fractures. **f)** Nano CAT (computerized axial tomography) scan image of a set 3 shear vein cluster highlighting variable material densities. Note disseminated gold is indicated by very dense anomalies (bright white) that are associated with pyrite and other Fe-oxides (light to medium grey) following late set 5 fractures.

corridor parallel to the basement-cover interface. Gold mining is entirely in former basement gneisses that have been pervasively retrogressed to quartz-sericite-chlorite schists immediately below the main D2 detachment (Figure 8). Mining in the mineralized part of the corridor at Kalukwete targets in-situ auriferous quartz veins and vein stockworks as well as alluvial gravel

consisting of up to boulder sized vein quartz. In-situ workings are hosted by zones of near-pervasive sericitization of the wall rock gneisses (Figure 6a, 9b). The workings expose the gradual increase in sericitization, ferruginization, from the weathering of original sulphides, and fabric intensities from weakly altered footwall gneisses to pervasively retrogressed and pervasively foliated phyllonites that constitute the actual detachment. Original quartz vein geometries and overprinting relationships are best developed in the footwall and some 5-20 m below the detachment. Quartz veins become progressively transposed and, in the process, brecciated and overprinted in the high-strain basement-cover detachment.

4.2.2.2 Quartz Veining

Cross-cutting relationships of quartz veins in mine diggings and gneissic pavements (Figure 9a) have indicated up to five distinct generations of veining. The earliest veins seem to pre-date D2 strains and are possibly associated with earlier Archaean- and/or Paleoproterozoic events bordering the TC. However, given their geometry and structural position, most veins can be related to progressive D2 strains and top-to-the NW and W kinematics along the detachment at various stages.

Set 1 and -2, -(early pre-D2) veins: Set 1 veins are the earliest and are transposed, isoclinally folded and often rootless within the regional basement gneissosity. Set 2 veins are later, cross-cutting, orientated either parallel or at low angles to the pre-D2 gneissosity. Both sets of veins show mostly NNE trends and are associated with pre-D2 mylonite bands into which they are either transposed (set 1) or emplaced (set 2). The mainly massive, smoky- to milky white, quartz veins are lensoid and commonly brecciated. Vein thicknesses range from several millimetre thick veinlets to 80 cm thick veins, the latter of which can be traced for up to 80 m along strike. Notably, Set 1 and 2 veins are intersected in boreholes to depths of up to at least 150 m, underlining the probably pre-D2 origin and forming part of earlier events that have affected the basement gneisses.

Set 3 - D2 shear veins: Set 3 veins cross-cut both fabrics in basement gneisses and earlier quartz vein generations (Figure 6a, 9a, 9d) and are the dominant vein set in the workings. Offsets of fabrics and earlier vein sets across set 3 veins indicate the veins are shear veins. Set 3 veins show predominantly NE strikes with moderate to steep dips to the NW. Vein thicknesses vary between ca. 0.02 – 1.5 m and the thickest veins can be traced for several hundred meters along strike (Figure 8). At depth, the veins become thinner and pinch out altogether at ca. 30 – 40 m into the footwall, whereas thicknesses are at a maximum in sericitized gneisses below the detachment. Most veins are brecciated and consist of milky- to light smoky quartz. Numerous set 3 veins contain fragments of

earlier dark smoky quartz, similar to that from set 1 and 2 veins, and wall-rock gneisses.

Set 4 - D2 lenticular veins: Set 4 veins are orientated sub-parallel with S2b phyllonites of the detachment. The milky white veins are invariably deformed and lensoidal, between 2 cm – 30 cm thick, and brecciated and/or boudinaged. Most set 4 veins are strongly ferruginous, indicating the abundance of former sulphides (Figure 9c). Multiple and renewed veining is evident in many of the set 4 veins. The absolute timing of set 4 veins is not unambiguous and many of the veins may form part of set 3 veins that have been caught up and transposed into the high-strain fabrics of the D2 detachment.

Set 5 - Late D2 extension veins: Late D2 tension veins are developed as highly ferruginous 2 to 5 mm thin quartz veins and brecciated quartz veins that cut the phyllonites of the detachment at high angles (Figure 9f). These veins are mostly developed in thick veins of earlier quartz vein generations (set 1 and 2 veins) or stock works of earlier vein sets (set 3 and 4 veins). The occurrence of these latest stage veins seem largely restricted to shallow depths below the main D2 detachment not exceeding 25 m.

4.2.2.3 Mineralization

Gold mineralization to depths ca. 20 m below the basement-cover detachment is associated with predominantly set 3 veins. Closer to the detachment, late set 5 tension veins become increasingly abundant and are the main mineralized set. Mineralized quartz veins are almost invariably ferruginous containing abundant limonite and/or hematite, whereas original sulphides, mainly pyrite, are only rarely preserved in the deep weathering profile. Gold occurs as up to 5mm large specks of free gold particularly in brecciated set 3 veins (Figure 9d, e). Specks of free gold also occur in thin late-stage set 5 veins (Figure 9f). The majority of the auriferous set 5 veins seems confined to larger quartz blows of earlier set 3 veins and, to a lesser extent, in quartz blows of early set 1 and 2 veins. The NE trending mineralized corridor at Kalukwete corresponds to undulations of the D2 detachment centred around a prominent basement high (Figure 5). On average, the detachment shows shallow (ca. <10°) dips to the southeast and east below the structurally overlying Muyaga Group rocks along the eastern margin of the MN-inlier. However, the detachment surface is not smooth and segmented by distinct flat- and- ramp structures. The NE-trending undulations correspond to frontal ramps during top-to-the-NW kinematic transport along the detachment. Local contacts and S2b foliations indicate that flats are characterized by shallow NW or sub-horizontal dips, whereas ramps show SE dips at dip angles of between ca. 20° and 30° (Figure 8). This undulating geometry is underlined by a high-resolution digital terrain model (DTM) that outlines undulations of up to 30 m in the basement-cover contact around the Kalukwete mining camp (Figure 5, see also

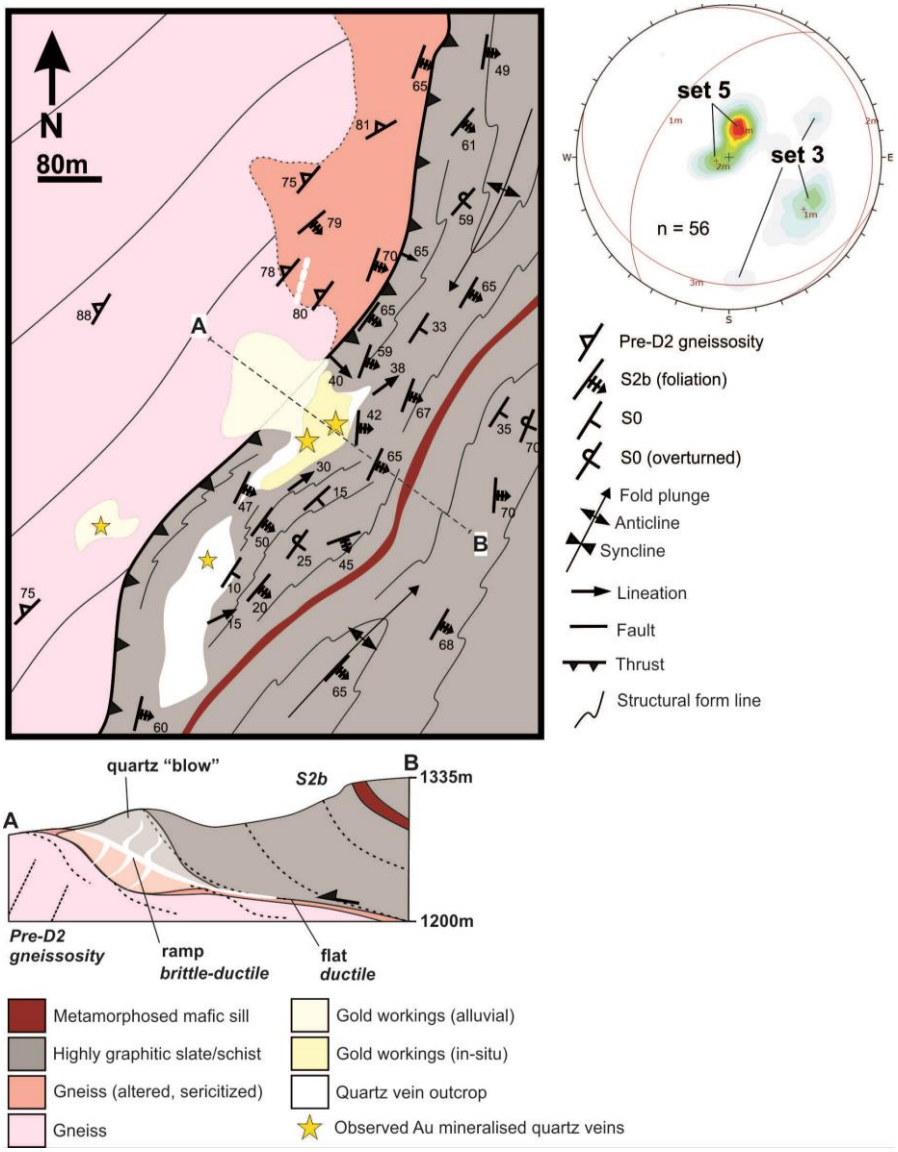

Figure 10: Geological map of Mapuli and surrounding country rock including a cross section (A-B). Dominant quartz vein geometries are shown as contours of poles-to-plane points on a lower hemisphere, equal area, stereonet.

outline on Figure 3). Considering alluvial overburden covering much of the contact and partial erosion of the basement, the extent of the ramps, as well as dips, are likely to be underestimates. Spatially mineralized set 3 and set 5 shear- and late extensional veins are preferentially developed on ramps that define the eastern slope of the basement high, whereas the western slope of the basement high is not mined (Figure 5).

4.2.3. Mapuli

4.2.3.1. Site Description

The Mapuli prospect is located directly above the basement-cover detachment in folded graphitic schist of the Upper Muyaga Group (Figure 10), some 3 km north of Kalukwete. Mining is confined to within a ca. 50m thick ridge of massive milky and partly brecciated quartz that can be followed for ca. 2 km along the basement-cover contact directly below the Muyaga Group

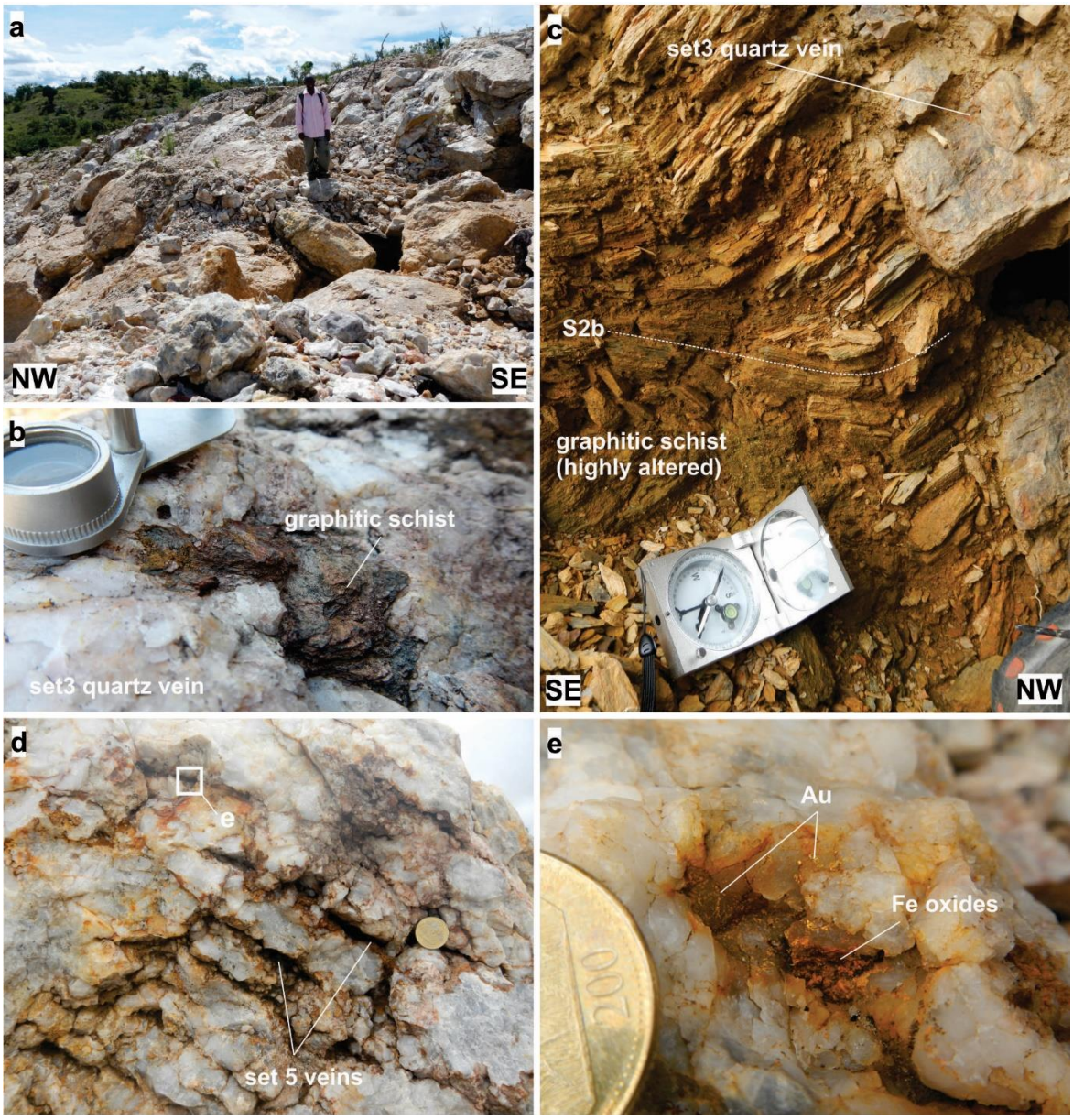

Figure 11: a) Extensive mine workings at Mapuli targeting massive quartz "blows". **b)** Clast of graphitic schist (Upper Muyaga Group) in set 3 shear quartz vein. **c)** Set 3 shear quartz vein cross-cutting intensely S2b foliated graphitic schists. Note slight rotation of S2b indicating slight reverse top-to-the-SE slip along fracture plane. **d)** Cluster of closely spaced set 5, sub-horizontal, extensional veins/fractures. **e)** Close view of an open set 5 extensional fracture showing limonite and disseminated specs of gold.

graphitic schists (previously slates) (Figure 11a). F2b folds in the schists show NNE trends and shallow plunges and a prominent NW vergence, corresponding to the overall top-to-the-NW kinematics recorded along the basement-cover detachment. Smaller-scale top-to-the-NW thrusts (D2b) in the sequence are defined by 1 – 50 cm thick phyllonite and/or mylonite bands localized in incompetent graphitic schists.

4.2.3.2. Quartz veining

In contrast to Kalukwete, Mapuli is characterized by a rather massive silicification and up to 50 m thick quartz-vein blows along the basement-

cover contact. The sheer volume of quartz makes a distinction of individual quartz vein generations difficult, but there is clear evidence for the multiple reactivation and brecciation of larger quartz blows by younger quartz-vein sets (e.g. Figure 11a). At Mapuli the transposition of quartz veins along the basement-cover interface is preserved in graphitic schists of the Upper Muyaga Group. Earlier set 1 and 2 vein sets are absent, but later vein sets, similar to those at Kalukwete are evidenced by cross-cutting relationships and their orientation.

Set 3 - D2 shear veins: Set 3 veins appear to be the most abundant at Mapuli and are predominantly massive, consisting of distinctive milky white quartz containing angular fragments of graphitic schist (Figure 11b), granite (gneiss) and dark smoky quartz (set 1, 2). In parts set 3 veins have been brecciated by later quartz veins. Individual shear veins are up to 2m thick and strike NE to NNE with steep dips (50º-75º) predominantly towards the NW. These vein sets are at moderate to high angles (ca. 60º) with the principal direction of shortening, as indicated by dominant S2b foliations (Figure 11c).

Set 5 – Late D2 extension veins: Set 5 tension veins are between 2mm and 15cm thick and are particularly prominent at the Mapuli mine. The late-stage veins are confined to earlier formed massive quartz veins created by the close spacing and clustering of multiple set 3 shear quartz veins (Figure 11d). Two nearly sub-horizontal geometries can be distinguished including moderately (5º-20º) SW and NE dipping veins. The sub-horizontal dip of set 5 veins indicates an origin as extensional veins that formed during regional sub-horizontal shortening (D2). Set 5 veins are mostly filled with yellow to dark red oxidized massive hematite, limonite and goethite, and vein quartz breccia.

4.2.3.3. Mineralization

Mining at Mapuli targets disseminated gold concentrated predominantly in late set 5 extensional veins characterized by abundant Fe oxides (Figure 11d, 11e). The auriferous veins are confined to the earlier formed massive and brecciated quartz blows along the basement-cover contact made up of numerous overprinting and amalgamated Set 3 veins. Extension veins are pervasive throughout quartz blows and form narrow clusters with a spacing of between 20cm to 2m. Mining follow the prominent clusters and/or thick single veins, but also alluvial gravel down slope.

The silicification and subsequent formation of late mineralized quartz blows at Mapuli is localized and can be traced southwards along the detachment for some ca. 2 – 3 km, indicated by prominent quartz ridges. Here the detachment corresponds with more steeply south-east dipping basement-cover contacts of up to 35º - 45º (Figure 10). These ramp structures spatially coincide with the voluminous, elongate quartz blows. In contrast, localized ramp contacts

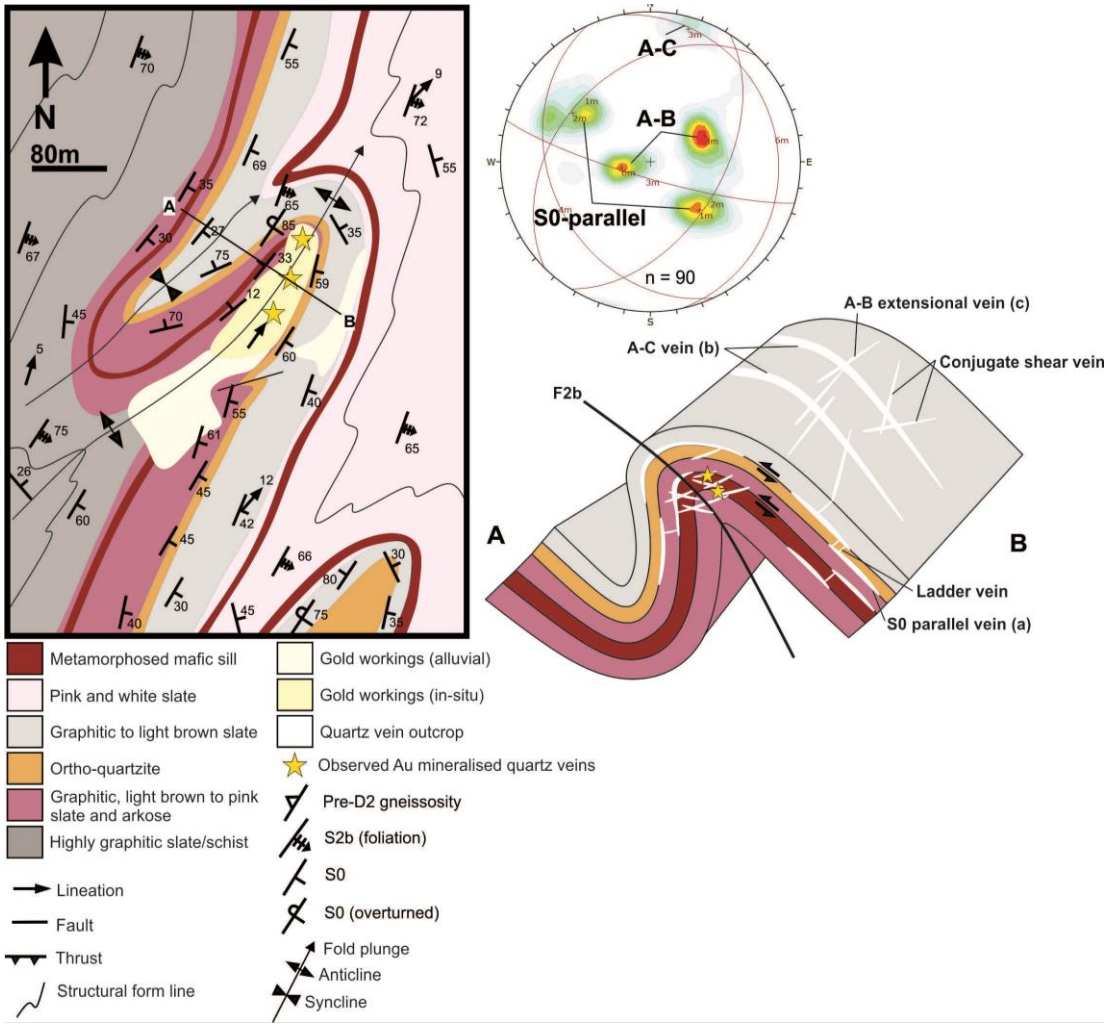

Figure 12: Geological map of Mtakuja and surrounding country rock including a scematic 3D cross section (A-B) with quartz vein geometries. Dominant quartz vein geometries are shown as contours of poles-to-plane points on a lower hemisphere, equal area, stereonet.

with dips steeper than 60° show (Figure 7a) significantly less silicification and are not mined.

5. Mine Operations in the Muyaga Group

5.1. Mtakuja

5.1.1. Site Description

Mtakuja is located stratigraphically higher up in rocks of the Muyaga Group some ca. 2 km east of the basement-cover detachment and at least ca. 300-400 m above the basal D2 detachment (Figure 3, 12, 13a). Mining operations can be followed along a prominent ridge structure for some 0.3 km and parallel to the NNE strike of the folded Muyaga Group. Mining mainly targets in-situ auriferous quartz veins, but also alluvial and a structurally higher ferricrete paleo-horizon forming the top of the ridge.

The area is underlain mainly by slates of the Muyaga Group and isolated interlayered quartzites and intrusive sills. The mining operations are located in the hinge of a shallow (5-10°) NNE-plunging, NW-verging, tight and overturned F2b anticline with a wavelength of ca. 0.4 km (Figure 12). The limbs of the F2b

anticline are delineated by an up to 3m thick marker horizon of quartzite, while the core of the fold consists of predominantly interlayered pink and white siliceous slate and arkose, and lesser graphitic slate. Importantly, an up to 5m thick mafic, but pervasively altered and strongly ferruginous, dolerite sill forms part of the folded sequence and has been duplicated in the hinge of the anticline. This folded sill is laterally extensive and can be traced along strike for several tens of kilometres to the north and south of Mtakuja.

5.1.2. Quartz veins

Silicification and quartz veining at Mtakuja are almost solely concentrated in and around the tightly folded quartzite bed (Figure 13b) and mafic sill. Both bedding-parallel and cross-cutting vein geometries are developed that indicate a focussed, structurally and lithologically controlled fluid flow. Incompetent slate layers show significantly lower quartz-vein abundances and densities compared to the central quartzite bed and mafic sill. Late quartz vein sets (see below) are transgressive through most lithotypes, but generally pinch out in slate. Distinct quartz-vein sets confined to the central quartzite unit and mafic sill include:

Bedding parallel- and ladder veins: Bedding-parallel veins predominantly extend along bedding contacts between quartzite or the central mafic sill and arkose (Figure 13c). Vein thicknesses on the fold limbs are ca. 20 cm, but can increase up to 45 cm in the crests of parasitic F2b folds. In the first-order F2b fold bedding-parallel veins can be continuous for > 200 m along strike. The veins are predominantly massive and consist of light grey- and milky quartz, with sub-ordinate iron oxides. On fold limbs, veins may be brecciated and cemented by later-generation vein quartz.

Ladder veins are transgressive through competent quartzite beds and the dolerite sill, orientated at high angles to bedding planes or intrusive contacts, but are connected with bedding-parallel veins. Ladder veins range in thickness between 2-15 cm. They are extensional veins that follow tension fractures on limbs and/or radial fanning joints in fold hinges. For the most part, ladder veins appear relatively unreformed, indicating a relatively late timing during folding.

Conjugate shear veins: Conjugate shear veins (Figure 13b) constitute a volumetrically subordinate vein set orientated at high angles to the steeply dipping bedding on fold limbs of second-order F2b folds. The veins cross-cut bedding and form single planar shear fractures or en-echelon arrays. Individual veins are up to 10 cm thick whereas veins in en-echelon vein arrays are much thinner, not exceeding 1 cm in thickness. Veins consist mostly of milky quartz with minor pyrite and iron oxides.

A-C veins: The term A-C quartz veins (Figure 13b, 13d, 13e) highlights the orientation of this

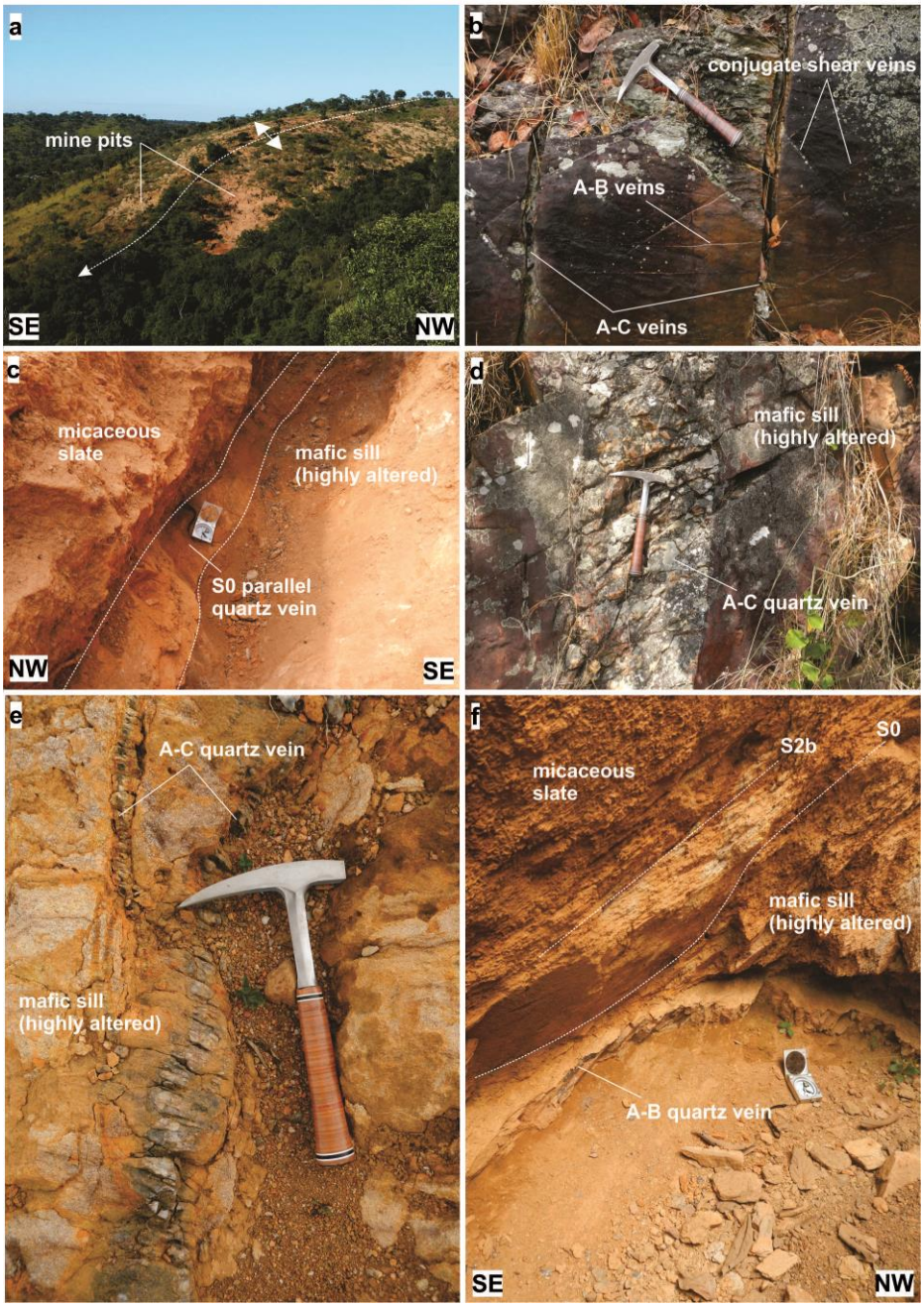

Figure 13: a) View of Mtakuja and NNE plunging anticline. **b)** Quartzite on tight F2b fold limb showing cross-cutting relationships of dominant quartz vein sets. **c)** Thick bedding parallel quartz vein in contact with mafic sill. **d)** Thick sub-vertical A-C quartz vein cross-cutting competent mafic sill. **e)** Exposed gently folded A-C quartz veins in highly altered mafic sill in mine pit. **f)** Sub-horizontal and highly mineralized late A-B quartz vein partially cutting through an altered mafic sill and slate.

vein set at high-angles to the shallow NNE plunge of the F2b host anticline. AC veins are planar, subvertical, striking WNW and at high angles to the regional NNE F2b fold-axial trend. Cross-cutting relationships show A-C veins cross-cutting bedding-parallel-, ladder- and shear veins (Figure 13b). The veins are gently deformed, with thicknesses between ca. 5-35 cm, and consist of massively textured milky quartz and only little iron oxides and hydroxides.

A-B veins: A-B quartz veins (Figure 13b, 13f) are the latest quartz vein set that cross-cut all other quartz-vein generations. The veins are sub-horizontal to shallow (10o – 23o) WSW to ENE dipping veins that are orientated at high angles to the regional axial planar S2b fabric. The veins are most abundant in F2b fold hinges where they are gently buckled. The veins cross-cut competent quartzites and the mafic sill, but are also developed in less competent slate and arkoses. Vein thicknesses vary between 0.2 – 2 cm in slate and up to 8-10 cm in the dolerite sill. The vein quartz has a distinct white to smoky colour with fractured blocky textures and abundant iron oxides.

5.1.3. Mineralization

Mining operations closely follow quartz veins in the highly altered and metamorphosed mafic sill and micaceous wall rock arkoses and slates laced with hematite and limonite pseudomorphs after pyrite. Late -stage B-C veins transecting the mafic sill and immediate wall rocks are the main target of the artisanal mining and contain abundant Fe-oxides and disseminated gold. Structurally late B-C quartz veins are preferentially developed within the anticlinal hinge zone of the host F2b fold (Figure 12). The overall spatial distribution of disseminated Au along the margins- or within highly altered mafic wall rock implicates an additional chemical control to mineralization.

6. Oxygen Isotopes

6.1. Sampling and analysis

A total of 13 whole-rock and 13 quartz-vein samples were analysed for oxygen isotopes (Table 1) in order to constrain potential fluid sources of the regional alteration and mineralization. The relative stratigraphic position of whole-rock samples are shown in Figure 4.

For oxygen isotopes, both conventional and laser fluorination methods were used. Whole-rock powders were analysed using a conventional silicate line following methods described by Harris and Ashwal (2002). Approximately 10 mg of sample was reacted with ClF_3, and the liberated O_2 converted to CO_2 using a hot platinized carbon rod. Quartz vein material was analysed by the laser fluorination method described by Harris and Vogeli (2010). In some cases, single pieces were analysed, in others multiple pieces were analysed. All samples were pre-fluorinated overnight, where after each 1-3 mg sample was reacted in the presence of approximately 10 kPa BrF_5, and the purified O_2 was collected onto a 5 Å molecular sieve contained in a glass storage bottle.

All O-isotope ratios were measured off-line using a Finnigan Delta XP mass spectrometer in dual-inlet mode on either CO_2 (conventional) or O_2 (laser) gas. All data are reported in δ notation where $\delta^{18}O$ = (Rsample/Rstandard -1)*1000, and R = the measured $^{18}O/^{16}O$ ratio. For the whole-rock data, duplicate splits of the quartz standard (MQ) were

Basement – Detachment footwall				
Sample	**$\delta^{18}O$ (‰)**	**Type**	**Location**	**Description**
B5	8.2	Quartz vein	Kalukwete	(Pre-D2), set 2 - shear vein
B6	10.0	Quartz vein	Kalukwete	(Pre-D2), set 2 - shear vein
D3	9.7	Quartz vein	Kalukwete	Early Pre-D2, set 1 - transposed vein
B7	11.4	Quartz vein	Kalukwete	Set 3 - shear vein, Au mineralized
B9	11.9	Quartz vein	Kalukwete	Set 3 - shear vein, Au mineralized
B8	12.9	Quartz vein	Kalukwete	Set 3 - shear vein, Au mineralized
B2	10.4	Whole rock	Kalukwete	Cataclastic textured biotite gneiss (Pre-D2)
B3	10.9	Whole rock	Kalukwete	Granite with moderate sericite alteration
D2	11.1	Whole rock	Kalukwete	Muscovite schist (granite protolith)
B4	12.0	Whole rock	Kalukwete	Biotite gneiss with pervasive sericite alteration
B1	8.7	Whole rock	Kalukwete	Biotite granite (no alteration)
D1	8.1	Whole rock	Kalukwete	Mylonite (Pre-D2)
Cover – Detachment hanging wall				
Sample	**$\delta^{18}O$ norm**	**Type**	**Location**	**Description**
C6a	16.1	Quartz vein	Mapuli	Set 3 - shear vein, Au mineralized
C7a	16.4	Quartz vein	Mapuli	Set 3 - shear vein, Au mineralized
C6b	16.1	Whole rock	Mapuli	Highly graphitic schist
C7b	14.3	Whole rock	Mtakuja	Highly graphitic slate
C1	16.1	Quartz vein	Mtakuja	Massive A-C vein
C5	12.7	Quartz vein	Mtakuja	A-B vein, Au mineralized
C4	12.4	Quartz vein	Mtakuja	A-B vein, Au mineralized
C8	14.8	Quartz vein	Mtakuja	Set 3 - shear vein
C9	13.8	Quartz vein	Mtakuja	Massive A-C vein
C2	14.8	Whole rock	Mtakuja	Ortho-quartzite
C3	12.4	Whole rock	Mtakuja	Micaceous and siliceous slate
C8	8.1	Whole rock	Mtakuja	Metamorphosed mafic sill (minor alteration)
C9	12.8	Whole rock	Mtakuja	Metamorphosed mafic sill (altered)
C11	16.0	Whole rock	Mtakuja	Metamorphosed mafic sill (highly altered)

Table 1: O-isotope results and sample descriptions. Notes: All quartz analysed by laser fluorination, all whole rock samples by conventional fluorination. All d18O values reported relative to SMOW (see text).

run with each batch of eight samples, and were used to convert the raw data to the SMOW scale using the $\delta^{18}O$ value of 10.1 % for MQ. The long-term variability of MQ suggests a 2σ error of 0.16 ‰. For the laser fluorination analyses, two splits of our internal standard MON GT (5.38 ‰,

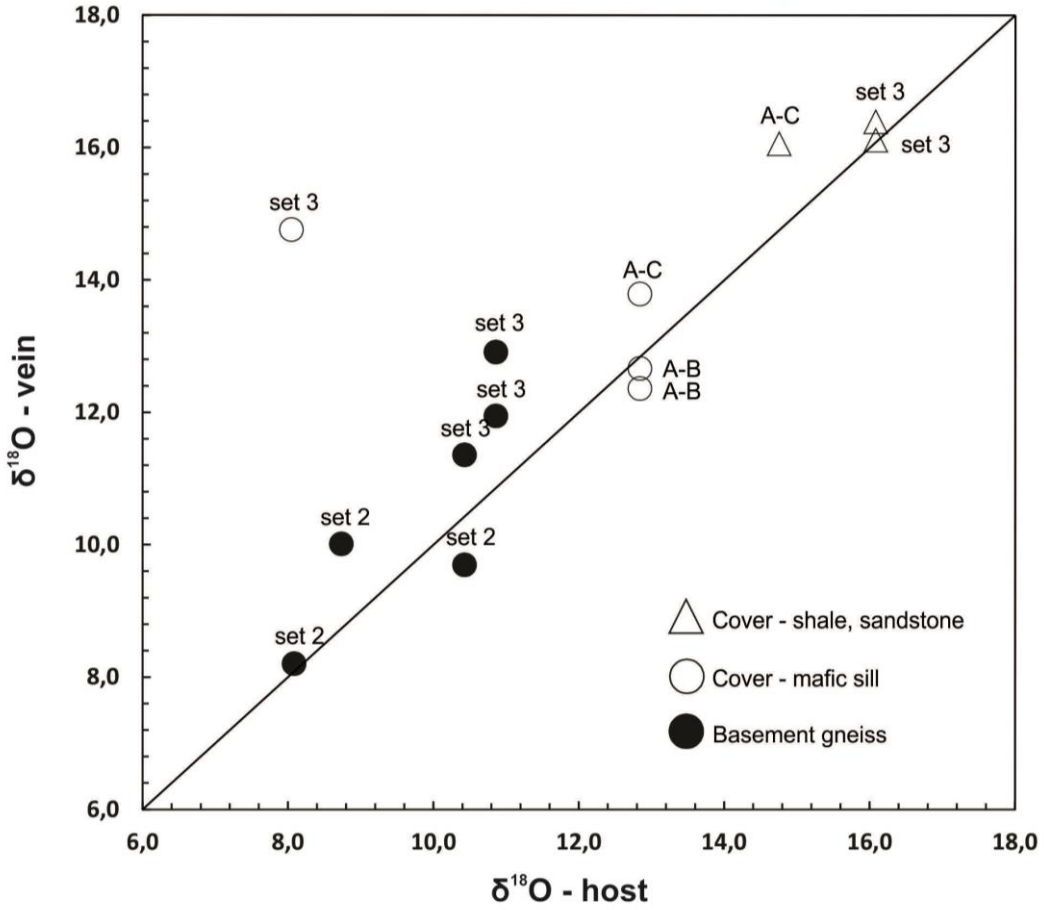

Figure 14: XY scatter plot of $\delta^{18}O$ values for sampled quartz veins and associated wall rocks (host).

Harris and Vogeli 2010) were analysed with each batch of 10 samples. The long-term average difference in $\delta^{18}O$ values of duplicates of MON GT is 0.12 ‰, which corresponds to a 2σ value of 0.15‰ (n=185). San Carlos olivine grains were also analysed during the course of this work and gave an average $\delta^{18}O$ value of 5.33 ‰ (± 0.32 ‰, 2σ n = 9) which is comparable to the $\delta^{18}O$ values of 5.35 ‰ reported by Eiler et al. (2011). Yields were measured for all conventional analyses by means of a small volume cold finger and a pressure transducer during the extraction procedure. For quartz analysed by laser fluorination, the yield was determined by measuring the pressure of gas in the mass spectrometer inlet at constant volume. In all cases, the yields were close to the expected 100% yield based on the weight of sample.

6.2. O-isotope results

Pre-D2 quartz veins from basement gneisses at Kalukwete have $\delta^{18}O$ values (Table 1) between 8.2 – 10.0‰ (B5, B6, D3), whereas quartz veins associated with D2 deformation, and the regional detachment, range from 11.4 – 12.9‰ (B7, B8, B9). Similarly, host basement rocks with the least amount of retrogression record $\delta^{18}O$ values of 8.1 – 8.7‰ (B1, D1), while moderately retrogressed gneisses range from 10.4 – 12.0‰ (B2, B3, D2, B4).

Quartz veins from Mapuli, which is situated in graphitic schists (previously slate) of the Upper Muyaga Group and also associated with the regional D2 detachment, have markedly higher $\delta^{18}O$ values of 16.1 – 16.4‰ (B5, B6). These values are similar to those of the host graphitic schists which have $\delta^{18}O$ value of 16.1‰ (C6b). Quartz veins from Mtakuja, by comparison with Mapuli, have more variable $\delta^{18}O$ values ranging from 13.8 – 16.1‰ (C1, C8, C9) and 12.4 – 12.7‰ (C4, C5). Host rocks of slate and quartzite have $\delta^{18}O$ values of 14.3 – 14.8‰ (C2, C7b), whereas mafic sills have $\delta^{18}O$ values of 8.1 and 12.1‰ (C8, C9). Lastly, an extremely altered part of the mafic sill (C11) has a $\delta^{18}O$ value of 16.0‰.

7. Discussion

7.1. D2 fluid flow along the detachment

The sheared basement-cover contact around the MN inlier in the eastern parts of the KAB represents a narrow, but regionally extensive zone where fluid flow has occurred as indicated by the pervasive alteration, silicification and syntectonic (D2) pyritization of both sheared rocks in the detachment, but also wall-rocks below and above the basement-cover contact (e.g. Koegelenberg and Kisters, 2014). The main D2 detachment combines a number of characteristics of low-angle faults. Voluminous quartz veining and overprinting vein generations indicate episodically close-to-lithostatic fluid pressures and fluid pressure cycling along the detachment. Elevated fluid pressures would result in lowering of the effective stress and thereby facilitate reactivation and slip along the shallowly-dipping fault. Fluid flow and associated alteration have, in turn, led to the formation of mica-dominated phyllonites. This reaction weakening of large parts of the D2 detachment would even further lower the shear resistance along the detachment fault during regional deformation. Quartz-vein stock works immediately below the detachment reflect the competence contrast between the weak detachment rocks and the much stronger quartzo-feldspathic gneisses. The prominent and voluminous vein networks suggest that ductile, aseismic creep in the low-cohesion detachment was accommodated by episodic brittle fracturing and quartz veining in the footwall gneisses. This relationship between fault slip and quartz veining is underlined by the development of quartz-vein stockworks in the footwall of the detachment fault and to depths of ca. 25 m and decreasing in abundance at depths > 25 m below the detachment. At larger depths, only older and poorly mineralized vein sets 1 and 2 are developed. The syn-kinematic (D2) timing of quartz veining during top-to-the-NW D2 low-angle thrusting is indicated by (1) the orientation of quartz vein sets (Set 3, 5), corresponding to extension- and shear fractures (Figure 6c, 11d), and (2) the progressive rotation and transposition of veins in closer proximity to and within the detachment. In fact, much of the phyllonitic detachment has formed through the hydration of originally quartzo-feldspathic footwall gneisses

rather than from schists of the overlying Muyaga Group. Hence, transposed and dismembered quartz veins in the detachment phyllonites are probably derived from earlier veining episodes in gneisses, recording the progressive hydration and downward widening of the detachment due to reaction weakening (retrogression) and subsequent strain softening.

Despite the regional extent of fluid flow around the basement-cover detachment, the localized occurrence of mineralized zones and mining operations suggest additional controls and the Kalukwete and Mapuli prospects demonstrate a case in point. Systematic changes in the dip of the basement-cover contact describe an undulating detachment geometry in which NE-trending ramp-like structures with dips of ca. 30-35° alternate with flatter (5-10°) parts of the detachment (Figure 8, 10). Mining at Kalukwete follows an intensely silicified zone that parallels a ramp-structure in the detachment (Figure 5). Steep (>60o) ramp structures along faults are commonly interpreted to represent asperities or zones where the steeper dips result in the misorientation of the faults and increased shear resistance and strain accumulation. However, ramp structures with dips closer to ca. 30 degrees are more optimally orientated for fault slip in the regional D2 stress field (σ1 horizontal; σ3 vertical), assuming an ideally Anderssonian fault-type behaviour (Fagereng et al., 2014). This implies that fault slip along the ramp occurs at relatively lower shear stresses and before fault reactivation along the flats of the detachment. Hence, the optimally orientated ramps are likely to lead to the preferential nucleation of fault slip along the weak detachment and associated brittle failure and quartz veining in the competent footwall gneisses. It is this combination of repeated slip and the juxtaposition of weak fault rocks against competent footwall gneisses that accounts for the localized pervasive quartz veining and mineralization at Kalukwete.

Mining at Mapuli, in contrast, focusses on massively silicified parts of the detachment. Silicification is, again, following NE-trending ramp structures where dips of the regionally low-angle detachment steepen to ca. 45o. These ramp dips are steeper than ramp structures at Kalukwete. The formation of large and massive quartz blows results in relatively competent inclusions within and along the detachment. This causes a steepening of the detachment as it wraps around the quartz blow. In this orientation, fault slip may be delayed and partially inhibited by increasing strain and shear resistance along the more steeply inclined detachment. Lock up of the detachment may instead favour the formation of sub-horizontal extension fractures and result in fault-valve action and associated fluid-pressure cycling, also referred to as seismic pumping (Sibson et al., 1988). Veins that have formed at this stage are represented by the prominent sub-horizontal late-stage D2 extension veins (set 5) that are confined to earlier formed quartz blows immediately below the detachment. Vault-valve mechanisms and subsequent fluid pressure

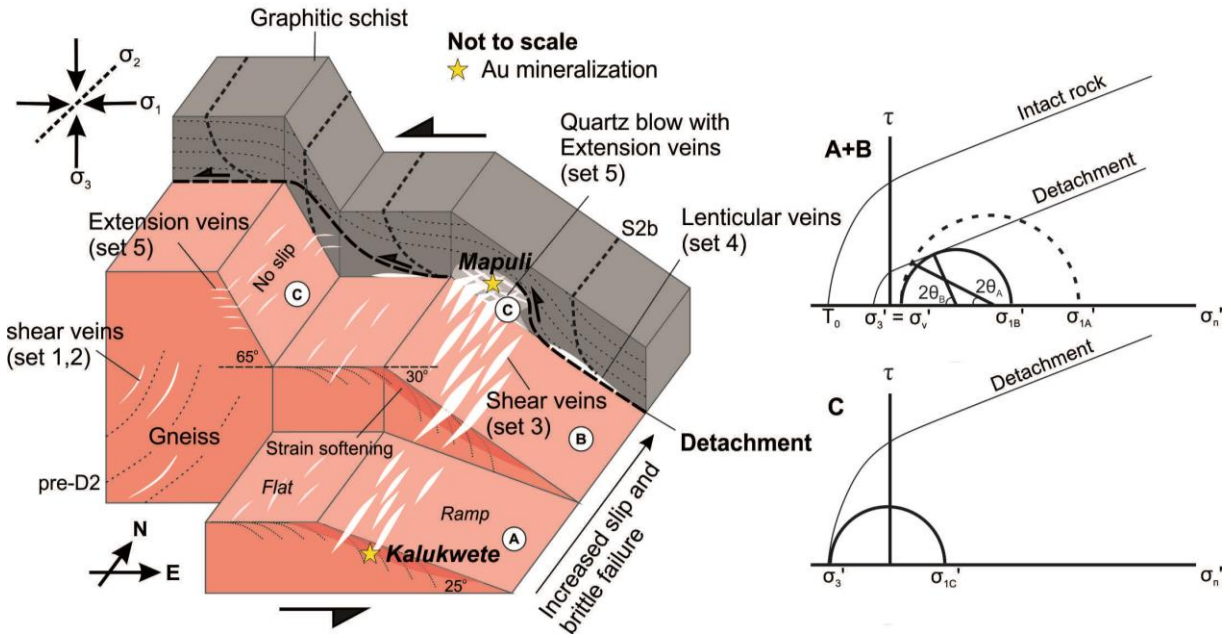

Figure 15: Schematic diagram of ramp structures along the detachment and general quartz vein geometries and abundancies. Locations A, B and C are described with Mohr-Coulomb diagrams showing conditions for failure along shallow to steep dipping sections of the detachment ($\theta_A = 25^o$; $\theta_B = 30^o$; $\theta_C = 65^o$). The regional stress orientation is inferred to be vertical for σ1 and σ2, and parallel with the strike of the detachment. Note orientation of ramp B is most favourable for the initiation of slip (e.g. Fagereng et al., 2014).

cycling is known to play an integral part in the development quartz vein hosted mesothermal gold deposits (Sibson et al., 1988; Sibson and Scott, 1998) where dissolution and precipitation of gold occurs in response to sudden brittle failure and subsequent drops in fluid pressure to hydrostatic values (e.g. Zhu et al., 2011, and references therein).

7.2. D2 fluid flow in the Muyaga Group

Auriferous quartz veins and associated alteration at the Mtakuja prospect in the structurally overlying Muyaga Group demonstrates the regional scale of fluid flow. The D2 timing of this fluid flow is illustrated by the close spatial and temporal relationship between auriferous quartz veins and F2b folds and, specifically, competent and chemically reactive units during folding. Bedding-parallel and connecting shorter ladder veins document fluid infiltration and veining during the initial stages of folding, when flexural slip was operative during fold amplification. The late-stage cross-cutting vein geometries, including fold-hinge normal, sub-vertical A-C and shallowly-dipping A-B veins, indicate veining during the fold lock up stage. Fold lock up occurs during the amplification and tightening of folds, when fold limbs rotate to dips > ca. 65-70 degrees (Fowler and Winsor, 1997; Kisters 2005). At this stage, further tightening of the fold can no longer be accommodated through flexural slip as the limbs have rotated to high angles to the regional shortening strain. Instead, fold tightening is accomplished by internal shortening of the fold and extensional fracturing that can accommodate the local stretch at high angles to

the regional shortening strain. This is the stage where the highly discordant A-C and sub-horizontal A-B veins are likely to have formed. The orientation of the vein sets suggests a component of sub-horizontal, NE-trending, fold-hinge-parallel extension (A-C veins) combined with near-orthogonal sub-vertical stretch (A-B veins) normal to NW-directed, subhorizontal shortening (D2). The bulk of the gold mineralization is hosted by these late vein sets and, similar to the Kalukwete and Mapuli prospects along the detachment, point to the introduction of the gold mineralization late in the evolution of the fluid system.

We also emphasize the importance of fluids with a high fugacity of H_2S that interact with iron rich meta-mafic sills and dykes. The leaching Fe^{2+} from ferruginous dykes and sills by sulphur- and gold-rich fluids, would have led to syn-D2 pyritization (FeS_2) and gold dissolution and precipitation (Zhu et al., 2011, and references therein). Fluids are indeed associated with abundant syn-D2 pyrite (Figure 6e and 6f). This process broadly corresponds with observed greenschist to sub-greenschist facies conditions of the Muyaga Group (< 350°C), i.e. conditions where $Au(HS)_2^-$ phases (complexes) have been shown as the dominant phase prior to dissolution (e.g. Gammons and William-Jones, 1997). This additional chemical control is considered a crucial component, along with structural fluid traps, for gold mineralization in the Muyaga Group.

7.3. Fluid sources

Quartz veins associated with D2 fluid flow all have relatively high $\delta^{18}O$ values from 11.6 – 12.9‰ in the basement, and 12.4 – 16.4‰ in the Upper Muyaga Group (Figure 14). These values are typical of clastic sedimentary rocks such as slates and quartzites of the Muyaga Group (Bindeman, 2008 and references therein). Quartz veining at Mapuli is massive compared to Kalukwete and Mtakuja and arguably indicates the area with the highest fluid throughput. Thus, $\delta^{18}O$ values of up to ca. 16‰ for set 3 quartz veins at Mapuli are likely to be the best reflection of the original $\delta^{18}O$ composition of the fluid. Fluid sources may be related to the dehydration of pelitic rocks and/or meteoric fluids that equilibrated with the supracrustal rocks. Pre-D2 shear veins in basement gneisses have lower $\delta^{18}O$ values of 8.2 – 10.1‰, which may indicate fluid of igneous or metamorphic origin unrelated to the D2 event.

Variations in $\delta^{18}O$ values for D2 quartz veins are largely attributed to wall-rock buffering either by basement gneisses, or mafic sills in the cover, which partially lower $\delta^{18}O$ values (Figure 14). A clear example of this could be seen at Mtakuja where late A-B veins, hosted within a prominent mafic sill, have lower than expected $\delta^{18}O$ values of 12.4 – 12.7‰. By comparison quartz veins in adjacent slate or quartzite have $\delta^{18}O$ values above 16‰ (e.g. Mapuli). Note that the quartz vein $\delta^{18}O$ values show a strong correlation with the host $\delta^{18}O$ values ($r = 0.74$). This is typical of

vein systems that are 'rock-buffered' (e.g. Gray et al., 1991).

Considering the relationship between fluid flow and D2 deformation (e.g. Koegelenberg et al., 2014), fluids are likely to have originated from low-grade metamorphism and dehydration of the Kagera Supergroup (Muyaga Group) which consists predominantly of (sub-) greenschist to amphibolite facies meta-quartzites and pelites. This is consistent with D2 fluid being rock buffered. Stable isotope data is also not consistent with influx of water from external sources, e.g. magmatic or surface water, which likely suggests a closed fluid system (e.g Kenis et al., 2000; Oliver et al., 1993). At least if it was meteoric water it would have to exchange with host rocks very thoroughly. More locally, subtle oxygen isotope variations are likely the result of fluid mixing from different sedimentary layers and interlayered mafic sills and dykes in the Kagera Supergroup during progressive D2 deformation (e.g. Berwouts et al., 2008). In addition, D2 fluid sources and mostly lower greenschist pressure and temperature conditions in the ED indicate that basement TTG gneisses, chlorite schists and amphibolites of the MN inlier, analogous with rocks of the Lake Nyanza Super Terrane (e.g. Kabete et al, 2012), seem unlikely to have undergone any significant hydrothermal remobilization. This suggests that the source of gold is not associated with the gold endowed Archaean greenstones of the TC, but rather inclusive of rocks that constitute the KAB.

8. Conclusion

Exploration of traditional greenstone-hosted gold deposits on the Tanzania Craton has reached a fairly mature stage and requires the identification of deposits outside the boundaries of the Archaean granitoid-greenstone basement. In this paper, we have described the occurrence and controls of gold prospects that are mined on a regional scale along the NW margin of the craton that is structurally overlain by Mesoproterozoic low-grade metamorphic sediments of the Karagawe-Ankole fold-and-thrust belt. Regional-scale fluid flow and gold mineralization are largely confined to the sheared low-angle detachment between Archaean basement gneisses and younger, allochthonous cover rocks. The formation of auriferous quartz veins is primarily controlled by the pronounced competence contrast between weak detachment rocks and competent quartzo-feldspathic footwall gneisses that promote brittle fracturing and veining. Gold mining concentrates around subtle ramp structures within the gently undulating detachment. The gently-inclined ramps are more optimally orientated (20º-45º) for fault slip and repeated reactivation of the detachment, thus, enhancing brittle fracture permeabilities in the underlying gneisses. Gold mining in the stratigraphically higher section above the main detachment in metasediments of the Muyaga Group is closely associated with fold structures of the main fold-and-thrust belt. Quartz veins are again preferentially developed in competent units such as quartzites and dolerite

sills. Overprinting vein generations record fluid infiltration during fold amplification and fold tightening. The bulk of the gold mineralization is associated with late-stage cross-cutting veins that document veining during the lock-up stage of the tight folds and orthogonal extension normal to the regional shortening strains.

Oxygen isotope data suggest that dehydration of the low-grade metapelites and minor metapsammites of the overlying Karagawe-Ankole Belt represented the likely fluid source of this regional-scale fluid system. Given the extent (> 100 km) of the main detachment and the artisanal mining that can intermittently be traced along much of this basement-cover contact, makes this region overlying the western margin of the Tanzania Craton a potentially significant gold province.

9. Acknowledgements

This project would not have been possible without the financial and logistical support from Anglo Gold Ashanti Exploration (AGA) and is published with permission from AGA. A special thanks to Esperius Kavako who provided invaluable guidance in the field as an assistant, and Gillian Williams for her thorough management of the exploration project. Special thanks to Joas Kabete, and the late Pieter Winkler who initiated the project. Lastly, thanks to Stellenbosch University's Central Analytical Facilities and Anton du Plessis for the use of their advanced nano-CT scanner. Bursary funding was also greatly appreciated from AGA, as well as an NRF Scarce Skills Development Grant (81573) to C. Koegelenberg.

10. References

Bindeman, I., 2008. Oxygen isotopes in Mantle and Crustal Magmas as Revealed by Single Crystal Analysis. Reviews in Mineralogy and Geochemistry 69, 445-478

Borg, G., Shackleton, R.M., 1997. The Tanzania and NE-Zaire Cratons. In: de Wit, M. & Ashwal, L.D. (Eds.), Greenstone Belts, Oxford University Press, 608-619.

Berwouts, I., Van Roorden, M., Muchez, P. H., Boyce, A. J. and Sintubin, M., 2008. Inferring intermediate-scale fluid flow in a heterogeneous metasedimentary multilayer sequence during progressive deformation: evidence from the Monts d'Arre´e slate belt (Brittany, France). Geofluids, 8, 143-158.

Borg, G., Krogh, T., 1999. Isotopic age data of single zircons from the Archaean Sukumaland Greenstone Belt Tanzania, Journal of African Earth Science 29, 301-312.

Coggon, R. and Holland, T.J.B., 2002. Mixing properties of phengitic micas and revised garnet-phengite thermobarometers. Journal of Metamorphic Geology 20(7), 683-696.

De Waele, B., Johnson, S.P., Pisarevski, S.A., 2008. Palaeoproterozoic to Neoproterozoic growth and evolution of the eastern Congo Craton: its role in the Rodinia puzzle. Precambrian Research 160, 127–141.

Deblond, A., Punzalan, L.E., Boven, A., Tack, L., 2001. The Malagarazi Supergroup of SE Burundi and its

correlative Bukoban Supergroup of NW Tanzania: Neo- and Mesoproterozoic chronostratigraphic constraints from Ar–Ar ages on mafic intrusive rocks. Journal of African Earth Sciences 32, 435–449.

Eiler, J., Stolper, E.M., McCanta, M.C., 2011. Intra- and intercrystalline oxygen isotope variations in minerals from basalts and peridotites. Journal of Petrology 52(7-9), 1393-1413.

Evans, D.M., Boadi, I., Byemelwa, L., Gilligan, J., Kabete, J., Marcet, P., 2000. Kabanga magmatic sulphide deposits, Tanzania: morphology and geochemistry of associated intrusions. Journal of African Earth Sciences 30, 651–674.

Fagereng, Å., Smith, Z., Rowe, C. D., Makhubu, B., Sylvester, F. Y. G., 2014. Stress, strain, and fault behavior at a thrust ramp: Insights from the Naukluft thrust, Namibia. Journal of Structural Geology 58, 95-107.

Fernandez-Alonso, M., Cutten, H., De Waele, B., Tack, L., Tahon, A., Baudet, D., Barritt, S.D., 2012. The Mesoproterozoic Karagwe-Ankole Belt (formerly the NE Kibara Belt): The result of prolonged extensional intracratonic basin development punctuated by two short-lived far field compressional events. Precambrian Research 216-219, 63-86.

Fowler, T.J., and Winsor, C.N., 1997. Characteristics and occurrence of bedding-parallel slip surfaces and laminated veins in chevron folds from the Bendigo-Castleman goldfields: Implications for flexural-slip folding. Journal of Structural Geology 19, 799-815.

Fritz, H., Abdelsalam, M., Ali, K.A., Bingen, B., Collins, A.S., Fowler, A.R., Ghebreab, W., Hauzenberger, C.A., Johnson, P.R., Kusky, T.M., Macey, P., Muhongo, S., Stern, R.J., 2013. Orogen styles in the East African Orogen: A review of the Neoproterozoic to Cambrian tectonic evolution. Journal of African Earth Sciences 86, 65-106.

Gray, D. R, Gregory, R. T. and Durney, D. W., 1991. Rock-buffered fluid-rock interaction in deformed quartz-rich turbidite sequences, eastern Australia. Journal of Geophysical Research, 96 19 681-19 704.

Harris, C., Ashwal, L.D., 2002. The origin of low d18O granites and related rocks from the Seychells. Contributions to Mineralogy and Petrology 143(3), 366-376.

Harris, C., Vogeli, J., 2010. Oxygen isotope composition of garnet in the Peninsula Granite, Cape Granite Suite, South Africa: Constraints on melting and emplacement mechanisms. South African Journal of Geology, vol. 113.4, 385-396.

Kabete, J.M., Groves, D.I., McNaughton, N.J., Mruma, A.H., 2012. A new tectonic and temporal framework for the Tanzanian Shield: implications for gold metallogeny and undiscovered endowment. Ore Geology Reviews, 44, 88-124.

Kenis I., Muchez Ph., Sintubin M., Mansy J.L., Lacquement F., 2000. The use of a combined structural, stable isotopic and fluid inclusion study to constrain the kinematic history at the northern Variscan front zone (Bettrechies, France). Journal of Structural Geology, 22, 598–602.

Kisters, F.M., 1995. Controls of gold-quartz vein formation during regional folding in amphibolite-facies, marble-dominated meta-sediments of the Navachab Gold Mine in the Pan-African Damara Belt, Namibia. South African Journal of Geology 108, 365-380.

5. Synopsis

5.1. Conclusions

This thesis collectively presents the first detailed overview of structure, timing of deformation and mineralization in the Kagera Supergroup and underlying Archaean basement rocks, and by implication, the first thorough insight into tectonic processes which have shaped the easternmost parts of the KAB. The results presented in chapters 2 to 4 have not only enhanced the understanding of the regional geodynamic context of the ED, compared to what was previously described in literature, but has also questioned the rationale behind recent models describing a protracted intracratonic rift setting for the KAB (e.g. Feranadez-Alonso et al., 2012). The following points summarize key findings of the thesis:

1) The structural geometry, kinematics and frontal position of the ED, with respect to the KAB, is entirely consistent with an origin of the KAB as an east to southeast propagating fold-and-thrust belt (D2). This rationale is underpinned by dominant top-to-the-southeast forethrusting and a regional scale back-thrusted domain that recorded opposite top-to-the-northwest and hinterland directed transport. Transport was facilitated by rheologically weak graphitic, metapelite sequences of the Muyaga Group at the base of the Kagera Supergroup, defining the prominent D2 basal décollement. Local back-thrust development and the reversal of fabrics was focussed above and in front of the regional scale MN inlier which may be interpreted as a thick-skinned, eastwards transported, basement wedge previously rooted to the TC. Back-thrust development in the Muyaga Group is further characterized by the subsequent under-thrusting of the overlying coarse clastic Bukoba Group to the east, which forms a relatively heavy pinning "buttress" in the frontal toe of the KAB. This structural architecture may be described as a typical "triangle zone" (e.g. Erickson, 1995).

   The timely formation of D2 structures in the ED was indicated by ^{39}Ar-^{40}Ar muscovite ages of 1326 ± 10 Ma from phyllonites sourced from the base of the Kagera Supergroup and regional décollement. This age is suggested to be at the young end of D2 deformation and overlaps with the youngest ages of the main phase of granite plutonism (ca. 1329 Ma, Buchwaldt et al., 2008) and mafic dyke emplacement that has been otherwise associated with crustal extension and intracratonic rifting. The new constraints of D2 timing, together with the newly defined structural fabric of the ED, suggest that the main D2 crustal shortening event is more consistent with a Mesoproterozoic collision between the Congo

Craton to the west and the TC in the east. This rationale also strengthens broad correlations with rocks of the southern Kibara belt for which similar tectonic scenarios have been proposed (e.g. Debruyne et al., 2015)

Lithological contrasts and preferred strain partitioning into the Muyaga Group, and only gentle southeast-verging synformal deformation of the Bukoba Group, indicates the Bukoba basin to be a relic of a pre-D2 Paleo- to Mesoproterozoic foreland. This rationale is supported by distinct reworking of the Muyaga Group sediments into the Bukoba Group before 1568 Ma, indicated by exhumation and erosion of ca. 1780 Ma felsic tuff layers at the base of the Muyaga Group. These detrital ages further correlate the Bukoba Group with the Bwezigoro Group in southwest Uganda, which consists of similarly coarse clastic sediments, and suggests a far more regionally extensive Paleo- to Early Mesoproterozoic foreland basin overlying the western margin of the TC and Paleoproterozoic Uganda Block (Ruwenzori belt). However, a reasonable understanding of the tectonic setting at that time remains largely enigmatic.

2) The eastern margin of the MN inlier has exposed a regional low angle and weak décollement/detachment between soft graphitic shale of the Upper Muyaga Group and competent basement gneisses. This competence contrast and focussed shearing has brought about extensive and laterally continuous fluid flow along the basement-cover contact indicated pervasive silicification and retrogression of gneisses to intensely foliated phyllonites and pyritization of meta-sediments in the hanging wall. Along the detachment several artisanal gold mines (Kalukwete and Mapuli) are spatially associated with (20º – 35º) NE trending ramp zones favourably orientated for slip and re-activation within the low angle detachment. Repeatedly overprinted auriferous quartz veining are associated with brittle failure (shear fractures) of competent footwall gneisses. The migration of fluids upwards from the detachment and into the tightly folded cover is strictly controlled by brittle fracture development during fold amplification and flexural slip of competent quartzites and mafic intrusions of the Muyaga Group. Auriferous quartz veining is most prominent in anticlines, cored by chemically re-active mafic sills, which have undergone significant tightening and eventual lock-up. Stable oxygen isotopes of D2 Fluids associated with Au mineralization are also consistent with the dehydration of mostly clastic sedimentary rocks and, as such, indicate

that fluids have been derived mainly from the Kagera Supergroup. This also implies that the Archaean grantoid-greenstone basement of the TC has not contributed to D2 fluid evolution and mineralization.

5.2. Future research

In general, much of the KAB remains poorly researched, including large parts of the KAB situated westwards into the DRC, i.e. west of the western branch of the East African Rift. With only an increased geological understanding of the ED much speculation with regards to the KAB's tectono-stratigraphy, basin correlations and crustal framework has been highlighted. These features are not only central to understanding the tectonic evolution of the KAB, but also describe broader comparisons with the contemporaneous KIB in the south. As a consequence research opportunities are plentiful. Below we consider a few key aspects.

Firstly, the timing of sedimentation and deformation of several tectono-stratigraphic units in the KAB are not fully constrained. No dates have been presented confirming the Archaean age of the MN inlier, although it is widely assumed to be part of the TC (e.g. Kabete et al., 2012). As a result the north-western margin of the TC and its relationship with Paleoproterozoic terranes including Rusizian basement rocks to the west, and Ruwenzori basement rocks in SW Uganda (Buganda-Toro Supergroup, after Westerhof et al., 2014) are not clear.

The overlying volcano-sedimentary rocks of the KAB, in particular the WD, has been documented only on a regional scale (e.g. Fernandez-Alonso et al., 2012 and references therein). It remains conspicuous that the base of the Akanyaru Supergroup has not been documented, while regional intrusive relationships, and basal contacts, are also poorly described. Perhaps most confusing of the KAB, is that the evolution of the KM alignment and the apparent regional structural boundary between the WD and ED has, in fact, not at all been described by any detailed structure showing the extent and kinematics thereof. In order to better constrain timing of sedimentation, regional stratigraphical correlations and deformation a much more detailed stratigraphical log and multiple structural traverses from the ED, across the KM alignment and into the Akanyaru Supergroup is required. This data needs to be supplemented by comprehensive geochronology including detrital ages, interlayered felsic volcanics and discreate mineral ages along structures.

Furthermore, the new timing of D2 crustal shortening (>1326 ± 10 Ma), has highlighted the need for a comprehensive structural review of much of the KAB, in particular the WD, which should distinguish (D2) Mesoproterozoic structural trends from superimposed Neoproterozoic and/or Pan-African structural overprints.

Lastly, a prominent feature of the Northern Kibaran Igneous Provence central to the KAB is the unique and regional scale, ca. 100 km wide, Lake Victoria Dyke (LVDS) Swarm. The LVDS has only recently been identified by regional scale magnetic surveys and shows a remarkable outer arcuate diameter of up to 500 km (e.g. Mäkitie et al., 2014). Typical rift related tectonic settings fail to account for the sheer scale and geometry of the circular dyke swarm given that expected rectilinear and/or radial dykes are completely absent (e.g. McKenzie Dyke swarm, after Ernst et al., 1998). Considering LVDS emplacement at ca. 1375 Ma (Mäkitie et al., 2014) and potentially contemporaneous D2 crustal shortening, intrusion of the LVDS may have occurred within an overall compressional setting. This could imply emplacement within an initial retro back-arc setting followed by eventual collision between the TC and Congo Craton at ca. 1326 Ma. This may also explain why the LVDS dyke swarm and associated dykes (Deblond et al., 2001) are pristine on the outer margin of the KAB, but more transposed in the interior. As such, the unique emplacement structure of the LVDS may be explained by pre-existing crustal scale stresses aligned with overall evolution of the KAB. This rationale or emplacement model remains to be fully developed.

5.3. References

Buchwaldt, R., Toulkeridis, T., Todt, W., Ucakuwun, E.K., 2008. Crustal age domains in the Kibaran belt of SW-Uganda: combined zircon geochronology and Sm–Nd isotopic investigation. Journal of African Earth Sciences 51, 4–20.

Deblond, A., Punzalan, I.E., Boven, A., Tack, L., 2001. The Malagarazi supergroup of southeast Burundi and its correlative Bukoba supergroup of northwest Tanzania: Neo- and Mesoproterozoic chronostratigraphic constraints from Ar–Ar ages on mafic intrusive rocks. J. Afr. Earth Sci. 32, 435–449

Debruyne, D., Hulsbosch, N., Van Wilderode, J., Balcaen, L., Vanhaecke, F., Muchez, P., 2015. Regional geodynamic context for the Mesoproterozoic Kibara Belt (KIB) and the Karagwe-Ankole Belt: evidence from geochemistry and isotopes in the KIB. Precambrian Res. 264, 82–97.

Erickson, S.G., 1995. Mechanics of triangle zones and passive-roof duplexes: implications of finite element models. Tectonophysics 245, 1-11.

Ernst, R.E., Wingate, M.T.D., Buchan, K.L., Li, Z.X., 2008. Global record of the 1600–700 Ma Large Igneous Provinces (LIPs): implications for the reconstruction of the proposed Nuna (Columbia) and Rodinia supercontinents. Precambr. Res. 160, 159–178.

Fernandez-Alonso, M., Cutten, H., De Waele, B., Tack, L., Tahon, A., Baudet, D., Barritt, S.D., 2012. The Mesoproterozoic Karagwe-Ankole Belt (formerly the NE Kibara Belt): The result of prolonged extensional intracratonic basin development punctuated by two short-lived far field compressional events. Precambrian Research 216-219, 63-86.

Kabete, J.M., Groves, D.I., McNaughton, N.J., Mruma, A.H., 2012. A new tectonic and temporal framework for the Tanzanian Shield: implications for gold metallogeny and undiscovered endowment. Ore Geology Reviews. doi:10.1016/j.oregeorev.2012.02.009

Mäkitie, H., Data, G., Isabirye, E., Manttari, I., Huhma, H., Klausen, M. B., Pakkanen, L. & Virransalo, P. 2014. Petrology, geochronology and emplacement model of the giant 1.37 Ga arcuate Lake Victoria Dyke Swarm on the margin of a large igneous province in eastern Africa. Journal of African Earth Science 97, 273–297.

Sibson, R.H., Robert, F., Poulsen, K.H., 1988. High-angle reverse faults, fluid-pressure cycling, and mesothermal gold-quartz deposits, Geology, Vol. 16, pp. 551-555.

Westerhof, A. B. P., Härmä, P., Isabirye, E., Katto, E., Koistinen, T., Kuosmanen, E., Letho, T., Lehtonen, M. I., Mäkitie, H., Manninen, T., Mänttäri, I., Pekkala, Y., Pokki, J., Saalmann, K., Virransalo, P., 2014. Geology and Geodynamic Development of Uganda with Explanation of the 1:1,000,000 Scale Geological Map. Geological Survey of Finland, Special Paper 55.

6. Appendices

6.1. Appendix A: Abstract presented at the 25th Colloquium of African Geology

Tectonic wedging, back-thrusting and basin development in the frontal parts of the Mesoproterozoic Karagwe-Ankole belt in NW Tanzania

Corné Koegelenberg*& Alex Kisters**

Department of Earth Science, Stellenbosch University, Private Bag X1, Matieland, 7620, South Africa;

e-mail: ckoegelenberg@sun.ac.za*; akisters@sun.ac.za**

Structural complexities in the Mesoproterozoic Karagwe-Ankole fold belt (KAB) in northwest Tanzania have led to conflicting interpretations of regional kinematics and the geodynamic significance of the belt within the broader system of Kibara-age (sensu lato) belts in Central Africa. Structural mapping of the eastern domain of the belt indicates that the regional-scale (> 100km) Mugera-Nyakahura Archean basement inlier represents a forethrusted tectonic wedge. Tectonic wedging in the frontal parts of the belt occurred during top-to-the southeast thick-skinned thrusting of the gneissic basement which forms part of the larger Tanzania Craton. The diagnostic feature of tectonic wedging is the reversal of vergence directions on either side of the basement wedge, resulting in hinterland-directed, top-to-the northwest thrusting of the cover in front and on top of the wedge. Strain is localized into the often graphitic metapelitic rocks of the Upper Muyaga Group (previously the Karagwe-Ankolean Middle division).

The mainly coarse-clastic Mesoproterozoic sediments of the Bukoba Group represent the foreland, molasse-type deposits of the Karagwe-Ankole fold belt. The only gently folded Bukoba Group is separated at the base from the underthrusted, highly deformed Muyaga Group by a passive roof thrust. In contrast the Bukoba unconformably overlies the Tanzania Craton to the far east. This corresponds to the regional-scale gently west verging asymmetry of the synclinal structure of the Bukoba basin in the frontal parts of the belt. Gentle folding of the basin is the result of the underthrusting and

subsequent upwards tilting of the Bukoba sediments above the basement wedge causing the formation of a triangle zone.

The kinematics and arcuate geometry of the frontal parts of the Karagwe-Ankole belt described here indicate the belt to represent a top-to-the-east and -southeast verging foreland fold-and-thrust belt. The actual timing of deformation is, at present, unknown, but regional-scale kinematics and the west to east decrease of metamorphic grades are compatible with an origin of the belt during the convergence and eventual collision between the Congo and Tanzania Cratons in the west.

6.2. **Appendix B:** Argon step heating data

Muscovite 1 from sample 1

Step #	Laser Amp.	Temp °C	cc stp ^{39}Ar	%^{39}Ar	^{36}Ar/^{40}Ar	± 1SE	Age Ma	± 95 %	Incl.	Cl/K	± 1SE
1	9.9	600	1.5E-11	1.2	3.7E-05	7.6E-06	1074	9	no	0.0020	0.0002
2	10.1		2.1E-11	1.62	3.4E-05	7.3E-06	1155	9	no	0.0016	0.0002
3	10.2		1.4E-10	10.9	3.5E-06	5.7E-07	1830	9	yes	0.0016	0.0002
4	10.4	800	5.2E-10	41.0	1.3E-06	1.9E-07	1867	8	yes	0.0016	0.0002
5	10.5		1.2E-10	9.7	3.5E-06	9.0E-07	1748	8	yes	0.0016	0.0002
6	10.7		1.3E-10	9.8	2.0E-06	7.9E-07	1796	8	yes	0.0015	0.0002
7	10.8		9.0E-11	7.0	1.9E-06	2.1E-06	1787	8	yes	0.0016	0.0002
8	11	1000	6.9E-11	5.4	1.6E-06	1.1E-04	1796	9	yes	0.0015	0.0002
9	11.1		3.6E-11	2.9	6.2E-06	2.8E-06	1797	11	yes	0.0016	0.0002
10	11.3		3.0E-11	2.4	2.2E-06	4.8E-05	1797	9	yes	0.0017	0.0002
11	11.4		2.4E-11	1.9	0	0	1805	12	yes	0.0017	0.0002
12	11.6	1100	2.0E-11	1.6	0	0	1814	11	yes	0.0016	0.0002
13	11.7		1.4E-11	1.1	0	0	1811	11	yes	0.0013	0.0002
14	11.9		1.1-11	0.83	0	0	1814	15	yes	0.0015	0.0003
15	12		9.2E-12	0.72	1.6E-05	3.1E-05	1809	12	yes	0.0014	0.0003
16	12.2	1200	7.7E-12	0.61	2.8E-05	1.1E-05	1798	16	yes	0.0017	0.0003
17	12.4		7.7E-12	0.60	1.2E-05	1.2E-04	1818	21	yes	0.0018	0.0003
18	12.5	1250	5.6E-12	0.44	1.7E-05	7.7E-05	1830	21	yes	0.0012	0.0003

Muscovite 2 from sample 1

Step #	Laser Amp.	Temp °C	cc stp ^{39}Ar	%^{39}Ar	^{36}Ar/^{40}Ar	± 1SE	Age Ma	± 95 %	Incl.	Cl/K	± 1SE
1	11	600	1.3E-11	0.7	2.98E-05	4.6E-05	1280	13	no	0.0023	0.0003
2	11.1		2.5E-11	1.4	3.04E-05	8.9E-06	1263	11	no	0.0019	0.0002
3	11.3		1.2E-10	6.5	4.01E-06	1.2E-06	1829	9	no	0.0016	0.0001
4	11.5	900	7.0E-11	3.7	1.06E-05	1.6E-06	1839	10	no	0.0016	0.0001
5	11.6		2.7E-10	14.3	4.81E-06	3.9E-07	1894	8	no	0.0015	0.0001
6	11.8		5.7E-10	30.5	2.37E-06	2.1E-07	1931	8	yes	0.0016	0.0001
7	12	1000	3.5E-10	18.7	1.39E-06	2.5E-07	1983	8	yes	0.0016	0.0001
8	12.1		3.9E-10	20.7	1.47E-06	2.2E-07	1973	8	yes	0.0015	0.0001
9	12.3		2.4E-11	1.3	1.93E-06	1.9E-05	1951	10	yes	0.0016	0.0001
10	12.5	1100	1.5E-11	0.8	0	0	1960	11	yes	0.0019	0.0002
11	12.6		1.0E-11	0.5	3.34E-06	1.9E-05	1946	18	yes	0.0020	0.0002
12	12.8	1200	8.3E-12	0.4	0	0	1945	22	yes	0.0023	0.0004

Muscovite 3 from sample 1

Step #	Laser Amp.	Temp °C	cc stp ^{39}Ar	%^{39}Ar	^{36}Ar/^{40}Ar	± 1SE	Age Ma	± 95 %	Incl.	Cl/K	± 1SE
1	10.1	600	1.2E-11	0.6	5.81E-05	2.1E-05	1185	15	0	0.0025	0.0003
2	10.3		2.7E-11	1.5	2.56E-05	9.9E-06	1086	9	0	0.0019	0.0002
3	10.4		1.8E-11	1.0	1.17E-05	4.8E-04	1189	12	0	0.0021	0.0002
4	10.6	800	2.6E-10	14.1	3.99E-06	3.1E-07	1840	8	0	0.0016	0.0001
5	10.7		7.2E-11	3.9	6.72E-06	2.2E-06	1851	8	0	0.0016	0.0001
6	10.9		3.4E-10	18.6	1.43E-06	2.3E-07	1901	9	1	0.0016	0.0001
7	11.1	900	2.3E-10	12.4	2.27E-06	3.2E-07	1939	8	1	0.0025	0.0001
8	11.2		2.6E-10	14.1	8.39E-07	3.4E-07	1946	7	1	0.0015	0.0001
9	11.4		3.2E-10	17.2	9.87E-08	4.0E-07	1939	8	1	0.0015	0.0001
10	11.6		1.4E-10	7.4	0	0	1927	8	1	0.0015	0.0001
11	11.7	1000	8.8E-11	4.8	6.94E-07	2.2E-05	1917	9	1	0.0015	0.0001
12	11.9		2.2E-11	1.2	6.02E-06	2.9E-05	1939	12	1	0.0016	0.0001
13	12.1		1.8E-11	1.0	0	0	1933	12	1	0.0014	0.0002
14	12.2	1100	1.3E-11	0.7	3.31E-06	32-05	1953	14	1	0.0017	0.0002
15	12.4		1.1E-11	0.6	2.27E-06	1.4E-05	1937	15	1	0.0022	0.0004
16	12.5		8.8E-12	0.5	1.46E-05	3.5E-05	1940	17	1	0.0025	0.0003
17	12.7	1200	5.7E-12	0.3	1.56E-05	1.3E-04	1946	22	1	0.0023	0.0004

Muscovite 1 from sample 2

Step #	Laser Amp.	Temp °C	cc stp ^{39}Ar	%^{39}Ar	^{36}Ar/^{40}Ar	± 1SE	Age Ma	± 95 %	Incl.	Cl/K	± 1SE
1	9.9	600	3.3E-11	0.6	1.4E-05	3.0E-04	933	7	no	0.0018	0.0002
2	10.1		6.3E-11	1.2	1.1E-05	2.3E-06	993	6	no	0.0016	0.0002
3	10.2		3.7E-11	0.7	3.8E-06	2.5E-05	1044	7	no	0.0016	0.0002
4	10.4	800	1.8E-10	3.4	1.5E-06	1.9E-05	1290	7	no	0.0015	0.0002
5	10.5		2.8E-10	5.2	2.7E-06	4.0E-07	1401	8	yes	0.0015	0.0002
6	10.7		4.0E-10	7.5	2.0E-06	5.0E-07	1429	7	yes	0.0015	0.0002
7	10.8	900	5.4E-10	10.0	9.3E-07	8.3E-07	1407	7	yes	0.0015	0.0002
8	11		4.7E-10	8.8	7.9E-07	4.3E-07	1399	8	yes	0.0015	0.0002
9	11.1		5.1E-10	9.6	1.5E-06	1.5E-06	1366	7	yes	0.0015	0.0002
10	11.3	1000	4.5E-10	8.4	1.0E-06	3.6E-06	1400	7	yes	0.0015	0.0002
11	11.4		7.3E-10	13.6	1.9E-07	1.9E-06	1486	6	yes	0.0015	0.0002
12	11.6		2.6E-10	4.8	4.8E-07	1.4E-05	1462	6	yes	0.0015	0.0002
13	11.7	1100	2.3E-10	4.2	0	0	1424	7	yes	0.0015	0.0002
14	11.9		1.1E-09	20.2	0	0	1545	6	yes	0.0015	0.0002
15	12.4	1200	2.4E-11	0.5	1.2E-05	3.0E-04	1075	9	no	0.0014	0.0002

Muscovite 2 from sample 2

Step #	Laser Amp.	Temp °C	cc stp ^{39}Ar	%^{39}Ar	^{36}Ar/^{40}Ar	± 1SE	Age Ma	± 95 %	Incl.	Cl/K	± 1SE
1	10	600	2.7E-11	0.5	2.9E-05	1.0E-05	869	10	no	0.0017	0.0001
2	10.1		4.1E-11	0.8	1.6E-05	5.8E-06	929	8	no	0.0016	0.0001
3	10.3		1.2E-10	2.2	3.9E-06	5.5E-05	1021	5	no	0.0016	0.0001
4	10.5	800	2.0E-10	3.7	3.3E-06	1.1E-06	1067	7	no	0.0016	0.0001
5	10.7		3.4E-10	6.2	9.2E-07	6.4E-06	1216	6	no	0.0015	0.0001
6	10.9	900	5.5E-10	10.1	2.6E-06	4.8E-07	1342	9	yes	0.0015	0.0001
7	11		7.7E-10	14.4	3.3E-06	4.4E-07	1354	11	yes	0.0016	0.0001
8	11.2		7.2E-10	13.4	6.3E-07	8.5E-06	1352	9	yes	0.0015	0.0001
9	11.4	1000	6.5E-10	12.0	3.5E-07	3.8E-06	1407	7	yes	0.0015	0.0001
10	11.6		9.5E-10	17.6	0	0	1499	6	yes	0.0015	0.0001
11	11.8	1100	6.6E-10	12.3	1.3E-07	1.0E-06	1520	6	yes	0.0015	0.0001
12	11.9		3.3E-10	6.1	7.0E-07	1.5E-06	1559	7	yes	0.0015	0.0001
13	12.1	1200	2.7E-11	0.5	9.5E-06	1.1E-05	1715	13	no	0.0015	0.0001

Muscovite 1 from sample 3

Step #	Laser Amp.	Temp °C	cc stp ^{39}Ar	% ^{39}Ar	^{36}Ar/^{40}Ar	± 1SE	Age Ma	± 95 %	Incl.	Cl/K	± 1SE
1	9.6	600	8.5E-12	0.6	3.5E-04	1.4E-04	282	15	no	0.0025	0.0004
2	9.8		6.3E-11	4.6	9.7E-06	3.4E-05	1025	7	no	0.0017	0.0002
3	9.9		7.7E-11	5.6	7.4E-06	4.8E-05	1197	7	no	0.0015	0.0002
4	10.1	800	1.7E-10	12.2	3.6E-06	6.7E-07	1329	6	yes	0.0016	0.0002
5	10.2		1.8E-10	13.1	1.4E-06	1.3E-05	1301	6	yes	0.0015	0.0002
6	10.4		1.1E-10	7.7	2.9E-06	2.3E-05	1265	6	yes	0.0015	0.0002
7	10.6	900	3.8E-10	28.1	6.0E-07	4.4E-05	1343	6	yes	0.0015	0.0002
8	10.7		2.4E-10	17.6	5.8E-07	1.0E-05	1350	6	yes	0.0015	0.0002
9	10.9	1000	9.8E-11	7.2	3.3E-06	2.2E-06	1338	6	yes	0.0015	0.0002
10	11		1.6E-11	1.2	1.7E-05	6.2E-05	1324	15	yes	0.0015	0.0002
11	11.2	1100	1.4E-11	1.0	6.0E-06	2.9E-04	1334	12	yes	0.0016	0.0003
12	11.3		5.2E-12	0.4	5.6E-05	1.8E-04	1336	20	yes	0.0015	0.0004
13	12.4	1200	9.0E-12	0.7	2.6E-05	9.4E-05	1295	11	no	0.0018	0.0003

Muscovite 2 from sample 3

Step #	Laser Amp.	Temp °C	cc stp ^{39}Ar	% ^{39}Ar	^{36}Ar/^{40}Ar	± 1SE	Age Ma	± 95 %	Incl.	Cl/K	± 1SE
1	9.8	550	3.4E-11	1.1	0	0	623	6	no	0.0020	0.0001
2	10		1.1E-10	3.6	0	0	970	6	no	0.0017	0.0001
3	10.2	700	1.6E-10	5.1	2.3E-06	9.3E-06	1090	6	no	0.0016	0.0001
4	10.4		2.2E-10	6.9	1.4E-06	1.7E-05	1206	6	no	0.0016	0.0001
5	10.6		3.1E-10	9.7	6.0E-07	5.5E-06	1264	6	no	0.0015	0.0001
6	10.7	900	4.2E-10	13.2	1.6E-06	3.0E-06	1305	7	yes	0.0015	0.0001
7	10.9		5.7E-10	18.1	1.7E-06	4.1E-07	1330	8	yes	0.0015	0.0001
8	11.1	1000	4.2E-10	13.2	2.5E-06	5.1E-07	1302	7	yes	0.0016	0.0001
9	11.3		4.5E-10	14.3	0	0	1351	6	yes	0.0016	0.0001
10	11.5	1100	2.5E-10	7.9	3.6E-07	2.9E-05	1259	6	no	0.0016	0.0001
11	11.7		1.5E-10	4.6	6.7E-07	9.9E-05	1208	6	no	0.0016	0.0001
12	11.9		4.3E-11	1.3	5.2E-07	2.9E-06	1245	9	no	0.0016	0.0001
13	12.6	1250	1.8E-11	0.6	2.2E-05	1.2E-05	1357	14	no	0.0016	0.0001

Muscovite 1 from sample 4

Step #	Laser Amp.	Temp °C	cc stp ^{39}Ar	% ^{39}Ar	^{36}Ar/^{40}Ar	± 1SE	Age Ma	± 95 %	Incl.	Cl/K	± 1SE
1	9.6	500	5.2E-12	0.1	4.4E-04	1.1E-04	381	18	no	0.0050	0.0006
2	9.7		1.4E-11	0.3	6.9E-04	2.3E-05	894	11	no	0.0031	0.0002
3	9.9		2.0E-11	0.5	2.2E-04	5.5E-06	1085	8	no	0.0018	0.0001
4	10	600	1.8E-11	0.4	9.9E-05	9.5E-06	1105	8	no	0.0018	0.0002
5	10.1		6.8E-11	1.6	1.0E-04	2.8E-06	1131	6	no	0.0016	0.0001
6	10.2		7.3E-11	1.7	5.0E-05	2.5E-06	1312	7	no	0.0016	0.0001
7	10.4	700	1.3E-10	3.2	2.0E-05	7.6E-07	1555	8	no	0.0016	0.0001
8	10.5		1.3E-10	3.2	7.5E-06	7.8E-07	1750	9	no	0.0016	0.0001
9	10.6		3.2E-10	7.6	1.6E-06	2.8E-07	1840	8	no	0.0016	0.0001
10	10.7	800	4.5E-10	10.7	1.3E-06	2.7E-07	1890	8	no	0.0016	0.0001
11	10.9		5.3E-10	12.8	6.7E-07	2.5E-06	1917	8	yes	0.0016	0.0001
12	11		2.4E-10	5.8	7.4E-07	7.1E-06	1919	8	yes	0.0016	0.0001
13	11.1	900	4.6E-10	11.1	5.6E-07	3.1E-07	1937	8	yes	0.0015	0.0001
14	11.2		4.4E-10	10.5	4.7E-07	5.8E-06	1946	8	yes	0.0015	0.0001
15	11.4	1000	2.3E-10	5.6	2.7E-06	4.3E-07	1921	9	yes	0.0015	0.0001
16	11.5		1.8E-10	4.3	2.8E-06	5.7E-07	1935	9	yes	0.0015	0.0001
17	11.6	1100	2.8E-10	6.7	1.6E-07	1.4E-04	1976	8	yes	0.0015	0.0001
18	11.8		4.2E-10	10.1	0	0	1993	8	yes	0.0015	0.0001
19	11.9		9.8E-11	2.3	2.1E-06	2.2E-06	1980	9	yes	0.0016	0.0001
20	12	1250	5.5E-11	1.3	1.1E-06	6.2E-05	1974	9	yes	0.0016	0.0001

Muscovite 2 from sample 4

Step #	Laser Amp.	Temp °C	cc stp ^{39}Ar	%^{39}Ar	^{36}Ar/^{40}Ar	± 1SE	Age Ma	± 95 %	Incl.	Cl/K	± 1SE
1	9.8	550	5.9E-12	0.3	1.7E-04	3.3E-05	804	15	no	0.0022	0.0004
2	9.9		1.8E-11	0.8	6.8E-05	9.5E-06	1029	8	no	0.0017	0.0002
3	10.1	600	1.8E-11	0.8	5.7E-05	1.0E-05	1175	9	no	0.0018	0.0002
4	10.3		6.7E-11	3.0	7.9E-06	1.6E-06	1661	8	no	0.0016	0.0002
5	10.4	800	1.1E-10	4.9	3.6E-06	7.7E-07	1794	8	no	0.0016	0.0002
6	10.6		1.5E-10	6.9	5.3E-07	7.3E-05	1860	8	yes	0.0016	0.0002
7	10.8	900	1.8E-10	8.2	9.4E-07	3.6E-06	1885	8	yes	0.0016	0.0002
8	11		2.6E-10	11.9	9.3E-07	2.6E-06	1843	8	yes	0.0016	0.0002
9	11.1		1.6E-10	7.1	0	0	1864	8	yes	0.0016	0.0002
10	11.3	1000	2.1E-10	9.4	0	0	1902	8	yes	0.0016	0.0002
11	11.5		1.5E-10	7.0	0	0	1914	8	yes	0.0015	0.0002
12	11.6		3.1E-10	13.9	0	0	1924	8	yes	0.0015	0.0002
13	11.8	1100	2.8E-10	12.9	0	0	1926	8	yes	0.0015	0.0002
14	12		2.7E-10	12.0	0	0	1935	8	yes	0.0015	0.0002
15	12.1		9.1E-12	0.4	7.8E-06	2.0E-04	1936	17	yes	0.0013	0.0003
16	12.3	1200	6.1E-12	0.3	2.6E-05	2.2E-05	1962	19	yes	0.0014	0.0004

Notes for Table 2:
Temperatures are optically estimated. Fusion generally occurred 3 steps before the last.
^{36}Ar/^{40}Ar values are corrected for contributions from ^{40}Ca and ^{39}Ar

6.3. Appendix C: LA-SF-ICP-MS U-Th-Pb dating methodology CAF, Stellenbosch University

Laboratory & Sample Preparation	
Laboratory name	Central Analytical Facility, Stellenbosch University
Sample type / mineral	Detrital zircons
Sample preparation	Conventional mineral separation, 1 inch resin mount, 1 µm polish to finish
Imaging	CL, LEO 1430 VP, 10 nA, 15 mm working distance
Laser ablation system	
Make, Model & type	Resonetics Resolution S155, ArF Excimer Coherent CompexPro 110
Ablation cell & volume	Laurin Technology S155 double Helix large volume cell
Laser wavelength	193 nm
Pulse width	20 ns
Fluence	2.8 J/cm^{-2} (measured with external energy meter above sample funnel)
Repetition rate	5.5 Hz
Spot size	30 µm
Sampling mode / pattern	20 µm single spot analyses
Cell carrier gas	100% He, Ar and N_2 make-up gases combined using injectors into double Helix sampling funnel
Pre-ablation laser warm-up (background collection)	3 cleaning shots followed by 20 seconds background collection
Ablation duration	20 seconds
Wash-out delay	15 seconds
Cell carrier gas flows	330 ml/min He
ICP-MS Instrument	
Make, Model & type	Thermo Finnigan Element2 single collector HR-SF-ICP-MS
Sample introduction	Via Nylon 10 tubing
RF power	1350 W
Make-up gas flow	910 ml/min Ar & 0.03 ml/min N_2
Detection system	Single collector secondary electron multiplier
Masses measured	202, 204, 206, 207, 208, 232, 233, 235, 238
Integration time per peak	4 ms
Total integration time per reading	1 sec *(represents the time resolution of the data)*
Sensitvity	30000 cps/ppm Pb
Dead time	6 ns
Data Processing	
Gas blank	20 second on-peak
Calibration strategy	GJ-1 used as primary reference material, Plešovice & M127 used as secondary reference material (Quality Control)

Reference Material info	M127 (Nasdala et al. 2008; Mattinson 2010), 91500 (Wiedenbeck et al. 1995), GJ-1 (Jackson et al. 2004)
Data processing package used / Correction for LIEF	In-house spreadsheet data processing using intercept method for LIEF correction
Mass discrimination	Standard-sample bracketing with $^{207}Pb/^{206}Pb$ and $^{206}Pb/^{238}U$ normalized to reference material GJ-1
Common-Pb correction, composition and uncertainty	204-method, Stacey & Kramers (1975) composition at the projected age of the mineral, 5% uncertainty assigned
Uncertainty level & propagation	Ages are quoted at 2 sigma absolute, propagation is by quadratic addition. Reproducibility and age uncertainty of reference material and common-Pb composition uncertainty are propagated.
Quality control / Validation	91500: Concordia age = 1066±10 Ma (2s, MSWD = 0.11) M127: Concordia age = 528±4 Ma (2s, MSWD = 0.98) Plešovice: Concordia age = 338±3 Ma (2s, MSWD = 0.40)
Other information	For detailed method description see Frei & Gerdes (2009)

Mattinson, J. M., 2010. Analysis of the relative decay constants of 235U and 238U by multi-step CA-TIMS measurements of closed-system natural zircon samples. Chemical Geology 275: 186–198.

Nasdala. L., Hofmeister, W., Norberg, N., Mattinson, J. M., Corfu, F., Dörr, W., Kamo, S. L., Kennedy, A. K., Kronz, A., Reiners, P. W., Frei, D., Košler, J., Wan, Y., Götze, J., Häger, T., Kröner, A., Valley, J. W., 2008. Zircon M257–a homogeneous natural reference material for the ion microprobe U-Pb analysis of zircon. Geostandards and Geoanalytical Research 32:247–265

Wiedenbeck, M., Alle, P., Corfu, F., Griffin, W.L., Meier, M., Oberli, F., Von Quadt, A., Roddick, W., Speigel, W., 1995. Three Natural Zircon Standards for U-Th-Pb, Lu-Hf, Trace-Element and REE Analyses. Geostandards Newsletter 19: 1–23.

6.4. Appendix D: LA-SF-ICP-MS U-Th-Pb data, CAF, Stellenbosch University

				RATIOS							AGES [Ma]						Conc.
Analysis	**U [ppm][a]**	**Pb [ppm][a]**	**Th/U[a]**	**$^{207}Pb/^{235}U$[b]**	**2 σ[d]**	**$^{206}Pb/^{238}U$[b]**	**2 σ[d]**	**rho[c]**	**$^{207}Pb/^{206}Pb$[e]**	**2 σ[d]**	**$^{207}Pb/^{235}U$**	**2 σ**	**$^{206}Pb/^{238}U$**	**2 σ**	**$^{207}Pb/^{206}Pb$**	**2 σ**	**%**
CK1_01	199	75	0.53	6.705	0.157	0.3791	0.0068	0.77	0.1283	0.0019	2073	49	2072	32	2075	26	100
CK1_03	841	238	0.99	5.120	0.107	0.2836	0.0049	0.82	0.1310	0.0016	1839	38	1609	24	2111	21	76
CK1_04	267	131	1.42	11.635	0.330	0.4909	0.0101	0.72	0.1719	0.0034	2575	73	2575	43	2576	33	100
CK1_05	273	141	0.69	13.142	0.297	0.5167	0.0093	0.80	0.1845	0.0025	2690	61	2685	40	2694	22	100
CK1_06	337	101	1.58	5.328	0.127	0.2989	0.0054	0.76	0.1293	0.0020	1873	45	1686	27	2088	27	81
CK1_07	257	99	0.66	6.931	0.164	0.3840	0.0070	0.76	0.1309	0.0020	2103	50	2095	32	2110	27	99
CK1_08	315	98	1.40	5.566	0.124	0.3111	0.0055	0.79	0.1298	0.0018	1911	43	1746	27	2095	24	83
CK1_09	229	82	0.60	6.039	0.138	0.3598	0.0064	0.78	0.1217	0.0018	1981	45	1981	30	1982	26	100
CK1_10	232	74	1.04	5.852	0.152	0.3209	0.0061	0.73	0.1323	0.0024	1954	51	1794	30	2128	31	84
CK1_11	294	131	0.77	9.482	0.214	0.4465	0.0079	0.79	0.1540	0.0021	2386	54	2380	35	2391	23	100
CK1_12	98	34	0.33	5.732	0.161	0.3505	0.0069	0.70	0.1186	0.0024	1936	55	1937	33	1936	36	100
CK1_13	153	59	0.53	6.919	0.167	0.3842	0.0070	0.75	0.1306	0.0021	2101	51	2096	33	2106	28	99
CK1_14	203	78	1.28	9.694	0.237	0.3863	0.0072	0.76	0.1820	0.0029	2406	59	2105	33	2671	26	79
CK1_15	948	242	0.79	4.356	0.093	0.2554	0.0044	0.81	0.1237	0.0016	1704	36	1466	23	2010	22	73
CK1_16	92	31	0.81	5.406	0.146	0.3406	0.0065	0.71	0.1151	0.0022	1886	51	1889	31	1882	34	100
CK1_17	197	91	0.57	10.290	0.283	0.4609	0.0092	0.72	0.1619	0.0031	2461	68	2443	40	2476	32	99

				RATIOS							AGES [Ma]						Conc.
Analysis	**U [ppm][a]**	**Pb [ppm][a]**	**Th/U[a]**	**$^{207}Pb/^{235}U$[b]**	**2 σ[d]**	**$^{206}Pb/^{238}U$[b]**	**2 σ[d]**	**rho[c]**	**$^{207}Pb/^{206}Pb$[e]**	**2 σ[d]**	**$^{207}Pb/^{235}U$**	**2 σ**	**$^{206}Pb/^{238}U$**	**2 σ**	**$^{207}Pb/^{206}Pb$**	**2 σ**	**%**
CK1_18	363	138	0.47	6.757	0.151	0.3803	0.0067	0.79	0.1289	0.0018	2080	46	2078	31	2083	24	100
CK1_19	255	69	1.44	4.946	0.131	0.2714	0.0051	0.71	0.1322	0.0024	1810	48	1548	26	2127	32	73
CK1_20	357	116	1.01	5.766	0.127	0.3255	0.0057	0.79	0.1285	0.0017	1941	43	1817	28	2077	24	87
CK1_21	262	101	0.51	6.887	0.155	0.3851	0.0068	0.78	0.1297	0.0018	2097	47	2100	31	2094	25	100
CK1_22	56	21	0.64	6.715	0.354	0.3779	0.0115	0.58	0.1289	0.0056	2075	109	2066	54	2083	75	99
CK1_23	313	120	0.56	6.853	0.152	0.3828	0.0067	0.79	0.1299	0.0018	2093	46	2089	31	2096	24	100
CK1_24	868	206	1.21	4.578	0.110	0.2374	0.0043	0.75	0.1399	0.0022	1745	42	1373	22	2225	27	62
CK1_25	171	81	0.53	10.761	0.250	0.4744	0.0085	0.77	0.1645	0.0024	2503	58	2503	37	2503	25	100
CK1_26	354	91	1.17	4.730	0.107	0.2587	0.0045	0.77	0.1326	0.0019	1773	40	1483	23	2133	25	70
CK1_27	152	39	1.40	4.587	0.121	0.2560	0.0048	0.71	0.1299	0.0024	1747	46	1470	25	2097	32	70
CK1_28	169	86	0.46	12.641	0.286	0.5088	0.0090	0.78	0.1802	0.0025	2653	60	2651	39	2655	23	100
CK1_29	193	62	1.63	7.683	0.262	0.3183	0.0072	0.66	0.1750	0.0045	2195	75	1782	35	2606	42	68
CK1_30	221	50	0.59	4.156	0.102	0.2283	0.0041	0.74	0.1321	0.0022	1665	41	1326	22	2125	29	62
CK1_31	305	165	0.65	14.842	0.330	0.5422	0.0095	0.79	0.1985	0.0027	2805	62	2793	40	2814	22	99
CK1_32	887	131	1.29	2.472	0.064	0.1473	0.0027	0.71	0.1218	0.0022	1264	33	886	15	1982	33	45
CK1_33	547	126	1.81	4.116	0.092	0.2298	0.0040	0.77	0.1299	0.0018	1658	37	1334	21	2097	25	64
CK1_34	454	150	1.37	8.814	0.193	0.3311	0.0057	0.79	0.1931	0.0026	2319	51	1844	28	2769	22	67
CK1_35	492	127	1.86	6.259	0.138	0.2577	0.0044	0.78	0.1761	0.0024	2013	44	1478	23	2617	23	56
CK1_36	173	66	0.50	6.769	0.170	0.3804	0.0069	0.73	0.1291	0.0022	2082	52	2078	32	2085	30	100
CK1_37	221	112	0.52	12.450	0.286	0.5050	0.0089	0.77	0.1788	0.0026	2639	61	2635	38	2642	24	100

				RATIOS							AGES [Ma]						Conc.
Analysis	**U [ppm][a]**	**Pb [ppm][a]**	**Th/U[a]**	**$^{207}Pb/^{235}U$[b]**	**2 σ[d]**	**$^{206}Pb/^{238}U$[b]**	**2 σ[d]**	**rho[c]**	**$^{207}Pb/^{206}Pb$[c]**	**2 σ[d]**	**$^{207}Pb/^{235}U$**	**2 σ**	**$^{206}Pb/^{238}U$**	**2 σ**	**$^{207}Pb/^{206}Pb$**	**2 σ**	**%**
CK1_38	823	135	1.35	3.585	0.104	0.1646	0.0032	0.68	0.1580	0.0034	1546	45	982	18	2434	36	40
CK1_39	232	70	1.47	4.911	0.134	0.3018	0.0057	0.69	0.1180	0.0023	1804	49	1700	28	1927	35	88
CK1_40	389	148	0.65	6.822	0.168	0.3809	0.0069	0.73	0.1299	0.0022	2089	51	2080	32	2097	29	99
CK1_41	326	122	0.66	6.672	0.158	0.3747	0.0066	0.75	0.1292	0.0020	2069	49	2052	31	2086	27	98
CK1_42	195	70	0.04	6.078	0.147	0.3614	0.0065	0.74	0.1220	0.0020	1987	48	1989	31	1985	29	100
CK1_43	214	77	0.05	6.100	0.146	0.3617	0.0064	0.74	0.1223	0.0020	1990	48	1990	30	1990	29	100
CK1_44	84	30	0.62	6.096	0.179	0.3611	0.0071	0.67	0.1225	0.0027	1990	58	1987	34	1992	38	100
CK1_45	163	51	0.73	5.161	0.246	0.3113	0.0084	0.57	0.1202	0.0047	1846	88	1747	42	1960	69	89
CK1_46	114	50	0.63	8.882	0.225	0.4352	0.0080	0.73	0.1480	0.0026	2326	59	2329	36	2323	30	100
CK1_47	303	117	0.30	6.979	0.161	0.3859	0.0067	0.75	0.1312	0.0020	2109	49	2104	31	2114	26	100
CK1_48	1424	220	0.79	2.603	0.064	0.1544	0.0027	0.72	0.1223	0.0021	1302	32	926	15	1990	30	47
CK1_49	545	142	0.75	4.026	0.092	0.2599	0.0045	0.75	0.1124	0.0017	1639	38	1489	23	1838	27	81
CK1_51	347	119	0.30	5.546	0.129	0.3440	0.0060	0.75	0.1169	0.0018	1908	44	1906	29	1910	28	100
CK1_52	169	47	0.89	5.129	0.133	0.2781	0.0051	0.71	0.1338	0.0025	1841	48	1582	26	2148	32	74
CK1_53	531	114	1.21	3.886	0.090	0.2151	0.0037	0.74	0.1310	0.0020	1611	37	1256	20	2111	27	59
CK1_54	141	35	1.32	4.213	0.123	0.2501	0.0048	0.66	0.1222	0.0027	1677	49	1439	25	1989	39	72
CK1_55	135	48	0.46	5.964	0.155	0.3577	0.0065	0.70	0.1209	0.0022	1971	51	1971	31	1970	33	100
CK1_56	87	31	0.72	5.924	0.181	0.3560	0.0071	0.66	0.1207	0.0028	1965	60	1963	34	1966	41	100
CK1_57	261	55	1.43	3.901	0.130	0.2108	0.0044	0.63	0.1342	0.0035	1614	54	1233	24	2154	45	57
CK1_58	304	85	1.35	4.704	0.123	0.2788	0.0051	0.70	0.1224	0.0023	1768	46	1585	26	1991	33	80

				RATIOS							AGES [Ma]						Conc.
Analysis	**U [ppm][a]**	**Pb [ppm][a]**	**Th/U[a]**	**$^{207}Pb/^{235}U$[b]**	**2 σ[d]**	**$^{206}Pb/^{238}U$[b]**	**2 σ[d]**	**rho[c]**	**$^{207}Pb/^{206}Pb$[e]**	**2 σ[d]**	**$^{207}Pb/^{235}U$**	**2 σ**	**$^{206}Pb/^{238}U$**	**2 σ**	**$^{207}Pb/^{206}Pb$**	**2 σ**	**%**
CK1_59	142	48	0.56	5.320	0.139	0.3369	0.0061	0.70	0.1145	0.0021	1872	49	1872	30	1872	34	100
CK1_60	168	66	0.42	7.109	0.182	0.3923	0.0071	0.71	0.1314	0.0024	2125	54	2134	33	2117	32	101
CK1_61	180	71	0.36	7.269	0.180	0.3955	0.0071	0.72	0.1333	0.0023	2145	53	2148	33	2142	30	100
CK1_62	236	97	0.40	7.881	0.190	0.4111	0.0072	0.73	0.1391	0.0023	2218	54	2220	33	2215	29	100
CK1_63	245	91	1.27	6.490	0.166	0.3734	0.0067	0.71	0.1261	0.0023	2045	52	2046	32	2044	32	100
CK1_64	223	84	1.36	6.518	0.176	0.3745	0.0070	0.69	0.1262	0.0025	2048	55	2051	33	2046	35	100
CK1_65	103	35	1.03	5.921	0.164	0.3345	0.0063	0.68	0.1284	0.0026	1964	54	1860	30	2076	35	90
CK1_66	114	37	0.71	6.104	0.166	0.3258	0.0061	0.68	0.1359	0.0027	1991	54	1818	30	2175	34	84
CK1_67	162	30	1.75	3.502	0.098	0.1855	0.0035	0.67	0.1369	0.0029	1528	43	1097	19	2189	36	50
CK1_68	605	191	1.14	7.130	0.166	0.3152	0.0054	0.74	0.1641	0.0026	2128	49	1766	26	2498	26	71
CK1_69	210	79	0.51	6.636	0.165	0.3769	0.0067	0.71	0.1277	0.0022	2064	51	2062	31	2067	31	100
CK1_70	407	153	0.47	6.655	0.162	0.3773	0.0066	0.72	0.1279	0.0022	2067	50	2064	31	2070	30	100
CK1_71	415	157	0.55	6.664	0.160	0.3788	0.0066	0.72	0.1276	0.0021	2068	50	2071	31	2065	29	100
CK1_72	190	75	0.58	7.264	0.185	0.3944	0.0071	0.70	0.1336	0.0024	2144	55	2143	33	2146	31	100
CK1_73	182	62	0.51	5.415	0.141	0.3394	0.0061	0.69	0.1157	0.0022	1887	49	1884	29	1891	34	100
CK1_74	48	26	0.44	13.891	0.419	0.5309	0.0109	0.68	0.1898	0.0042	2742	83	2745	46	2740	36	100
CK1_75	37	19	0.41	13.723	0.424	0.5266	0.0110	0.67	0.1890	0.0043	2731	84	2727	46	2733	37	100
CK1_76	42	15	0.51	5.514	0.192	0.3444	0.0073	0.61	0.1161	0.0032	1903	66	1908	35	1897	49	101
CK1_77	53	18	0.50	5.570	0.183	0.3454	0.0071	0.62	0.1170	0.0030	1911	63	1913	34	1910	46	100
CK1_78	953	170	1.52	3.153	0.077	0.1783	0.0031	0.71	0.1283	0.0022	1446	35	1058	17	2074	30	51

				RATIOS							AGES [Ma]						Conc.
Analysis	**U [ppm][a]**	**Pb [ppm][a]**	**Th/U[a]**	**$^{207}Pb/^{235}U$[b]**	**2 σ[d]**	**$^{206}Pb/^{238}U$[b]**	**2 σ[d]**	**rho[c]**	**$^{207}Pb/^{206}Pb$[e]**	**2 σ[d]**	**$^{207}Pb/^{235}U$**	**2 σ**	**$^{206}Pb/^{238}U$**	**2 σ**	**$^{207}Pb/^{206}Pb$**	**2 σ**	**%**
CK1_79	897	188	1.60	3.707	0.094	0.2096	0.0037	0.69	0.1282	0.0023	1573	40	1227	20	2074	32	59
CK1_80	216	77	0.41	5.937	0.153	0.3574	0.0063	0.69	0.1205	0.0023	1967	51	1970	30	1963	33	100
CK1_81	107	39	1.71	6.107	0.181	0.3623	0.0070	0.65	0.1222	0.0028	1991	59	1993	33	1989	40	100
CK1_82	262	94	0.58	5.988	0.156	0.3576	0.0064	0.68	0.1214	0.0023	1974	52	1971	30	1978	34	100
CK1_84	465	120	1.18	4.418	0.111	0.2583	0.0045	0.69	0.1240	0.0023	1716	43	1481	23	2015	32	73
CK1_85	124	41	0.90	5.325	0.160	0.3270	0.0063	0.64	0.1181	0.0027	1873	56	1824	31	1928	41	95
CK3_001	511	125	1.36	4.338	0.093	0.2447	0.0042	0.80	0.1286	0.0017	1701	36	1411	22	2079	23	68
CK3_002	109	41	1.35	8.839	0.214	0.3808	0.0070	0.75	0.1684	0.0027	2322	56	2080	33	2541	27	82
CK3_003	240	77	1.32	6.097	0.139	0.3217	0.0056	0.77	0.1375	0.0020	1990	45	1798	27	2196	25	82
CK3_004	287	79	0.67	5.524	0.123	0.2755	0.0048	0.78	0.1454	0.0020	1904	42	1569	24	2293	24	68
CK3_005	176	67	0.63	6.740	0.167	0.3803	0.0070	0.74	0.1285	0.0022	2078	52	2078	32	2078	30	100
CK3_006	280	132	0.31	10.535	0.223	0.4702	0.0080	0.81	0.1625	0.0020	2483	53	2484	35	2482	21	100
CK3_007	174	66	0.57	6.734	0.164	0.3805	0.0069	0.74	0.1284	0.0021	2077	51	2078	32	2076	29	100
CK3_008	130	43	0.70	5.099	0.130	0.3299	0.0060	0.72	0.1121	0.0020	1836	47	1838	29	1834	32	100
CK3_009	443	168	0.48	6.723	0.144	0.3794	0.0065	0.80	0.1285	0.0017	2076	44	2073	30	2078	23	100
CK3_010	210	80	0.95	6.795	0.154	0.3812	0.0067	0.77	0.1293	0.0019	2085	47	2082	31	2088	25	100
CK3_011	131	47	0.29	6.105	0.148	0.3610	0.0065	0.74	0.1227	0.0020	1991	48	1987	31	1995	29	100
CK3_012	191	51	1.24	4.273	0.161	0.2681	0.0061	0.60	0.1156	0.0035	1688	64	1531	31	1889	54	81
CK3_013	214	81	0.52	6.703	0.151	0.3793	0.0066	0.77	0.1282	0.0018	2073	47	2073	31	2073	25	100
CK3_014	147	74	0.54	12.285	0.284	0.5030	0.0090	0.77	0.1771	0.0026	2626	61	2627	39	2626	24	100

				RATIOS							AGES [Ma]						Conc.
Analysis	**U [ppm][a]**	**Pb [ppm][a]**	**Th/U[a]**	**$^{207}Pb/^{235}U$[b]**	**2 σ[d]**	**$^{206}Pb/^{238}U$[b]**	**2 σ[d]**	**rho[c]**	**$^{207}Pb/^{206}Pb$[c]**	**2 σ[d]**	**$^{207}Pb/^{235}U$**	**2 σ**	**$^{206}Pb/^{238}U$**	**2 σ**	**$^{207}Pb/^{206}Pb$**	**2 σ**	**%**
CK3_015	267	134	0.47	12.208	0.286	0.5002	0.0090	0.77	0.1770	0.0027	2621	61	2615	39	2625	25	100
CK3_016	398	153	0.54	6.858	0.146	0.3839	0.0065	0.80	0.1296	0.0017	2093	44	2094	30	2092	23	100
CK3_017	84	38	0.70	9.933	0.255	0.4585	0.0086	0.73	0.1571	0.0027	2429	62	2433	38	2425	29	100
CK3_018	443	154	0.47	6.412	0.137	0.3469	0.0059	0.79	0.1341	0.0018	2034	44	1920	28	2152	23	89
CK3_019	111	48	0.90	9.895	0.237	0.4323	0.0078	0.76	0.1660	0.0026	2425	58	2316	35	2518	26	92
CK3_020	245	121	0.35	11.662	0.253	0.4910	0.0084	0.79	0.1723	0.0023	2578	56	2575	37	2580	22	100
CK3_021	42	13	1.28	5.363	0.195	0.2959	0.0067	0.62	0.1314	0.0038	1879	68	1671	33	2117	50	79
CK3_022	33	9	1.00	4.510	0.175	0.2601	0.0061	0.60	0.1258	0.0039	1733	67	1491	31	2039	54	73
CK3_023	48	18	0.83	6.411	0.210	0.3699	0.0078	0.65	0.1257	0.0031	2034	67	2029	37	2039	44	100
CK3_024	422	155	0.71	7.571	0.162	0.3673	0.0062	0.79	0.1495	0.0020	2181	47	2016	29	2340	22	86
CK3_025	157	59	1.79	6.654	0.229	0.3747	0.0082	0.64	0.1288	0.0034	2066	71	2051	39	2082	46	99
CK3_027	58	27	0.67	10.288	0.288	0.4661	0.0092	0.70	0.1601	0.0032	2461	69	2466	40	2457	33	100
CK3_028	190	72	0.57	6.726	0.160	0.3799	0.0067	0.74	0.1284	0.0021	2076	49	2076	31	2077	28	100
CK3_029	216	98	0.54	10.146	0.228	0.4540	0.0078	0.77	0.1621	0.0023	2448	55	2413	35	2478	24	97
CK3_030	319	121	0.56	6.689	0.148	0.3790	0.0064	0.77	0.1280	0.0018	2071	46	2072	30	2071	25	100
CK3_031	285	107	0.49	6.626	0.151	0.3777	0.0065	0.76	0.1273	0.0019	2063	47	2065	30	2060	26	100
CK3_032	146	59	0.30	7.534	0.183	0.4020	0.0072	0.73	0.1359	0.0022	2177	53	2178	33	2176	29	100
CK3_033	59	30	0.87	12.615	0.373	0.5091	0.0105	0.70	0.1797	0.0038	2651	78	2653	45	2650	35	100
CK3_034	125	60	0.35	10.909	0.264	0.4769	0.0086	0.74	0.1659	0.0027	2515	61	2514	37	2517	27	100
CK3_035	247	74	0.99	4.827	0.113	0.3014	0.0052	0.74	0.1162	0.0018	1790	42	1698	26	1898	28	89

				RATIOS							AGES [Ma]						Conc.
Analysis	**U [ppm][a]**	**Pb [ppm][a]**	**Th/U[a]**	**$^{207}Pb/^{235}U$[b]**	**2 σ[d]**	**$^{206}Pb/^{238}U$[b]**	**2 σ[d]**	**rho[c]**	**$^{207}Pb/^{206}Pb$[e]**	**2 σ[d]**	**$^{207}Pb/^{235}U$**	**2 σ**	**$^{206}Pb/^{238}U$**	**2 σ**	**$^{207}Pb/^{206}Pb$**	**2 σ**	**%**
CK3_036	279	80	2.42	4.585	0.107	0.2874	0.0050	0.74	0.1157	0.0018	1747	41	1629	25	1891	28	86
CK3_037	180	101	0.38	16.070	0.368	0.5611	0.0098	0.77	0.2077	0.0031	2881	66	2871	41	2888	24	99
CK3_038	372	135	0.51	6.097	0.136	0.3632	0.0062	0.76	0.1218	0.0018	1990	44	1997	29	1982	26	101
CK3_039	81	41	1.11	12.229	0.370	0.5005	0.0104	0.69	0.1772	0.0039	2622	79	2616	45	2627	36	100
CK3_040	53	20	1.23	6.770	0.220	0.3814	0.0080	0.64	0.1287	0.0032	2082	68	2083	37	2081	44	100
CK3_041	243	87	0.95	8.074	0.185	0.3568	0.0061	0.75	0.1641	0.0025	2239	51	1967	29	2498	25	79
CK3_042	17	6	0.87	6.627	0.441	0.3770	0.0138	0.55	0.1275	0.0071	2063	137	2062	65	2064	96	100
CK3_043	127	45	0.65	5.797	0.149	0.3516	0.0063	0.70	0.1196	0.0022	1946	50	1942	30	1950	32	100
CK3_044	61	24	0.58	7.363	0.219	0.3981	0.0079	0.67	0.1342	0.0030	2156	64	2160	36	2153	38	100
CK3_045	77	29	0.51	6.694	0.197	0.3791	0.0074	0.67	0.1281	0.0028	2072	61	2072	35	2072	39	100
CK3_046	173	87	0.84	12.371	0.355	0.5024	0.0101	0.70	0.1786	0.0037	2633	76	2624	43	2640	34	99
CK3_047	182	86	0.45	10.647	0.248	0.4710	0.0082	0.75	0.1640	0.0025	2493	58	2488	36	2497	26	100
CK3_048	729	210	0.73	5.525	0.121	0.2877	0.0048	0.76	0.1393	0.0020	1905	42	1630	24	2218	25	73
CK3_049	205	79	0.65	6.870	0.163	0.3846	0.0067	0.73	0.1296	0.0021	2095	50	2098	31	2092	28	100
CK3_050	198	75	0.62	6.724	0.165	0.3796	0.0067	0.72	0.1285	0.0022	2076	51	2075	31	2077	30	100
CK3_051	191	73	0.48	6.722	0.164	0.3796	0.0067	0.72	0.1284	0.0022	2076	51	2075	31	2077	30	100
CK3_052	274	103	0.53	6.631	0.158	0.3765	0.0065	0.73	0.1277	0.0021	2064	49	2060	31	2067	29	100
CK3_053	137	66	0.60	11.177	0.281	0.4822	0.0087	0.72	0.1681	0.0029	2538	64	2537	38	2539	29	100
CK3_054	131	51	1.29	7.405	0.271	0.3858	0.0088	0.62	0.1392	0.0040	2162	79	2104	41	2217	49	95
CK3_055	46	26	0.34	16.270	0.474	0.5658	0.0116	0.70	0.2086	0.0043	2893	84	2891	48	2894	34	100

				RATIOS							AGES [Ma]						Conc.
Analysis	**U [ppm][a]**	**Pb [ppm][a]**	**Th/U[a]**	**$^{207}Pb/^{235}U$[b]**	**2 σ[d]**	**$^{206}Pb/^{238}U$[b]**	**2 σ[d]**	**rho[c]**	**$^{207}Pb/^{206}Pb$[e]**	**2 σ[d]**	**$^{207}Pb/^{235}U$**	**2 σ**	**$^{206}Pb/^{238}U$**	**2 σ**	**$^{207}Pb/^{206}Pb$**	**2 σ**	**%**
CK3_056	79	44	1.05	15.582	0.401	0.5550	0.0103	0.72	0.2036	0.0036	2852	73	2846	43	2856	29	100
CK3_057	167	77	0.99	10.928	0.286	0.4622	0.0085	0.71	0.1715	0.0032	2517	66	2449	38	2572	31	95
CK3_058	454	128	0.52	6.820	0.157	0.2818	0.0048	0.74	0.1755	0.0027	2088	48	1601	24	2611	26	61
CK3_059	189	67	1.00	6.269	0.156	0.3534	0.0062	0.71	0.1287	0.0023	2014	50	1951	30	2080	31	94
CK3_060	191	58	4.17	4.855	0.124	0.3028	0.0054	0.69	0.1163	0.0021	1795	46	1705	26	1900	33	90
CK3_061	294	54	1.44	3.482	0.124	0.1832	0.0039	0.61	0.1378	0.0039	1523	54	1085	21	2200	49	49
CK3_062	246	94	0.77	6.767	0.167	0.3805	0.0066	0.71	0.1290	0.0022	2081	51	2078	31	2084	30	100
CK3_063	89	33	0.79	6.199	0.187	0.3640	0.0071	0.65	0.1235	0.0028	2004	61	2001	34	2008	41	100
CK3_064	211	80	0.68	6.719	0.166	0.3799	0.0066	0.71	0.1283	0.0022	2075	51	2076	31	2075	31	100
CK3_065	695	183	1.13	5.960	0.137	0.2633	0.0044	0.73	0.1642	0.0026	1970	45	1507	23	2499	26	60
CK3_066	174	65	1.65	6.630	0.221	0.3756	0.0079	0.63	0.1280	0.0033	2063	69	2056	37	2071	45	99
CK3_067	173	66	0.68	6.856	0.174	0.3837	0.0068	0.70	0.1296	0.0024	2093	53	2094	32	2092	32	100
CK3_068	186	71	0.63	6.751	0.172	0.3796	0.0067	0.69	0.1290	0.0024	2079	53	2075	31	2084	32	100
CK3_069	116	55	0.32	10.861	0.278	0.4782	0.0086	0.70	0.1647	0.0030	2511	64	2519	37	2505	31	101
CK3_070	260	98	0.79	6.679	0.192	0.3776	0.0072	0.66	0.1283	0.0028	2070	59	2065	33	2075	38	100
CK3_071	132	50	0.83	6.797	0.222	0.3829	0.0079	0.63	0.1288	0.0033	2085	68	2090	37	2081	45	100
CK3_072	319	130	0.84	9.619	0.233	0.4059	0.0069	0.70	0.1719	0.0030	2399	58	2196	32	2576	29	85
CK3_073	141	48	0.49	5.462	0.149	0.3411	0.0062	0.66	0.1161	0.0024	1895	52	1892	30	1898	37	100
CK3_074	145	56	0.85	6.804	0.183	0.3823	0.0069	0.67	0.1291	0.0026	2086	56	2087	32	2085	35	100
CK3_075	124	47	0.62	6.824	0.199	0.3815	0.0072	0.65	0.1297	0.0029	2089	61	2083	34	2094	39	99

				RATIOS							AGES [Ma]						Conc.
Analysis	**U [ppm][a]**	**Pb [ppm][a]**	**Th/U[a]**	**$^{207}Pb/^{235}U$[b]**	**2 σ[d]**	**$^{206}Pb/^{238}U$[b]**	**2 σ[d]**	**rho[c]**	**$^{207}Pb/^{206}Pb$[e]**	**2 σ[d]**	**$^{207}Pb/^{235}U$**	**2 σ**	**$^{206}Pb/^{238}U$**	**2 σ**	**$^{207}Pb/^{206}Pb$**	**2 σ**	**%**
CK3_076	213	81	0.57	6.782	0.181	0.3810	0.0068	0.67	0.1291	0.0026	2083	56	2081	32	2086	35	100
CK3_077	149	83	0.55	16.438	0.516	0.5575	0.0117	0.67	0.2139	0.0050	2903	91	2856	49	2935	37	97
CK3_079	107	38	0.67	6.256	0.224	0.3512	0.0076	0.60	0.1292	0.0037	2012	72	1940	36	2087	50	93
CK3_080	99	32	0.68	6.122	0.178	0.3260	0.0061	0.65	0.1362	0.0030	1993	58	1819	30	2180	38	83
CK6_001	103	36	0.89	5.637	0.150	0.3457	0.0064	0.70	0.1183	0.0022	1922	51	1914	31	1930	34	99
CK6_002	347	107	1.43	7.295	0.155	0.3084	0.0052	0.80	0.1715	0.0022	2148	46	1733	26	2573	21	67
CK6_003	183	65	0.46	5.908	0.136	0.3549	0.0062	0.75	0.1207	0.0018	1962	45	1958	29	1967	27	100
CK6_004	58	27	1.08	10.834	0.552	0.4724	0.0148	0.62	0.1663	0.0067	2509	128	2494	65	2521	67	99
CK6_005	38	14	0.89	6.091	0.206	0.3602	0.0077	0.64	0.1227	0.0032	1989	67	1983	37	1996	46	99
CK6_006	116	39	0.71	5.486	0.140	0.3408	0.0062	0.71	0.1168	0.0021	1898	49	1890	30	1907	32	99
CK6_007	233	88	0.34	6.636	0.166	0.3774	0.0069	0.73	0.1275	0.0022	2064	52	2064	32	2064	30	100
CK6_008	242	83	0.56	8.249	0.180	0.3432	0.0059	0.78	0.1743	0.0024	2259	49	1902	28	2600	22	73
CK6_009	127	48	0.63	6.863	0.164	0.3828	0.0068	0.74	0.1300	0.0021	2094	50	2089	32	2098	28	100
CK6_011	465	131	1.21	6.281	0.133	0.2813	0.0047	0.79	0.1619	0.0021	2016	43	1598	24	2476	22	65
CK6_012	79	38	0.76	11.113	0.289	0.4802	0.0091	0.73	0.1679	0.0030	2533	66	2528	40	2537	30	100
CK6_013	295	77	0.73	4.611	0.103	0.2606	0.0045	0.77	0.1283	0.0018	1751	39	1493	23	2075	25	72
CK6_014	208	114	0.63	15.237	0.343	0.5508	0.0097	0.78	0.2006	0.0028	2830	64	2829	40	2831	23	100
CK6_015	53	21	0.50	7.138	0.262	0.3889	0.0089	0.63	0.1331	0.0038	2129	78	2118	42	2140	49	99
CK6_016	200	73	0.50	6.202	0.140	0.3657	0.0063	0.76	0.1230	0.0018	2005	45	2009	30	2000	26	100
CK6_017	218	79	0.53	6.152	0.137	0.3637	0.0062	0.77	0.1227	0.0018	1998	45	2000	29	1995	25	100

				RATIOS							AGES [Ma]						Conc.
Analysis	**U [ppm][a]**	**Pb [ppm][a]**	**Th/U[a]**	**$^{207}Pb/^{235}U$[b]**	**2 σ[d]**	**$^{206}Pb/^{238}U$[b]**	**2 σ[d]**	**rho[c]**	**$^{207}Pb/^{206}Pb$[e]**	**2 σ[d]**	**$^{207}Pb/^{235}U$**	**2 σ**	**$^{206}Pb/^{238}U$**	**2 σ**	**$^{207}Pb/^{206}Pb$**	**2 σ**	**%**
CK6_018	99	36	0.33	6.142	0.157	0.3638	0.0066	0.71	0.1225	0.0022	1996	51	2000	31	1992	32	100
CK6_019	681	141	1.48	3.581	0.076	0.2078	0.0035	0.79	0.1250	0.0016	1545	33	1217	18	2029	23	60
CK6_020	660	138	0.83	3.670	0.078	0.2099	0.0035	0.79	0.1268	0.0017	1565	33	1228	19	2055	23	60
CK6_021	195	72	1.23	8.614	0.192	0.3683	0.0064	0.77	0.1696	0.0024	2298	51	2021	30	2554	24	79
CK6_022	128	65	0.53	12.754	0.297	0.5112	0.0091	0.76	0.1810	0.0027	2662	62	2662	39	2662	25	100
CK6_023	791	109	0.85	2.399	0.052	0.1378	0.0023	0.77	0.1263	0.0017	1242	27	833	13	2046	24	41
CK6_024	246	73	0.83	4.828	0.110	0.2984	0.0051	0.75	0.1174	0.0018	1790	41	1683	25	1916	27	88
CK6_025	161	115	0.39	29.590	0.655	0.7135	0.0126	0.79	0.3008	0.0040	3473	77	3472	47	3474	21	100
CK6_026	143	73	0.81	12.620	0.289	0.5089	0.0089	0.77	0.1799	0.0026	2652	61	2652	38	2652	24	100
CK6_027	86	30	1.04	5.653	0.162	0.3480	0.0067	0.67	0.1178	0.0025	1924	55	1925	32	1923	38	100
CK6_028	105	35	0.63	5.261	0.138	0.3343	0.0061	0.70	0.1141	0.0021	1862	49	1859	30	1866	34	100
CK6_029	361	117	1.55	7.165	0.169	0.3248	0.0057	0.75	0.1600	0.0025	2132	50	1813	28	2456	26	74
CK6_030	122	46	0.52	6.658	0.164	0.3777	0.0067	0.73	0.1279	0.0022	2067	51	2065	32	2069	30	100
CK6_031	120	42	0.46	6.828	0.168	0.3529	0.0063	0.73	0.1403	0.0024	2089	52	1949	30	2231	29	87
CK6_032	224	105	0.61	10.540	0.231	0.4682	0.0080	0.78	0.1633	0.0023	2483	54	2476	35	2490	23	99
CK6_033	74	25	1.16	5.417	0.159	0.3388	0.0066	0.66	0.1160	0.0026	1888	55	1881	32	1895	39	99
CK6_034	169	64	0.37	6.660	0.160	0.3775	0.0066	0.73	0.1280	0.0021	2067	50	2065	31	2070	28	100
CK6_035	294	94	0.70	5.712	0.127	0.3179	0.0054	0.76	0.1303	0.0019	1933	43	1779	26	2102	25	85
CK6_036	173	66	0.72	6.733	0.175	0.3792	0.0070	0.70	0.1288	0.0024	2077	54	2072	33	2081	32	100
CK6_037	310	94	1.00	5.442	0.121	0.3027	0.0051	0.76	0.1304	0.0019	1891	42	1705	25	2103	25	81

				RATIOS							AGES [Ma]						Conc.
Analysis	**U [ppm][a]**	**Pb [ppm][a]**	**Th/U[a]**	**$^{207}Pb/^{235}U$[b]**	**2 σ[d]**	**$^{206}Pb/^{238}U$[b]**	**2 σ[d]**	**rho[c]**	**$^{207}Pb/^{206}Pb$[e]**	**2 σ[d]**	**$^{207}Pb/^{235}U$**	**2 σ**	**$^{206}Pb/^{238}U$**	**2 σ**	**$^{207}Pb/^{206}Pb$**	**2 σ**	**%**
CK6_038	114	44	0.48	7.052	0.175	0.3889	0.0070	0.72	0.1315	0.0023	2118	53	2118	32	2118	30	100
CK6_039	139	47	0.74	5.311	0.131	0.3364	0.0060	0.72	0.1145	0.0020	1871	46	1869	29	1872	31	100
CK6_040	82	47	0.40	16.598	0.400	0.5719	0.0104	0.75	0.2105	0.0033	2912	70	2916	43	2909	26	100
CK6_041	142	70	1.00	11.554	0.281	0.4923	0.0089	0.74	0.1702	0.0028	2569	62	2581	38	2560	27	101
CK6_042	159	60	0.64	6.697	0.159	0.3794	0.0066	0.74	0.1280	0.0021	2072	49	2074	31	2071	28	100
CK6_043	52	27	0.32	12.611	0.346	0.5082	0.0099	0.71	0.1800	0.0035	2651	73	2649	42	2653	32	100
CK6_044	126	40	0.21	4.729	0.122	0.3157	0.0057	0.70	0.1086	0.0020	1772	46	1769	28	1777	34	100
CK6_045	97	50	0.89	13.116	0.325	0.5161	0.0094	0.74	0.1843	0.0031	2688	67	2682	40	2692	27	100
CK6_046	107	31	0.51	4.747	0.132	0.2948	0.0055	0.67	0.1168	0.0024	1776	49	1666	27	1908	37	87
CK6_047	84	32	0.81	6.773	0.202	0.3805	0.0075	0.66	0.1291	0.0029	2082	62	2079	35	2086	39	100
CK6_048	23	8	0.66	5.446	0.235	0.3399	0.0085	0.58	0.1162	0.0041	1892	81	1886	41	1899	63	99
CK6_049	22	7	1.43	5.148	0.220	0.3309	0.0082	0.58	0.1129	0.0039	1844	79	1843	40	1846	63	100
CK6_050	197	56	0.99	4.766	0.117	0.2863	0.0050	0.72	0.1207	0.0021	1779	44	1623	25	1967	30	83
CK6_051	115	39	0.99	5.352	0.172	0.3373	0.0069	0.63	0.1151	0.0029	1877	60	1874	33	1881	44	100
CK6_052	405	114	1.22	5.305	0.118	0.2808	0.0047	0.76	0.1370	0.0020	1870	42	1595	24	2190	25	73
CK6_053	361	94	0.94	4.383	0.100	0.2598	0.0044	0.74	0.1224	0.0019	1709	39	1489	23	1991	27	75
CK6_054	83	28	0.74	5.406	0.157	0.3387	0.0065	0.66	0.1158	0.0025	1886	55	1881	31	1892	39	99
CK6_055	114	36	1.14	4.717	0.127	0.3160	0.0058	0.68	0.1083	0.0021	1770	48	1770	28	1770	36	100
CK6_056	83	29	0.63	5.930	0.164	0.3566	0.0067	0.68	0.1206	0.0024	1966	54	1966	32	1966	36	100
CK6_057	151	76	0.32	12.385	0.289	0.5040	0.0088	0.75	0.1782	0.0028	2634	61	2631	38	2636	26	100

				RATIOS							AGES [Ma]						Conc.
Analysis	**U [ppm][a]**	**Pb [ppm][a]**	**Th/U[a]**	**$^{207}Pb/^{235}U$[b]**	**2 σ[d]**	**$^{206}Pb/^{238}U$[b]**	**2 σ[d]**	**rho[c]**	**$^{207}Pb/^{206}Pb$[e]**	**2 σ[d]**	**$^{207}Pb/^{235}U$**	**2 σ**	**$^{206}Pb/^{238}U$**	**2 σ**	**$^{207}Pb/^{206}Pb$**	**2 σ**	**%**
CK6_058	313	126	0.77	9.580	0.218	0.4010	0.0068	0.75	0.1733	0.0026	2395	54	2174	31	2590	25	84
CK6_059	258	68	0.41	3.906	0.109	0.2620	0.0049	0.66	0.1081	0.0023	1615	45	1500	25	1768	38	85
CK6_060	63	23	1.40	6.565	0.241	0.3752	0.0085	0.61	0.1269	0.0037	2055	76	2054	40	2056	51	100
CK6_061	49	25	0.54	13.109	0.376	0.5145	0.0103	0.70	0.1848	0.0038	2688	77	2676	44	2696	34	99
CK6_062	191	72	0.75	6.585	0.158	0.3774	0.0066	0.72	0.1266	0.0021	2057	49	2064	31	2051	29	101
CK6_063	79	36	0.66	12.114	0.313	0.4570	0.0085	0.72	0.1923	0.0035	2613	67	2426	37	2762	29	88
CK6_064	82	28	0.67	5.600	0.243	0.3412	0.0086	0.58	0.1190	0.0042	1916	83	1892	41	1942	63	97
CK6_065	112	53	0.32	10.790	0.266	0.4753	0.0085	0.72	0.1647	0.0028	2505	62	2507	37	2504	28	100
CK6_066	77	29	0.45	7.048	0.194	0.3817	0.0072	0.68	0.1339	0.0027	2118	58	2084	33	2150	35	97
CK6_067	163	53	0.51	5.028	0.130	0.3272	0.0058	0.69	0.1114	0.0021	1824	47	1825	28	1823	34	100
CK6_068	270	76	1.34	4.963	0.119	0.2806	0.0048	0.72	0.1283	0.0021	1813	44	1595	24	2074	29	77
CK6_069	254	72	1.15	4.884	0.118	0.2823	0.0049	0.72	0.1255	0.0021	1799	43	1603	24	2036	30	79
CK6_070	79	29	1.59	6.302	0.177	0.3651	0.0069	0.67	0.1252	0.0026	2019	57	2006	32	2032	36	99
CK6_071	146	74	0.72	12.716	0.315	0.5086	0.0091	0.72	0.1813	0.0031	2659	66	2651	39	2665	28	99
CK6_072	373	139	0.79	8.819	0.203	0.3726	0.0063	0.74	0.1717	0.0027	2319	53	2042	30	2574	26	79
CK6_073	249	77	0.62	5.578	0.143	0.3078	0.0055	0.69	0.1314	0.0024	1913	49	1730	27	2117	32	82
CK6_074	176	86	0.41	11.556	0.277	0.4889	0.0085	0.73	0.1714	0.0028	2569	61	2566	37	2571	27	100
CK6_075	256	79	0.54	5.349	0.130	0.3090	0.0053	0.71	0.1256	0.0021	1877	45	1736	26	2037	30	85
CK6_076	150	73	0.91	11.531	0.286	0.4887	0.0087	0.72	0.1711	0.0030	2567	64	2565	37	2569	29	100
CK6_077	206	63	0.42	4.538	0.154	0.3070	0.0063	0.61	0.1072	0.0029	1738	59	1726	31	1753	49	98

				RATIOS							AGES [Ma]						Conc.
Analysis	**U [ppm][a]**	**Pb [ppm][a]**	**Th/U[a]**	**$^{207}Pb/^{235}U$[b]**	**2 σ[d]**	**$^{206}Pb/^{238}U$[b]**	**2 σ[d]**	**rho[c]**	**$^{207}Pb/^{206}Pb$[e]**	**2 σ[d]**	**$^{207}Pb/^{235}U$**	**2 σ**	**$^{206}Pb/^{238}U$**	**2 σ**	**$^{207}Pb/^{206}Pb$**	**2 σ**	**%**
CK6_078	248	137	0.58	15.240	0.353	0.5528	0.0094	0.73	0.1999	0.0031	2830	66	2837	39	2826	26	100
CK6_079	151	55	0.48	6.202	0.159	0.3650	0.0065	0.69	0.1232	0.0023	2005	51	2006	31	2004	33	100
CK6_080	482	144	0.90	5.516	0.129	0.2993	0.0051	0.72	0.1337	0.0022	1903	45	1688	25	2147	28	79
CK6_081	858	165	1.51	4.311	0.101	0.1925	0.0033	0.72	0.1624	0.0026	1695	40	1135	18	2481	27	46
CK6_082	156	56	0.49	6.062	0.156	0.3612	0.0064	0.69	0.1217	0.0023	1985	51	1988	30	1982	33	100
CK6_083	215	65	0.99	5.558	0.139	0.3044	0.0053	0.70	0.1324	0.0024	1910	48	1713	26	2130	31	80
CK6_084	371	98	1.16	4.604	0.111	0.2635	0.0045	0.71	0.1267	0.0022	1750	42	1508	23	2053	30	73
CK6_085	245	78	0.73	5.720	0.141	0.3177	0.0055	0.70	0.1306	0.0023	1934	48	1778	27	2106	31	84
CK6_086	67	33	0.58	11.637	0.322	0.4914	0.0093	0.68	0.1718	0.0035	2576	71	2577	40	2575	34	100
CK6_087	268	80	0.53	6.753	0.168	0.2967	0.0052	0.70	0.1651	0.0029	2080	52	1675	26	2508	30	67
CK6_088	114	41	0.86	5.953	0.192	0.3564	0.0072	0.63	0.1211	0.0030	1969	63	1965	34	1973	44	100
CK6_089	87	29	0.58	5.316	0.157	0.3360	0.0064	0.64	0.1148	0.0026	1871	55	1867	31	1876	40	100
CK6_090	65	41	0.62	21.257	0.610	0.6297	0.0126	0.70	0.2448	0.0050	3150	90	3148	50	3152	32	100
CK6_091	64	24	0.29	6.599	0.199	0.3750	0.0073	0.64	0.1276	0.0029	2059	62	2053	34	2066	40	99
CK6_092	64	34	0.38	14.395	0.406	0.5379	0.0104	0.68	0.1941	0.0040	2776	78	2774	44	2777	34	100
CK6_093	67	34	0.64	12.388	0.350	0.5038	0.0097	0.68	0.1783	0.0037	2634	74	2630	41	2637	34	100
CK6_094	148	100	0.19	25.330	0.622	0.6728	0.0118	0.71	0.2731	0.0047	3321	82	3317	45	3324	27	100
CK6_095	193	61	0.59	4.743	0.126	0.3156	0.0056	0.67	0.1090	0.0022	1775	47	1768	27	1783	36	99
CK6_096	119	41	0.56	5.645	0.166	0.3460	0.0066	0.64	0.1183	0.0027	1923	57	1916	31	1931	40	99
CK6_097	85	33	0.26	7.044	0.266	0.3878	0.0088	0.60	0.1318	0.0040	2117	80	2113	41	2121	52	100

				RATIOS							AGES [Ma]						Conc.
Analysis	**U [ppm][a]**	**Pb [ppm][a]**	**Th/U[a]**	**$^{207}Pb/^{235}U$[b]**	**2 σ[d]**	**$^{206}Pb/^{238}U$[b]**	**2 σ[d]**	**rho[c]**	**$^{207}Pb/^{206}Pb$[c]**	**2 σ[d]**	**$^{207}Pb/^{235}U$**	**2 σ**	**$^{206}Pb/^{238}U$**	**2 σ**	**$^{207}Pb/^{206}Pb$**	**2 σ**	**%**
CK6_098	270	113	0.78	10.426	0.264	0.4166	0.0073	0.69	0.1815	0.0033	2473	63	2245	33	2667	30	84
CK6_099	150	57	0.45	6.668	0.187	0.3785	0.0070	0.66	0.1278	0.0027	2068	58	2069	33	2068	37	100
CK6_100	116	55	0.37	11.020	0.291	0.4786	0.0086	0.68	0.1670	0.0032	2525	67	2521	38	2528	32	100
CK7_001	217	68	0.12	4.690	0.112	0.3149	0.0057	0.76	0.1080	0.0017	1765	42	1765	28	1766	28	100
CK7_002	130	50	0.96	6.826	0.213	0.3837	0.0081	0.68	0.1290	0.0030	2089	65	2094	38	2085	40	100
CK7_003	64	23	0.47	5.955	0.179	0.3566	0.0073	0.68	0.1211	0.0027	1969	59	1966	35	1973	39	100
CK7_004	225	107	0.42	10.741	0.231	0.4762	0.0084	0.82	0.1636	0.0020	2501	54	2511	37	2493	21	101
CK7_005	159	55	0.76	5.543	0.142	0.3441	0.0065	0.73	0.1168	0.0020	1907	49	1906	31	1908	31	100
CK7_006	191	69	1.17	5.996	0.140	0.3593	0.0065	0.78	0.1211	0.0018	1975	46	1979	31	1972	26	100
CK7_009	91	31	0.68	5.545	0.179	0.3437	0.0073	0.66	0.1170	0.0028	1908	61	1904	35	1911	43	100
CK7_010	57	21	0.45	6.041	0.177	0.3605	0.0073	0.69	0.1215	0.0026	1982	58	1985	34	1979	38	100
CK7_011	285	83	0.89	5.294	0.123	0.2913	0.0052	0.77	0.1318	0.0019	1868	43	1648	26	2122	26	78
CK7_012	144	66	0.85	10.364	0.415	0.4612	0.0120	0.65	0.1630	0.0050	2468	99	2445	53	2487	51	98
CK7_013	377	133	0.54	8.648	0.198	0.3539	0.0064	0.79	0.1772	0.0025	2302	53	1953	30	2627	23	74
CK7_014	221	104	0.46	10.838	0.322	0.4716	0.0100	0.71	0.1667	0.0035	2509	75	2491	44	2525	35	99
CK7_015	141	48	1.16	5.353	0.130	0.3385	0.0062	0.75	0.1147	0.0018	1877	46	1880	30	1875	29	100
CK7_016	99	38	0.32	7.075	0.178	0.3851	0.0072	0.74	0.1333	0.0022	2121	53	2100	34	2141	29	98
CK7_017	138	44	0.12	4.839	0.144	0.3201	0.0064	0.67	0.1096	0.0024	1792	53	1790	31	1793	40	100
CK7_018	312	116	0.35	9.249	0.196	0.3728	0.0065	0.82	0.1800	0.0022	2363	50	2042	30	2653	20	77
CK7_019	89	35	0.55	7.198	0.183	0.3926	0.0074	0.74	0.1330	0.0023	2136	54	2135	34	2138	30	100

				RATIOS							AGES [Ma]						Conc.
Analysis	**U [ppm][a]**	**Pb [ppm][a]**	**Th/U[a]**	**$^{207}Pb/^{235}U$[b]**	**2 σ[d]**	**$^{206}Pb/^{238}U$[b]**	**2 σ[d]**	**rho[c]**	**$^{207}Pb/^{206}Pb$[e]**	**2 σ[d]**	**$^{207}Pb/^{235}U$**	**2 σ**	**$^{206}Pb/^{238}U$**	**2 σ**	**$^{207}Pb/^{206}Pb$**	**2 σ**	**%**
CK7_020	74	37	0.70	12.295	0.376	0.5015	0.0109	0.71	0.1778	0.0038	2627	80	2620	47	2632	36	100
CK7_021	114	39	0.76	5.519	0.142	0.3422	0.0064	0.73	0.1170	0.0021	1904	49	1897	31	1911	31	99
CK7_022	1092	194	0.51	4.035	0.100	0.1772	0.0033	0.75	0.1652	0.0027	1641	41	1052	18	2509	28	42
CK7_023	69	23	0.72	6.077	0.175	0.3300	0.0066	0.69	0.1336	0.0028	1987	57	1839	32	2145	36	86
CK7_024	247	97	0.43	7.214	0.158	0.3931	0.0069	0.80	0.1331	0.0018	2138	47	2137	32	2140	23	100
CK7_025	149	53	0.46	5.896	0.140	0.3547	0.0064	0.76	0.1206	0.0019	1961	47	1957	30	1965	27	100
CK7_026	58	20	0.73	5.264	0.170	0.3348	0.0070	0.65	0.1141	0.0028	1863	60	1862	34	1865	44	100
CK7_027	23	12	0.74	13.152	0.593	0.5181	0.0152	0.65	0.1841	0.0063	2691	121	2691	64	2690	56	100
CK7_028	155	50	0.34	4.902	0.143	0.3206	0.0064	0.68	0.1109	0.0024	1803	53	1793	31	1814	39	99
CK7_029	47	24	0.68	12.487	0.341	0.5047	0.0101	0.73	0.1794	0.0033	2642	72	2634	43	2648	30	99
CK7_030	369	87	0.44	4.230	0.093	0.2350	0.0041	0.79	0.1306	0.0018	1680	37	1361	21	2105	24	65
CK7_031	133	47	0.42	5.846	0.150	0.3541	0.0066	0.73	0.1197	0.0021	1953	50	1954	31	1952	31	100
CK7_032	112	59	0.53	13.570	0.320	0.5226	0.0096	0.78	0.1883	0.0028	2720	64	2710	41	2728	24	99
CK7_033	452	237	0.46	13.462	0.280	0.5247	0.0090	0.82	0.1861	0.0022	2713	57	2719	38	2708	19	100
CK7_034	147	54	0.74	6.178	0.151	0.3637	0.0066	0.75	0.1232	0.0020	2001	49	2000	31	2003	29	100
CK7_035	223	79	0.46	5.881	0.134	0.3553	0.0063	0.78	0.1200	0.0017	1958	44	1960	30	1957	25	100
CK7_036	92	31	0.68	5.408	0.144	0.3400	0.0064	0.71	0.1154	0.0022	1886	50	1887	31	1886	33	100
CK7_037	114	41	0.73	6.051	0.153	0.3596	0.0067	0.73	0.1220	0.0021	1983	50	1980	32	1986	31	100
CK7_038	283	76	0.52	4.822	0.126	0.2686	0.0050	0.72	0.1302	0.0024	1789	47	1534	26	2101	32	73
CK7_039	164	53	0.52	4.969	0.125	0.3227	0.0059	0.73	0.1117	0.0019	1814	46	1803	29	1827	31	99

				RATIOS							AGES [Ma]						Conc.
Analysis	**U [ppm][a]**	**Pb [ppm][a]**	**Th/U[a]**	**$^{207}Pb/^{235}U$[b]**	**2 σ[d]**	**$^{206}Pb/^{238}U$[b]**	**2 σ[d]**	**rho[c]**	**$^{207}Pb/^{206}Pb$[e]**	**2 σ[d]**	**$^{207}Pb/^{235}U$**	**2 σ**	**$^{206}Pb/^{238}U$**	**2 σ**	**$^{207}Pb/^{206}Pb$**	**2 σ**	**%**
CK7_040	126	42	0.69	5.161	0.149	0.3313	0.0065	0.68	0.1130	0.0024	1846	53	1845	31	1848	38	100
CK7_041	157	51	0.75	4.936	0.120	0.3246	0.0058	0.74	0.1103	0.0018	1808	44	1812	28	1804	29	100
CK7_042	91	30	0.95	5.175	0.139	0.3332	0.0063	0.70	0.1127	0.0022	1848	50	1854	30	1843	34	101
CK7_043	191	66	0.72	5.527	0.144	0.3436	0.0064	0.72	0.1167	0.0021	1905	50	1904	31	1906	32	100
CK7_044	46	16	0.73	6.019	0.189	0.3579	0.0074	0.66	0.1220	0.0029	1979	62	1972	35	1985	42	99
CK7_045	189	66	2.07	5.705	0.135	0.3502	0.0063	0.75	0.1182	0.0018	1932	46	1935	30	1928	28	100
CK7_046	75	27	1.15	5.948	0.164	0.3568	0.0069	0.70	0.1209	0.0024	1968	54	1967	33	1970	35	100
CK7_047	112	56	0.57	11.979	0.308	0.4970	0.0095	0.74	0.1748	0.0030	2603	67	2601	41	2604	28	100
CK7_049	188	47	0.85	3.959	0.105	0.2469	0.0046	0.70	0.1163	0.0022	1626	43	1423	24	1900	34	75
CK7_051	115	41	0.45	6.066	0.153	0.3596	0.0066	0.73	0.1224	0.0021	1985	50	1980	31	1991	31	99
CK7_052	179	59	0.84	5.941	0.140	0.3272	0.0058	0.76	0.1317	0.0020	1967	46	1825	28	2121	27	86
CK7_053	170	61	0.71	5.920	0.140	0.3569	0.0064	0.75	0.1203	0.0019	1964	47	1967	30	1961	28	100
CK7_054	163	59	0.38	6.124	0.145	0.3614	0.0064	0.75	0.1229	0.0019	1994	47	1989	30	1999	28	99
CK7_055	154	77	0.58	14.082	0.322	0.4994	0.0089	0.78	0.2045	0.0029	2755	63	2611	38	2863	23	91
CK7_056	124	42	0.59	5.347	0.137	0.3381	0.0062	0.72	0.1147	0.0021	1876	48	1878	30	1875	32	100
CK7_057	275	72	0.60	4.883	0.142	0.2631	0.0052	0.68	0.1346	0.0029	1799	52	1505	27	2159	37	70
CK7_058	130	62	0.29	10.721	0.250	0.4734	0.0085	0.77	0.1643	0.0025	2499	58	2498	37	2500	25	100
CK7_059	45	16	0.55	5.701	0.186	0.3496	0.0073	0.65	0.1183	0.0029	1932	63	1933	35	1931	44	100
CK7_060	249	89	0.39	9.203	0.206	0.3599	0.0063	0.78	0.1855	0.0026	2358	53	1982	30	2703	23	73
CK7_061	118	42	0.60	5.978	0.152	0.3574	0.0066	0.72	0.1213	0.0021	1973	50	1970	31	1976	31	100

				RATIOS							AGES [Ma]						Conc.
Analysis	**U [ppm][a]**	**Pb [ppm][a]**	**Th/U[a]**	**$^{207}Pb/^{235}U$[b]**	**2 σ[d]**	**$^{206}Pb/^{238}U$[b]**	**2 σ[d]**	**rho[c]**	**$^{207}Pb/^{206}Pb$[e]**	**2 σ[d]**	**$^{207}Pb/^{235}U$**	**2 σ**	**$^{206}Pb/^{238}U$**	**2 σ**	**$^{207}Pb/^{206}Pb$**	**2 σ**	**%**
CK7_062	283	86	0.60	5.024	0.127	0.3025	0.0055	0.72	0.1205	0.0021	1823	46	1704	27	1963	31	87
CK7_063	356	101	0.62	5.241	0.128	0.2822	0.0051	0.74	0.1347	0.0022	1859	45	1602	25	2160	29	74
CK7_064	164	59	0.39	5.943	0.144	0.3579	0.0064	0.74	0.1205	0.0020	1968	48	1972	30	1963	29	100
CK7_065	167	52	3.23	5.718	0.141	0.3144	0.0057	0.73	0.1319	0.0022	1934	48	1763	28	2123	29	83
CK7_066	540	127	0.68	4.403	0.108	0.2354	0.0042	0.73	0.1357	0.0023	1713	42	1363	22	2173	29	63
CK7_067	277	94	0.54	5.337	0.121	0.3384	0.0059	0.76	0.1144	0.0017	1875	43	1879	28	1870	27	100
CK7_068	404	115	1.19	8.181	0.179	0.2849	0.0049	0.79	0.2083	0.0028	2251	49	1616	25	2892	22	56
CK7_070	183	93	1.22	12.525	0.281	0.5078	0.0089	0.78	0.1789	0.0025	2645	59	2647	38	2643	23	100
CK7_071	68	34	0.58	12.375	0.324	0.5048	0.0097	0.73	0.1778	0.0032	2633	69	2635	41	2632	29	100
CK7_072	116	34	1.08	4.617	0.123	0.2902	0.0054	0.70	0.1154	0.0022	1752	47	1642	27	1886	34	87
CK7_073	51	18	0.49	5.969	0.189	0.3571	0.0074	0.65	0.1212	0.0029	1971	62	1969	35	1975	43	100
CK7_074	107	45	0.54	10.636	0.291	0.4152	0.0081	0.71	0.1858	0.0036	2492	68	2239	37	2705	31	83
CK7_075	106	31	0.97	4.377	0.122	0.2897	0.0055	0.68	0.1096	0.0022	1708	47	1640	27	1792	37	92
CK7_076	182	62	0.87	5.397	0.135	0.3388	0.0061	0.72	0.1156	0.0020	1884	47	1881	29	1889	31	100
CK7_077	41	18	0.66	8.575	0.262	0.4274	0.0088	0.68	0.1455	0.0033	2294	70	2294	40	2294	39	100
CK7_078	73	38	0.51	13.560	0.395	0.5229	0.0108	0.71	0.1881	0.0039	2720	79	2711	46	2726	34	99
CK7_079	156	56	0.88	6.073	0.148	0.3614	0.0064	0.73	0.1219	0.0020	1986	49	1989	30	1984	30	100
CK7_080	87	46	0.52	13.536	0.363	0.5265	0.0102	0.72	0.1865	0.0035	2718	73	2727	43	2711	30	101
CK7_081	178	61	0.90	5.373	0.130	0.3398	0.0060	0.73	0.1147	0.0019	1881	46	1886	29	1875	30	101
CK7_082	51	18	0.65	6.055	0.187	0.3612	0.0073	0.66	0.1216	0.0028	1984	61	1988	35	1980	41	100

				RATIOS							AGES [Ma]						Conc.
Analysis	**U [ppm][a]**	**Pb [ppm][a]**	**Th/U[a]**	**$^{207}Pb/^{235}U$[b]**	**2 σ[d]**	**$^{206}Pb/^{238}U$[b]**	**2 σ[d]**	**rho[c]**	**$^{207}Pb/^{206}Pb$[e]**	**2 σ[d]**	**$^{207}Pb/^{235}U$**	**2 σ**	**$^{206}Pb/^{238}U$**	**2 σ**	**$^{207}Pb/^{206}Pb$**	**2 σ**	**%**
CK7_083	209	103	0.37	13.344	0.300	0.4925	0.0085	0.77	0.1965	0.0028	2704	61	2581	37	2798	23	92
CK7_084	174	91	0.44	13.201	0.358	0.5192	0.0101	0.72	0.1844	0.0035	2694	73	2696	43	2693	31	100
CK7_085	146	49	0.40	5.369	0.136	0.3377	0.0061	0.71	0.1153	0.0021	1880	48	1876	29	1885	32	100
CK7_086	235	92	1.01	9.312	0.213	0.3919	0.0068	0.76	0.1723	0.0026	2369	54	2132	31	2581	25	83
CK7_087	191	68	1.03	5.943	0.144	0.3578	0.0063	0.73	0.1205	0.0020	1968	48	1972	30	1963	29	100
CK7_088	167	54	0.73	5.146	0.129	0.3257	0.0058	0.71	0.1146	0.0020	1844	46	1818	28	1873	32	97
CK7_089	157	80	0.65	12.628	0.313	0.5088	0.0093	0.74	0.1800	0.0030	2652	66	2652	40	2653	28	100
CK7_090	356	102	0.50	6.549	0.166	0.2859	0.0052	0.72	0.1662	0.0029	2053	52	1621	26	2519	30	64
CK7_091	77	40	0.43	13.611	0.348	0.5250	0.0098	0.73	0.1880	0.0033	2723	70	2721	41	2725	29	100
CK7_092	100	43	0.74	11.746	0.298	0.4319	0.0080	0.73	0.1972	0.0034	2584	66	2314	36	2803	28	83
CK7_093	75	25	0.89	5.224	0.160	0.3337	0.0066	0.65	0.1136	0.0027	1857	57	1856	32	1857	42	100
CK7_094	200	87	0.71	10.818	0.262	0.4331	0.0077	0.74	0.1812	0.0030	2508	61	2320	35	2663	27	87
CK7_095	34	11	1.02	4.986	0.193	0.3246	0.0074	0.59	0.1114	0.0035	1817	70	1812	36	1823	56	99
CK7_096	166	54	0.80	5.058	0.144	0.3278	0.0062	0.67	0.1119	0.0024	1829	52	1828	30	1831	38	100
CK7_097	86	29	0.58	5.399	0.152	0.3400	0.0064	0.67	0.1152	0.0024	1885	53	1887	31	1883	37	100
CK7_098	77	40	0.42	13.421	0.360	0.5241	0.0100	0.71	0.1857	0.0035	2710	73	2717	42	2705	31	100
CK7_099	81	38	0.60	12.199	0.411	0.4742	0.0107	0.67	0.1866	0.0047	2620	88	2502	47	2712	41	92
CK7_100	66	22	0.85	5.384	0.163	0.3399	0.0067	0.65	0.1149	0.0026	1882	57	1886	32	1878	41	100
CK7_101	84	29	0.81	5.457	0.173	0.3410	0.0069	0.64	0.1161	0.0028	1894	60	1891	33	1897	44	100
CK7_103	173	88	0.27	12.552	0.296	0.5060	0.0088	0.74	0.1799	0.0029	2647	62	2640	38	2652	26	100

				RATIOS							AGES [Ma]						Conc.
Analysis	**U [ppm][a]**	**Pb [ppm][a]**	**Th/U[a]**	**$^{207}Pb/^{235}U$[b]**	**2 σ[d]**	**$^{206}Pb/^{238}U$[b]**	**2 σ[d]**	**rho[c]**	**$^{207}Pb/^{206}Pb$[e]**	**2 σ[d]**	**$^{207}Pb/^{235}U$**	**2 σ**	**$^{206}Pb/^{238}U$**	**2 σ**	**$^{207}Pb/^{206}Pb$**	**2 σ**	**%**
CK7_104	65	23	0.89	5.862	0.175	0.3542	0.0069	0.65	0.1200	0.0027	1956	59	1955	33	1957	40	100
CK7_105	111	41	0.66	6.408	0.169	0.3726	0.0068	0.69	0.1247	0.0024	2033	54	2042	32	2025	34	101
CK7_106	111	38	0.68	5.535	0.167	0.3436	0.0067	0.65	0.1168	0.0027	1906	57	1904	32	1908	41	100
CK7_107	167	55	0.37	5.190	0.133	0.3323	0.0059	0.70	0.1133	0.0021	1851	47	1849	29	1853	33	100
CK7_108	126	60	0.41	10.666	0.269	0.4738	0.0085	0.71	0.1633	0.0029	2494	63	2500	37	2490	29	100
CK7_109	190	67	0.69	5.827	0.149	0.3551	0.0063	0.70	0.1190	0.0022	1950	50	1959	30	1942	33	101
CK7_110	248	73	0.55	5.444	0.175	0.2933	0.0060	0.64	0.1346	0.0033	1892	61	1658	30	2159	43	77
CK7_111	772	177	0.46	3.970	0.092	0.2294	0.0039	0.73	0.1255	0.0020	1628	38	1332	20	2036	28	65
CK7_112	147	50	0.95	5.387	0.142	0.3393	0.0061	0.68	0.1152	0.0022	1883	50	1883	30	1882	34	100
CK7_113	91	27	1.03	4.975	0.249	0.2907	0.0081	0.56	0.1241	0.0052	1815	91	1645	41	2016	73	82
CK7_114	14	6	0.14	7.011	0.343	0.3889	0.0110	0.58	0.1308	0.0052	2113	103	2118	51	2108	69	100
CK7_115	133	47	0.76	5.849	0.157	0.3540	0.0065	0.68	0.1198	0.0024	1954	52	1954	31	1954	35	100
CK16_001	214	76	0.59	5.852	0.160	0.3542	0.0065	0.67	0.1198	0.0024	1954	53	1955	31	1954	36	100
CK16_002	179	58	0.77	5.385	0.138	0.3253	0.0057	0.69	0.1201	0.0022	1883	48	1815	28	1957	33	93
CK16_003	134	46	0.81	5.434	0.146	0.3408	0.0062	0.67	0.1157	0.0023	1890	51	1890	30	1890	36	100
CK16_004	141	48	0.96	5.442	0.144	0.3407	0.0061	0.68	0.1159	0.0023	1891	50	1890	29	1893	35	100
CK16_005	201	77	0.40	6.857	0.172	0.3829	0.0067	0.70	0.1299	0.0023	2093	53	2090	31	2097	31	100

				RATIOS							AGES [Ma]						Conc.
Analysis	**U [ppm][a]**	**Pb [ppm][a]**	**Th/U[a]**	**$^{207}Pb/^{235}U$[b]**	**2 σ[d]**	**$^{206}Pb/^{238}U$[b]**	**2 σ[d]**	**rho[c]**	**$^{207}Pb/^{206}Pb$[e]**	**2 σ[d]**	**$^{207}Pb/^{235}U$**	**2 σ**	**$^{206}Pb/^{238}U$**	**2 σ**	**$^{207}Pb/^{206}Pb$**	**2 σ**	**%**
CK16_006	218	83	0.37	6.746	0.170	0.3797	0.0067	0.69	0.1289	0.0023	2079	52	2075	31	2083	32	100
CK16_007	309	117	0.47	6.740	0.162	0.3800	0.0065	0.71	0.1287	0.0022	2078	50	2076	30	2080	30	100
CK16_012	185	92	0.50	12.242	0.321	0.4999	0.0089	0.68	0.1776	0.0034	2623	69	2614	38	2631	32	99
CK16_013	208	104	0.42	12.051	0.319	0.5003	0.0089	0.67	0.1747	0.0034	2608	69	2615	38	2603	32	100
CK16_014	55	20	1.16	6.090	0.237	0.3619	0.0082	0.59	0.1221	0.0038	1989	77	1991	39	1987	55	100
CK16_015	151	72	0.30	10.823	0.298	0.4754	0.0086	0.66	0.1651	0.0034	2508	69	2507	38	2509	35	100
CK16_016	111	57	0.39	13.071	0.372	0.5170	0.0096	0.66	0.1834	0.0039	2685	76	2686	41	2684	35	100
CK16_018	378	102	0.61	5.580	0.156	0.2707	0.0049	0.64	0.1495	0.0032	1913	53	1544	25	2341	36	66
CK16_019	212	78	0.41	6.802	0.202	0.3689	0.0069	0.63	0.1337	0.0031	2086	62	2024	32	2147	40	94
CK19_001	67	26	0.43	6.97	0.19	0.386	0.008	0.71	0.1309	0.0025	2108	58	2106	36	2110	34	100
CK19_002	85	32	0.62	6.70	0.21	0.378	0.008	0.68	0.1286	0.0029	2073	63	2067	37	2078	39	99
CK19_003	246	112	0.22	9.81	0.21	0.455	0.008	0.81	0.1564	0.0020	2417	53	2418	36	2417	22	100
CK19_004	111	40	0.73	6.60	0.17	0.356	0.007	0.74	0.1346	0.0023	2060	52	1962	32	2159	30	91

				RATIOS							AGES [Ma]						Conc.
Analysis	**U [ppm][a]**	**Pb [ppm][a]**	**Th/U[a]**	**$^{207}Pb/^{235}U$[b]**	**2 σ[d]**	**$^{206}Pb/^{238}U$[b]**	**2 σ[d]**	**rho[c]**	**$^{207}Pb/^{206}Pb$[c]**	**2 σ[d]**	**$^{207}Pb/^{235}U$**	**2 σ**	**$^{206}Pb/^{238}U$**	**2 σ**	**$^{207}Pb/^{206}Pb$**	**2 σ**	**%**
CK19_005	115	42	0.64	6.23	0.17	0.366	0.007	0.71	0.1236	0.0024	2009	56	2009	34	2009	35	100
CK19_006	170	54	0.31	4.76	0.13	0.317	0.006	0.71	0.1090	0.0020	1778	47	1774	29	1782	34	100
CK19_007	162	59	0.20	6.13	0.15	0.363	0.007	0.77	0.1227	0.0019	1995	47	1995	31	1995	27	100
CK19_008	141	39	1.53	4.61	0.12	0.278	0.005	0.74	0.1201	0.0021	1750	44	1582	26	1958	31	81
CK19_009	100	40	0.34	7.47	0.20	0.398	0.008	0.73	0.1361	0.0025	2169	58	2160	36	2178	32	99
CK19_010	335	105	0.50	5.11	0.13	0.313	0.006	0.75	0.1185	0.0019	1838	45	1754	28	1934	29	91
CK19_011	147	75	0.48	12.59	0.29	0.508	0.009	0.79	0.1796	0.0025	2650	61	2650	40	2650	23	100
CK19_012	89	32	0.52	6.20	0.18	0.366	0.007	0.70	0.1231	0.0025	2005	57	2009	34	2001	36	100
CK19_013	222	68	0.65	4.85	0.11	0.305	0.005	0.77	0.1154	0.0017	1793	42	1715	27	1885	27	91
CK19_014	105	35	0.80	5.31	0.18	0.335	0.007	0.65	0.1148	0.0029	1870	62	1865	35	1876	46	99
CK19_015	183	62	1.08	5.34	0.13	0.337	0.006	0.75	0.1149	0.0018	1876	46	1873	30	1878	29	100
CK19_016	86	28	0.87	5.77	0.16	0.330	0.006	0.71	0.1268	0.0025	1942	54	1839	31	2054	34	90
CK19_017	351	117	0.85	5.23	0.13	0.333	0.006	0.75	0.1140	0.0019	1857	46	1851	29	1864	29	99

				RATIOS							AGES [Ma]						Conc.
Analysis	**U [ppm][a]**	**Pb [ppm][a]**	**Th/U[a]**	**$^{207}Pb/^{235}U$[b]**	**2 σ[d]**	**$^{206}Pb/^{238}U$[b]**	**2 σ[d]**	**rho[c]**	**$^{207}Pb/^{206}Pb$[e]**	**2 σ[d]**	**$^{207}Pb/^{235}U$**	**2 σ**	**$^{206}Pb/^{238}U$**	**2 σ**	**$^{207}Pb/^{206}Pb$**	**2 σ**	**%**
CK19_020	84	28	0.53	5.42	0.15	0.339	0.007	0.71	0.1161	0.0023	1888	52	1881	32	1897	35	99
CK19_021	197	90	0.74	11.22	0.26	0.459	0.008	0.79	0.1773	0.0025	2542	58	2436	37	2628	23	93
CK19_022	604	110	0.88	3.40	0.09	0.181	0.003	0.71	0.1360	0.0026	1505	41	1075	19	2177	33	49
CK19_023	56	19	1.38	5.18	0.17	0.332	0.007	0.65	0.1132	0.0028	1850	60	1848	34	1852	45	100
CK19_024	101	34	0.71	5.24	0.14	0.333	0.006	0.71	0.1141	0.0021	1859	50	1854	31	1865	34	99
CK19_025	88	30	0.84	5.28	0.15	0.335	0.007	0.69	0.1142	0.0023	1865	53	1864	32	1867	37	100
CK19_026	112	38	0.69	5.48	0.14	0.342	0.006	0.72	0.1162	0.0021	1897	50	1896	31	1899	33	100
CK19_028	64	23	0.93	6.01	0.18	0.358	0.007	0.67	0.1216	0.0027	1977	60	1974	35	1979	39	100
CK19_029	172	85	0.55	11.78	0.28	0.492	0.009	0.77	0.1737	0.0026	2587	61	2579	39	2594	25	99
CK19_030	73	36	0.69	11.90	0.48	0.494	0.013	0.65	0.1749	0.0053	2597	105	2587	56	2605	50	99
CK19_032	107	35	1.10	5.10	0.16	0.330	0.007	0.66	0.1123	0.0026	1836	57	1836	33	1837	42	100
CK19_033	102	37	0.99	6.05	0.17	0.360	0.007	0.69	0.1220	0.0025	1984	56	1983	33	1985	36	100
CK19_034	117	50	0.31	8.79	0.22	0.433	0.008	0.75	0.1474	0.0024	2317	57	2318	36	2315	28	100

				RATIOS							AGES [Ma]						Conc.
Analysis	**U [ppm][a]**	**Pb [ppm][a]**	**Th/U[a]**	**$^{207}Pb/^{235}U$[b]**	**2 σ[d]**	**$^{206}Pb/^{238}U$[b]**	**2 σ[d]**	**rho[c]**	**$^{207}Pb/^{206}Pb$[e]**	**2 σ[d]**	**$^{207}Pb/^{235}U$**	**2 σ**	**$^{206}Pb/^{238}U$**	**2 σ**	**$^{207}Pb/^{206}Pb$**	**2 σ**	**%**
CK19_035	147	62	0.50	8.22	0.20	0.419	0.008	0.76	0.1424	0.0022	2256	54	2255	35	2256	27	100
CK19_036	242	89	0.21	6.31	0.15	0.368	0.007	0.77	0.1245	0.0018	2020	47	2019	31	2021	26	100
CK19_037	212	82	0.35	7.06	0.17	0.389	0.007	0.76	0.1318	0.0020	2120	50	2117	32	2122	27	100
CK19_038	145	53	0.75	6.14	0.15	0.363	0.007	0.73	0.1226	0.0021	1995	50	1996	32	1995	30	100
CK19_039	460	138	1.01	5.88	0.13	0.301	0.005	0.78	0.1419	0.0020	1959	44	1695	26	2251	24	75
CK19_040	24	12	1.09	12.14	0.76	0.501	0.019	0.61	0.1760	0.0088	2616	165	2616	83	2615	82	100
CK19_041	100	51	1.18	13.00	0.46	0.512	0.012	0.67	0.1842	0.0048	2680	95	2666	52	2691	43	99
CK19_042	139	47	0.69	5.43	0.14	0.340	0.006	0.72	0.1157	0.0021	1890	48	1889	30	1891	32	100
CK19_043	147	49	1.03	5.29	0.14	0.336	0.006	0.71	0.1142	0.0021	1867	49	1867	30	1867	34	100
CK19_044	64	21	0.68	5.28	0.16	0.335	0.007	0.66	0.1144	0.0027	1866	58	1862	33	1870	42	100
CK19_045	117	40	0.76	5.57	0.15	0.345	0.007	0.70	0.1171	0.0022	1911	51	1911	31	1912	34	100
CK19_046	98	31	1.13	4.73	0.13	0.316	0.006	0.68	0.1087	0.0022	1773	50	1769	30	1777	37	100
CK19_047	76	24	0.66	4.88	0.15	0.320	0.006	0.65	0.1107	0.0026	1800	56	1790	32	1811	43	99

				RATIOS							AGES [Ma]						Conc.
Analysis	**U [ppm][a]**	**Pb [ppm][a]**	**Th/U[a]**	**$^{207}Pb/^{235}U$[b]**	**2 σ[d]**	**$^{206}Pb/^{238}U$[b]**	**2 σ[d]**	**rho[c]**	**$^{207}Pb/^{206}Pb$[e]**	**2 σ[d]**	**$^{207}Pb/^{235}U$**	**2 σ**	**$^{206}Pb/^{238}U$**	**2 σ**	**$^{207}Pb/^{206}Pb$**	**2 σ**	**%**
CK19_048	84	28	1.22	5.31	0.21	0.335	0.008	0.59	0.1150	0.0037	1871	76	1862	39	1880	58	99
CK19_049	126	43	1.03	5.50	0.15	0.343	0.006	0.70	0.1163	0.0022	1901	51	1901	31	1900	34	100
CK19_050	93	32	0.61	5.43	0.15	0.341	0.007	0.68	0.1156	0.0024	1890	53	1891	32	1889	37	100
CK19_051	330	167	0.46	12.55	0.29	0.507	0.009	0.76	0.1795	0.0027	2647	62	2645	39	2648	25	100
CK19_052	44	16	1.12	6.01	0.20	0.358	0.008	0.64	0.1216	0.0032	1977	67	1974	37	1980	47	100
CK19_053	219	81	0.35	6.92	0.17	0.369	0.007	0.74	0.1360	0.0023	2101	52	2025	31	2177	29	93
CK19_055	68	22	0.63	5.12	0.16	0.330	0.007	0.65	0.1125	0.0026	1840	56	1840	32	1841	41	100
CK19_056	142	54	0.69	6.68	0.19	0.379	0.007	0.69	0.1280	0.0026	2070	58	2071	34	2070	35	100
CK19_057	68	34	0.57	12.38	0.34	0.505	0.010	0.72	0.1778	0.0034	2634	72	2635	42	2633	31	100
CK19_058	126	87	0.48	27.29	0.65	0.694	0.013	0.76	0.2853	0.0044	3394	81	3397	48	3392	24	100
CK19_059	208	79	0.55	6.79	0.17	0.382	0.007	0.73	0.1290	0.0022	2084	51	2083	32	2085	29	100
CK19_060	168	57	0.68	5.37	0.14	0.338	0.006	0.71	0.1153	0.0021	1881	49	1877	30	1885	32	100
CK19_061	277	80	0.87	4.66	0.12	0.290	0.005	0.72	0.1163	0.0020	1760	43	1644	26	1900	31	86

				RATIOS							AGES [Ma]						Conc.
Analysis	**U [ppm][a]**	**Pb [ppm][a]**	**Th/U[a]**	**$^{207}Pb/^{235}U$[b]**	**2 σ[d]**	**$^{206}Pb/^{238}U$[b]**	**2 σ[d]**	**rho[c]**	**$^{207}Pb/^{206}Pb$[e]**	**2 σ[d]**	**$^{207}Pb/^{235}U$**	**2 σ**	**$^{206}Pb/^{238}U$**	**2 σ**	**$^{207}Pb/^{206}Pb$**	**2 σ**	**%**
CK19_06 2	769	184	0.70	5.20	0.12	0.240	0.004	0.75	0.1575	0.0024	1853	43	1385	22	2429	26	57
CK19_06 3	114	36	1.38	4.74	0.15	0.315	0.006	0.63	0.1090	0.0027	1774	57	1766	32	1783	45	99
CK19_06 4	79	27	0.97	5.50	0.17	0.343	0.007	0.65	0.1162	0.0028	1900	59	1901	33	1899	42	100
CK19_06 5	715	176	0.84	6.04	0.14	0.246	0.004	0.75	0.1781	0.0027	1982	46	1419	22	2635	25	54
CK19_06 6	774	140	1.15	4.47	0.11	0.181	0.003	0.74	0.1789	0.0029	1726	41	1074	17	2643	27	41
CK19_06 7	153	33	1.67	3.84	0.11	0.212	0.004	0.67	0.1311	0.0028	1601	46	1242	22	2112	37	59
CK19_06 8	174	18	2.51	1.86	0.06	0.106	0.002	0.63	0.1277	0.0032	1067	34	647	12	2066	44	31
CK19_06 9	121	30	1.35	3.86	0.11	0.249	0.005	0.65	0.1125	0.0025	1605	47	1432	25	1841	40	78
CK19_07 0	98	52	0.57	13.96	0.37	0.529	0.010	0.71	0.1915	0.0036	2747	73	2737	42	2755	31	99
CK19_07 1	135	48	0.82	6.04	0.16	0.360	0.007	0.68	0.1216	0.0024	1981	54	1983	32	1979	35	100
CK19_07 2	134	47	0.71	5.77	0.18	0.351	0.007	0.64	0.1192	0.0029	1942	62	1939	34	1944	44	100
CK19_07 4	125	45	0.72	6.04	0.17	0.360	0.007	0.67	0.1216	0.0025	1982	56	1984	32	1980	37	100
CK19_07 5	130	47	0.75	6.06	0.17	0.361	0.007	0.68	0.1216	0.0025	1984	55	1988	32	1980	37	100